

# INVESTIGATION OF THE FRACTURE CHARACTERISTICS OF LAMELLAR NANOCOMPOSITES AND *IN SITU*-FORMED COMPOSITES DESIGNED FOR HIGH TEMPERATURE SERVICE

By

David L. Davidson  
Kwai S. Chan

## AFOSR FINAL REPORT Volume I. Nb-Based Materials Development

This research was sponsored by the Air Force Office of Scientific Research,  
Directorate of Aerospace and Materials Science  
Under Contract F49620-95-C-0043  
Approved for Release; Distribution Unlimited

*The views and conclusions contained in this document are those of the authors and should not be interpreted as necessarily representing the official policies or endorsements, either expressed or implied, of the Air Force Office of Scientific Research or the U.S. Government*

October 1998



*AFOSR Quality Award*  
**SOUTHWEST RESEARCH INSTITUTE**  
SAN ANTONIO      HOUSTON  
DETROIT      WASHINGTON, DC

02 NOV 1998

# INVESTIGATION OF THE FRACTURE CHARACTERISTICS OF LAMELLAR NANOCOMPOSITES AND *IN SITU*-FORMED COMPOSITES DESIGNED FOR HIGH TEMPERATURE SERVICE

By

David L. Davidson  
Kwai S. Chan

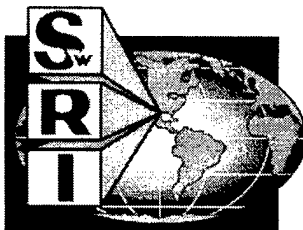
AFOSR FINAL REPORT  
Volume I. Nb-Based Materials Development

This research was sponsored by the Air Force Office of Scientific Research,  
Directorate of Aerospace and Materials Science  
Under Contract F49620-95-C-0043  
Approved for Release; Distribution Unlimited

**APPROVED:**

19981127 077

James Lankford, Ph.D., Director  
Materials Engineering Department



## REPORT DOCUMENTATION PAGE

proved  
0704-0188

ata sources, gathering  
collection of information.  
, Suite 1204, Arlington.

# REPORT DOCUMENTATION PAGE

proved  
0704-0188

AFRL-SR-BL-TR-98-

0756

ata sources, gathering  
collection of information,  
, Suite 1204, Arlington.

<p>Public reporting burden for this collection of information is estimated to average 1 hour per response, in and maintaining the data needed, and completing and reviewing the collection of information. Send comments including suggestions for reducing this burden, to Washington Headquarters Services, Directorate for Information Operations and Reports, 12202-4302, and to the Office of Management and Budget, Paperwork Reduction Project (0704-0188).</p>			
<b>1. AGENCY USE ONLY (Leave Blank)</b>	<b>2. REPORT DATE</b> October 1998	<b>3. REPORT TYPE AND DATES COVERED</b> Final Report, 9/1/95 through 10/31/98	
<b>4. TITLE AND SUBTITLE</b> Investigation of the Fracture Characteristics of Lamellar Nanocomposites and <i>In Situ</i> -Formed Composites Designed for High Temperature Service -- Vol. I. Nb-Based Materials Development		<b>5. FUNDING NUMBERS</b>	
<b>6. AUTHOR(S)</b> David L. Davidson and Kwai S. Chan			
<b>7. PERFORMING ORGANIZATION NAME(S) AND ADDRESS(ES)</b> Southwest Research Institute 6220 Culebra Road San Antonio, TX 78238		<b>8. PERFORMING ORGANIZATION REPORT NUMBER</b> 06-7275	
<b>9. SPONSORING/MONITORING AGENCY NAME(S) AND ADDRESS(ES)</b> AFOSR 801 North Randolph Street, Mail Room 732 Arlington, VA 22203-1977		<b>10. SPONSORING/MONITORING AGENCY REPORT NUMBER</b> F49620-95-C-0043	
<b>11. SUPPLEMENTARY NOTES</b>			
<b>12a. DISTRIBUTION/AVAILABILITY STATEMENT</b> APPROVED FOR PUBLIC RELEASE; DISTRIBUTION IS UNLIMITED		<b>12b. DISTRIBUTION CODE</b>	
<b>13. ABSTRACT (Maximum 200 words)</b>  <p>There were three objectives: (1) Determine the origin of high fracture toughness for the 50Nb-13Cr-37Ti alloy. (2) Increase the fracture toughness of composites containing 40 v/o Cr<sub>2</sub>Nb. (3) Determine the influence of Al on the fracture resistance of the 50Nb-13Cr-37Ti alloy. The high fracture toughness of the alloy was explained by finding that (1) alloying Nb-Cr with Ti has little effect on the emission from the crack tip. (2) Adding Ti decreased the P-N stress, especially for edge dislocations. (3) The detailed crack tip analysis confirmed the ease of deformation at the crack tip, and TEM confirmed that edge dislocations were moving easier than screws.</p> <p>The low fracture toughness of the in situ composites were found to be caused by (1) fracture of the large Cr<sub>2</sub>Nb particles, and (2) constraint of deformation in the matrix by the particles. The microstructure of the in situ composites was modified by rapid solidification and mechanical alloying to reduce particle size. Both these fabrication methods resulted in reduction of the size of the Cr<sub>2</sub>Nb particles, but the magnitude of the fracture toughness was not increased. Constraint was measured and found to be high in these composites. Modeling indicated that the highest fracture toughness that could be expected was 25 MPa<math>\sqrt{m}</math>.</p> <p>When all these results are considered together, it appears that high fracture toughness values at ambient temperatures cannot be obtained in composites with Cr<sub>2</sub>Nb particles, because they do not deform. If the particles are small enough to prevent their fracture, then they provide so much constraint that plasticity in the matrix is limited to values that prevent the achievement of high fracture toughness. Fracture studies of in situ composites containing Nb<sub>5</sub>Si<sub>3</sub> indicated that particles of this intermetallic deform before breaking near a crack tip. Therefore, composites based on this intermetallic may be preferable to those based on Cr<sub>2</sub>Nb.</p>			
<b>14. SUBJECT TERMS</b>		<b>15. NUMBER OF PAGES</b>	
		<b>16. PRICE CODE</b>	
<b>17. SECURITY CLASSIFICATION OF REPORT</b> UNCLASSIFIED	<b>18. SECURITY CLASSIFICATION OF THIS PAGE</b> UNCLASSIFIED	<b>19. SECURITY CLASSIFICATION</b> UNCLASSIFIED	<b>20. LIMITATION OF ABSTRACT</b>

# Table of Contents

## Vol. I

### **Executive Summary**

### **Introduction**

#### **Fracture Toughness and Fatigue Crack Growth in Rapidly Quenched Nb-Cr-Ti In Situ Composites**

#### **The Fatigue and Fracture Resistance of a Nb-Cr-Ti-Al Alloy**

#### **Microstructural and Fracture Characterization of Nb-Cr-Ti Mechanically Alloyed Materials**

#### **Fatigue and Fracture Toughness of a Commercially Made Nb-Ti-Base Single Phase Alloy at Ambient Temperature**

#### **The Fracture of Lamellar Composites**

#### **Cluster Model for Calculation of Unstable Stacking Energy to Assist in the Alloying of Transition Metals**

#### **Transition Metal Alloys: Elastic Properties and Peierls-Nabarro Stresses**

#### **Effects of Ti Addition on Cleavage Fracture in Nb-Cr-Ti Solid Solution Alloys**

#### **Optimizing the Design of Particulate Composites for Maximum Fracture Resistance Through Modeling**

#### **Tensile Experiments with a High Toughness Niobium Alloy at Ambient Temperature**

#### **Transmission Electron Microscopy of Nb-Base Alloy and Composite**

#### **FEM Simulation of Effects of Microstructure, Stress State, and Interface Strength on Flow Localization and Constraint Development in Nb/Cr<sub>2</sub>Nb *In-Situ* Composites**

#### **Evidence of Void Nucleation and Growth on Planar Slip Bands in a Nb-Cr-Ti Alloy**

#### **Summary and Conclusions**

#### **Publications from this Program**

## EXECUTIVE SUMMARY

The current program had three objectives: (1) Explain the reasons for the high fracture toughness of the 50Nb-13Cr-37Ti alloy. This material formed the matrix for several *in situ* composites containing Cr<sub>2</sub>Nb particles. (2) Increase the fracture toughness of composites containing  $\approx$  40 v/o Cr<sub>2</sub>Nb, or explain why high fracture toughness values cannot be increased. (3) Determine the influence of Al on the fracture resistance of the 50Nb-13Cr-37Ti alloy.

The tasks undertaken to explain the high fracture toughness of the 50Nb-13Cr-37Ti alloy were: (1) perform a detailed experimental crack tip analysis, (2) devise a model for computing the effect of alloying on the unstable stacking energy that assesses the ease of dislocation emission at crack tips, (3) compute the anisotropic Peierls-Nabarro (P-N) stress for edge and screw dislocations and how they were affected by alloying, and (4) perform transmission electron microscopy (TEM) on the deformed alloy.

The high fracture toughness of the 50Nb-13Cr-37Ti alloy was explained by finding that (1) alloying Nb-Cr with Ti has little effect on the emission from the crack tip, but (2) adding Ti decreases the P-N stress, especially for edge dislocations, thereby making dislocation motion easier and the plastic zone larger. (3) The detailed crack tip analysis confirmed the ease of deformation at the crack tip, and TEM confirmed that edge dislocations were moving easier than screws.

The tasks undertaken to examine the low fracture toughness of the Nb-Cr-Ti *in situ* composites were: (1) perform a detailed experimental crack tip analysis, (2) measure and compute the constraining effect of particles on matrix deformation, (3) model the fracture process so that microstructure could be described that would optimize fracture toughness, and (4) fabricate altered microstructures to examine the concepts derived.

The low fracture toughness of the *in situ* composites were found to be caused by (1) fracture of the large Cr<sub>2</sub>Nb particles and (2) constraint of deformation in the matrix by the particles. Modeling indicated that the size of the Cr<sub>2</sub>Nb should be reduced to avoid fracture, but that particle size reduction would increase constraint; therefore, there was an optimum size for the particles.

The microstructure of the *in situ* composites was modified by rapid

solidification and mechanical alloying to reduce particle size. Both of these fabrication methods resulted in reduction of the size of the  $\text{Cr}_2\text{Nb}$  particles, but the magnitude of the fracture toughness was not increased. Constraint was measured and found to be high in these composites. The model indicated that the highest fracture toughness that could be expected from an optimum microstructure was  $\approx 25 \text{ MPa}\sqrt{\text{m}}$ .

Examination of one of the mechanically alloyed materials by TEM indicated that the heat treatment that precipitated the  $\text{Cr}_2\text{Nb}$  particles altered the composition of the matrix, thereby lowering its toughness.

When all these results are considered together, it appears that high fracture toughness values at ambient temperatures cannot be obtained in composites with  $\text{Cr}_2\text{Nb}$  particles, because they cannot be deformed. If the particles are small enough to prevent their fracture, then they provide so much constraint that plasticity in the matrix is limited to values that prevent the achievement of high fracture toughness.

Detailed fracture studies of *in situ* composites containing  $\text{Nb}_5\text{Si}_3$  indicated that particles of this intermetallic could deform before breaking in the elevated stress field of a crack tip. Therefore, composites based on this intermetallic may be preferable to those based on  $\text{Cr}_2\text{Nb}$ .

Single phase alloys containing Cr and Al were found to have lower fracture toughness values than alloys containing only Cr. Estimation of the USE indicates that Al raises its magnitude. A recent TEM study indicates that if the concentration of Al exceeds 4 at.%, then the bcc lattice will order, becoming B2. The reasons that Al addition decreases fracture toughness are that USE is increased, thereby making dislocation emission from a crack tip more difficult, and ordering makes motion of dislocations in the plastic zone more difficult. Both of these factors lower fracture toughness.

Fatigue crack growth resistance of all the materials examined were similar. At very low growth rates, the slope of the crack growth rate - stress intensity factor curve was very high, while above a rate of  $10^{-9} \text{ m/cycle}$ , the slope of the growth rate curve was dependent on the fracture toughness. Threshold stress intensity factors were in the range  $6 \pm 1 \text{ MPa}\sqrt{\text{m}}$ , with materials containing Al on the low side and materials containing  $\text{Cr}_2\text{Nb}$  on the high side.

## INTRODUCTION

As the previous program was completed, the fatigue crack growth and fast fracture characteristics of a series of Nb-Cr-Ti alloys and *in situ* composites had been investigated. A high toughness matrix alloy had been identified with the composition of 50Nb-13Cr-23Ti, and a much lower toughness composite containing about 35 volume % Cr<sub>2</sub>Nb had been investigated. The reasons for the low toughness of the composite were still under investigation, but it had been determined that fracture of the relatively large Cr<sub>2</sub>Nb intermetallic particles was one factor.

The current program has had a number of objectives: (1) to obtain microstructural control over the composite architecture so that fracture properties could be optimized, and (2) to explain how alloying led to the attainment of the high fracture toughness of the matrix alloy. To achieve objective (1), a number of materials made by different manufacturing methods were obtained and evaluated. To achieve objective (2), detailed experiments and computations were performed.

Microstructural control of these composites was accomplished by the use of several fabrication techniques for making materials. The first technique that was available was rapid solidification, then the plasma arc melting process was used, and finally, mechanical alloying was used.

Rapid solidification: United Technologies Research Center made a series of composites that had been rapidly solidified in order to decrease the size of the intermetallic, which would decrease the probability of particle fracture during crack growth. These rapidly solidified alloys had very different microstructures than previously investigated. The intermetallic was much smaller than obtained through conventional solidification, but it was not in the form of well dispersed particles. Instead, the intermetallic was highly connected in strings and clumps, and, in many ways, it could be considered to be as large as in the slow cooled composites. These materials were characterized metallographically and fracture toughness was measured. These results are given in detail in [x,y] and are summarized in **Chapter 1**.

Plasma arc melting: Los Alamos National Laboratory prepared several materials, at no charge, using plasma arc melting, that were evaluated by our program. A summary of the material, its characteristics, and our evaluation is given in **Chapter 2**.

Mechanical alloying: The Defence Research Agency, Farnborough, UK, as a subcontractor, prepared several materials by mechanical alloying and hot isostatic press consolidation using their proprietary equipment built especially to prevent interstitial contamination of reactive metals. With these materials, more microstructural control was achieved than by any of the other methods of materials production. The results of microstructural and fracture toughness evaluations of these materials is included in **Chapter 3**.

Industrial processing: Reference Metals Company, Inc., furnished, a single phase alloy of composition similar to our high toughness matrix material. This material was made by "industrial processing." Our description of the processing and evaluation of the microstructure and fracture characteristics of this alloy is included in **Chapter 4**.

Lamellar composites were also investigated in the current program. The Basic Industrial Research Laboratory (BIRL) of Northwestern University made some of the materials evaluated under contract, and Johns Hopkins University provided some composites made under another contract from AFOSR. BIRL experienced considerable difficulty in preparing useful materials, and the effort ended when the laboratory was disbanded. The material from Johns Hopkins was much better, and it was possible to evaluate partially the fracture characteristics of this material. The results of this effort are included in **Chapter 5**.

Atomic bonding to explain the effects of alloying was used as a tool for examining the effects of alloying elements. A cluster model was developed to examine the effects of alloying on the generation of dislocations at crack tips. A summary of this work is included as **Chapter 6**.

The anisotropic Peierls-Nabarro stresses were computed from elastic constants found in the literature for edge and screw dislocation motion on the {110} and {112}. The results of these computations are given in **Chapter 7**.

The high fracture toughness of the single phase 50Nb-13Cr-37Ti alloy was investigated using several modeling procedures, in conjunction with detailed fracture experiments. From this work, an explanation has been offered that is based on theoretical analysis, fracture mechanics, and metal physics. This work is summarized in **Chapter 8**.

A model for optimizing the fracture toughness of particulate composites was developed that is based on the experimental determination of the constraint caused by non-deforming particles dispersed in a ductile matrix. Besides constraint, the model includes the effects of particle size and fracture toughness, and deformation characteristics of the matrix. The model can be used to determine what effects particle size, volume fraction, and toughness have on the overall fracture toughness of the composite. This model can be used as an aid in guiding development of the high toughness composites and for determining the limitations of any composite design. The model is developed in **Chapter 9**.

Tensile experiments were conducted on the single phase material 50Nb-13Cr-23Ti to better understand the origin of its excellent fracture resistance. The results of macroscopic and microscopic strain measurements are given in **Chapter 10**.

Transmission electron microscopy of the single phase 50Nb-13Cr-23Ti and one of the mechanically alloyed materials was accomplished using the facilities at Oak Ridge National Laboratory under the SHARE program. Some of the results obtained to date are given in **Chapter 11**.

FEM model to simulate stress state, microstructure and interface strength of particulate reinforced composites. The results are given in **Chapter 12**.

A model for void formation on planar slip bands in Nb-Cr-Ti alloys is given in **Chapter 13**.

# **Fracture Toughness and Fatigue Crack Growth in Rapidly Quenched Nb-Cr-Ti In Situ Composites**

**K. S. Chan, D. L. Davidson, and D. L. Anton**

**Metallurgical and Materials Transactions A**

## FRACTURE TOUGHNESS AND FATIGUE CRACK GROWTH IN RAPIDLY QUENCHED Nb-Cr-Ti IN SITU COMPOSITES

K.S. Chan and D.L. Davidson  
Southwest Research Institute  
San Antonio, TX 78228

D.L. Anton  
United Technologies Research Center  
East Hartford, CT 06108

### SUMMARY OF THE PUBLISHED PAPER

*In situ* composites of several Nb-Cr-Ti compositions that had previously been made by casting technology were processed by rapid solidification to reduce the size of the reinforcing intermetallic phase. Previous results of a fracture analysis had shown that reduction in the size of the Cr<sub>2</sub>Nb particles would be expected to increase the fracture toughness of these composites. Nominal compositions of these materials were (37-43)Nb-(31-34)Cr-(26-28)Ti, (35-40)Nb-(40-44)Cr-20Ti, and (42-52)Nb-(28-33)Cr-(20-25)Ti. The materials averaged about 0.12 wt. ppm of oxygen, which is rather high for a good Nb-base alloy.

Fracture toughness values of these materials, as shown in **Fig. 1**, were in the range 7.5 to 9.6 MPa $\sqrt{m}$ , as compared to 13 to 19 MPa $\sqrt{m}$  for similar compositions in the slow cooled materials.

The microstructures that resulted from rapid solidification are shown in **Fig. 2**. The sizes of the Cr<sub>2</sub>Nb particles are 1-4  $\mu$ m, but the contiguity of particles is high. The reduction in Cr<sub>2</sub>Nb by rapid solidification was to about 2  $\mu$ m from 17  $\mu$ m as obtained by slow cooling.

The reasons found for the low fracture toughness of these materials were:

1. The poor dispersion, or high degree of contiguity, of the Cr<sub>2</sub>Nb particles caused high constraint in the matrix, thereby preventing deformation of the matrix that resulted in a low crack tip fracture strain and a small plastic zone size.
2. The high oxygen level in the material limited its ductility.

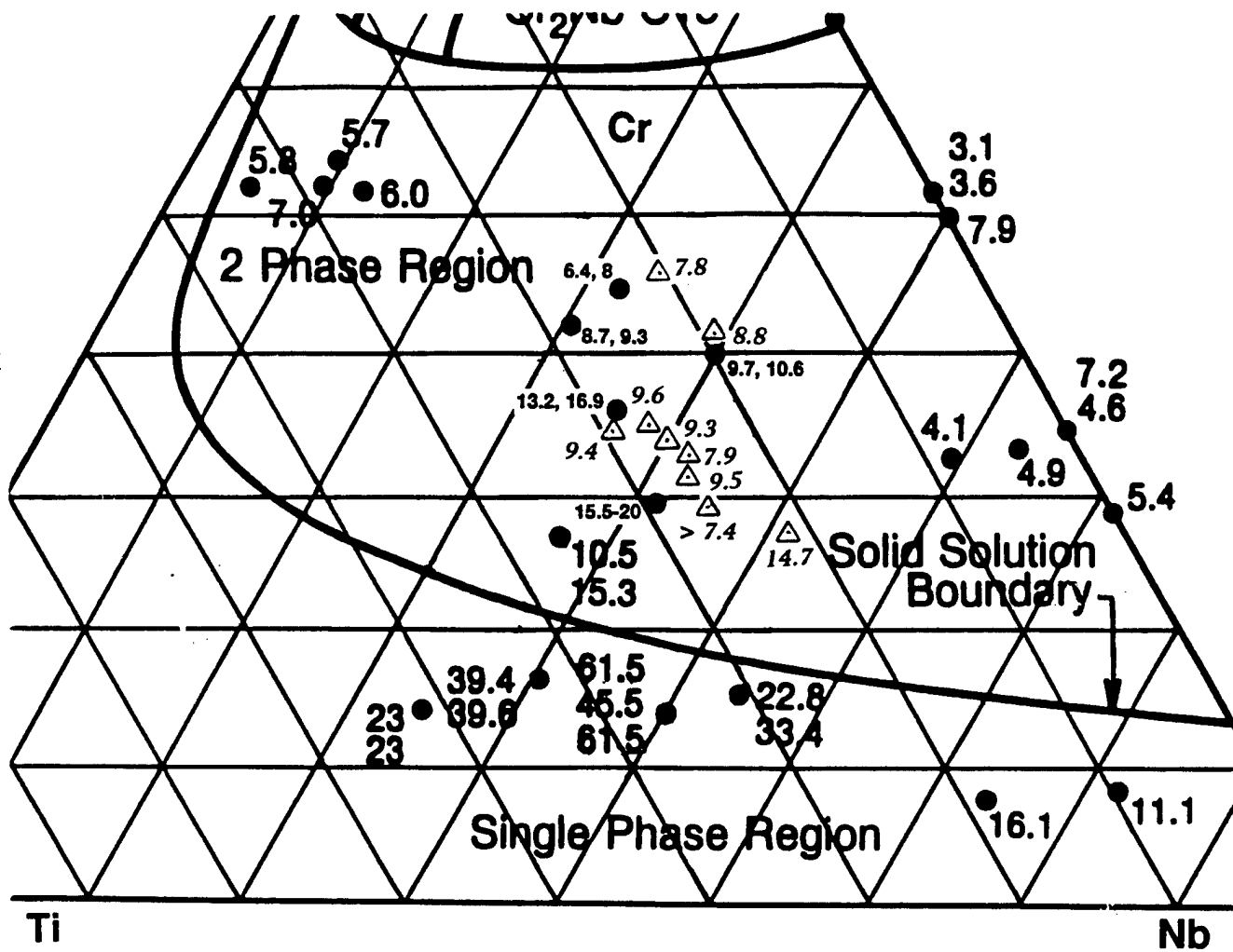


Fig. 1 Center section of the Nb-Cr-Ti phase diagram (1400°C isotherm) showing fracture toughness values of slowly solidified materials (●) and rapidly solidified materials (△).

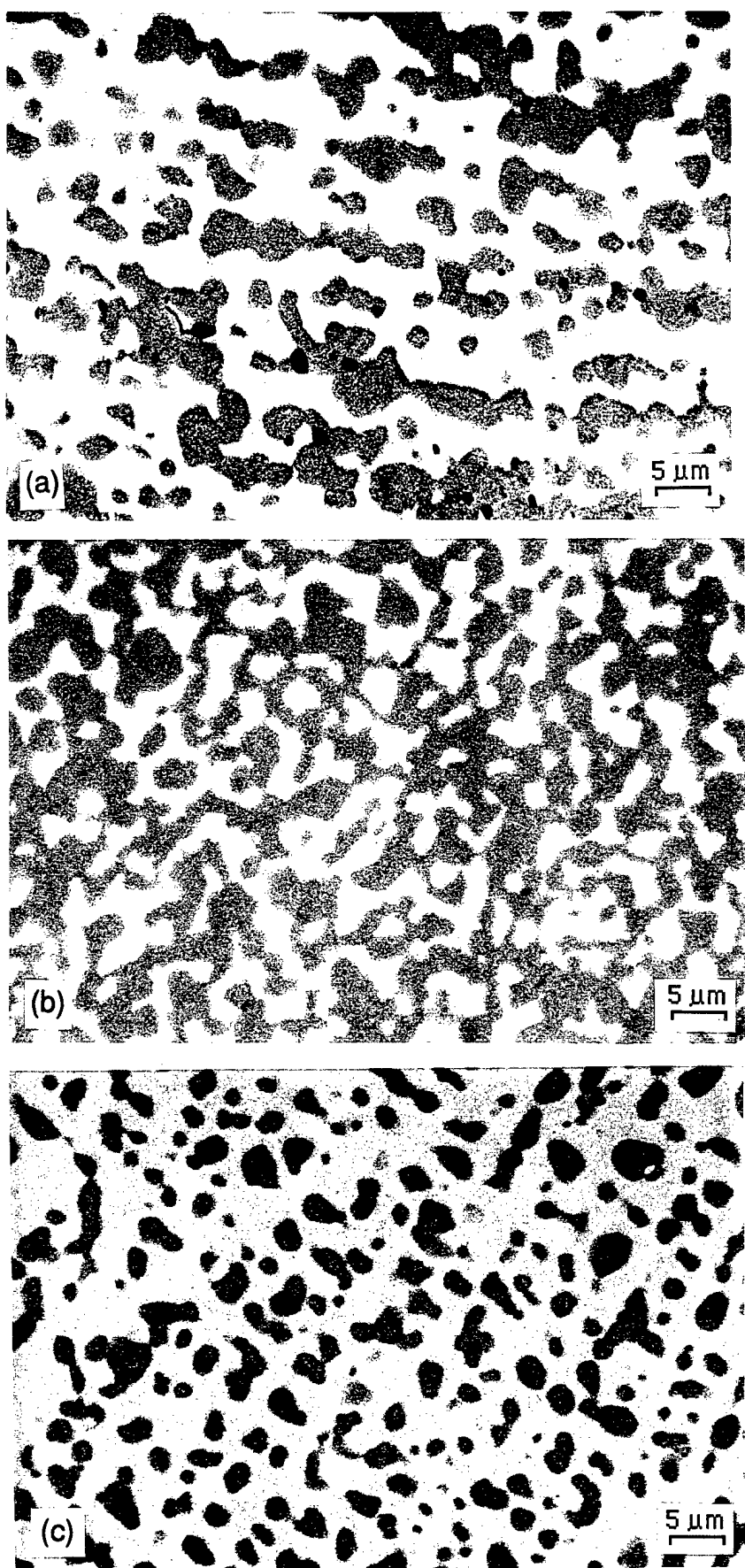


Fig. 2 Backscattered electron images. (a) (37-43)Nb-(31-34)Cr-(26-28)Ti, containing 30-38 v/o  $\text{Cr}_2\text{Nb}$ , (b) (35-40)Nb-(40-44)Cr-20Ti containing 70-80 v/o  $\text{Cr}_2\text{Nb}$ , and (c) (42-52)Nb-(28-33)Cr-(20-25)Ti containing 20-35 v/o  $\text{Cr}_2\text{Nb}$ .

# **The Fatigue and Fracture Resistance of a Nb-Cr-Ti-Al Alloy**

**D. L. Davidson and K. S. Chan**

**Metallurgical and Materials Transactions A**

**(in review)**

# The Fatigue and Fracture Resistance of a Nb-Cr-Ti-Al Alloy

D. L. Davidson and K. S. Chan

Southwest Research Institute  
San Antonio, TX 78238

## Abstract

The microstructure, fatigue, and fracture behavior of a cast and heat-treated Nb-Cr-Ti-Al alloy were investigated. The microstructure of the cast alloy was manipulated by annealing at a temperature ranging from 500°C to 1500°C for 1 to 24 hrs. Heat-treatment produced Cr<sub>2</sub>Nb precipitates along grain boundaries in all cases except in the 500°C heat-treated material. Fracture toughness tests indicated low fracture resistance in both the as-cast and heat-treated materials. Fatigue crack growth tests performed on the 500°C heat-treated material also indicated a low fatigue crack growth resistance. Direct observations of the near-tip region revealed a cleavage dominated fracture process, in accordance with fractographic evidence. The fracture behavior of the Nb-Cr-Ti-Al alloy was compared against those of other Nb-Cr-Ti alloys and theoretical calculations of unstable stacking energy and Peierl-Nabarro barrier energy. Both the experimental and theoretical results are used to elucidate the role of Al addition in cleavage fracture of the Nb-Cr-Ti-Al alloy. The results indicate that Al alloying addition increases the unstable stacking energy which, in turn, prevents the emission of dislocations, promotes the nucleation and propagation of cleavage cracks from the crack tip, and leads to a reduction in the fracture toughness.

## Introduction

Recent studies have shown that fracture toughness on the order of 10 to 20 MPa $\sqrt{m}$  can be achieved in Nb-based *in-situ* composites based on Nb-Cr-Ti [1-3], Nb-Si [4-7], Nb-Al-Ti [8, 9], and Nb-Ti-Hf-Cr-Al-Si [10-13] systems. These materials are characterized by a two-phase microstructure comprised of intermetallic hard particles embedded in a solid solution matrix. In the Nb-Cr-Ti system, the intermetallic particles are Cr<sub>2</sub>Nb, which is a Laves phase with the C15 structure at ambient temperature [14, 15]. The Cr<sub>2</sub>Nb particles are brittle with a fracture toughness of about 1 MPa $\sqrt{m}$  [1-3]. Because of the low toughness of the particles, most, if not all, of the fracture toughness of the *in-situ* composites based on the Nb-Cr-Ti system originates from the matrix, which is a Nb solid solution containing Cr and Ti.

It has been demonstrated that Ti addition in the range of 30 to 40 at. pct. enhances the fracture resistance of Nb-Cr alloys by reducing the Peierl-Nabarro barrier energy and stress, thereby increasing the dislocation mobility [16]. This has the effect of promoting the emission of dislocations and suppressing the propagation of cleavage cracks from the

crack tip. As a result, the plane-strain fracture toughness of Nb-Cr-Ti solid solution alloys increases with increasing Ti contents. The presence of hard Cr<sub>2</sub>Nb particles increases the plastic constraint in the matrix and reduces the fracture resistance if the matrix phase does not have sufficient ductility. With a ductile Nb solid solution matrix, a fracture toughness as high as 20 MPa $\sqrt{m}$  has been achieved in Nb/Cr<sub>2</sub>Nb *in-situ* composites containing 38 vol. pct. Cr<sub>2</sub>Nb particles.

The oxidation resistance of Nb-Cr-Ti solid solution alloys and *in-situ* composites, however, is inadequate for high temperature applications. One possible means of increasing the oxidation resistance is to add Al to Nb-Cr-Ti to form solid solution alloys and *in-situ* composites based on the Nb-Cr-Ti-Al system. An example for the former is Nb-40Ti-10Cr-10Al and it is Nb-27Ti-10Cr-24Al for the latter [10]. Other alloying strategies include the addition of Hf and Si, which has been used to produce a variety of *in-situ* composites based on a solid solution matrix with either silicide particles, (Nb,Ti,Cr)<sub>2</sub>Al, or (Nb,Ti,Hf)<sub>2</sub>Al particles [10]. The characteristics of these emerging alloys and *in-situ* composites are summarized in recent review articles.[9-13]

The effect of Al addition on the fatigue and fracture properties of Nb-Cr-Ti-Al alloys is not well understood. Limited previous work on Nb-40Ti-10Cr-10Al indicated that the addition of Al to Nb-Cr-Ti solid solution alloys led to a reduction in the fracture toughness [3, 16]. When correlated with the fracture toughness of other Nb-Cr-Ti alloys on the basis of the number of d+s electrons per atom in the system, the Nb-40Ti-10Cr-10Al alloy showed a negative deviation from the trend line of increasing toughness with decreasing number of d + s electrons per atom [2]. The mechanism responsible for the decrease in fracture toughness with Al addition has not been established.

The objective of this article is to report results on the microstructure, fatigue, and fracture behavior of a cast Nb-Ti-Cr-Al alloy. The results of this alloy are compared against those of cast Nb-Ti-Cr and Nb-Ti-Cr-Al alloys in the literature to determine the effect of Al alloying addition on the fatigue and fracture resistance and the controlling fracture mechanism. In addition, theoretical calculations of the unstable stacking energy and Peierl-Nabarro barrier energy are performed to estimate the ease of dislocation nucleation at the crack tip and the dislocation mobility. These experimental and theoretical results are used to elucidate the effects of Al alloying addition and microstructure on the fatigue and fracture resistance of the Nb-Ti-Cr-Al alloy.

## Experimental Procedures

Materials: Three ingots were prepared at Los Alamos National Laboratory (LANL) from pure elements using the plasma arc melting method [17]. The three elements were melted in a 10 cm diameter water-cooled copper hearth. Each alloy was remelted six times to ensure homogeneous distribution of the elements. Two of the materials were similar to compositions from which previous results had been obtained, and one included aluminum because of its effect of increasing oxidation resistance of Nb alloys. Each ingot weighed approximately 1.8 kg. The designations of these alloys and the target compositions are shown in Table 1. Also in the table are the levels of interstitials measured by Los Alamos National Laboratory.

Table 1. A summary of LANL-made Nb-Cr-Ti-Al alloys investigated in this study.

Alloy Designation	Composition Atomic %				Interstitials ppm, weight		
	Nb	Cr	Ti	Al	O	N	C
LANL-1	50	13	37	-	690	17	-
LANL-2	37	36	27	-	690	18	-
LANL-3	46	11	34	9	820	60	-

LANL-1 was cut longitudinally and found to have a large piece of unalloyed Nb included in it. This material was returned to LANL for remelting, but higher priority work delayed the remelting, and it was not returned to us for further evaluation.

The microstructure of LANL-2 (37Nb-36Cr-27Ti) contained continuous networks of Cr<sub>2</sub>Nb particles along grain boundaries. This microstructure had previously been found to produce a low fracture toughness because of cracking along the grain boundaries [2]. Consequently, only a small effort was expended to screen the mechanical properties of this material. Fracture toughness values of 7.6 and 6.8 MPa $\sqrt{m}$  were measured using notched 3-point bend specimens.

The ingot of LANL-3 was cut axially in half using EDM, and a second cut was made to produce a slice approximately 3 mm thick. One side of this slab was polished and found to have several regions exhibiting different light diffraction and contrast conditions. A region of high porosity was found in the center in the last part of the ingot solidified. Hardness was measured at several locations on the slice and found to be somewhat different.

The slice taken from the ingot of LANL-3 was cut by EDM into 4 compact tension (CT) specimens approximately 25 mm square and two beams suitable for 3-point bend fracture toughness specimens. Composition of two of the CT specimens was checked by energy dispersive x-ray microprobe and found to be within less than 1 at. pct. of the desired composition. The fracture toughness of the as-received alloy was measured using a 3-point bend specimen as 18.5 MPa $\sqrt{m}$ , which was below expectations. Optical microscopy revealed only a single-phase microstructure.

## Microstructures

The as-received material, shown in Figure 1(a), showed a single phase, large-grained microstructure with an average grain size of 230  $\mu$ m. One of the possible reasons for the low fracture toughness of the as-received material was thought to be that the matrix contained a high dislocation content. Thus, heat treatment might recover, or possibly recrystallize the matrix, thereby increasing fracture toughness. Based on this reasoning, a series of heat treatments were conducted. The as-received material was encapsulated and given a 1-hr. anneal at a selected temperature followed by furnace-cool. The annealing temperature was 1000°C, 1200°C, 1350°C, or 1500°C. The heat-treated materials all

showed a two-phase microstructure containing precipitates mostly on the grain boundaries. Many of the grain boundary precipitates were continuous, but some took a pearl-string-like morphology, as illustrated in Figure 1 (c) to (f). Both are expected to lead to poor fracture toughness. The second phase particles were unexpected because the Nb-Cr-Ti ternary phase diagram suggested a single-phase solid solution. Apparently, the addition of Al altered the phase boundary, leading to the formation of the second phase particles on grain boundaries.

To prevent grain boundary precipitation, heat-treatment at 900°C for 24 hrs. and 500°C for 6 hrs. were also attempted, Figure 1(b). The former led to grain boundary precipitates, while the latter did not. To gage the effects of heat-treatment on mechanical properties, Vickers hardness and three-point bend fracture toughness were measured. Table 2 lists heat treatments and measured values of hardness and fracture toughness. The hardness value is the average of at least ten measurements, while the fracture toughness value is for an individual specimen.

Table 2. Heat treatment of LANL-3 and the corresponding results on hardness, fracture toughness, and volume fraction of  $\text{Cr}_2\text{Nb}$  particle.

No.	Heat Treatment		Vickers Hardness	Fracture Toughness	Volume Fraction of $\text{Cr}_2\text{Nb}$
	Temp, °C	Time, hrs	kg/mm <sup>2</sup>	MPa $\sqrt{\text{m}}$	%
1	as received	—	435	12.6, 15.5, 18.5	0
2	500	6	372	11.7, 15.2	0
3	1000	1	392	12.8	7.6
4	1200	1	410	—	3.7
5	1350	1	425	—	11
6	1500	1	432	—	1.2
7	900	24	485	—	8.1

It was apparent from these results that heating caused hardness to change from the as-received value, with a minimum at 500°C for 6 hrs., as shown in Figure 2. Increased hardness probably meant that  $\text{Cr}_2\text{Nb}$  was being precipitated. Examination of the material using X-ray diffraction indicated no intermetallic in the as-received material, and that heat treatment led to the precipitation of  $\text{Cr}_2\text{Nb}$ . All the peaks found during x-ray diffraction were either from the matrix or  $\text{Cr}_2\text{Nb}$ , except for the heat treatment at 1350°C which had 13 peaks that are unidentified. The volume fraction of intermetallic was estimated from the intensity of the  $\{311\}$  peak from  $\text{Cr}_2\text{Nb}$ , with the  $\{110\}$  peak of the matrix normalized to an intensity of 100%. The hardness trend is inconsistent with the amount of  $\text{Cr}_2\text{Nb}$  that was caused by heat treatment, as determined by x-ray diffraction. Using x-ray peak intensity to estimate volume fraction is known to have limited accuracy; perhaps this is the reason for the inconsistency. One specimen was heat treated to 1000°C for 1 hr. and broken in 3-point bending to measure fracture toughness:  $K_c = 12.8 \text{ MPa}\sqrt{\text{m}}$ , as listed in Table 2.

Lattice parameter of the matrix and Cr<sub>2</sub>Nb were determined from the x-ray diffraction peaks, and these are listed in Table 3. The relationship between amount of intermetallic and lattice parameter is shown in Figure 3. The structure of C15 is cubic and its unit cell is close to twice the size of the unit cell of the bcc matrix; thus, half the lattice parameter of Cr<sub>2</sub>Nb is shown in the figure. The difference between the two can be considered as the strain between the two lattices that would be required for them to be coherent. The average strain determined, Table 3, is about 7.5%, and there is no consistent variation with heat treatment or amount of intermetallic.

Table 3. Lattice parameters and strain of the LANL-3 alloy.

Heat Treatment	Lattice Parameter		Cr <sub>2</sub> Nb (Vol. %)	Lattice Strain (%)
	matrix (Å)	Cr <sub>2</sub> Nb (Å)		
as received	3.2380	-	0	-
500°C/6 hr	3.2388	-	0	-
1000°C/1 hr	3.2453	7.0253	7.5	8.2
1200°C/1 hr	3.2712	7.0007	3.7	7.0
1350°C/1 hr	3.2646	6.9791	11	6.9*
1500°C/1 hr	3.2406	7.0007	1.2	8.0
900°C/24 hr	3.3170	7.1385	8.1	7.6

\* 13 extra diffraction peaks

The lattice parameter of Cr<sub>2</sub>Nb decreases with addition of Ti, according to Thoma [15] as follows:

$$\text{Half the lattice parameter of Cr}_2\text{Nb} = 3.5125 - 0.00015(\text{at. \% Ti}) \quad (1)$$

If the data in Figure 3 are combined with Eq. (1), then it implies that the Cr<sub>2</sub>Nb that has precipitated in the alloy due to heat treatment incorporates Ti because the lattice parameter decreases with volume of Cr<sub>2</sub>Nb precipitated. When this occurs, the lattice parameter of the matrix increases because Ti has been removed by the formation of Cr<sub>2</sub>Nb(Ti). Diffusion of Ti from matrix to Cr<sub>2</sub>Nb lowers the incoherency strains between the two phases, as seen in Table 3.

The presence of Cr<sub>2</sub>Nb in this alloy, with only 11 at. pct. Cr, appears to indicate that the amount of Cr that could be kept in solid solution was lowered by addition of Al from about 15 at.% to maybe half that amount, or less. Since hardness was lowered somewhat by heat treatment at 500°C, it was concluded that this treatment might recover the matrix with the precipitation of a minimum of intermetallic. This heat treatment would allow the matrix to deform as much as possible, thereby maximizing the fracture toughness. Several CT specimens were prepared of the as-cast and the 500°C heat-treated materials for more detailed fracture evaluation.

Grain size was measured from the as-cast and one of the specimen that was heat treated to 500°C for 6 hrs. Grain size was determined from the number of intercepts of grain boundaries along a straight line. The grain size measured in this way was 230±60 µm.

## Fatigue and Fracture Testing

All but one specimen was notched and fatigue precracked under cyclic tensile loads at a ratio,  $R$ , of 0.1 and a starting  $\Delta K$  value of  $5 \text{ MPa}\sqrt{\text{m}}$  and a frequency of 10 Hz. One of the fracture toughness specimen was tested in the notched condition without a fatigue precrack. Fatigue and fracture toughness tests were performed in a servo-hydraulic testing machine and in a SEM equipped with a loading stage [18]. Fatigue tests were performed in air outside the SEM and periodically placed in the SEM for *in-situ* observations of the fatigue crack growth process and characterization of the near-tip deformation behavior. Fracture toughness tests were conducted in the SEM exclusively. To characterize the fracture process, the near-tip region was photographed as a function of the stress intensity factor and crack extension. Still photographs of the near-tip region under the unloaded and loaded conditions were analyzed via a machine-vision-based stereomimaging technique [19] to obtain the near-tip displacement and strain fields.

## Fatigue Crack Growth Results

Measurements of fatigue crack growth made from two CT-specimens of LANL-3 are shown in Figure 4. These specimens were cycled at  $R = 0.1$  in air at 10 Hz. Both specimens were heat treated to  $500^\circ\text{C}$  for 6 hrs. in vacuum. The first specimen (CT-1) broke unexpectedly while cycling in the laboratory machine at  $K_c = 11.7 \text{ MPa}\sqrt{\text{m}}$ . The crack in the second specimen (CT-2) was grown under  $5 < \Delta K < 14 \text{ MPa}\sqrt{\text{m}}$ . Several times this specimen was transferred to the SEM loading stage for measurement of crack opening load and to make photographs of the crack tip region for subsequent analysis. This specimen broke while being loaded in the SEM stage, giving a fracture toughness of  $K_c = 15.2 \text{ MPa}\sqrt{\text{m}}$ . Crack opening loads were directly measured in the SEM at  $K = 6.9$ , 7.2, and  $14 \text{ MPa}\sqrt{\text{m}}$ . As a fraction of the maximum load, the opening loads for these  $\Delta K$  levels were 0.65, 0.79, and 0.76, respectively.

Fatigue crack growth in this heat treatment of LANL-3 may be typified as being "intermittently critical" because of occasional and sudden, rapid crack growth. During one experiment while the specimen was being loaded in the SEM, the crack grew nearly  $50 \mu\text{m}$  and then arrested. This characteristic of crack growth is illustrated in Figure 5, where the lack of a smooth curve indicates the erratic nature of crack growth. The large scatter shown in Figure 4 is also thought to result from this crack growth behavior.

Crack tip analyses: Figures 6-8 show micromechanical analyses of the crack region at two interesting locations. The analysis shown in Figure 6 is for a crack growing approximately parallel to a grain boundary. Apparently, the grain on the right side is more favorably oriented for slip; thus, the plasticity within that grain is greater than in the grain containing the crack. The crack tip seen in Figure 7 is the same location, but the analysis is at higher resolution, showing that within the grain containing the crack tip, the strain distribution is relatively smooth with two shear bands emanating from the tip at high angles to the direction of crack growth, which is typical for a blunted crack tip. The grain boundary does not appear to cause a disturbance in the strain distribution.

The crack tip in the analysis shown in Figure 8 is within 2  $\mu\text{m}$  of a grain boundary that is about  $80^\circ$  to the direction of the crack growth. Stereoimaging indicated that what appears to be a crack parallel to the grain boundary was not opening due to the applied load. However, the misorientation of slip systems between the two grains has affected the distribution of strain much more than shown in the other examples.

**Fractography:** The fracture surface of LANL-2, shown in Figure 9, exhibited an extremely brittle appearance. The cleavage facets shown in the figure appear to be mainly transgranular, but some intergranular failure may also be seen. Much of the debris seen on the fracture surface is probably  $\text{Cr}_2\text{Nb}$  particles dislodged from the grain boundaries during fracture.

Fracture surfaces of LANL-3 are shown in Figures 10 and 11. Fatigue striations (periodic crack arrest marks) are seen on many transgranular fracture planes seen in Figure 10(a). The higher magnification view of Figure 10(b) shows the striations better, and indicated that the average spacing (about 25  $\mu\text{m}$ ) of the striations is much larger than the average crack growth rate (about 0.2  $\mu\text{m}/\text{cycle}$ ).

The fractography of fast fracture is shown in Figure 11. Planar surfaces at many angles to the loading axis, some nearly parallel to it, may be seen in Figure 11(a), and many of these fracture facets have little topography. The detail in Figure 11(b) shows that there are indications of slip on planes at an angle to the fracture plane; thus, the material flowed plastically during failure.

## Fracture Toughness Results

The K-resistance,  $K_R$ , curves for the as-received material are shown in Figure 12 for notched specimens with and without a fatigue precrack. The two  $K_R$  curves are similar indicating that the material is brittle and that plastic flow at the notch root is limited. For the cracked specimen, the onset of crack extension occurred at 11 MPa $\sqrt{\text{m}}$ . The fracture resistance increased to 14 MPa $\sqrt{\text{m}}$  with a crack extension of  $\approx 1300 \mu\text{m}$ . At 14.8 MPa $\sqrt{\text{m}}$ , the crack propagated and caused ultimate fracture at  $\approx 15.5 \text{ MPa}\sqrt{\text{m}}$ . For the notched specimen, crack initiation occurred at 8 MPa $\sqrt{\text{m}}$  and the fracture resistance increases with crack extension to  $\approx 12.6 \text{ MPa}\sqrt{\text{m}}$  at the onset of ultimate fracture.

A summary of the fracture process in the notched specimen is presented in Figure 13, which shows the near-tip region of the main crack at  $K = 8 \text{ MPa}\sqrt{\text{m}}$ . Examination of the crack tip at high magnification revealed that there was little plastic flow in the near-tip region and that there was no emission of slip from the crack tip. The crack path, in Figure 13, showed a series of cleavage cracks and grain boundary cracks separated by intact, though small, ligaments. Most of these ligaments were located between cleavage cracks and were able to sustain some plastic deformation, as shown in Figure 14. In other cases, the ligaments were located between cleavage cracks and grain boundary cracks. The presence of these ligaments in the crack wake gave rise to the resistance-curve behavior observed in this alloy. Eventually, these small ligaments were fractured upon loading and the specimen failed at  $K = 12.6 \text{ MPa}\sqrt{\text{m}}$ .

Figure 15 shows the near-tip region of the fatigue precracked specimen at  $K = 11 \text{ MPa}\sqrt{\text{m}}$ . A cleavage microcrack formed ahead of the main crack during fatigue. This cleavage microcrack opened up when the main crack was loaded. At  $11 \text{ MPa}\sqrt{\text{m}}$ , the crack grew toward the microcrack, reducing the width of the interconnecting ligament, while the tips of the micorcracks deflected and extended to lie normal to the applied stress. When  $K$  is increased to  $14 \text{ MPa}\sqrt{\text{m}}$ , at least two cleavage cracks nucleated and propagated unstably over a distance of  $\approx 1300 \mu\text{m}$ , running through grains and along grain boundaries, Figure 15(b). The cracks eventually all arrested. The crack path contained a few small ligaments which remained intact at  $K = 14.8 \text{ MPa}\sqrt{\text{m}}$ , but the specimen fractured at  $K = 15.5 \text{ MPa}\sqrt{\text{m}}$  when these ligaments failed.

**Crack-Tip Analysis:** The near-tip displacement and strain fields of the main crack just before the nucleation of cleavage cracks ( $K = 11 \text{ MPa}\sqrt{\text{m}}$ ) are shown in Figures 15(a) and (c), respectively. From Figure 15(a), it is clear that emission of slip or dislocations from the crack tip did not happen. Instead, two cleavage cracks formed in the process zone and propagated across the entire grain, Figure 15(b). The locations of the two cleavage cracks, shown as the dashed lines in Figure 15(c), were strained only lightly and elastically; cleavage cracks occurred with little plastic deformation. There was, however, some plastic deformation within the ligament in the crack wake, which led to the resistance-curve fracture behavior manifested by the alloy.

**Fractography:** The fracture surfaces of the as-received alloy exhibited mostly cleavage facets, as shown in Figure 16(a). Many of the facets showed the river line pattern characteristics of cleavage I. Some of the facets corresponded to grain boundary fracture facets and they showed some evidence of slip within the grain and slip impingement at the grain boundary, Figure 16(b). The extent of plastic flow, however, appeared to be quite limited since the lengths of slip lines were very short.

## Discussion

A careful fracture analysis of this alloy clearly shows the important influence of both atomic bonding and microstructure. The growth of fatigue cracks is clearly influenced by microstructure, as illustrated by the microanalyses. The growth of fatigue cracks is intermittent, and that is caused partially by differences in the slip systems in different grains. The same factors that influence fatigue crack growth are also controlling fracture toughness.

The alloy composition of LANL-3 is a variation of one of the alloys previously studied [16] that showed very high fracture toughness ( $> 60 \text{ MPa}\sqrt{\text{m}}$ ). The difference between these two alloys is that in LANL-3, a substitution of some Al was made for Cr. This addition of Al resulted in the precipitation of  $\text{Cr}_2\text{Nb}$  on grain boundaries during heat treatment, while the previous alloy contained no intermetallic. Because of cracking of grain boundary particles, the heat-treated materials showed lower fracture toughness values than the as-cast material, which does not have  $\text{Cr}_2\text{Nb}$  particles. In the  $500^\circ\text{C}$  heat treatment, precipitated intermetallic particles were not detected by X-ray diffraction or metallographically at  $2000\times$ . However, the particles could have been too small to image

(less than about 15 mm), and too low a volume fraction to be detected by X-rays. This heat treatment resulted in a decrease in hardness, which has been interpreted as recovery of the matrix and an indication of the absence of precipitation of intermetallic. The fracture toughness of the 500°C heat-treated material is essentially identical to that of the as-received alloy.

A comparison of the fracture resistance curves of the Nb-Cr-Ti-Al and Nb-Cr-Ti solid solution alloys is presented in Figure 17, which indicates that the Nb-Cr-Ti-Al alloy is less fracture-resistant than the Nb-Cr-Ti alloy. In particular, the plane-strain initiation toughness of the Nb-Cr-Ti alloy is reduced from 34 MPa $\sqrt{m}$  to 14 MPa $\sqrt{m}$  with 9 at. pct. Al addition. The present result is consistent with the fracture toughness of 23 MPa $\sqrt{m}$  reported for Nb-40Ti-10Cr-10Al [3, 16].

Figure 18 shows a comparison of the fatigue crack growth curve of the Nb-Cr-Ti-Al alloy against that of the tough Nb-Cr-Ti alloy reported earlier [25]. It is evident that the former is considerably less fatigue-resistant than the latter alloy by virtue of a steeper slope. As alluded to earlier, the steep slope in the  $da/dN$  curve for the Nb-Cr-Ti-Al alloy was the consequence of an intermittently critical crack extension process where cleavage cracks nucleated and propagated over a substantial distance.

Recent work [26] indicated that as little as 4 at. Pct. Al led to an ordered B2 structure in Ti-V-Cr alloys. A possibility exists that Al addition in Nb-Cr-Ti can result in ordering in the matrix and lead to a reduction in fracture resistance. Ordered B2 alloys have been developed and studied extensively by researchers at Ohio State University [8, 27]. Some of the ordered B2 alloys, however, exhibited high ductility and fracture toughness at ambient temperature. Thus, it is uncertain whether or not ordering is responsible for the lowering of fracture toughness in Nb-Cr-Ti alloy by Al addition.

Instead, it is thought that aluminum addition to Nb-Cr-Ti affected the interatomic bonding such that cleavage fracture is favored over dislocation emission from the crack tip. A measure of the propensity for dislocation nucleation from a crack tip is the unstable stacking energy (UES) [20], while a measure of the mobility of dislocations moving away from the crack tip is the Peierl-Nabarro (P-N) barrier energy or stress [21, 22]. Estimates of the UES and P-N barrier energy were made using the equations of Rice [20] and Wang [23, 24], respectively, via the procedures described earlier [16]. The results are compared against those for Nb, Nb-13Cr-37Ti, and Nb-10Cr-40Ti-10Al in Table 4. The values of the P-N barrier energy for the LANL-3 alloy are low for both (110) and (112) slip, suggesting that high dislocation mobility on the (110) and (112) planes. On the other hand, the values of the unstable stacking energy are high for both the (110) and (112) slip, implying that the nucleation of dislocations at the crack

Table 4. A summary of the composition, number of d+s electrons per atom, surface energy ( $\gamma_s$ ), unstable stacking energy ( $\gamma_{us}$ ), P-N barrier energy ( $U_{P-N}$ ), and fracture toughness of LANL-3 and other Nb-based alloys.

Alloy	Composition in Atomic Percent Nb-Cr-Ti-Al	No. of d+s electrons per atom	$\gamma_s$ (J/m <sup>2</sup> )	$\gamma_{us}$ (J/m <sup>2</sup> )	$U_{P-N}$ (J/m <sup>2</sup> )	Plane Strain Fracture Toughness MPa $\sqrt{m}$
G	100-0-0-0	5	2.42	0.875	1.52	0.322
D	53-13-37-0	4.76	2.19	0.721	1.26	0.947
F	40-10-40-10	4.66	2.13	0.686	1.18	0.441
LANL-3	46-11-34-9	4.5	2.13	2.02	3.50	0.020
						15

tip is difficult. The absence of direct observations of slip emission from the crack tip is consistent with the high UES,  $\gamma_{us}$ , values. The ratio of  $\gamma_s/\gamma_{us}$  is about 1 or less, where  $\gamma_s$  is the surface energy; this value of  $\gamma_s/\gamma_{us}$  is considerably lower than the values of 3.5 to 6 that is considered necessary for ductile behavior to occur [20]. Because of the high UES value, fracture of the LANL-3 alloy is expected to occur predominantly by cleavage, which is in accordance with experimental observations.

Unlike Ti addition [16], aluminum alloying addition affected the interatomic bonding of the Nb-Cr-Ti-Al alloy in an adverse way. It is unclear whether Al donates electrons to the bonding electrons (d + s) of the alloy, or lowers the electron concentration, but from these results, when compared to previous results [16], it appears that Al donates d+s electrons to the alloy, thereby increasing bonding between atoms. This effect was anticipated during the design of the alloy, so a substitution was made for Cr, but it appears that Al adds more electrons per atom than does Cr. The effect on mechanical properties of Al alloying addition is through an increase in the difficulty of nucleating dislocations at the crack tip, a process governed by the UES. The large increase in the UES as the result of Al alloying addition prevents the emission of dislocations from the crack tip, but promotes the nucleation and propagation of cleavage cracks and sometimes grain boundary cracks. As a consequence, the fatigue and fracture resistance of the Nb-11Cr-34Ti-9Al alloy is lower when compared to that of the Nb-13Cr-37Ti alloy.

## Conclusions

The conclusions reached in this study are as follows:

1. Aluminum alloying addition in the amount of 9 to 10 at. pct. has an adverse effect on the fatigue and fracture resistance of Nb-Cr-Ti-Al alloys.
2. Aluminum addition increases the unstable stacking energy, prevents the emission of dislocations from the crack tip, and promotes the nucleation and propagation of cleavage cracks in the Nb-Cr-Ti-Al alloy. Consequently, the fatigue and fracture resistance is lowered by Al addition.
3. Heat-treating the Nb-Cr-Ti-Al alloy at a temperature in the 900 to 1500°C range results in grain boundary precipitation and a low fracture toughness for the heat-treated microstructures.
4. Fatigue and quasi-static crack growth occurred in the Nb-Cr-Ti-Al alloys in an intermittently critical manner via the nucleation and propagation of cleavage cracks with little plastic flow.
5. The Nb-Cr-Ti-Al alloy exhibited a limited resistance-curve fracture behavior as the result of the crack-wake ligaments formed between cleavage planes.

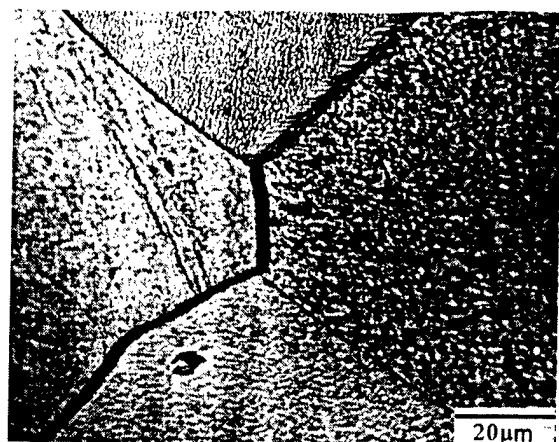
## ACKNOWLEDGMENTS

This research was sponsored by the Air Force Office of Scientific Research (AFSC) under Contract No. F49620-95-0043, Program Monitor, Dr. Spencer Wu. The United States Government is authorized to reproduce and distribute reprints for governmental purposes notwithstanding any copyright notation hereon. Supply of Nb-Cr-Ti-Al alloys by Dr. Dan J. Thoma at Los Alamos National Laboratory, Los Alamos, New Mexico, is acknowledged. Technical assistance by Mr. Byron Chapa and Mr. Jim Spencer, as well as clerical assistance by Ms. Lori Salas and Ms. Patty Soriano, all of Southwest Research Institute, are appreciated.

## References

1. K. S. Chan: *Metall. Mater. Trans. A*, 1995, Vol. 27A, pp. 2518-31.
2. D. L. Davidson, K. S. Chan, and D. L. Anton: *Metall. Mater. Trans. A*, 1996, Vol. 7A, pp. 3007-18.
3. K. S. Chan and D. L. Davidson: *JOM*, 1996, Vol. 48 (9), pp. 62-68.
4. R. M. Nekkanti and D. M. Dimiduk: *Mat. Res. Soc. Symp. Proc.*, Vol. 194, Pittsburgh, PA, 1990, pp. 175-182.
5. M. G. Mendiratta and D. M. Dimiduk: *Metall. Trans. A*, Vol. 24A, 1993, pp. 501-504.
6. J. D. Rigney, P. M. Singh, and J. J. Lewandowski: *JOM*, Vol. 44 (8), 1992, pp. 36-41.
7. J. Kajuch, J. Short, and J. J. Lewandowski: *Acta Metall. Mater.*, Vol. 43, 1995, pp. 1955-1967.
8. J. Dipasquale, D. Gahutu, D. Konitzer, and W. Soboyejo: *Materials Research Society Proceedings*, Materials Research Society, Pittsburgh, PA, Vol. 364, 1995, pp. 1347-52.
9. M. R. Jackson and K. D. Jones: Refractory Metals: Extraction, Processing and Applications, eds. K. Nona, C. Kiddell, D. R. Sadoway, and R. G. Bautista, TMS, Warrendale, PA, 1990, pp. 311-319.
10. P. R. Subramanian, M. G. Mendiratta, and D. M. Dimiduk: *JOM*, Vol. 48, January 1996, pp. 33-38.
11. P. R. Subramanian, M. G. Mendiratta, D. M. Dimiduk, and M. A. Stucke, *Mat. Sci. Eng.*, 1998 (in press).
12. M. R. Jackson, B. P. Bewlay, R. G. Rowe, D. W. Skelly, and H. A. Lipsitt: *JOM*, Vol. 48, January 1996, pp. 39-44.
13. B. P. Bewlay, M. R. Jackson, and H. A. Lipsitt: *Metall. Mater. Trans. A*, Vol. 27A, 1996, pp. 3801-3808.
14. D. L. Anton and D. M. Shah: *MRS Symp. Proceedings*, Vol 194, 1990, pp. 175-82.

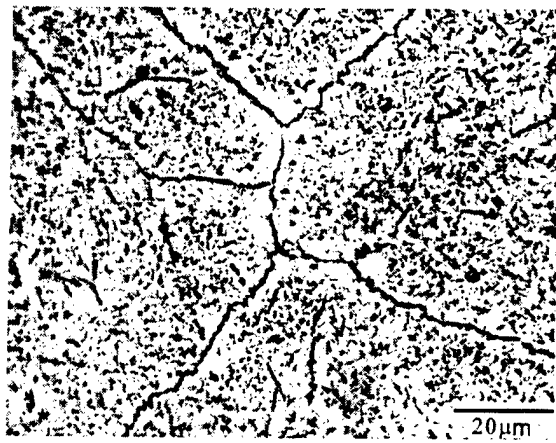
15. D. J. Thoma: Ph.D. Thesis, University of Wisconsin, Madison, WI, 1992, available from University Microfilms, Ann Arbor, MI.
16. K.S. Chan and D.L. Davidson: "Effects of Ti addition on cleavage fracture in Nb-Cr-Ti solid solution alloys," *Met. and Mat. Trans.* (in press, Aug. 1998).
17. K. C. Chen, D. J. Thoma, P. G. Kotula, F. Chu, C. M. Cady, G. T. Gray, P. S. Dunn, D. R. Korzekwa, C. Mercer, and W. Soboyejo: "Processing and properties of dual phase alloys in the Nb-Cr-Ti system," Third Pacific Rim International Conference on Advanced Materials and Processing, M.A. Imam, et al., Eds, TMS, 1998, pp. 1431-1436.
18. A. Nagy, J. B. Campbell, and D. L. Davidson: *Rev. Sci. Instrum.*, Vol. 55, 1984, pp. 778-782.
19. E. A. Franke, D. J. Wenzel, and D. L. Davidson: *Rev. Sci. Instrum.*, Vol. 62, No. 5, 1990, pp. 1270-1279.
20. J. R. Rice: *J. Mech. Phys. Solids*, 1992, Vol. 40, pp. 239-271.
21. R. E. Peierls: *Proc. Phys. Soc.*, 1940, Vol. 52, pp. 34-37.
22. F. R. N. Nabarro: *Proc. Phys. Soc.*, 1947, Vol. 59, pp. 236-394.
23. J. N. Wang: *Mat. Sci. & Eng. A*, 1996, Vol. A206, pp. 259-269.
24. J. N. Wang: *Acta Mater.*, 1996, Vol. 44, pp. 1541-1546.
25. D. L. Davidson, K. S. Chan and D. L. Anton: *Met. And Mat. Trans. A*, 1996, Vol. 27A, pp. 3007-3018.
26. T. G. Li, P. A. Blenkinsop, M. H. Loretto, and N. A. Walker: *Mat. Sci. Tech.*, 1998, Vol. 14, pp. 732-737.
27. R. Grylls, S. Perungulan, H. A. Lipsitt, H. L. Faser, R. Wheeler, and S. Banerjee: presented at '98 TMS Annual Meeting, February 15-19, 1998, San Antonio, TX.



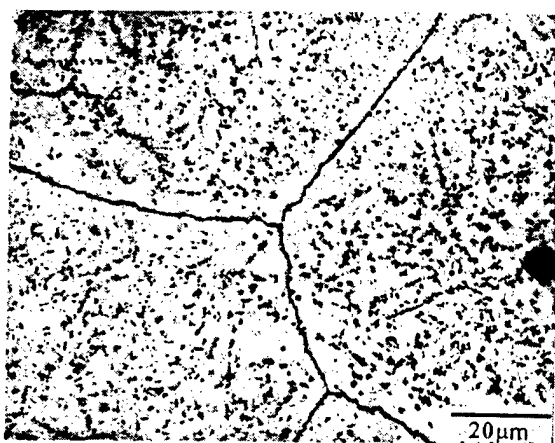
(a) as-received



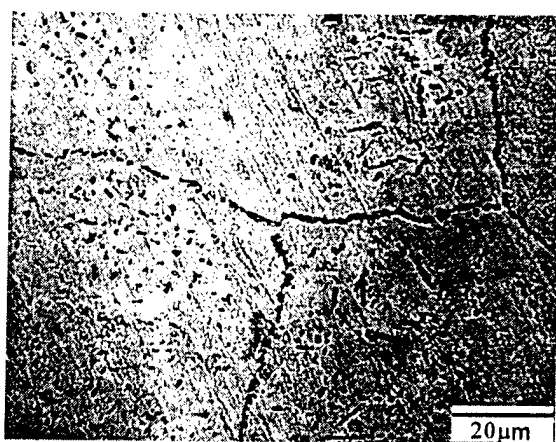
(b) 500°C, 6 hrs.



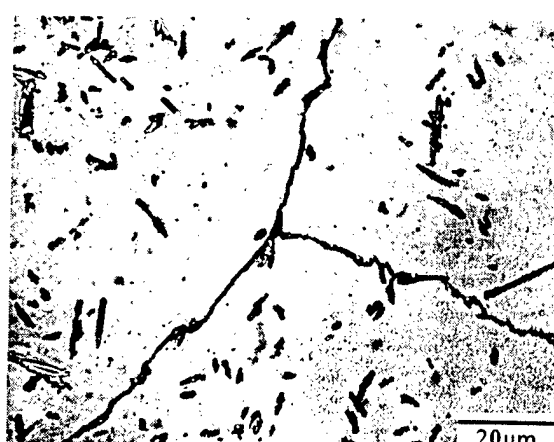
(c) 900°C, 24 hrs.



(d) 1000°C, 1 hr.



(e) 1200°C, 1 hr.



(f) 1500°C, 1 hr.

Fig. 1 Microstructures of LANL-3 (46Nb-11Cr-34Ti-9Al) in various heat-treat conditions: (a) as-cast, (b) 500°C, 6 hrs., (c) 900°C, 24 hrs., (d) 1000°C, 1 hr., (e) 1200°C, 1 hr., (f) 1500°C, 1 hr.

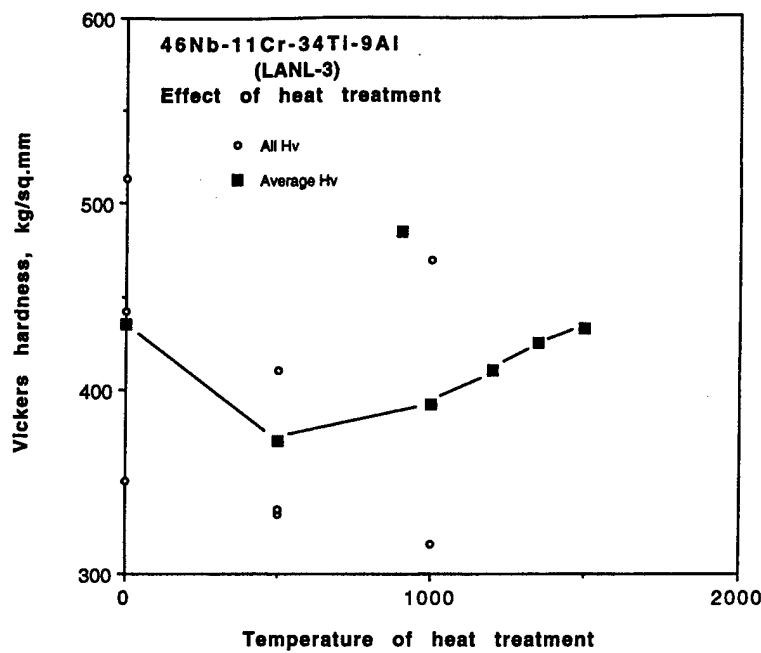


Fig. 2 Hardness vs. heat treatment temperature for the 46Nb-11Cr-34Ti-9Al alloy, designated as LANL-3. Each data point represents the average of ten hardness readings.

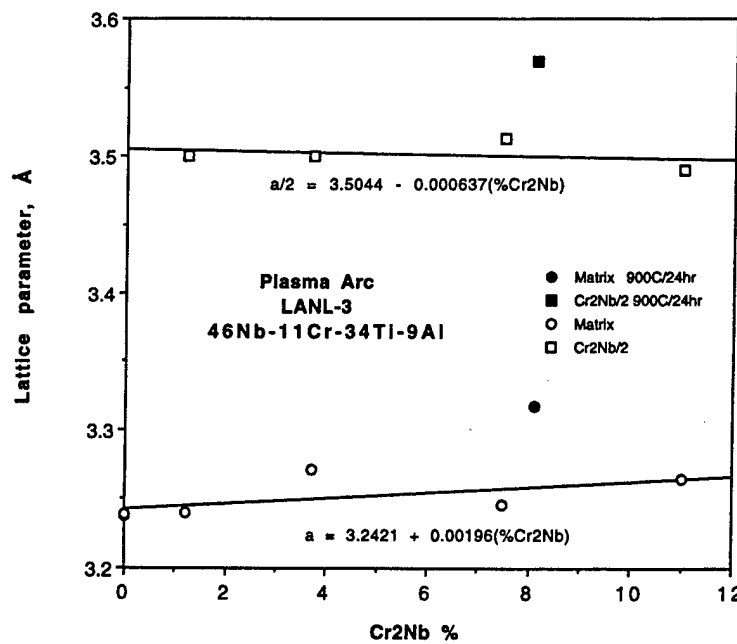


Fig. 3 Correlation between measured lattice parameters of matrix and intermetallic with amount of intermetallic, as determined by x-ray diffraction.

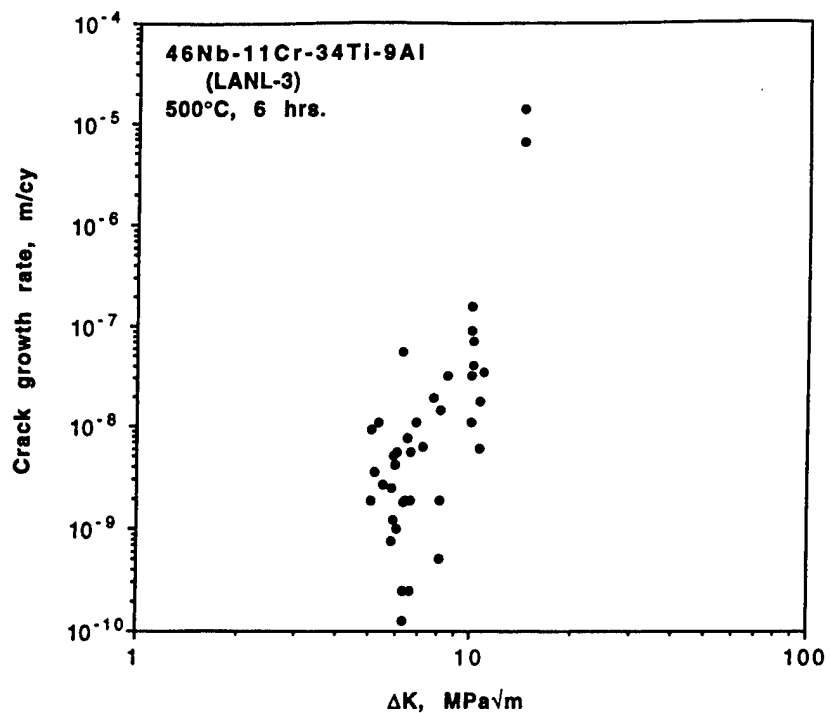


Fig. 4 Fatigue crack growth rate for LANL-3 heat treated to 500°C for 6 hrs.

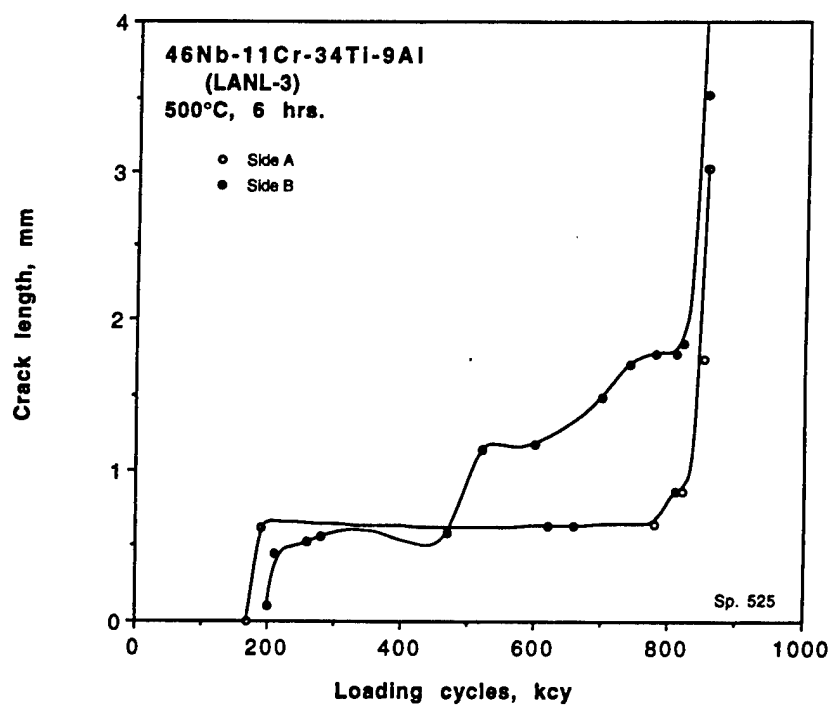


Fig. 5 An example of the highly erratic nature of crack growth.

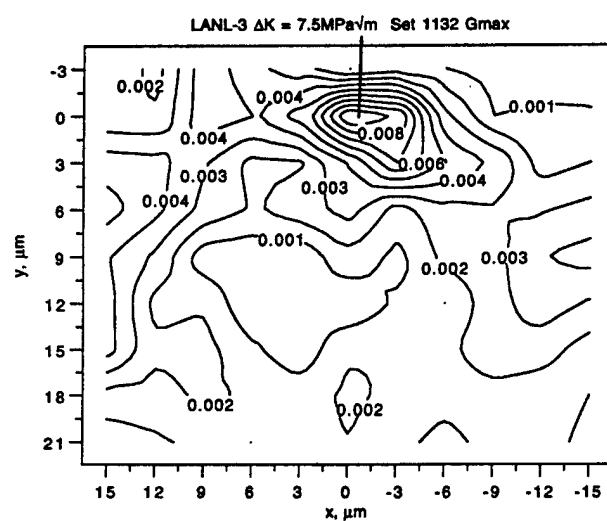
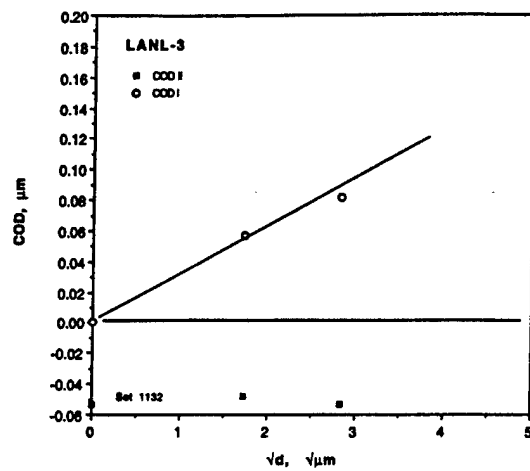
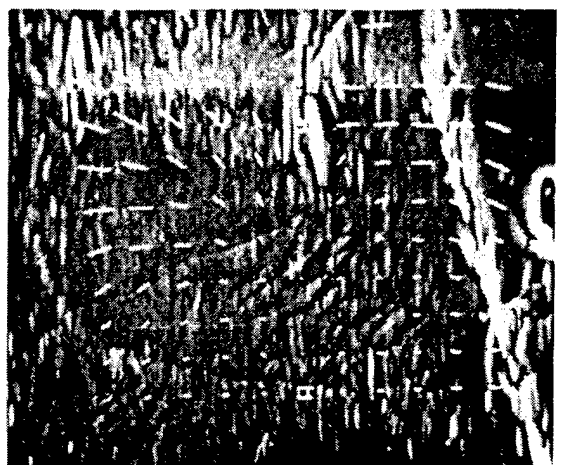


Fig. 6 Fatigue crack growth through LANL-3 at  $\Delta K = 7.5 \text{ MPa}\sqrt{\text{m}}$ , approximately parallel to a grain boundary and 12  $\mu\text{m}$  from it. Microanalysis indicated that the grain on the right was deforming easier than the grain containing the crack tip.

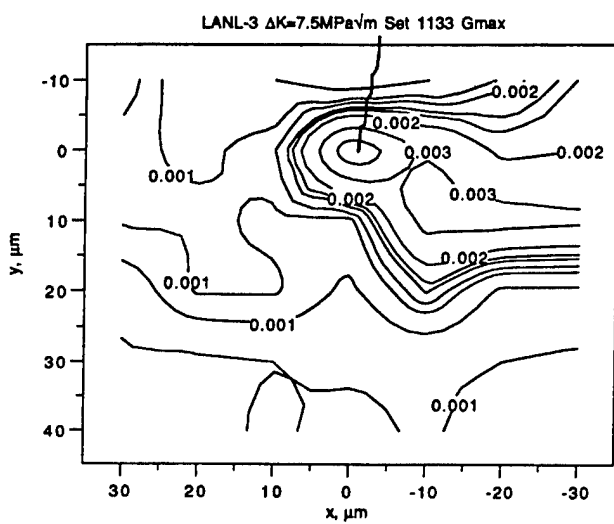
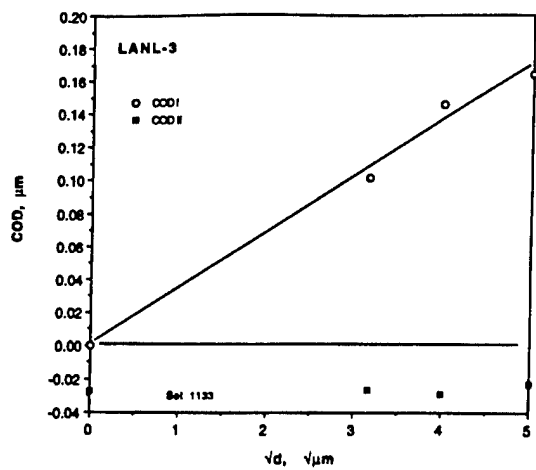
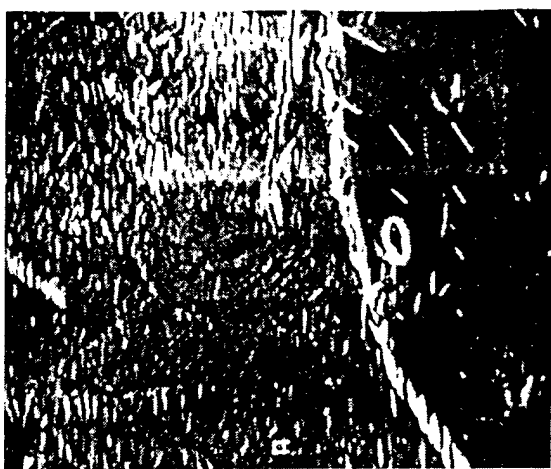


Fig. 7 A more detailed analysis of the crack tip shown in Figure 6. A shear band emanates from the crack tip on the right side.

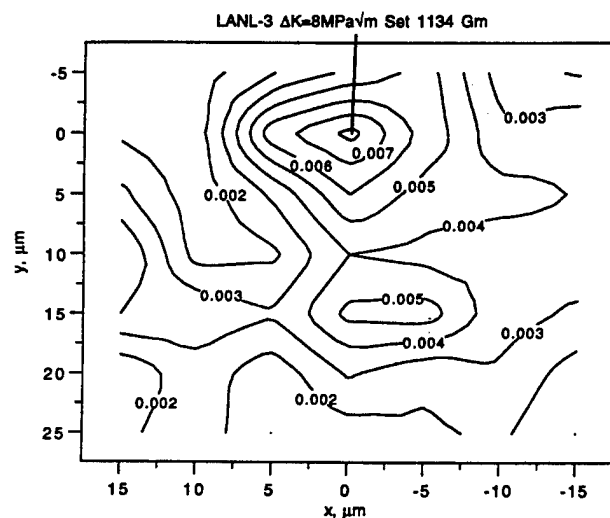
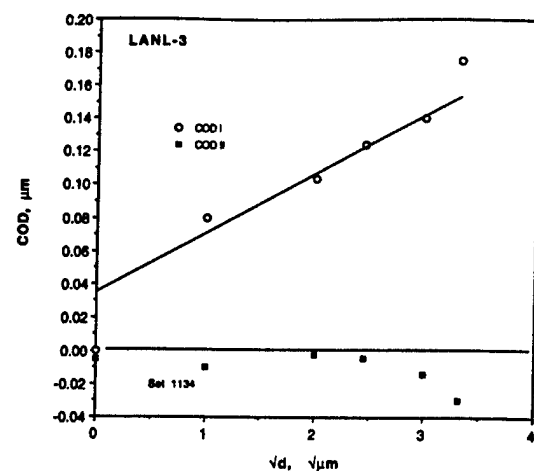


Fig. 8 Fatigue crack growth through LANL-3 at  $\Delta K = 8.0 \text{ MPa}\sqrt{\text{m}}$ . The crack tip is approximately  $2 \mu\text{m}$  from a grain boundary, and the crack is growing nearly perpendicular to it. There appears to be a crack parallel to the grain boundary; however, it did not open when the specimen was loaded. Microanalysis indicated that the strain distribution was disrupted by the differences in slip characteristics between the two grains.

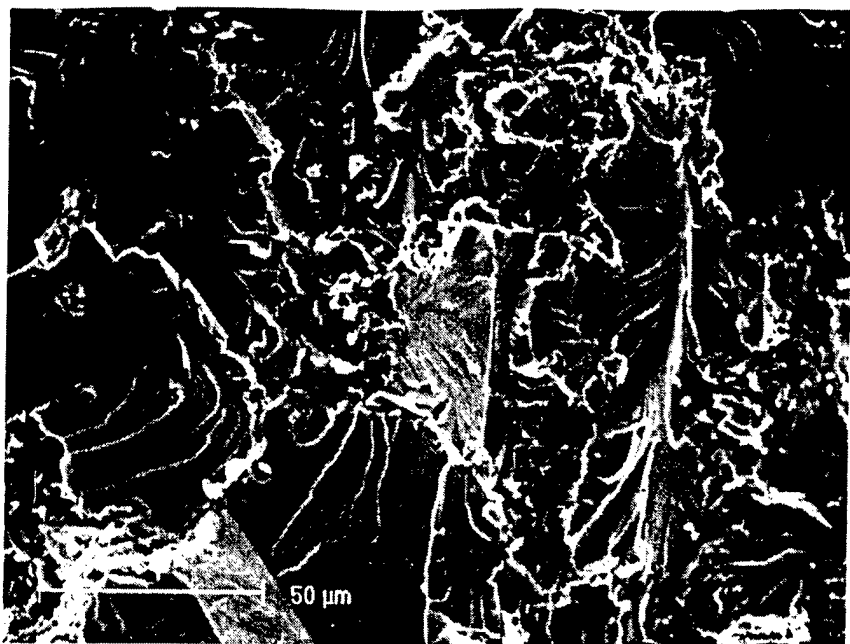
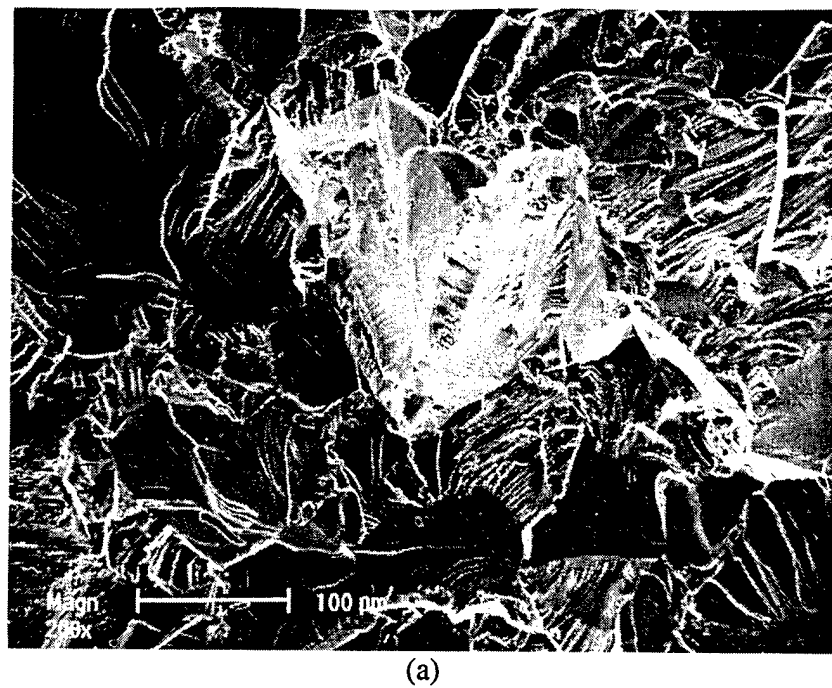
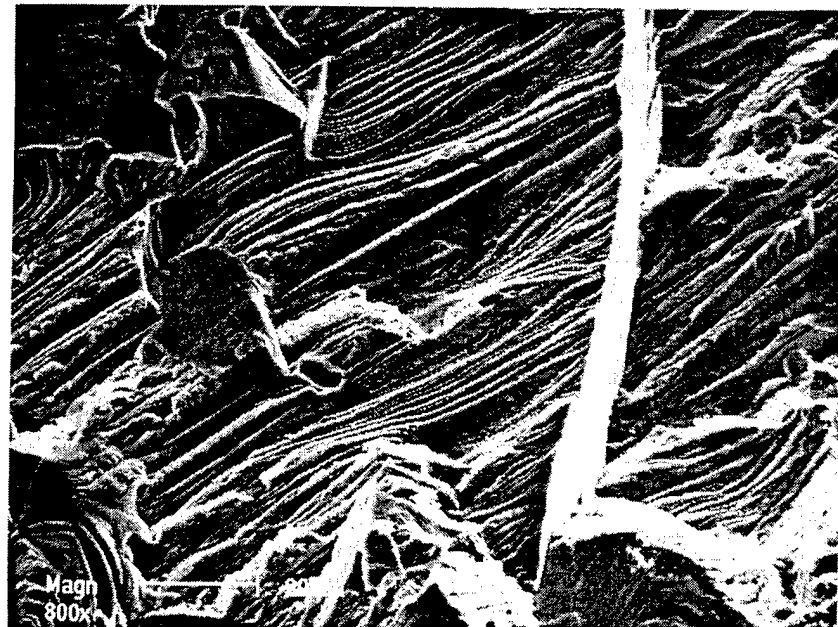


Fig. 9 Fractography for LANL-2 showing the generally brittle nature of the fracture process. The crack path appears to be a combination of transgranular and intergranular fracture. Some of the very fine features seen are interpreted as being failure through the intermetallic within grain boundaries.

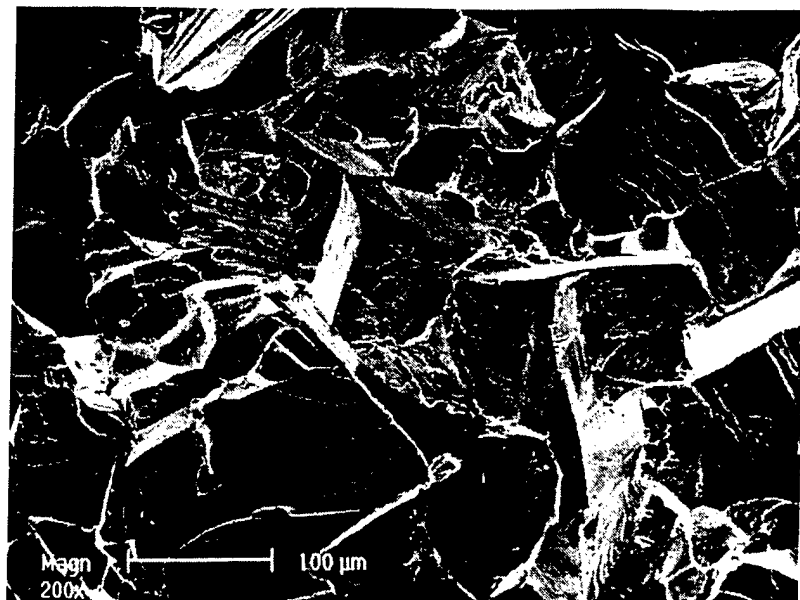


(a)

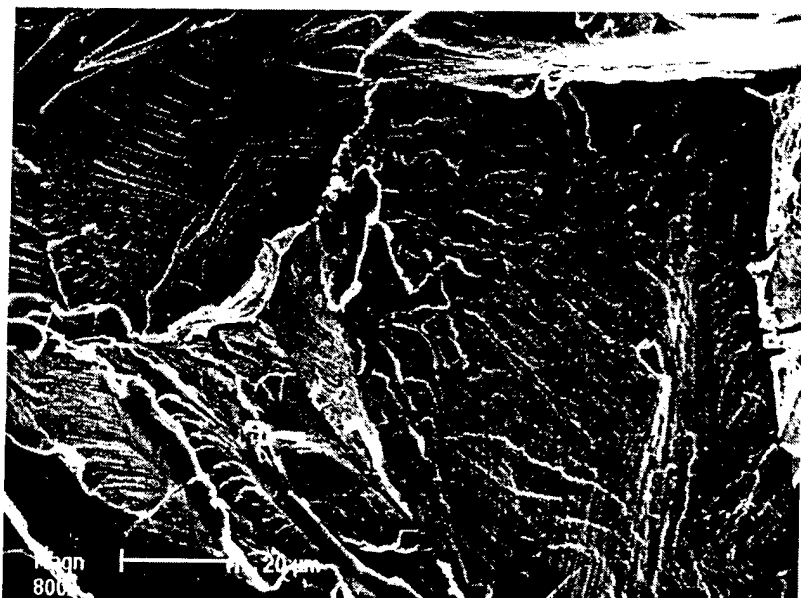


(b)

Fig. 10 Fractography of fatigue crack growth in LANL-3 at about  $\Delta K = 8$  MPa/m. Crack growth was from bottom to top. The periodic markings are interpreted as being crack arrest marks (fatigue striations).



(a)



(b)

Fig. 11 Fractography of fast fracture in LANL-3. Crack growth was from bottom to top. Crack growth was very planar, but on many different planes, some nearly parallel to the loading axis. The detail in (b) shows what are interpreted as slip lines intersecting the fracture surface on the right side and curved edges in other areas. These features are indicative of plasticity.

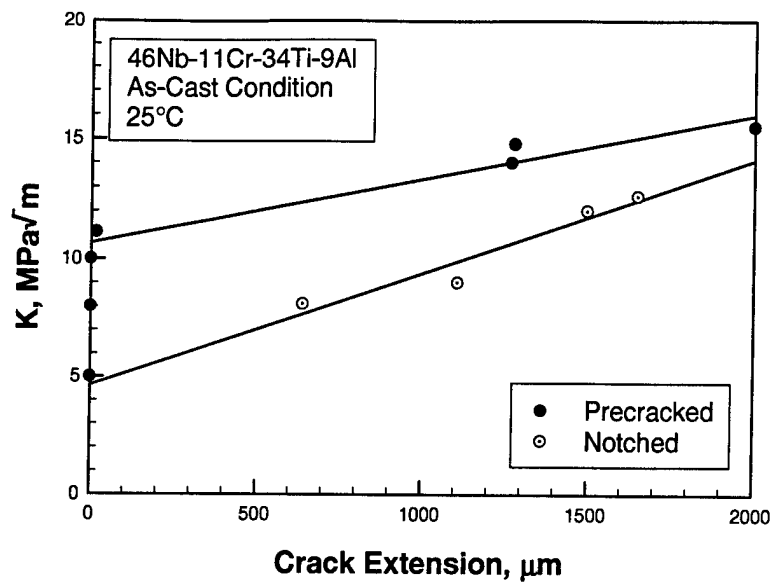


Fig. 12 K-resistance curves of 46Nb-11Cr-34Ti-9Al.

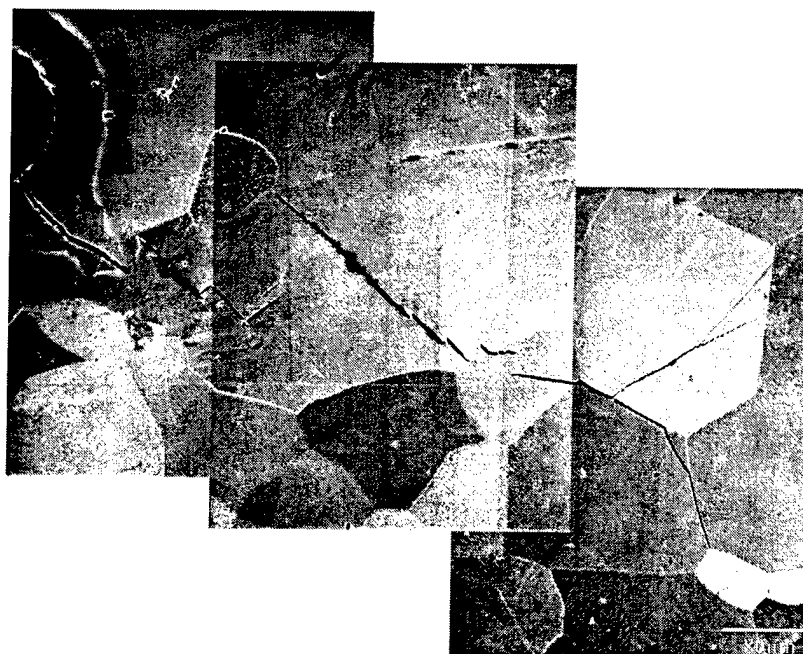
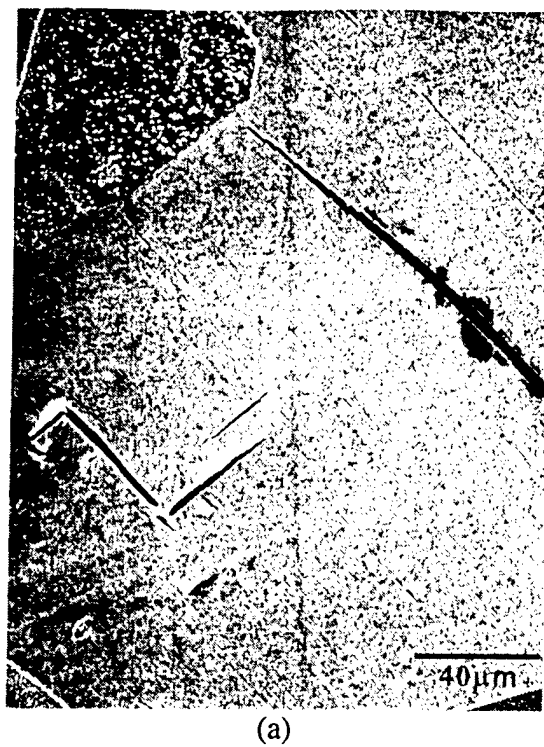
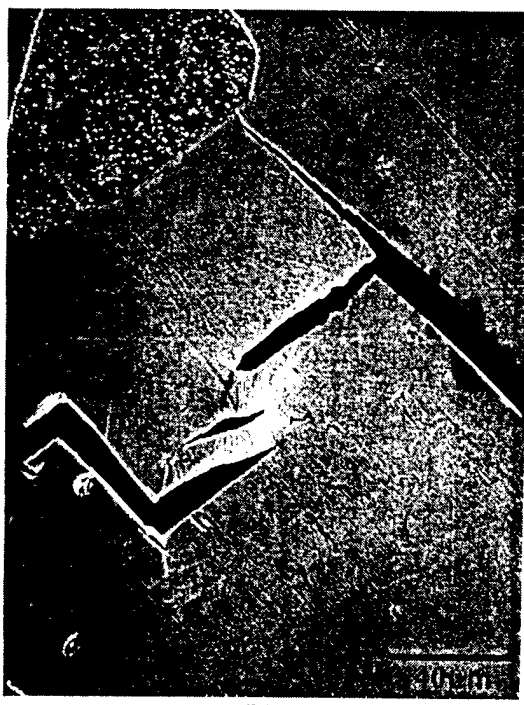


Fig. 13 A summary of the fracture process in 46Nb-11Cr-34Ti-9Al. The crack path shows a series of arrested cleavage and grain boundary cracks separated by intact ligaments.

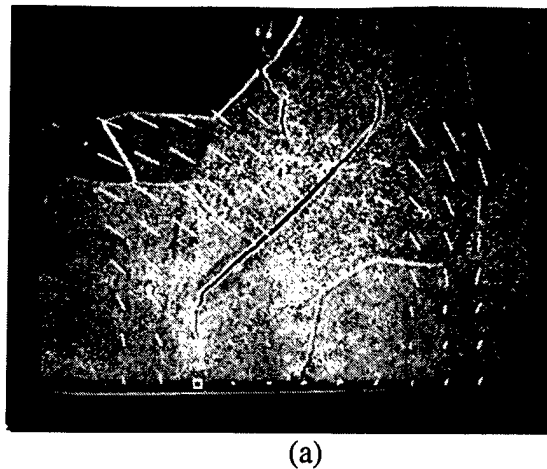


(a)

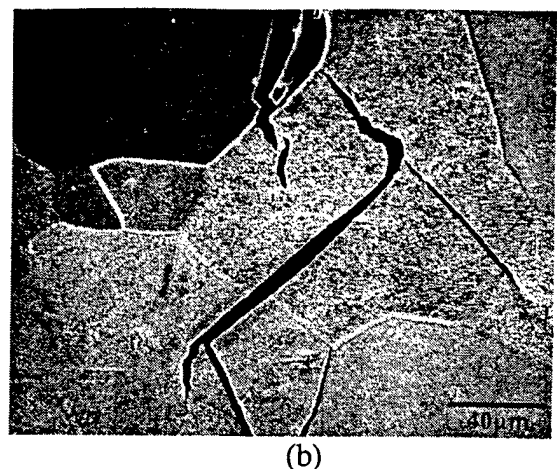


(b)

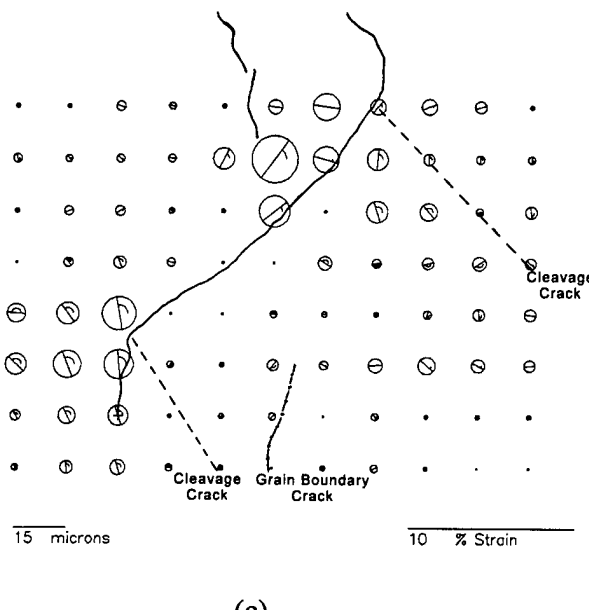
Fig. 14 Plastic deformation in a ligament located between two parallel cleavage cracks. The crack-wake ligaments are responsible for the resistance-curve fracture behavior.



(a)

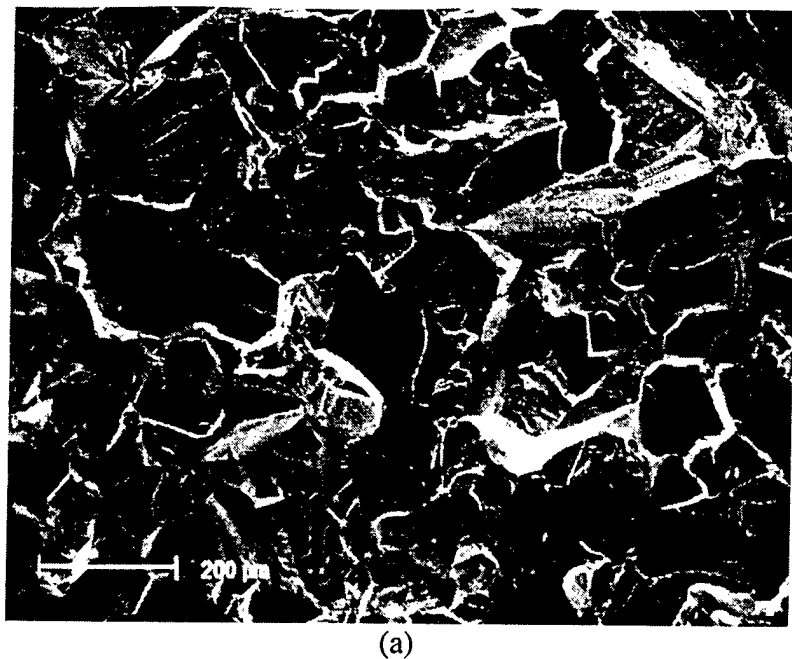


(b)

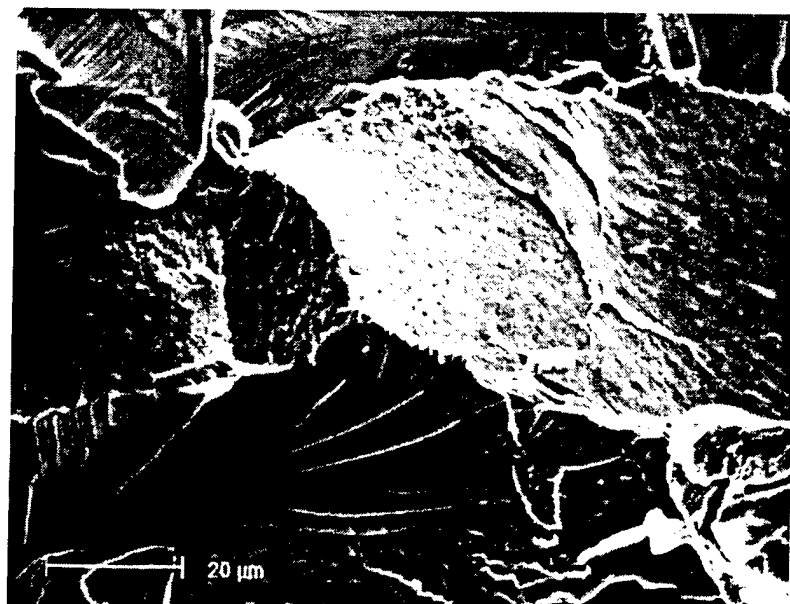


(c)

Fig. 15 Crack-tip displacement and strain fields of the main crack in 46Nb-11Cr-34Ti-9Al at  $K = 11 \text{ MPa}\sqrt{\text{m}}$  before the nucleation of cleavage cracks: (a) displacement field at  $K = 11 \text{ MPa}\sqrt{\text{m}}$  superimposed on a micrograph of the near-tip region, (b) near-tip region at  $K = 14 \text{ MPa}\sqrt{\text{m}}$ , and (c) strain field at  $K = 11 \text{ MPa}\sqrt{\text{m}}$  superimposed with cleavage cracks (dashed lines) and a grain boundary crack (dot-dashed line). Crack growth was from top to bottom.



(a)



(b)

Fig. 16 (a) Fracture surfaces of 46Nb-11Cr-34Ti-9Al show a combination of cleavage and grain boundary facets, (b) high magnification views of grain boundary and cleavage facets.

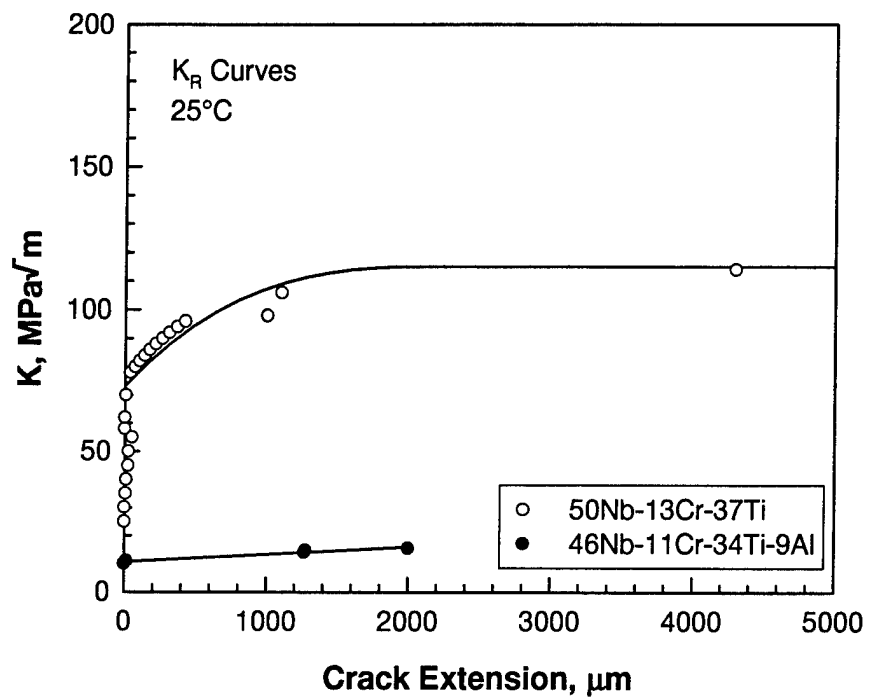


Fig. 17 A comparison of the K-resistance curves of Nb-Cr-Ti-Al and Nb-Cr-Ti solid solution alloys.

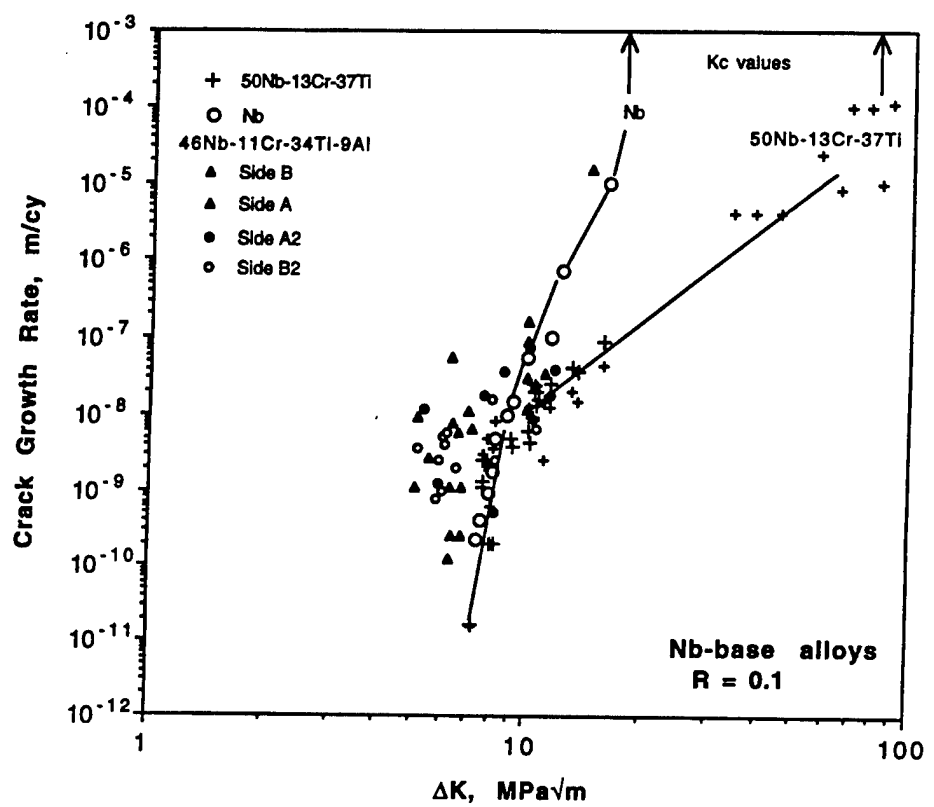


Fig. 18 A comparison of the fatigue crack growth curves of Nb-Cr-Ti-Al and Nb-Cr-Ti solid solution alloys with pure Nb.

## **Microstructural and Fracture Characterization of Nb-Cr-Ti Mechanically Alloyed Materials**

**D. L. Davidson and K. S. Chan**

## MICROSTRUCTURAL AND FRACTURE CHARACTERIZATION OF Nb-Cr-Ti MECHANICALLY ALLOYED MATERIALS

D.L. Davidson and K.S. Chan  
Southwest Research Institute  
San Antonio, TX 78228

### ABSTRACT

Materials containing Nb, Cr, and Ti were fabricated by consolidating powders made by mechanical alloying. The Nb/Ti ratio was maintained at about 1.3 and Cr was increased to form the intermetallic  $\text{Cr}_2\text{Nb}$ . The material was characterized by x-ray diffraction and metallography, and the tensile, fatigue and fracture toughness properties were evaluated at ambient temperature. The alloyed powders contained only small amounts of intermetallic, but during the consolidation heat treatment, two of the materials precipitated large volume fractions of  $\text{Cr}_2\text{Nb}$ . It was found that  $\text{Cr}_2\text{Nb}$  could be precipitated by heat treatment in the third material, although this was not expected from the composition. The maximum fracture toughness measured was 11 MPa $\sqrt{\text{m}}$ , and the maximum tensile strength was 620 MPa. The reasons for the limited fracture toughness were constraint of deformation by the  $\text{Cr}_2\text{Nb}$  and compositional change in the matrix that lowered its toughness.

### INTRODUCTION

Very high fracture toughness values have been measured for the composition Nb-13Cr-37Ti (at.-%), which is a single phase alloy [1]. If the same Nb/Ti ratio is maintained ( $\approx 1.3$ ) as more Cr is added to this composition,  $\text{Cr}_2\text{Nb}$  forms *in situ*, which is advantageous because this intermetallic is stable at high temperatures; thus, the composite can better resist creep deformation. However, gaining control of the size and dispersion of the intermetallic has proven to be difficult. Cast materials that were relatively slowly cooled resulted in large particles of  $\text{Cr}_2\text{Nb}$  that in some cases were well dispersed, but in other cases were contiguous in the grain boundaries [2]. Rapid solidification of these material compositions resulted in completely different microstructures that had  $\text{Cr}_2\text{Nb}$  particles with high contiguity [3]. In an attempt to gain more control of the microstructures of these materials, mechanical alloying was chosen as a possible solution.

This paper reports the extensive effort that was made to describe the microstructures that were formed by this manufacturing process and gives the results of a fatigue and fracture toughness evaluation of the materials, all at ambient temperature. Tensile properties were also measured.

## MATERIALS

Mechanically alloyed materials were produced by the Structural Materials Centre, Defence Evaluation and Research Agency (DERA), which is part of the Ministry of Defence, and is located in Farnborough, UK.

Three materials were produced by DERA using a proprietary process. A high energy mill was used to produce powders that were canned and hot isostatically pressed (HIP) into billets. The whole process was designed for reactive metals; thus, the inclusion of unwanted interstitials (O, N, C, H) was minimized. An analysis of the powders before consolidation was made at DERA by x-ray analysis. The x-ray diffraction peaks were identified as shown in **Table 1**. In each alloy, 1 peak was identified as  $\beta$ -Ti, with  $a = 3.33\text{\AA}$ . A few percent of  $\text{Cr}_2\text{Nb}$  was found in materials A and B, but none was found in material C. The peaks labeled "Nb" have a lattice parameter that is too low; it should be  $3.302\text{\AA}$ . Thus, these peaks may be from a Nb-rich phase that has a low concentration of Ti and Cr. The phase labeled "Alloy" has a much higher concentration of Ti and Cr as determined from the smaller lattice parameter.

**Table 1**  
X-ray diffraction from mechanically alloyed powders

Material	Total no. of peaks	Nb peaks No. a( $\text{\AA}$ )	Alloy peaks No. a( $\text{\AA}$ )	Cr peaks No. a( $\text{\AA}$ )	$\text{Cr}_2\text{Nb}$ a( $\text{\AA}$ )	Unknown Peaks
A	16	4 3.295	4 3.228	4 2.880	6.983	1
B	17	5 3.298	5 3.16- 3.27	3 2.882	7.005	2
C	16	5 3.291	3 3.163	3 2.880	----	3

Each billet received was nominally 75 mm in diameter by 55 mm high, including the Ti-6Al-4V canning material that was approximately 10 mm thick.

Material compositions and interstitials were measured at SwRI by Auger Electron Spectroscopy and by conventional chemical analysis techniques at a commercial testing company (Charles Kawin). The designations used for the alloys, their compositions, and the levels of O, C, and N are shown in **Table 2**.

**Table 2**  
Material compositions

Material Name	Can Desig.	Target			Alloy Analysis			Interstitials		
		Nb	Cr	Ti	Nb	Cr	Ti	O	C	N
		(Atomic %)			(Atomic %)			(ppm. by wt.)		
A	1	40	30	30	40.9	30.8	27.0	410	50	28
B	2	37	35	28	35.5	31.2	31.9	490	40	100
C	3	48	15	37	42.4	16.3	40.2	310	40	32
					43.6	15.9	39.5	300	40	58

As may be seen from the table, the compositions achieved were fairly close to the target values and the levels of O, C and N were maintained at a low level. The final HIP consolidation was at 1300°C, and that caused Cr<sub>2</sub>Nb intermetallic to precipitate in materials A and B (letters were used to designate the alloys in this study, rather than alloy number). In material C, which should have been a solid solution material according to the phase diagram [4], the as-received material had intermetallic particles on some of the grain boundaries. If these alloys were to be made again, the HIP process could be, and should be, scheduled to carefully control the size, dispersion, and volume fraction of the intermetallic.

Microstructures of the as-received alloys are shown by optical microscopy in **Fig. 1**. In the as-consolidated form, materials A and B have intermetallic particles approximately 2  $\mu\text{m}$  in diameter, and there is significant contiguity (particle touching) in both alloys. As determined from the phase diagram, materials A and B should have contained 24 and 38 vol. % intermetallic respectively, while material C should have contained no intermetallic.

The approximate levels of intermetallic were measured in the alloys using x-ray diffraction. The intensity of the {311} peak of the C15 structure of  $\text{Cr}_2\text{Nb}$  was used as a measurement of the volume fraction of intermetallic when the intensity of the {110} peak of the bcc matrix was normalized to 100% [4]. Some  $\text{Cr}_2\text{Nb}$  was detected in material C by x-ray diffraction; thus, heat treatments were undertaken as a method for varying the volume fraction of intermetallic in this material. From these diffraction patterns, the lattice parameters of the matrix and intermetallic were determined, and are listed in **Table 3**, together with the volume fraction of  $\text{Cr}_2\text{Nb}$  and the strain between the matrix and intermetallic lattices. Strain was computed from the following equation

$$\text{mismatch strain} = [\text{a}_{\text{IM}}/2 - \text{a}_m]/\text{a}_m$$

where  $\text{a}_{\text{IM}}$  = lattice parameter of  $\text{Cr}_2\text{Nb}$ , and  $\text{a}_m$  = matrix lattice parameter. Since half the lattice parameter of the intermetallic is only slightly greater than the lattice parameter of the matrix, the mismatch strain is that strain which these lattices would have to sustain to be coherent.

For material C, results from the "test series" conducted on small samples indicated a systematic increase in volume fraction of  $\text{Cr}_2\text{Nb}$  with time. Microstructures of the heat treatment test series are shown in **Fig. 2**, where the volume fraction of  $\text{Cr}_2\text{Nb}$  may be seen to be increasing; also, the size of the intermetallic is increasing, and it appears to have an approximately spherical shape and is well dispersed. The longest heat treatment (338 hrs.) resulted in the grain boundary intermetallic becoming discontinuous. However, when another slab of material was sliced from the billet and cut into CT-sized specimens and heat treated, the same correlation was not found. Thus, specimens were cut into specimens, then heat treated, then the volume fraction of precipitated  $\text{Cr}_2\text{Nb}$  was estimated from x-ray diffraction line intensities.

Using all the data for heat treatment of material C, except for the test series, no correlation was found between time of heat treatment (all at 1000°C) and magnitude of the lattice parameter. However, when the lattice parameters were plotted against the amount of  $\text{Cr}_2\text{Nb}$ , as shown in **Fig. 3(a)**, a correlation was found. The mismatch strain between half the lattice parameter of  $\text{Cr}_2\text{Nb}$  and that of the matrix, shown in **Fig. 3(b)**, also correlates with the amount of  $\text{Cr}_2\text{Nb}$  present.

**Table 3**  
Lattice parameters of mechanically alloyed materials

Material/Heat Treatment	Lattice Parameter matrix (Å)	Cr <sub>2</sub> Nb (Å)	Cr <sub>2</sub> Nb (%)	Strain (%)	Extra lines
<u>Material A:</u> AR 1000°C/338hr	3.2525 3.2600	7.0024 6.9752	32 36	7.65 3.5	3 5
<u>Material B:</u> AR 1000°C/338hr	3.2533 3.2622	6.9968 6.9727	40 45	7.5 6.9	3 6
<u>Material C:</u> <u>Test Series</u>					
As received	3.2446	6.9941	1.5	7.8	0
1000°C/72hr	3.2627	6.9966	2.8	7.2	3
1000°C/173hr	3.2553	6.9669	13	7.0	1
1000°C/338hr	3.2712	7.0025	15	7.0	3
<u>CT-1</u>					
AR	3.2237	6.9861	1.8	8.4	0
1000°C/3hr	3.3085	7.0021	22	5.5	3
1000°C/3hr	3.3099	6.9800	25	5.4	1
<u>CT-2</u> AR	3.2478	7.0107	0.8	7.9	0
<u>CT-3</u> AR	3.2415	7.0097	1.3	8.1	0
<u>CT-4</u> AR	3.2377	7.0007	1.5	8.2	0
<u>CT-5</u>					
1000°C/25hr	3.3102	6.9726	30	5.3	7
<u>CT-6</u>					
1000°C/175hr	3.3059	7.0085	30	6.0	13
As received	3.2237	6.9861	1.8	8.3	0

The lattice parameter of  $\text{Cr}_2\text{Nb}$  decreases with addition of Ti, according to Thoma [4, Fig. 5.24] as follows:

$$\text{Half the lattice parameter of } \text{Cr}_2\text{Nb} = 3.5125 - 0.00015(\text{at.\% Ti}) \quad (1)$$

If the data in Fig. 3(a) are combined with eq. (1), it implies that the  $\text{Cr}_2\text{Nb}$  that has precipitated in the alloy due to heat treatment incorporates Ti because the lattice parameter decreases with volume precipitated. When that occurs, the lattice parameter of the matrix increases because Ti has been removed by formation of  $\text{Cr}_2(\text{Nb}-\text{Ti})$ . Diffusion of Ti from matrix to  $\text{Cr}_2\text{Nb}$  lowers the incoherency strains between the two phases, as seen in Fig. 3(b).

The "extra lines" that appear in some of the diffraction patterns were investigated. Many of the lines are common to several of the patterns that exhibited extra lines. The best match for the most extra lines was with  $\text{Ti}_2\text{O}_3$ , leaving only one or two very weak lines unidentified. Thus, it is assumed that much of the oxygen that entered during processing was "gettered" by titanium.

Auger electron spectrometry (AES) was used to investigate the constituents of the alloys, and specifically to look for oxygen and its distribution. The effect of heat treatment of material C on the combined secondary and backscattered electron images produced in the AES is shown in Fig. 4, where it may be seen that the material as-received appears to be nearly homogeneous, but with increasing time of exposure to 1000°C, the segregation of elements increases. The electron image is shown in Fig. 5 together with the Cr, Ti, and O maps. The Cr is segregating to form  $\text{Cr}_2\text{Nb}$  at the locations shown in Fig. 5(b), and Ti is segregating to the dark regions shown in Fig. 5(a), and these regions are near some of the Cr-rich regions ( $\text{Cr}_2\text{Nb}$ ). There appears to be some O segregation to Ti, but it is not strong. The Nb map, not shown, was approximately complementary to the Cr map.

The AES derived information for material B after heating to 1000°C for 72 hrs., shown in Fig. 6, is more complex. The dark particles are Ti, the dark gray areas are rich in Cr, which means that they are  $\text{Cr}_2\text{Nb}$ , and the lighter gray areas are rich in Nb (not shown) and Ti, which is the matrix alloy. In this alloy, Ti is segregated more to the Ti particles and the matrix; thus the  $\text{Cr}_2\text{Nb}$  is lean in O relative to the remainder of the material.

## SPECIMEN PREPARATION AND EXPERIMENTAL PROCEDURES

Specimens of these materials were formed by electric discharge machining (EDM) slabs of material approximately 3 mm thick from the center portions of each of the billets. Small compact tension (CT) specimens approximately 25 mm x 25 mm by 3 mm thick were then cut from the slabs. Notches, also introduced by EDM, and usually  $\approx 0.13$  mm wide to give  $a/w \approx 0.3$ , were used as crack starters. Cracks were initiated in compression/tension (C/T) or in tension/tension (T/T) loading, depending on the expected fracture characteristics of the alloy. Cracks in materials A and B were initiated in C/T loading, and in Alloy C by T/T loading, after some initial efforts. Several specimens broke unexpectedly during precracking, and several specimens developed cracks in the loading holes during EDM machining.

Specimen preparation techniques were as follows: After EDM cutting, the flat sides of the specimen were mechanically polished with a series of SiC papers and on polishing wheels using diamond and alumina polishing grit. The specimens were precracked in this condition so that the cracks could be easily detected in the optical microscope. After precracking, specimens were often loaded inside the SEM using a special stage capable of exerting 4400 N so that high resolution photographs could be made for further analysis of displacements around the crack tips. For this step in the experiments, ion etching at about 10 keV was used to reveal the microstructure and provide minutely detailed topography on the surface to aid in the subsequent analysis.

The experimental procedure typically used in this evaluation was to obtain fatigue crack growth data as a function of load and crack length. During this time, the crack tips were periodically observed in the SEM using the loading stage to measure crack opening load and make photographs at maximum and minimum cyclic loads. When sufficient fatigue data and analysis had been collected, the specimen was loaded to failure within the SEM and photographs obtained at various loads for analysis of crack tip deformation.

Two tensile specimens that were tapered on the ends for load application and about 3.85 mm wide by 0.770 mm thick in the straight center gage length were EDM cut from each material. A strain gage with 1.58 mm gage length was cemented to one specimen of each material and it was deformed in a laboratory servohydraulic loading frame to obtain a stress-strain curve. The other specimen was deformed within the SEM using a loading stage so that high

resolution photographs could be used to search for cracks and to make photographs at various load levels for the subsequent measurement of displacements using DISMAP [5]. The specimens deformed in the SEM were polished and then ion etched to reveal microstructure.

## RESULTS

Tensile tests in the laboratory machine did not result in stress-strain curves that indicated yield behavior. The specimens deformed elastically and failed. During tensile tests in the SEM, final failure initiated from cracks that pre-existed from processing were observed in all the materials. From the laboratory experiments, the tensile elastic modulus was measured for materials B and C; material A failed during loading into the grips. Failure stress was measured from tensile loading in the SEM, but not modulus. The results are summarized in **Table 4**.

**Table 4**  
Tensile Properties

Material	Modulus GPa	Fracture stress MPa
A	--	355
B	147	440
B		432
C	121	560
C		621

Cracks in materials A and B are shown in **Fig. 7**. Because of these, and other similar cracks, the tensile tests of these materials were essentially fracture toughness tests; thus, little macroscopic ductility would be expected.

Fatigue crack growth through material C is shown in **Fig. 8** for several heat treatments. From these results, it appears that heat treatment has had a small effect on the curves, with a shifting to the left of the curves in the order 25, 75, and 175 hrs. at 1000°C, corresponding to an increase in volume fraction of  $\text{Cr}_2\text{Nb}$ . Several attempts were made to initiate and grow fatigue cracks in materials A and B, but the specimens broke each time before more than a few data points were obtained.

Fracture toughness was determined both from the maximum K level sustained during fatigue crack growth and from notched CT specimens. Summarized in **Table 5** are all the fracture toughness data obtained from these materials.

**Table 5**  
Fracture toughness

Specimen	Material	Heat treatment	Fracture toughness MPa $\sqrt{m}$
572	A	As received	11.2
583	A	As received	8.9
573	B	As received	9.7
568	C	As received	10.0
579	C	25 hrs., 1000°C	11.1
582	C	75 hrs., 1000°C	
577	C	175 hrs., 1000°C	10.6

The path of the crack through the microstructures of these materials is shown in **Fig. 9**. In **Figs. 9(a) and 9(b)**, materials A and B, the smooth, darker gray phase is Cr<sub>2</sub>Nb and the rougher texture, lighter phase is matrix alloy. For these materials, the crack path is across both the phases, and intergranular, or interphase fracture does not predominate.

For material C, the microstructural units are much finer, and the crack was not selective of either matrix or intermetallic. This is illustrated in **Fig. 10**, where the crack path can be seen sometimes to have passed through the interface between the Cr<sub>2</sub>Nb and the matrix, but the crack apparently did not deliberately choose the interface.

An analysis of the strains surrounding the crack tip at a stress intensity factor close to the fracture value is shown in **Fig. 11**. Plasticity is evident at the crack tip, but the magnitude of strain is not very large, and the extent of the plastic zone is small. There is no apparent effect of the adjacent grain boundary, and the presence of Cr<sub>2</sub>Nb in the boundary does not appear to be detrimental. The strains are small because the level of constraint imposed by the particles on deformation in the matrix is high. Constraint, defined as the ratio of mean strain divided to effective strain is large. For the crack tip

region shown in Fig. 11, the constraint level is shown in Fig. 12. The magnitude of constraint is approaching the plane strain value of 0.5 in most of the region shown in the figure, and is much higher than for deformation in the matrix without  $\text{Cr}_2\text{Nb}$  particles.

An analysis for a crack tip in material B is shown in Fig. 13 where, as with material C, strain near the crack tip is not very large. This analysis was made at  $K = 9.2 \text{ MPa}\sqrt{\text{m}}$ , and fast fracture initiated at  $K = 9.4 \text{ MPa}\sqrt{\text{m}}$

Fractography: The fracture surfaces generated by fatigue crack growth and during the fast fracture that accompanied the measurement of fracture toughness were examined for each material. The fatigue crack growth surface shown in Fig. 14(a), shows evidence of some fracture arrest markings, while the fast fracture surface seen in Fig. 14(b) shows little evidence of deformation. The fractography of material B is shown in Fig. 15, where a few regions of crack arrest markings can be seen in (a), but there is only limited evidence of any plasticity seen in (b) the fast fracture region.

For crack growth through material C, there is less fractographic evidence of periodic crack arrest in the fatigue region, Fig. 16(a), than for the other two materials, even though fatigue crack growth through this material was the most stable of the three. In the fast fracture region, Fig. 16(b), there is more evidence of deformation than seen for the other materials.

## DISCUSSION

The microstructure of materials A and B appears to have been defined by the HIP treatment. The  $\text{Cr}_2\text{Nb}$  was formed during HIP and subsequent heat treatment did very little to alter the microstructure. As a consequence of this uncontrolled precipitation, networks of contiguous  $\text{Cr}_2\text{Nb}$  were formed in these materials, which limited their fracture resistance. The size of the  $\text{Cr}_2\text{Nb}$  was controlled, which was one of the objectives, but the volume fraction of intermetallic was large, thus, continuous networks resulted.

However, for material C, the microstructure remained as a solid solution with some, but very little, intermetallic after consolidation processing. Subsequent heat treatment precipitated the  $\text{Cr}_2\text{Nb}$  from what must have been a supersaturated solid solution, although that should not have been the condition of this material, as derived from the equilibrium phase diagram. The presence

of Ti indicates that the decomposition path for this material is not known. The result of a controlled precipitation of  $\text{Cr}_2\text{Nb}$  is that the particles were small and generally separated. The goal of this method of processing, which was to reduce the size of the intermetallic and obtain a good dispersion, was met. The volume fraction of intermetallic was too large, however, to produce a high fracture toughness material. The large number of small particles resulted in a high degree of constraint that was manifest as low fracture toughness.

The measured lattice parameter of the matrix increases with increasing volume fraction of intermetallic, which indicates that Ti is being lost from the matrix. The magnitude of  $\approx 3.3 \text{ \AA}$  with precipitation of  $\approx 30 \text{ v/o } \text{Cr}_2\text{Nb}$  indicates that the matrix has nearly the composition of Nb ( $a = 3.302 \text{ \AA}$ ). Thus, not only has heat treatment formed  $\text{Cr}_2\text{Nb}$ , it has also altered the composition of the matrix to a lower toughness material.

The lower than expected fracture toughness of material C can be attributed to the following: (1) the toughness of the matrix was lowered by compositional change during heat treatment, and (2) the  $\text{Cr}_2\text{Nb}$  was reduced to  $\approx 1 \mu\text{m}$  as the volume fraction was increased to  $\approx 25 \text{ v/o}$  and this led to very high constraint in the matrix that prevented it from deforming.

Lattice parameter measurements indicate that the precipitation of  $\text{Cr}_2\text{Nb}$  from material C lowers the strain between the particles and matrix, i.e., the interfacial incoherency. Even after 338 hrs of exposure to  $1000^\circ\text{C}$ , the incoherency strain remains at  $\approx 5\%$ , which is far too great to ever achieve coherency with the matrix alloy. For comparison, the incoherency strains for superalloys are closer to 0.1%, and about 1% is thought to be about the largest strain that is tolerable.

It is unlikely that further alloying can be used to increase the lattice parameter of the matrix alloy because the Goldschmid radius of Nb is the largest of any of the transition metals, and all the desirable alloying additions to Nb have smaller radii [6]. Therefore, it is unlikely that the lattice parameter of the matrix can be increased to fit with  $\text{Cr}_2\text{Nb}$ . Furthermore, alloying of  $\text{Cr}_2\text{Nb}$  is not expected to result in any substantial change in lattice parameter [7]. Thus, it appears to be impossible, through alloying, to bring the matrix and intermetallic into coherence. The important consequence of this lattice mismatch is that dislocations cannot be expected to cut  $\text{Cr}_2\text{Nb}$  particles. Thus, the lowering of constraint by the mechanism of particle cutting is not likely to be available in

this combination of matrix and intermetallic, regardless of the alloy.

Modeling (see Chapter 9) of fracture under the conditions found in these materials, e.g., without formation of microvoids, has shown that if the fracture toughness of  $\text{Cr}_2\text{Nb}$  could be increased from 2 to 6 MPa $\sqrt{\text{m}}$ , then by decreasing the particle size to about 1  $\mu\text{m}$ , the fracture toughness of a composite containing about 40 v/o particles could be increased to  $\approx$  25 MPa $\sqrt{\text{m}}$ , and this is about the maximum amount that could be expected.

## SUMMARY AND CONCLUSIONS

1. Producing composites in the Nb-Cr-Ti system by mechanical alloying has demonstrated that some microstructural control can be obtained over the size and dispersion of  $\text{Cr}_2\text{Nb}$  particles. If additional control to that obtained here is to be gained, heating during the powder consolidation process must be carefully controlled because intermetallic will form during this fabrication step.
2. Intermetallic formation in the material with the least Cr, material C, was not expected from the equilibrium phase diagram. Heat treatment during consolidation of this material resulted in small amounts of  $\text{Cr}_2\text{Nb}$ , but subsequent heat treatment precipitated 25 v/o or more intermetallic. For the size intermetallics that were precipitated (1-3  $\mu\text{m}$ ), the numbers of them caused high constraint, which limited the fracture toughness of the material.
3. The lattice parameter of the matrix of material C increased to approximately that of Nb during heat treatment because of the formation of Ti particles. Thus, the fracture toughness of the matrix was not that of the tough 50Nb-13Cr-37Ti alloy.
4. To increase fracture toughness of the low Cr material, the size of the particles would have to be increased, their numbers would have to be reduced, or the particles would have to shear during the fracture process.
5. An analysis of the material lattice parameters indicated that coherency cannot be obtained between matrix and  $\text{Cr}_2\text{Nb}$  through alloying. Thus, the only way to increase fracture toughness will be to reduce the volume fraction of  $\text{Cr}_2\text{Nb}$  particles.

**REFERENCES**

1. D.L. Davidson, K.S. Chan, and D.L. Anton, Metal. and Mat. Trans. A, 1996, v. 27A, pp. 3007-3018.
2. K.S. Chan, Metal. and Mat. Trans. A, 1996, v. 27A, pp. 2518-2531.
3. K.S. Chan, D.L. Davidson, and D.L. Anton, Metal. and Mat. Trans. A, 1997, v. 28A, pp. 1797-1808.
4. D.J. Thoma, PhD Dissertation, University of Wisconsin, 1992, available from university microfilms.
5. E.A. Franke, D. Wenzel, and D.L. Davidson, Rev. Sci. Instrum., 1991, v. 62, pp. 1270-1279.
6. F. Laves, Theory of Alloy Phases, Am. Soc. Metals, OH, 1956, p. 131.
7. C.T. Liu, P.F. Tortorelli, J.A. Horton, and C.A. Carmichael, Mat. Sci. & Eng., 1996, v. 214, pp. 23-32.

**ACKNOWLEDGEMENTS**

We gratefully acknowledge contribution of DERA to this research, who were successful in producing material on a small budget. The original contact at DERA was made through Dr. Malcolm Ward-Close, and the subsequent sub-contract project manager and technical contact was Dr. Paul S. Goodwin. Final material was delivered in mid-August 1997. The large contributions of Jim Spencer and Byron Chapa, technical specialists, is also gratefully acknowledged. Several discussions with Dr. Dan Thoma, Los Alamos National Laboratory were very helpful in understanding some of the results. Thanks to J.H. Zhu and P.K. Liaw for help in obtaining the Goldschmidt radii of the elements. This research was funded by the Air Force Office of Scientific Research, Contract F49620-95-C-0043.

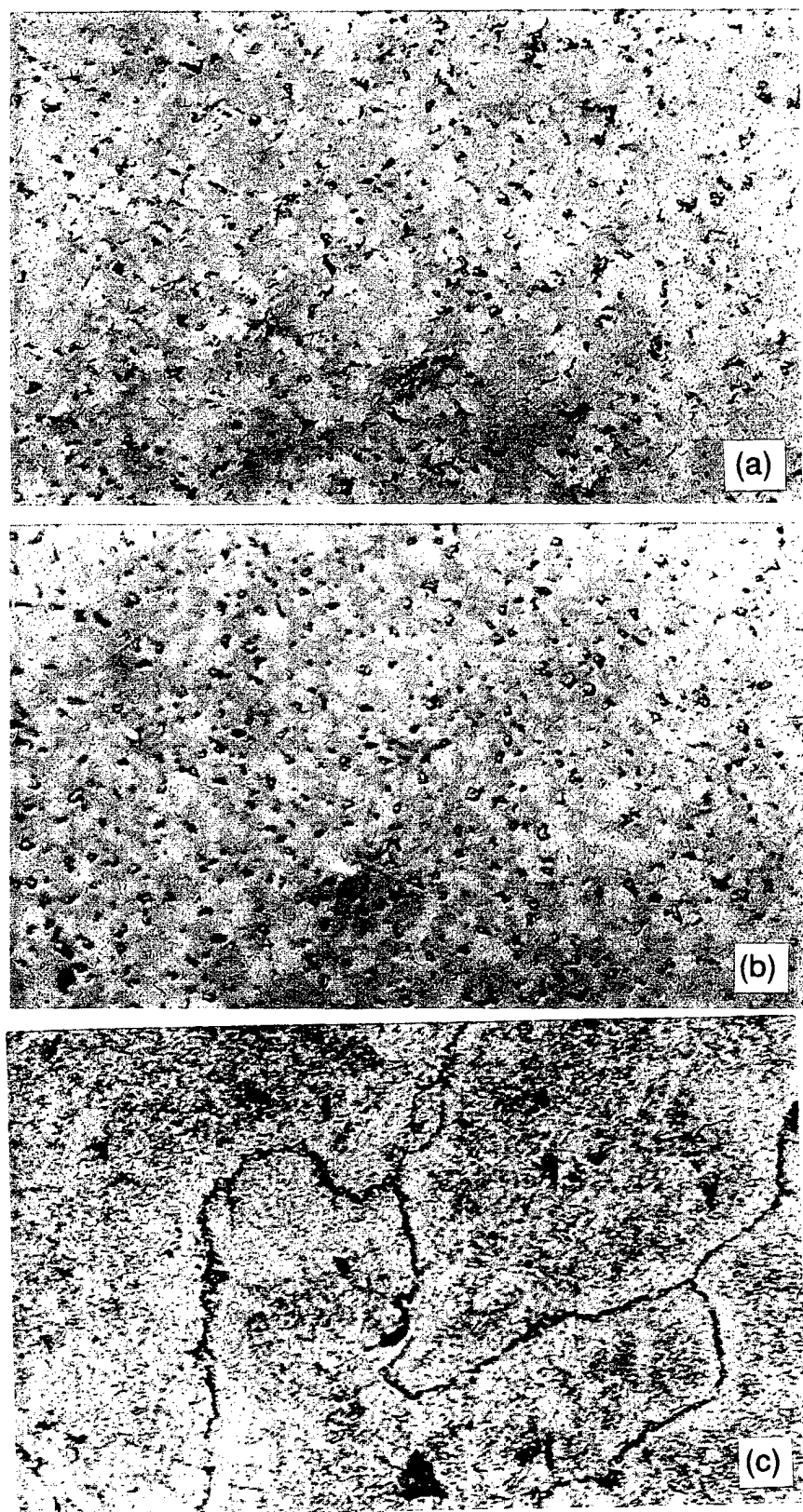


Fig. 1 Microstructures of the as-received materials by optical microscopy.  
(Etch: 31Hf, 15HNO<sub>3</sub>, 30HCl by vol.) (a) Material A (40Nb-30Cr-30Ti), (b)  
material B (37Nb-35Cr-28Ti), and (c) material C (48Nb-15Cr-37Ti). The lightest  
gray phase in materials A and B is Cr<sub>2</sub>Nb. In material C, not all as-received  
material had Cr<sub>2</sub>Nb.

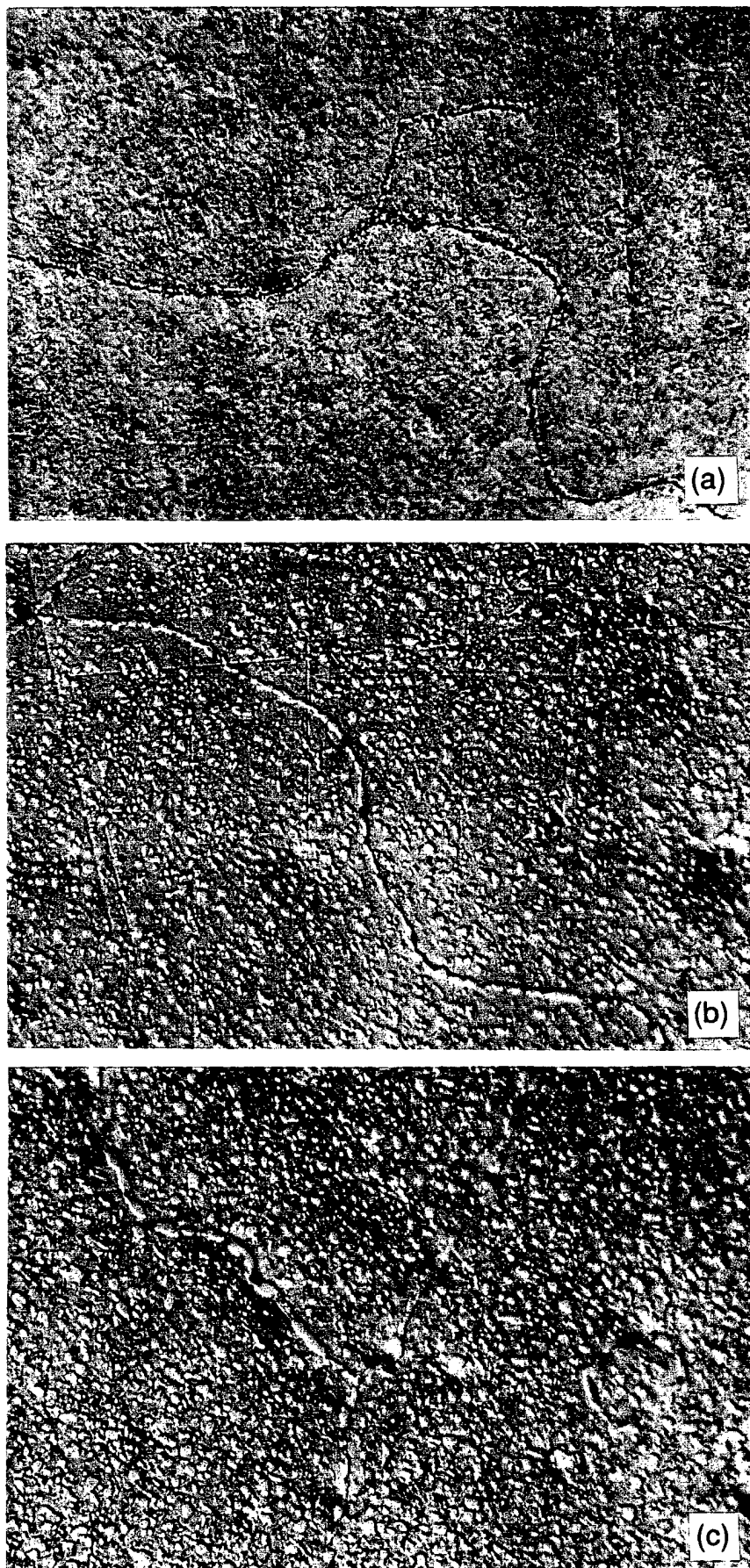


Fig. 2 Microstructures of material C as a function of time at 1000°C in vacuum, as seen by Nomarski contrast in the optical microscope. (a) as received, (b) 173 hrs., and (c) 338 hrs. The volume fraction and size of the  $\text{Cr}_2\text{Nb}$  increases with time at temperature.

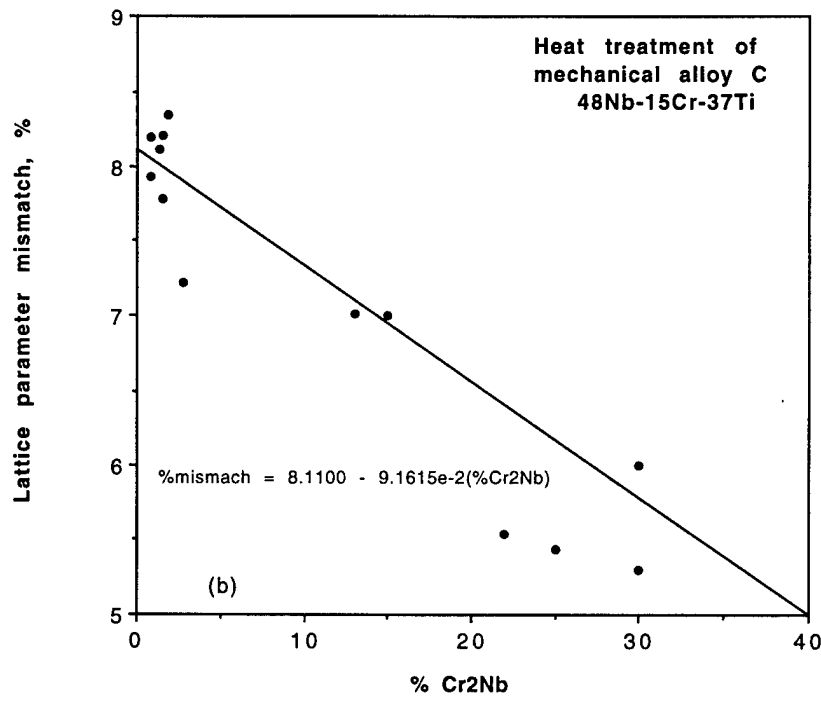
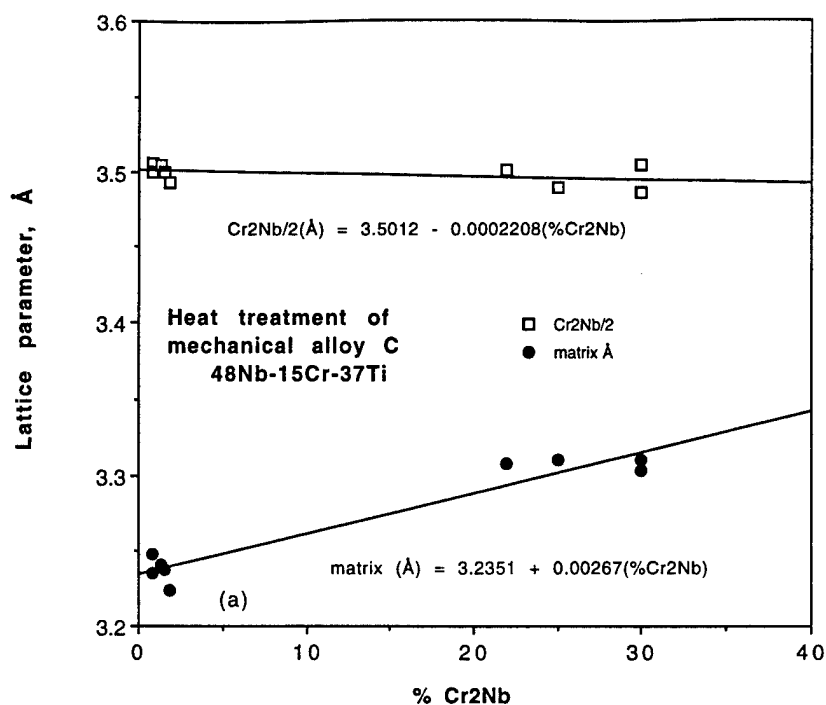


Fig. 3 (a) Correlation between the lattice parameter of the matrix, and (b) the lattice mismatch between the matrix and Cr<sub>2</sub>Nb, and the amount Cr<sub>2</sub>Nb in the material.

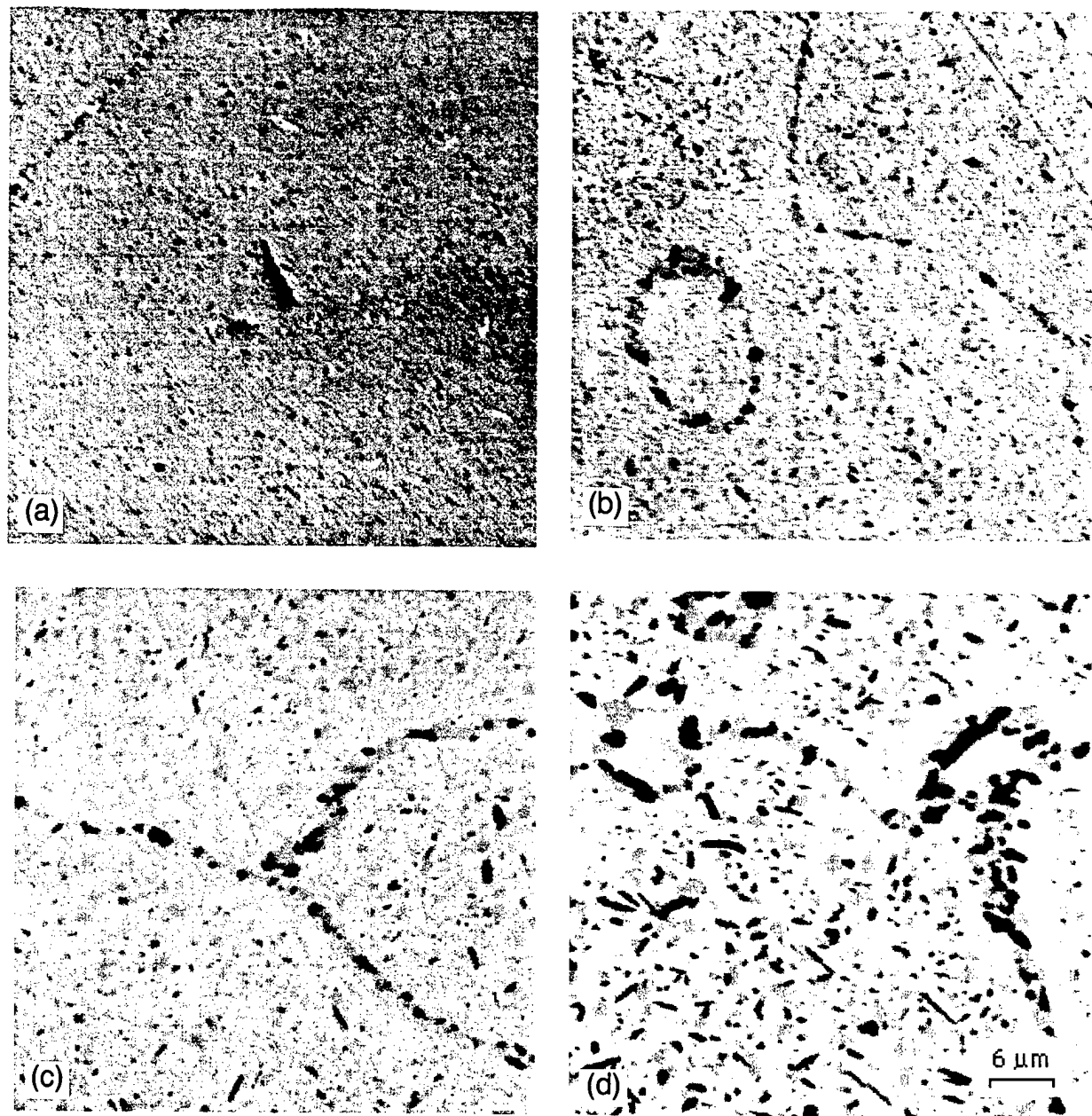


Fig. 4 The effect of heat treatment at 1000°C in vacuum on material C, as determined in the Auger Electron Spectrometer by combined secondary (SE) and backscattered electron (BSE) imaging. (a) As received, (b) 72 hrs., (c) 173 hrs., (d) 338 hrs. The increase in  $\text{Cr}_2\text{Nb}$  with time at temperature may be seen.

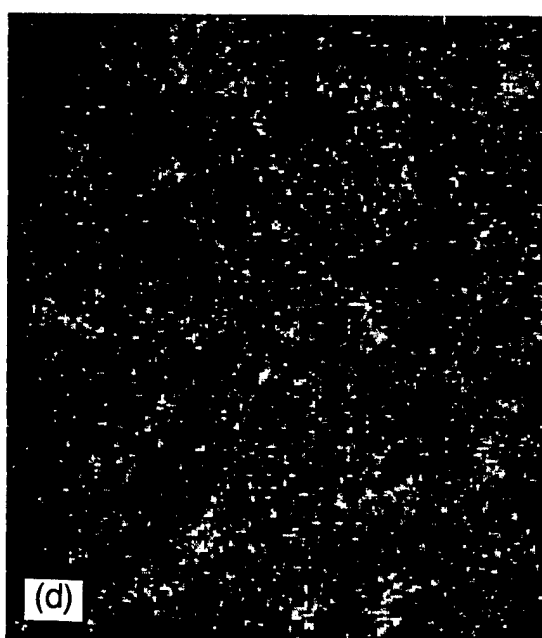
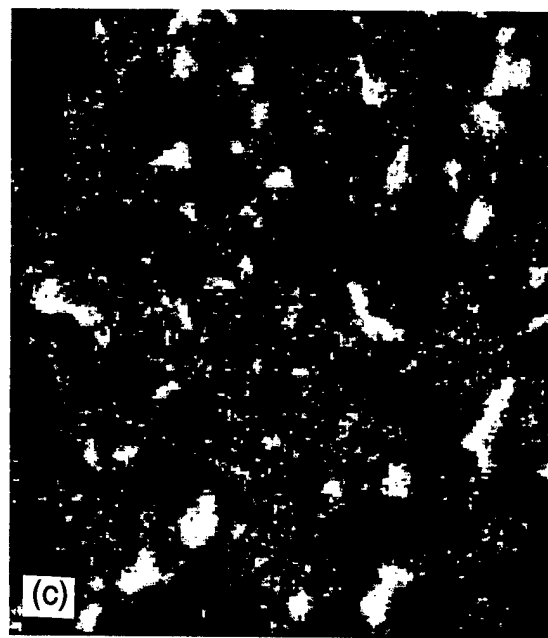
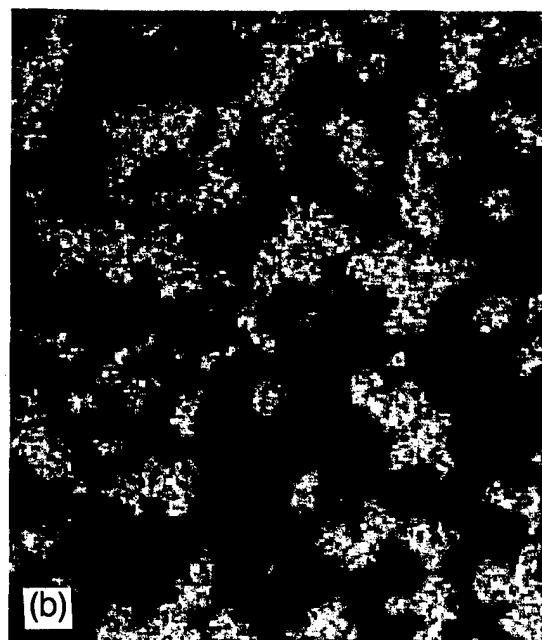
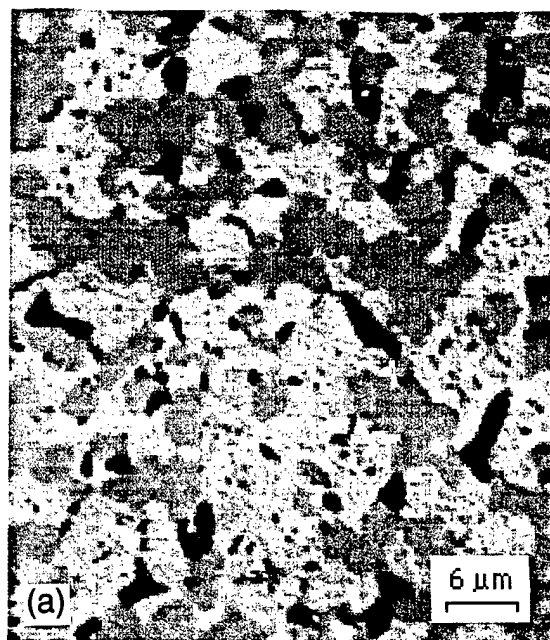


Fig. 5 The distribution of elements in material C after 173 hrs. at 1000°C in vacuum. (a) SE and BSE image, (b) Cr map, (c) Ti map, and (d) O map. Many of the dark particles seen in (a) are rich in Ti; the darker gray particles are rich in Cr, and O is distributed uniformly. The Nb map is not shown because it is approximately complementary to the Cr map; thus, the matrix is rich in Nb and Ti.

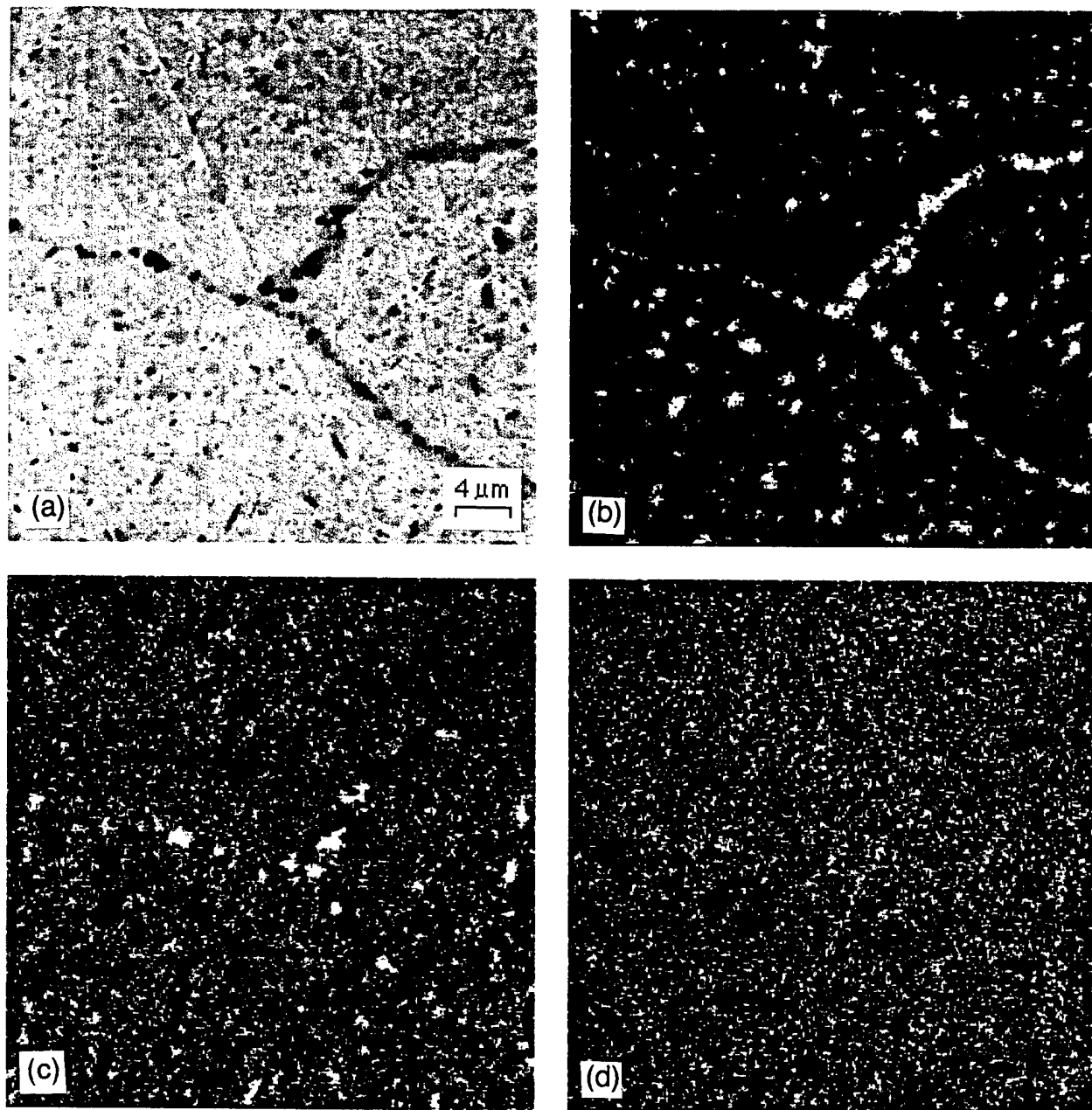


Fig. 6 The distribution of elements in material B after 72 hrs. at 1000°C in vacuum. (a) SE and BSE image, (b) Cr map, (c) Ti map, and (d) O map. The dark particles seen in (a) are rich in Ti, the dark gray particles are rich in Cr, and are probably  $\text{Cr}_2\text{Nb}$ , and the light gray material is rich in Nb (map not shown) and Ti which indicates that it is the matrix alloy. The distribution of O correlates with Ti, which indicates that Ti has gettered the O during processing or heat treatment.

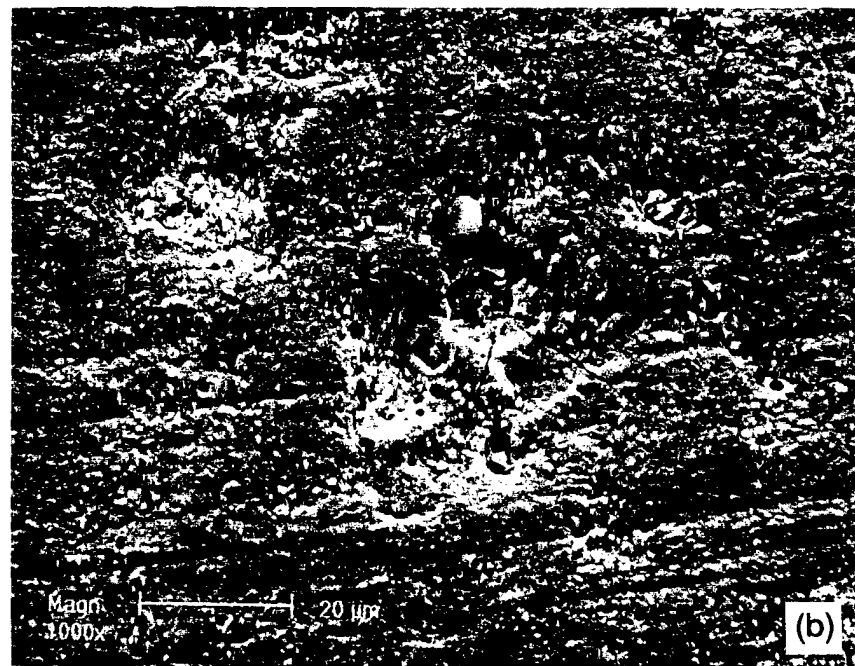
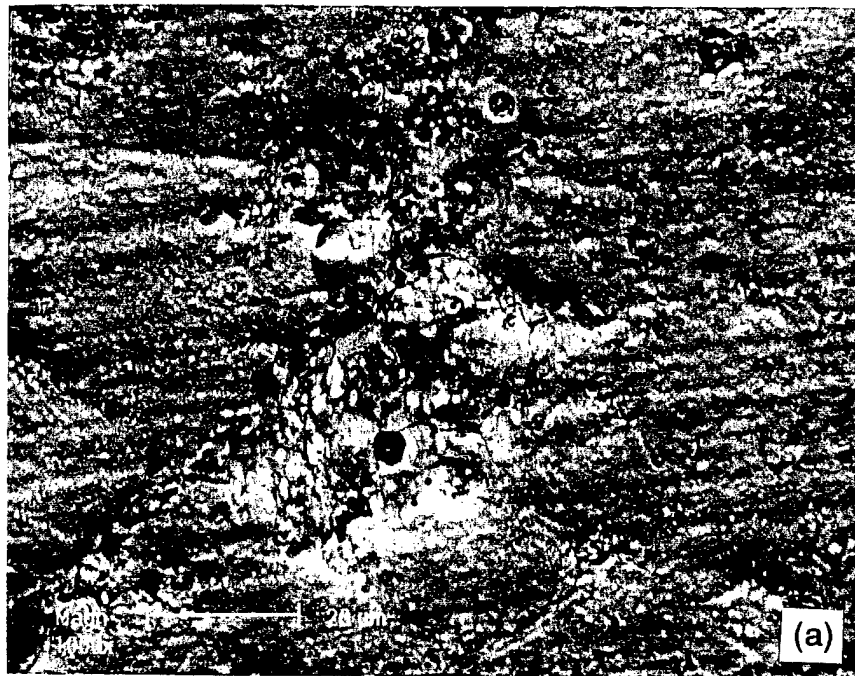


Fig. 7 Cracks in tensile samples. (a) Material A, and (b) material B. Such cracks limited the tensile strengths of these materials.

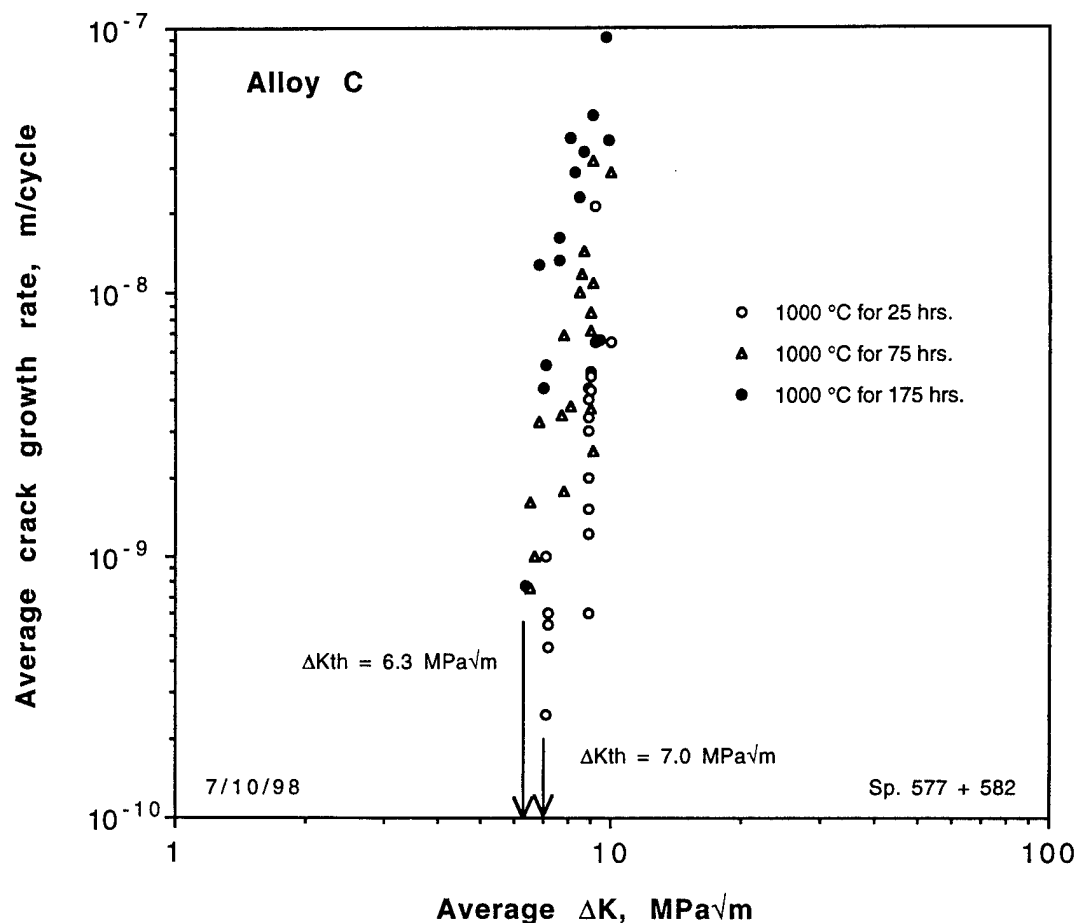


Fig. 8 Fatigue crack growth rates for material C as a function of heat treatment.

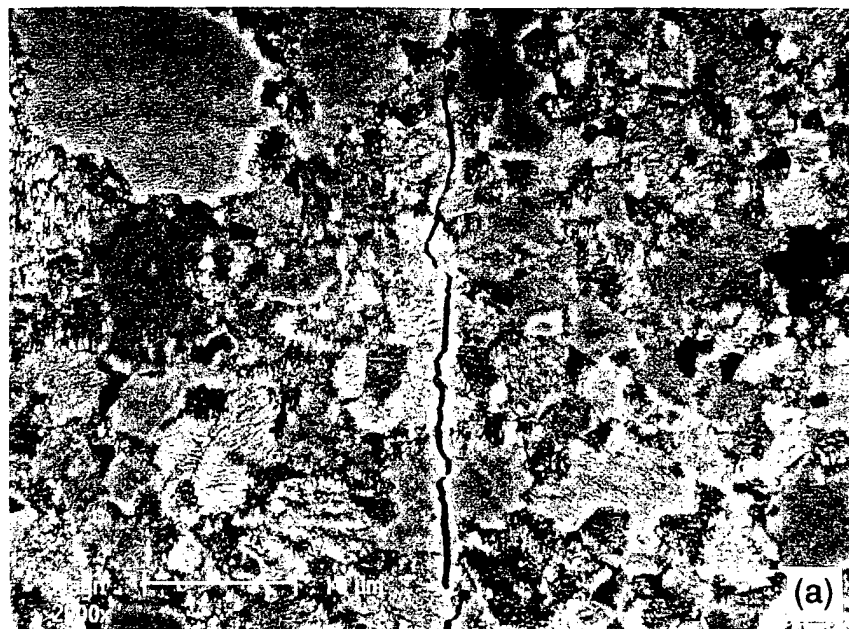


Fig. 9 Crack paths through the microstructures of materials A and B. Smooth particles are  $\text{Cr}_2\text{Nb}$  and rougher particles are matrix alloy.

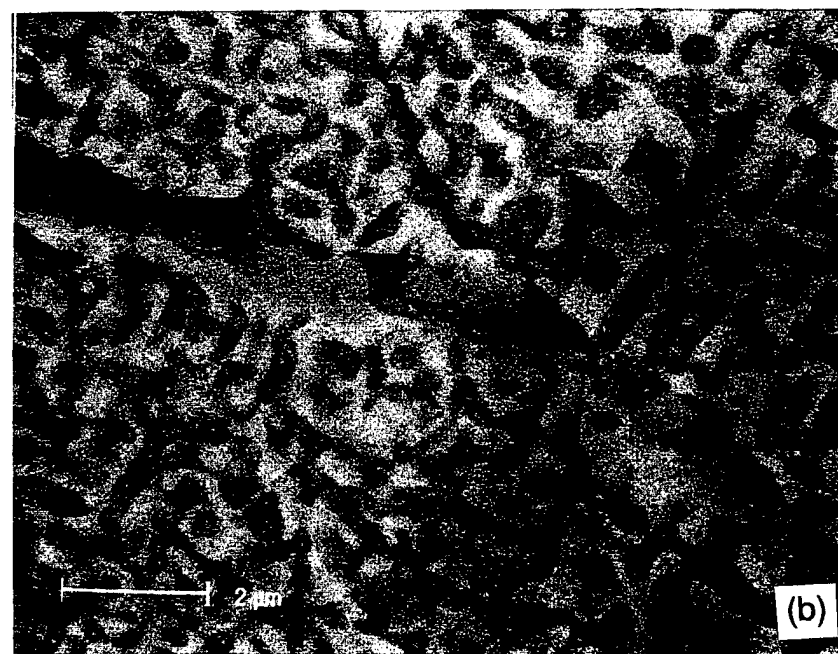
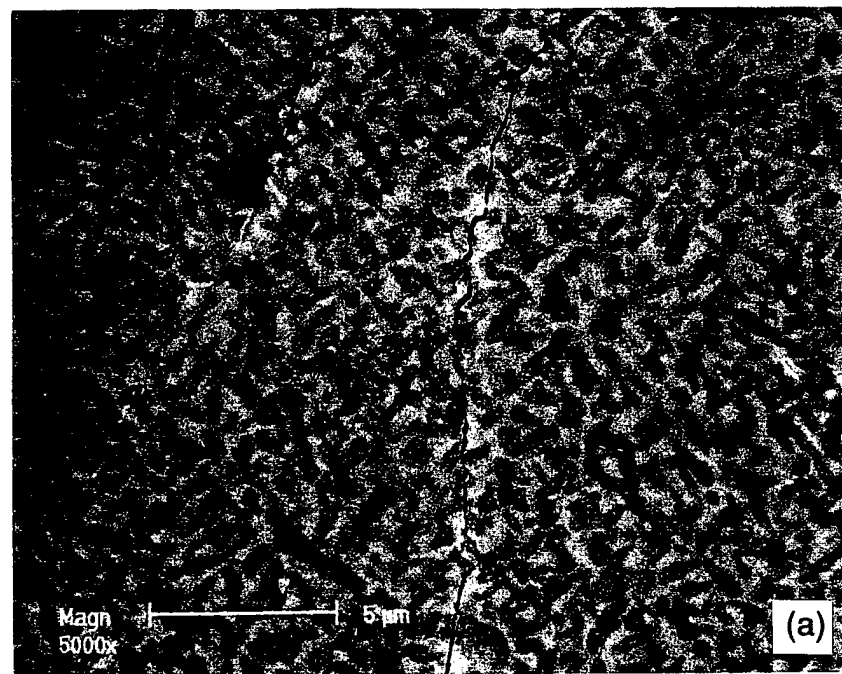
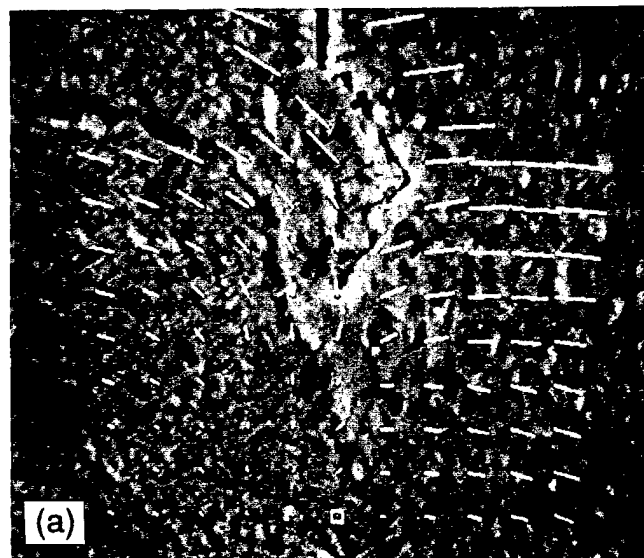


Fig. 10 The crack path through material C appears to be independent of the microstructural elements.



(a)

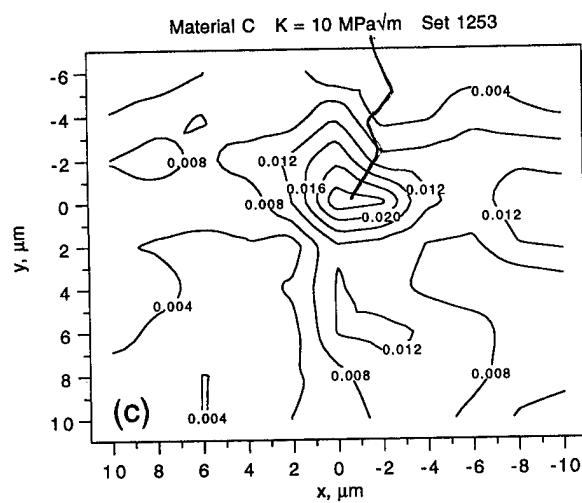
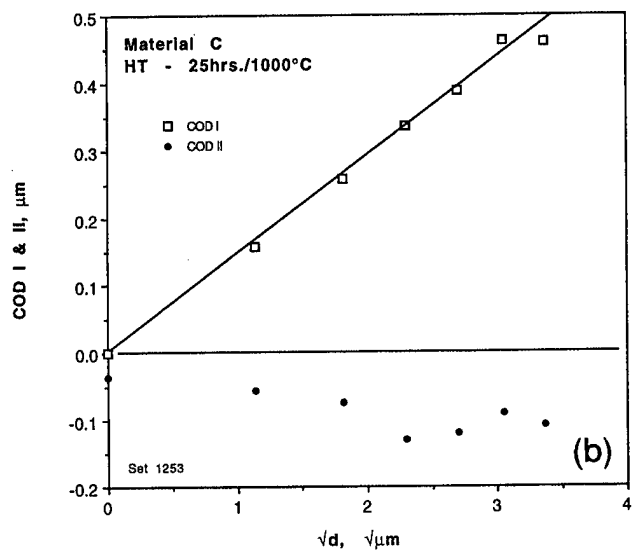


Fig. 11 Analysis of crack tip deformation in material C heat treated at 1000°C for 25 hrs. in vacuum at  $K = 10 \text{ MPa}/\text{m}$ , near  $K_c$ . (a) Photograph of the crack tip region with overlay of displacements each 2  $\mu\text{m}$  shown 10X actual size. (b) Crack opening displacement change with square root of distance behind the crack tip, and (c) contour map of maximum shear strain.

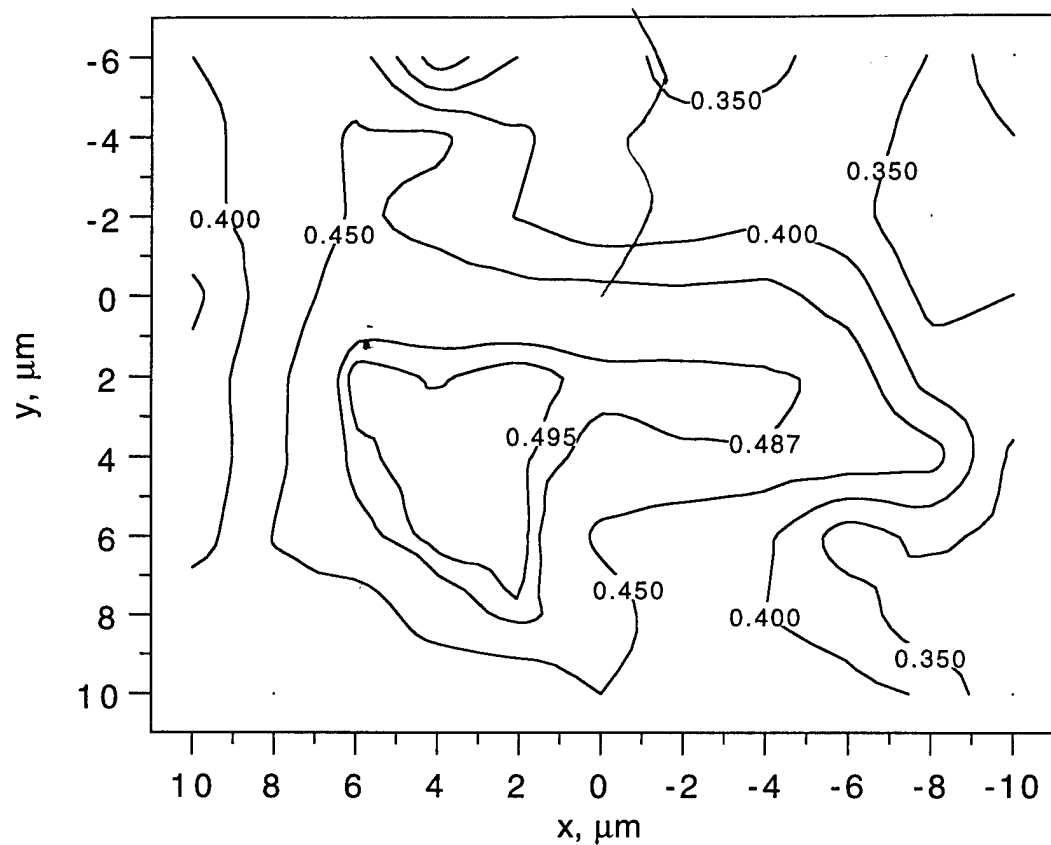
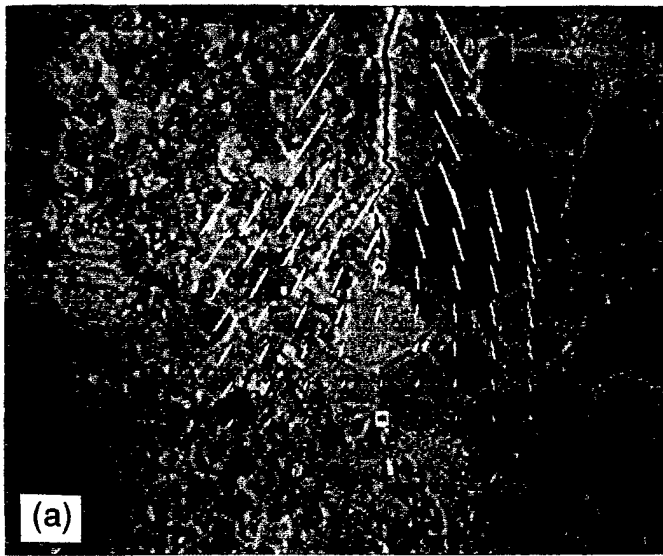
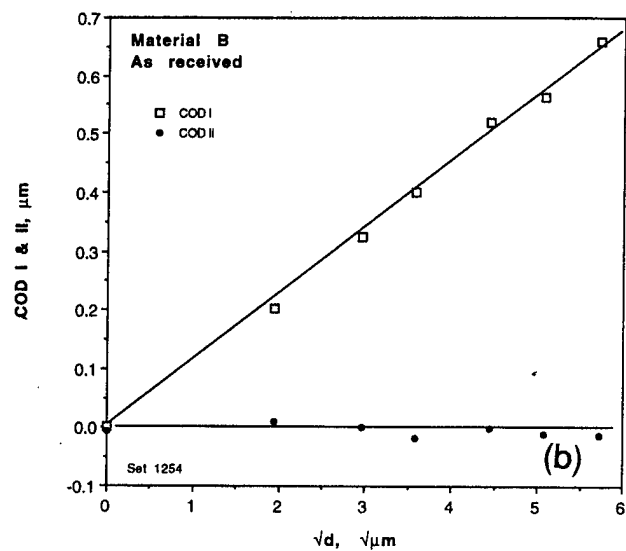


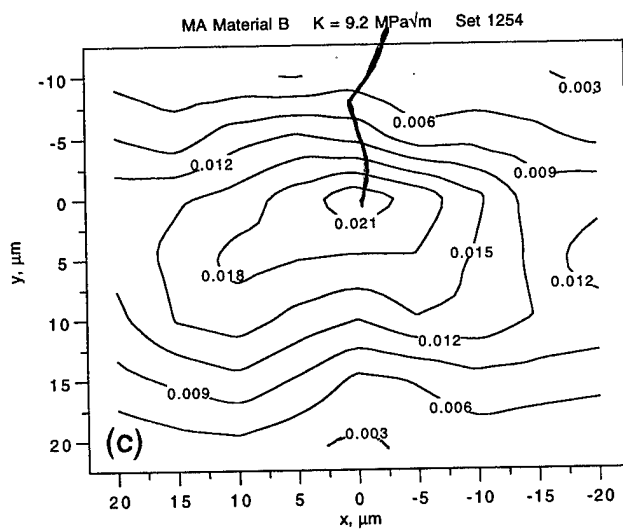
Fig. 12 Constraint in the crack tip region shown in Fig. 11. Maximum value of constraint possible is 0.5 (plain strain), so constraint is very high in the region shown.



(a)



(b)



(c)

Fig. 13 Analysis of crack tip deformation in material B at  $K = 9.2 \text{ MPa}\sqrt{\text{m}}$ , near  $K_c$ . (a) Photograph of the crack tip region with overlay of displacements measured each 5  $\mu\text{m}$  shown 15X actual size. (b) Crack opening displacement change with square root of distance behind the crack tip, and (c) contour map of maximum shear strain.

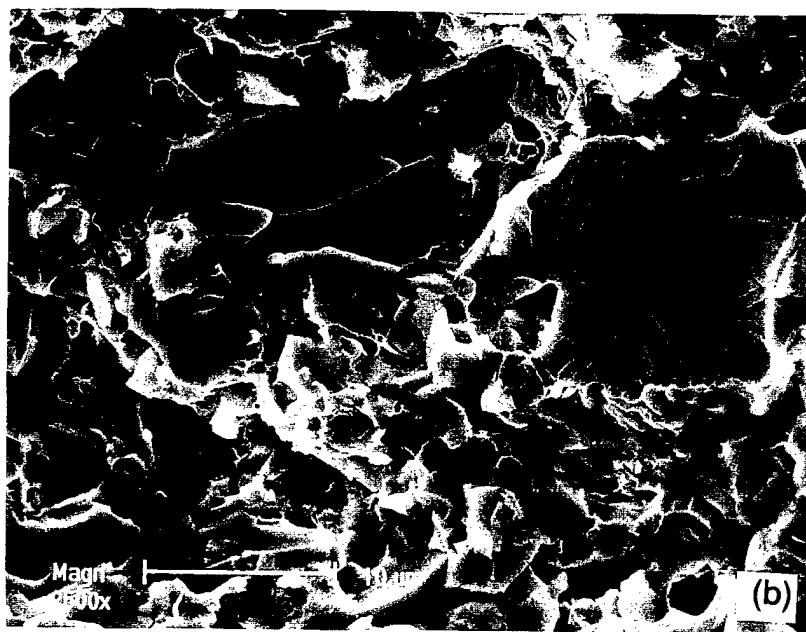
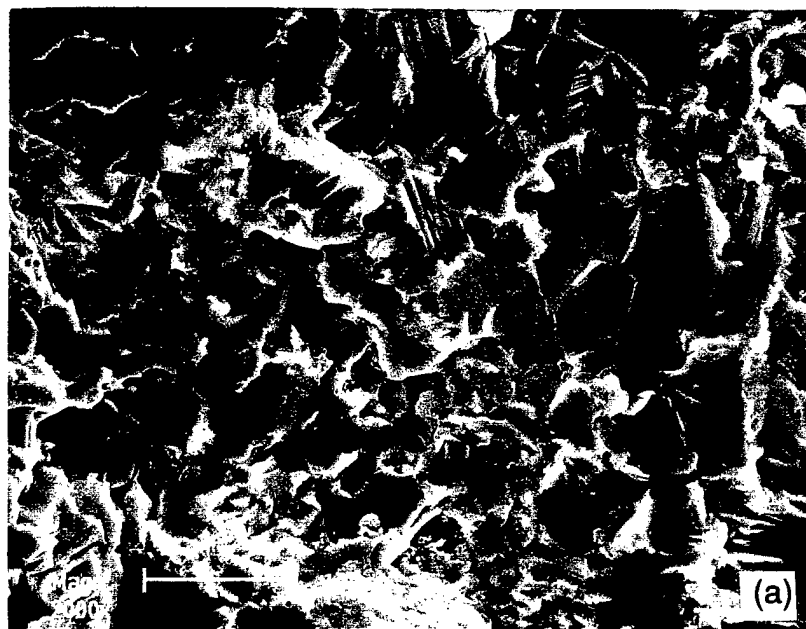


Fig. 14 Fractography of material A. (a) fatigue region, and (b) fast fracture region. Crack growth was from bottom to top.

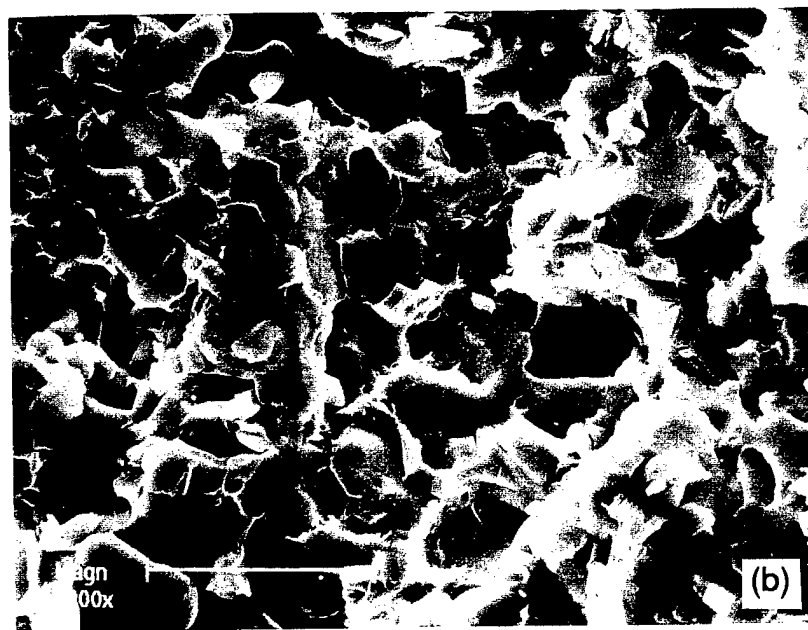
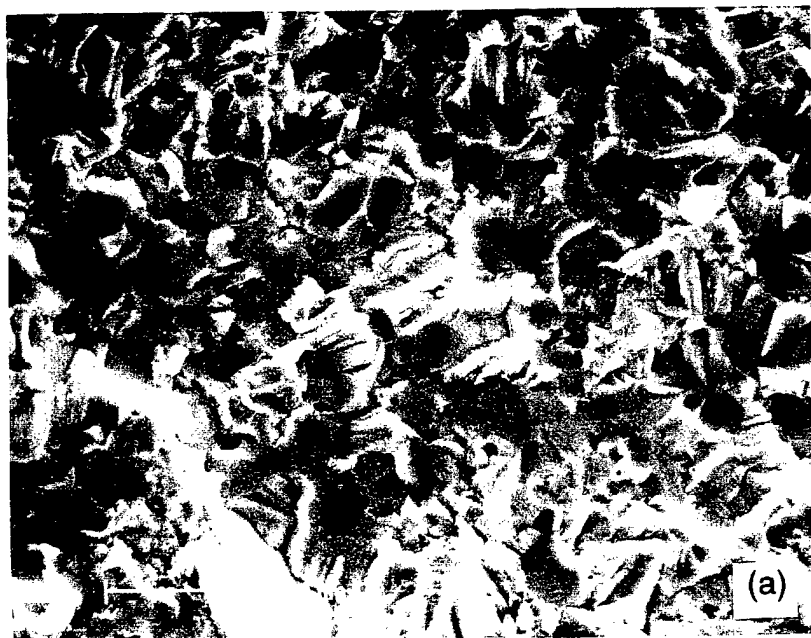


Fig. 15. Fractography of material B. (a) fatigue region, and (b) fast fracture region. Crack growth was from bottom to top.

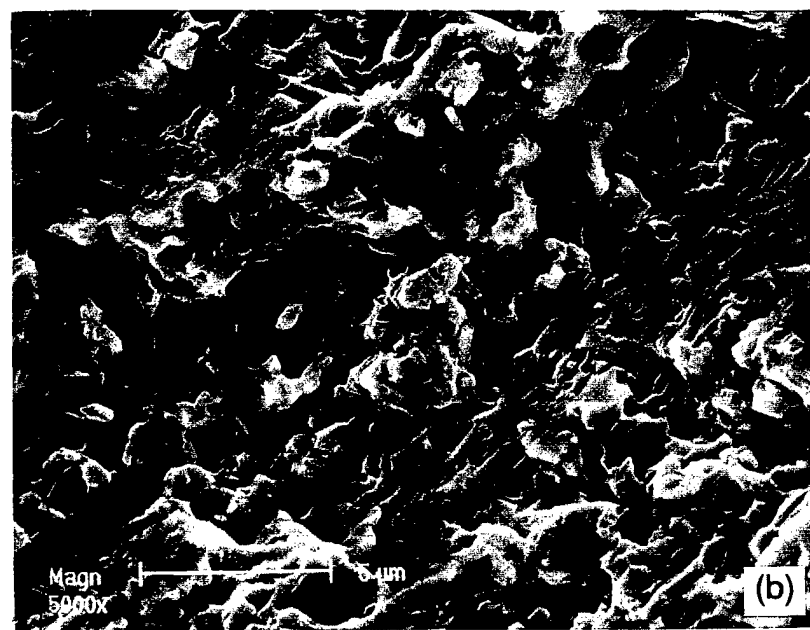
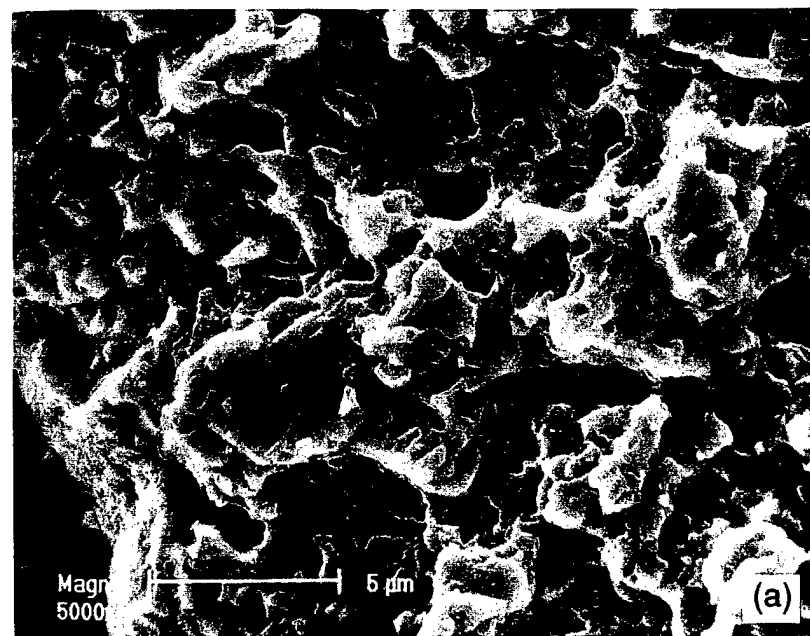


Fig. 16. Fractography of material C. (a) fatigue region, and (b) fast fracture region. Crack growth was from bottom to top.

**Fatigue and Fracture Toughness of a Commercially Made  
Nb-Ti-Base Single Phase Alloy at Ambient Temperature**

**D. L. Davidson, K. S. Chan and M. A. Crimp**

## FATIGUE AND FRACTURE TOUGHNESS OF A COMMERCIALLY MADE Nb-Ti-BASE SINGLE PHASE ALLOY AT AMBIENT TEMPERATURE

D.L. Davidson and K.S. Chan  
Southwest Research Institute  
San Antonio, TX 78228

M.A. Crimp  
Michigan State University  
East Lansing, MI

### ABSTRACT

The fatigue and fracture resistance of a commercially made, single phase Nb-base alloy with 35 at.% Ti, Cr, Al, and several elements to increase solid solution strengthening have been investigated. Threshold for fatigue crack growth was found to be  $\approx 7 \text{ MPa}\sqrt{\text{m}}$ , and fracture toughness  $\approx 35 \text{ MPa}\sqrt{\text{m}}$ . Crack growth is crystallographic and found to favor the {110} and {112}.

### INTRODUCTION

Niobium alloys with 30 to 50 at.%Ti have been shown to have very good ductility and fracture toughness characteristics. On this basis, an alloy was formulated that could be made in fairly large quantity by commercial practices so that its properties could be more completely evaluated. The composition of this material was: Nb-35Ti-6Al-5Cr-8V-1W-0.3Hf-0.5Mo-0.05C. Thus, it is similar to the high toughness alloy Nb-13Cr-37Ti with solid solution strengthening elements W and Mo, and with Al, V and Hf, which should improve high temperature strength and oxidation resistance. This paper examines in some detail the fracture resistance of this material at ambient temperature.

### MATERIAL AND EXPERIMENTAL TECHNIQUE

A 300 mm long piece of a much longer extruded bar about 62 mm in diameter was furnished to us by Reference Metals Company [1]. Although details of the processing and properties for this alloy have been published [2-4], a brief description is given here. Commercially available powders were blended and formed into disks by pressing at Oremet, then double plasma arc melted on a cold hearth at Retech, to produce an ingot. The ingot was machined, canned and extruded at 1100°C at Amex to a 81 mm diameter bar (including the stainless steel can).

This alloy was found to have a tensile elongation of  $\approx 16\%$ , a yield strength of  $\approx 1100 \text{ MPa}$ , both at ambient temperature, with a fracture toughness of  $\approx 35$

MPa $\sqrt{m}$  [5]. At 800°C the tensile strength was measured as 580 MPa, while at 1000°C, strength was about 150 MPa.

Interstitials, which greatly influence the mechanical behavior of body centered cubic alloys, were measured at the following levels (in ppmw): O = 116, C = 54, N = 10, and H = 3. Thus, this is a clean alloy, and mechanical properties should not have been affected by these interstitial levels.

A section of the bar was cut so that the plane of the small CT-type specimens was perpendicular to the extrusion direction. Specimens were heat treated at 1000°C for 4 hours in vacuum before final specimen preparation. The direction of crack growth was perpendicular to the extrusion axis. As shown in Fig. 1, the grain structure consisted of a combination of large and small grains. Many of the large grains were 500  $\mu m$ , or longer, in the extrusion direction by up 200  $\mu m$  in the transverse direction. The crack seen in the figure was grown by fatigue to the arrow, and above that point by fast (overload) fracture while evaluating fracture toughness. Electron backscattered patterns (EBSP) were used to determine the crystallography of crack growth for the specimen shown in the figure.

Fatigue crack growth rates were measured in several specimens of this material in air in a laboratory machine. Cracks were initiated from notches several mm deep by about 0.5 mm wide. Periodically, these specimens were transferred to the SEM for detailed analysis of the crack opening loads and crack tip deformation characteristics. An unusual level of effort was expended on measuring the crack opening characteristics of this material because of a number of questions that were of current interest about the opening of fatigue cracks and the level of fatigue crack closure. Thus, the hysteresis of crack opening was measured during increasing and decreasing loads, and crack opening loads were directly measured. Upon completion of fatigue crack growth rate measurements, specimens were loaded within the SEM to measure fracture toughness.

## RESULTS

Optical microscopy indicated that the alloy was single phase material with spherical carbides in very small volume fraction. All the lines of the x-ray diffraction pattern could be indexed as bcc, giving the lattice parameter as 3.234  $\text{\AA}$ , which is about as expected, based on other work, from the alloy composition. No superlattice or intermetallic lines were found in the x-ray diffraction data.

From the fatigue crack growth rates shown in **Fig. 2**, a threshold stress intensity factor for crack growth,  $\Delta K_{th} \approx 7 \text{ MPa}\sqrt{\text{m}}$  may be inferred for growth at  $\approx 10^{-12} \text{ m/cycle}$ . Consistent with crack growth rate measurements from other alloys, the slope of the curve in the near-threshold region is very steep,  $\approx 70$ . A measured fracture toughness value [5] is shown at  $10^{-6} \text{ m/cycle}$ , and it is logical that this point be connected with the crack growth rate data, showing that there is a change in slope at about  $10^{-9} \text{ m/cycle}$ , which is also consistent with data gathered from other, similar Nb alloys. Thus, the slope of the curve, which is  $\approx 4.2$ , above about  $10^{-9} \text{ m/cycle}$  is dependent on the magnitude of fracture toughness, while growth rates below that rate are related to  $\Delta K$  values relative to  $\Delta K_{th}$ . The factors controlling  $\Delta K_{th}$  are poorly understood, but Youngs modulus does contribute to its magnitude.

It should be noted that fatigue crack growth in this material, as in other, similar alloys is intermittent and sporadic. The crack was observed to be stationary for thousands of cycles, then grow tens of micrometers in just a few cycles. Similarly, during the experiment to measure the fracture toughness, the crack initiated, grew rapidly for  $\approx 1 \text{ mm}$ , then arrested, did not grow as load was increased, then grew and arrested again.

Several measurements of crack opening load were made, and these are shown in **Fig. 3**, together with a line that shows typical behavior as derived from many other materials. As might be expected from the erratic and intermittent crack growth behavior, there is a wide variation in crack opening loads and the computed value of  $\Delta K_{eff}$ . Perhaps of more interest are the measurements of crack mouth opening displacement (CMOD) and load vs. strain shown in Figs. 4-6.

Determination of opening load from **Fig. 4** is made from the point where the slope changes, or at about 200 N. Refined methods of measuring CMOD are used to measure opening loads in many laboratories. The value of opening load determined by this method is well below the actual opening loads measured directly at the crack tip.

Two measurements of load divided by specimen area, a pseudo-stress, vs. maximum shear strain determined at the crack tip are shown in **Fig. 5**. The hysteresis in strain between loading and unloading is shown in **Fig. 5(a)**, as are the differences in opening and closing loads, although small in this case. As seen in **Fig. 5(b)**, the shape of the curve shown in (a) is not always the same, and a well formed hysteresis loop was not always found.

Three different measurements of strain - the maximum shear strain, strain in the loading direction, and effective strain, are compared in **Fig. 6**. Maximum shear strain is the smoothest curve, but the trends are the same for all the strains. Normalized values of load and strain are plotted in **Fig. 7**, which shows that the variation is not quite linear, and that crack opening load occurs at a strain that approximates the yield value. The implication of this strain value is that loading must overcome a compressive stress at the crack tip of approximately yield magnitude before the crack can open to the tip, which is consistent with many other measurements of residual stress surrounding fatigue crack tips. For the conditions of the experiment shown, yield strain is about half the maximum strain exhibited by the crack tip at full load, and opening load is  $\approx 0.6$  of maximum load.

Fracture toughness experiments were conducted on several specimens at the completion of the crack tip characterizations during fatigue crack growth. In one experiment, rapid crack growth initiated unexpectedly, and the specimen fractured, yielding little data, except for a value of the initiation fracture toughness. A second specimen exhibited two episodes of crack initiation and arrest. The crack path during rapid fracture was shown in Fig. 1 in the upper part of the figure, above the arrow, and are shown again in **Fig. 8**. The first episode of crack growth resulted in a crack that grew 17  $\mu\text{m}$ , then split into two branches and arrested after the longest of the two (right side) grew 200  $\mu\text{m}$ . Crack initiation occurred at  $K = 33.3 \text{ MPa}\sqrt{\text{m}}$ . Increasing the load caused the crack to initiate again at  $K = 35.1 \text{ MPa}\sqrt{\text{m}}$ , grow 540  $\mu\text{m}$  and again arrest. At this point the experiment was terminated with the specimen still unbroken so that EBSP could be used to determine the orientation of the crack, which appears to be highly crystallographic. Previously, several fracture toughness tests had been conducted that indicated  $K_c \approx 35 \text{ MPa}\sqrt{\text{m}}$  [3].

Electron Backscattered Patterns (EBSP) were made at Michigan State University from several large grains that had been traversed by the crack so that the trace of the crack could be determined. More than 20 EBSP were made from 6 locations along the crack path. The locations of some of these patterns are shown in Figs. 1 and 8.

Orientation of the EBSP located in Fig. 1 indicated that the normal to the specimen surface was within  $10^\circ$  of the  $\langle 111 \rangle$  and that the trace of the crack path was close to  $\{110\}$ . Orientation of the EBSP shown in Fig. 8 indicated that normal to the specimen surface was  $\langle 112 \rangle$  or  $\langle 115 \rangle$ ; i.e., within  $\approx 15$  deg. to the

<001>, while the path of the crack was approximately along a {112} trace. Thus, the straight cleavage-appearing cracks of rapid crack growth appeared to favor the {112} rather than the {001} as is often the case for bcc alloys.

Fractography of surfaces created by fatigue and fast fracture is shown in **Figs. 9 and 10**. A typical low magnitude image of the surface created in fatigue is shown in Fig. 9(a). The surface is transgranular and generally rough, but with some facets that indicate crystallographic growth planes. Some fatigue striations were found, as shown in Fig. 9(b). In this figure, crack growth was from bottom to top. Illustrated in Figs. 9(c) and 9(d) are details of fatigue fracture that are unusual. Small particles, such as those seen in Fig. 9(c) were found associated with relatively flat facets that suggested growth near a crystallographic plane of low index. The particles may be carbides that are found in this material in low volume fraction. They seem too well organized near a grain boundary to be debris from the fatigue process, such as seen in Fig. 9(d). The periodic marks seen in this figure were caused by fatigue, but are very different from typical fatigue striations.

The fracture surfaces created by fast fracture shown in **Fig. 10** are much more crystallographic in appearance than those caused by fatigue. No dimpled rupture was found. Some possible intergranular crack propagation may be evident in small grains, as seen in Fig. 10(a), but most of the fracture surface is more typically shown in Figs. 10(b) and 10(c). In Fig. 10(b), the surface has many steps and river lines often associated with crack growth that is near, but not on, a crystal plane of low index. A much more tortious crack path, but still highly crystallographic is shown in Fig. 10(c).

## DISCUSSION

This alloy, with the composition 52.2Nb-11(Cr,Al)-35Ti-1.8(V,W,Mo), is similar to the 50Nb-13Cr-37Ti; yet the latter alloy has a fracture toughness approaching 100 MPa $\sqrt{m}$ , while this commercially made material has a fracture toughness of only  $\approx 32 \pm 5$  MPa $\sqrt{m}$ . Although this is an excellent level of toughness for a transition metal alloy, it does raise the question as to why there is such a large difference in fracture toughness values between these two alloys so similar in composition. Recently, a series of Nb-(32-37)V alloys with 15Cr and a combination of Cr and Al were examined by transmission electron microscopy (TEM) [6]. That work found that when only Cr was present, the alloy showed no signs of ordering, but when both Cr and Al were present, the ordered bcc structure B2 readily formed, when the Al content exceeded about 4 at.%.

If these results are applicable to Nb-Ti-Cr-Al alloys, then the present alloy would be expected to have an ordered B2 structure because of the 6 at.% Al in its composition. Investigators of the Nb-V-Cr-Al alloys found no superlattice lines by x-ray diffraction [6], just as none were found for this alloy, so it will be necessary to perform TEM to determine if, in fact, the material is ordered. If the material is ordered, then it could help explain why the fracture toughness is so much lower than expected from the high toughness 50Nb-13Cr-37Ti alloy, which was found by both x-ray and TEM to show no signs of an ordered structure or of intermetallic formation.

Fatigue crack growth results from this alloy were similar to those measured from other Nb alloys with fewer constituents manufactured by laboratory techniques that have been studied. The growth of fatigue cracks is erratic and intermittent, as with other, similar alloys. Strains measured at fatigue crack tips at  $\Delta K \approx 10 \text{ MPa}\sqrt{\text{m}}$  were 2 to 3%. Fatigue crack closure measurements were as expected from similar, previous measurements on other alloys, except that opening load was highly variable, which agrees with the crack growth characteristics.

Fractography indicated that fatigue striations form, as with other ductile alloys, while in fast fracture, considerable ductility can be seen on otherwise flat facets. Use of EBSP to orient the planes of fracture indicated that fast fracture occurred preferentially on {110} or {112}, which are the expected planes for slip in bcc metals.

## CONCLUSIONS

1. This commercially made single phase alloy has a  $\Delta K_{th} \approx 7 \text{ MPa}\sqrt{\text{m}}$ , and a fracture toughness of  $\approx 35 \text{ MPa}\sqrt{\text{m}}$ , at ambient temperature, which is excellent fracture resistance for transition metal multielement alloys.
2. The slope of the fatigue crack growth rate curve is high ( $\approx 70$ ) below  $10^{-9} \text{ m/cycle}$  and similar to other Nb-based alloys, but above  $10^{-9} \text{ m/cycle}$ , the slope decreases to  $\approx 4.2$  which reflects a relatively high value of fracture toughness.
3. Fracture planes were identified as {110} or {112} using EBSP.
4. The reason that the fracture toughness of this alloy is below that of the 50Nb-13Cr-37Ti alloy is because of the presence of 6 at.% Al, which has been shown in Nb-V-Cr alloys to induce an ordered B2 structure of lower toughness.

## ACKNOWLEDGEMENTS

Thanks to Mr. E.A. Loria of Reference Metals for furnishing the material. Michigan State University PhD. candidate Reza Loloec made the EBSP, and technical assistance was furnished by Byron Chapa and Jim Spencer of SwRI. Research funding came from Air Force Office of Scientific Research, Contract F49620-95-C-0043.

## REFERENCES

1. Reference Metals Company, 1000 Old Pond Road, Bridgeville, PA 15017-0217.
2. E.A. Loria "Processing capability of structural intermetallics and Nb-Ti-Al alloys via plasma arc melting" in Structural Intermetallics, R. Darolia, J.J. Lewandowski, C.T. Liu, P.L. Martin, D.B. Miracle, and M.V. Nathal, eds., The Minerals, Metals, and Materials Soc., Warrendale, PA., 1993, pp. 699-705.
3. E.A. Loria "Development of ductile Nb-Ti-Al alloys: Perspective and selected successes" in Proceeding of the 2nd Inter. Conf. on Heat-Resistant Materials, Am. Soc. for Mat., 1995, pp. 613-619.
4. V.K. Sikka and E.A. Loria "Characteristics of a multicomponent Nb-Ti-Al alloy via industrial-scale practice" **Mat. Sci. and Eng.**, 1997, A239-240, pp. 745-751.
5. P.R. Subramanian and E.A. Loria "Plane strain fracture toughness of a multicomponent Nb-Ti-Al alloy" manuscript in preparation, 1997.
6. Y.G. Li, P.A. Blenkinsop, M.H. Loretto, and N.A. Walker, **Mat. Sci. and Tech.**, 1998, v. 14, pp. 732-737.

Fig. 9 Fractography of fatigue crack growth. General growth direction was from bottom to top. (a) A low magnification view showing transgranular cracking with some formation of flat facets. (b) At higher magnification, striations are visible in some areas. (c) Flat facets show river lines, and in this example, fine particles distributed systematically on the surface. (d) Very coarse structure on another relatively flat region that are similar to striations.

Fig. 10 Fractography of fast fracture. General growth direction was from bottom to top. No dimpled rupture was found. (a) A low magnification view shows much greater formation of flat facets than seen in fatigue. Some intergranular fracture in regions of small grains may be indicated. (b) Higher magnification views of flat facets shown features indicating considerable plasticity during fracture. (c) Another region of crystallographic cracking involving considerable plasticity.



Fig. 1 Optical microscope view of the crack path through one of the two specimens. Loading axis was horizontal and crack growth was from bottom to top. Below the arrow, crack was grown by cyclic loading,  $R = 0.1$ , and above the arrow, the crack was grown by monotonic loading. EBSP patterns were made in large grains at the locations shown.

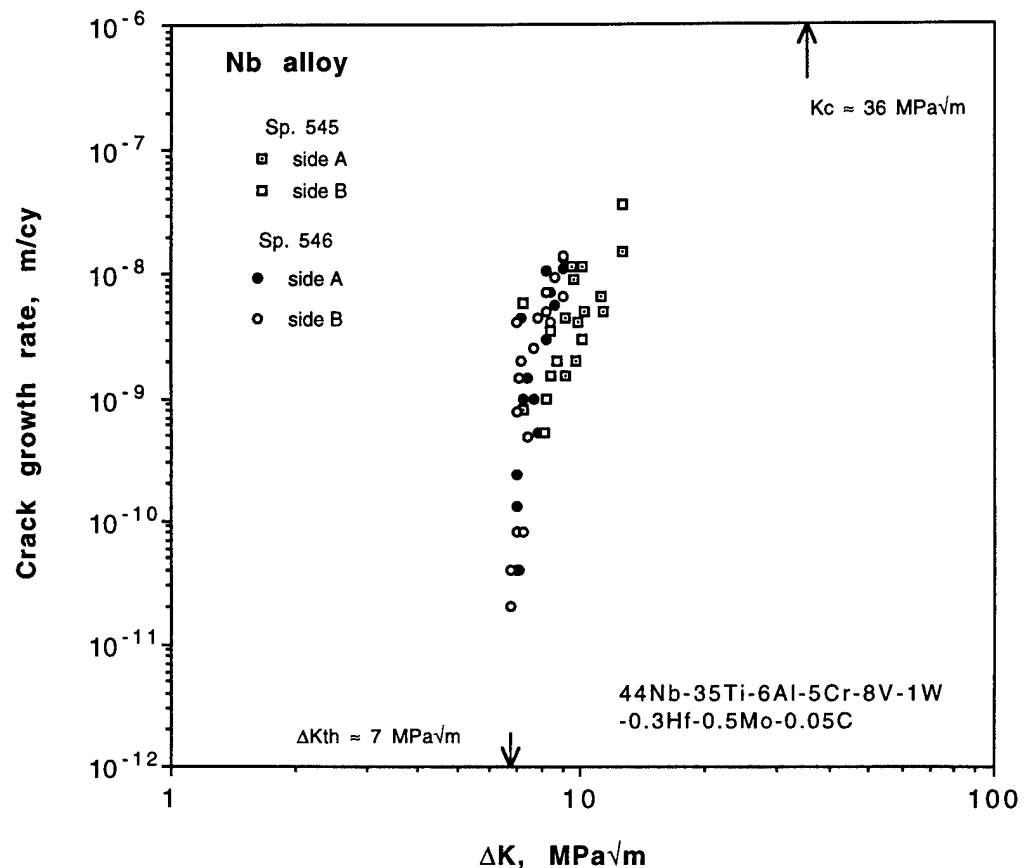


Fig. 2 Fatigue crack growth rates correlated with cyclic stress intensity factor. Shown are results from both specimens. The indicated  $\Delta K_{th} \approx 7 \text{ MPa}\sqrt{\text{m}}$ , and the fracture toughness  $\approx 36 \text{ MPa}\sqrt{\text{m}}$ . The intermittent and sporadic nature of crack growth is not reflected in these average values.

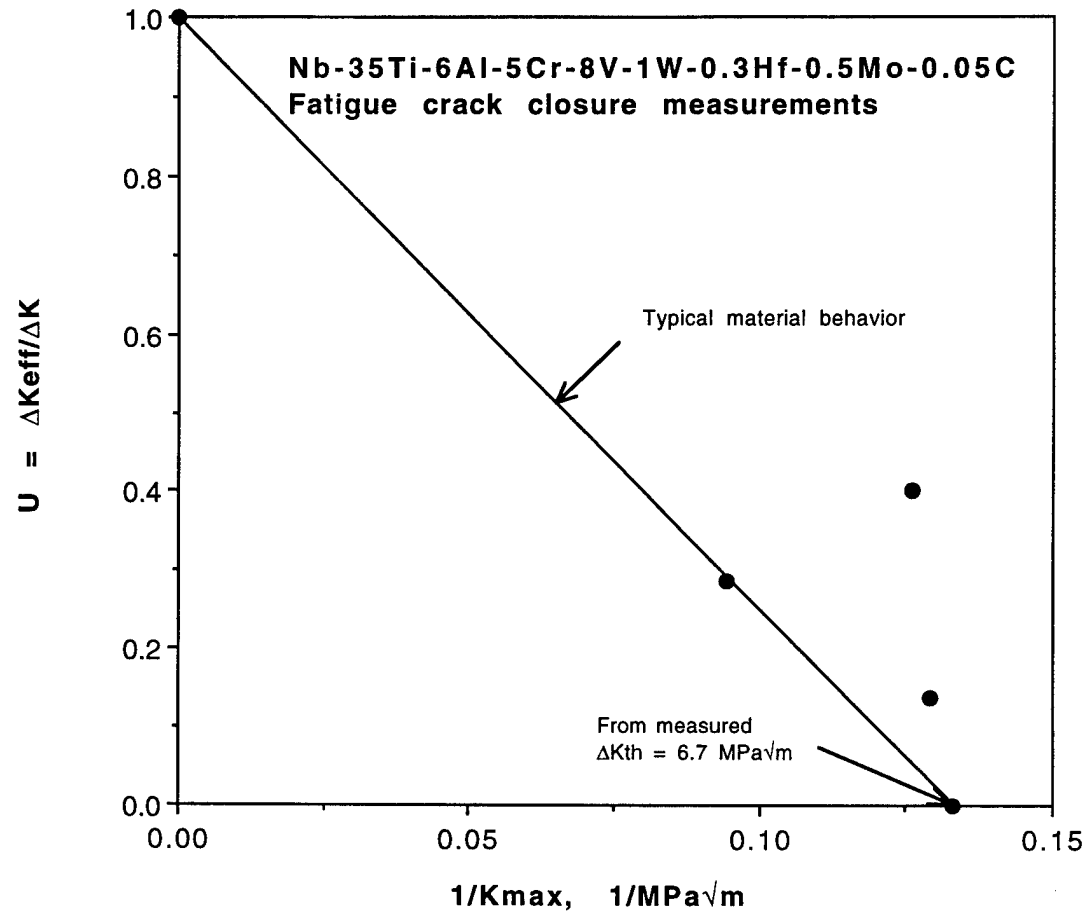


Fig. 3 Fatigue crack closure measurements shown relative to those measured for many other alloys. The erratic nature of crack growth is thought to be the reason for the large deviation of the measurements from typical behavior.

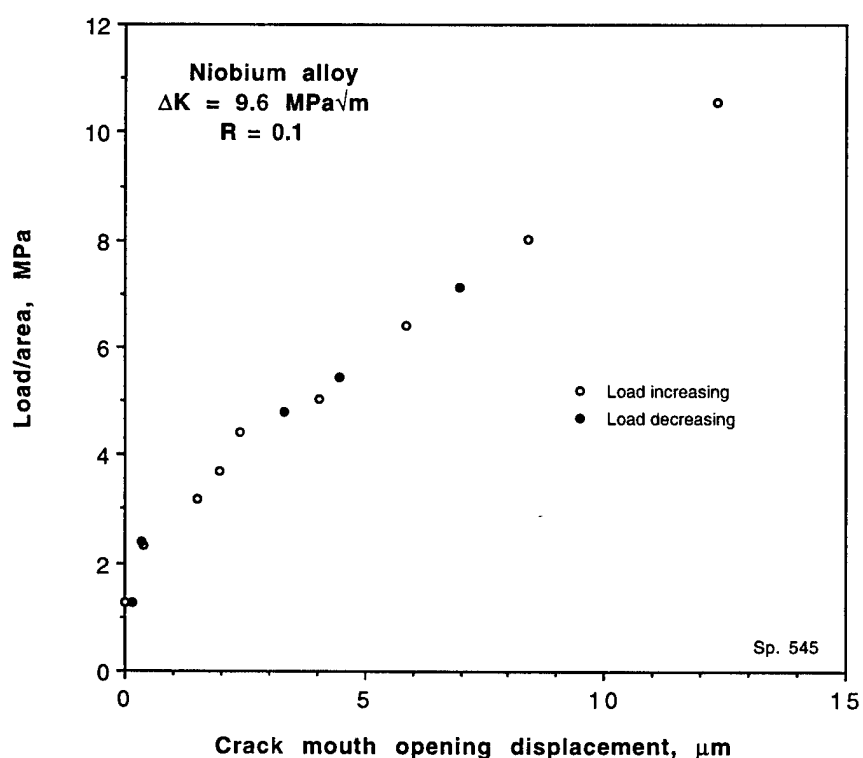
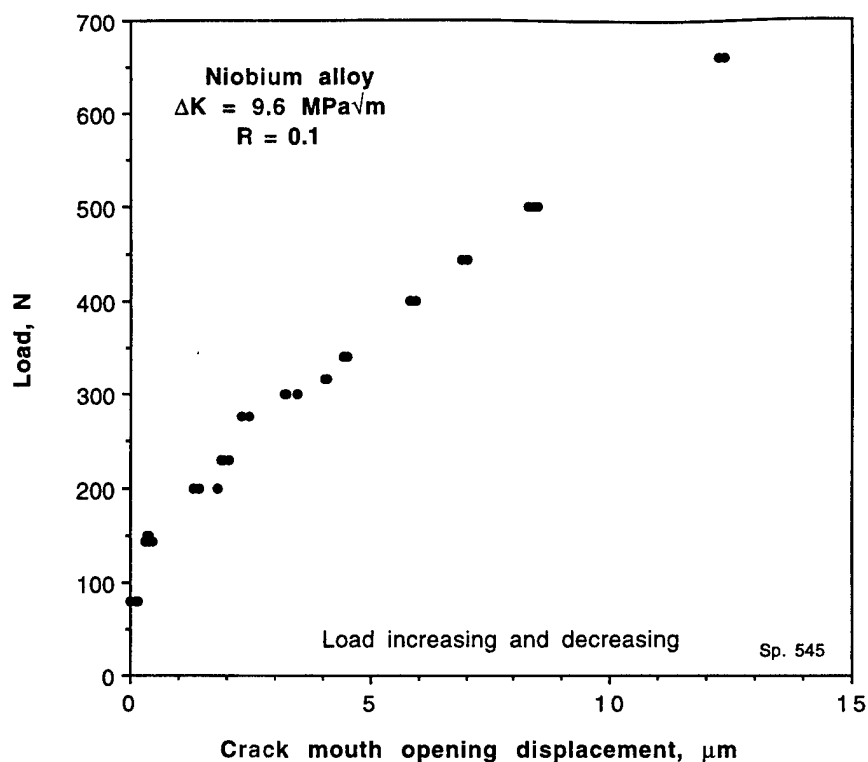


Fig. 4 Crack mouth opening displacements (CMOD) measured during loading to determine the value of opening load by departure from linearity. Top figure shows applied load vs. CMOD, while the same data are shown as stress vs. CMOD in the lower figure. Crack opening load measure by CMOD is far below the values derived by direct observation.

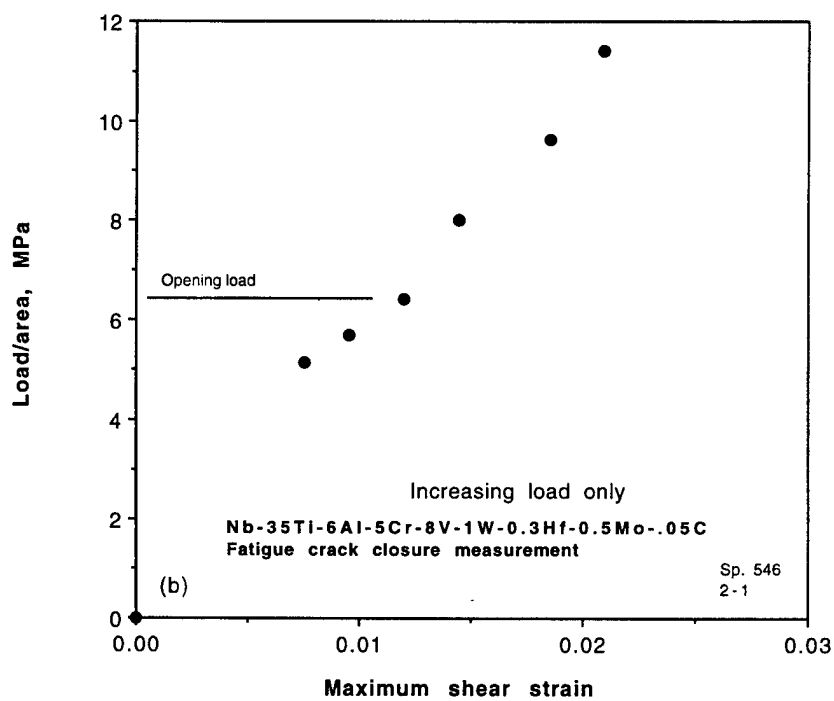
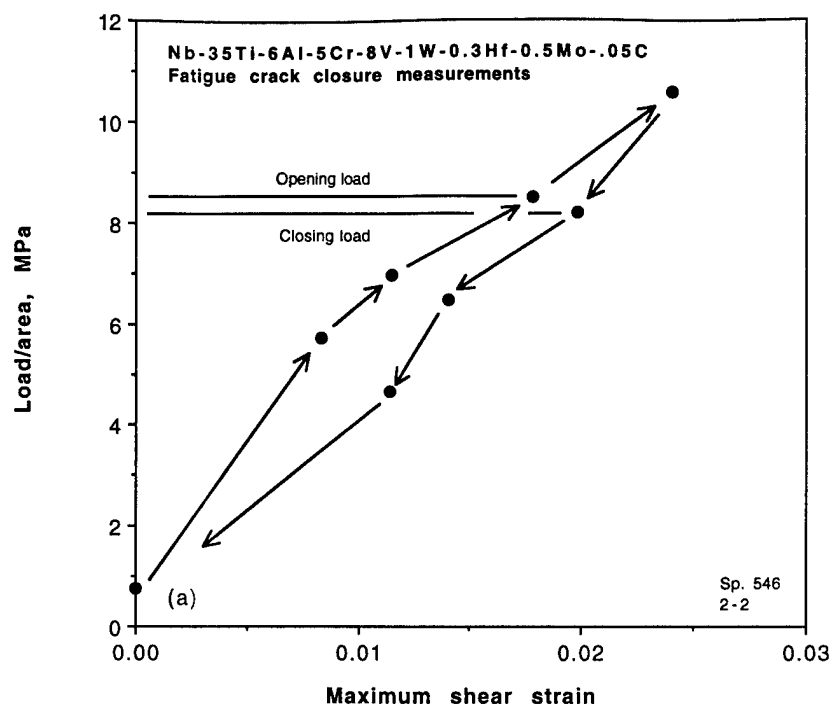


Fig. 5 Two different determinations of strains at the crack tip as a function of load at approximately the same  $\Delta K$ . Both figures show opening load as  $\approx 7$  to 9 MPa, while in Fig. 4, the value is about 2 MPa at apparent crack opening.

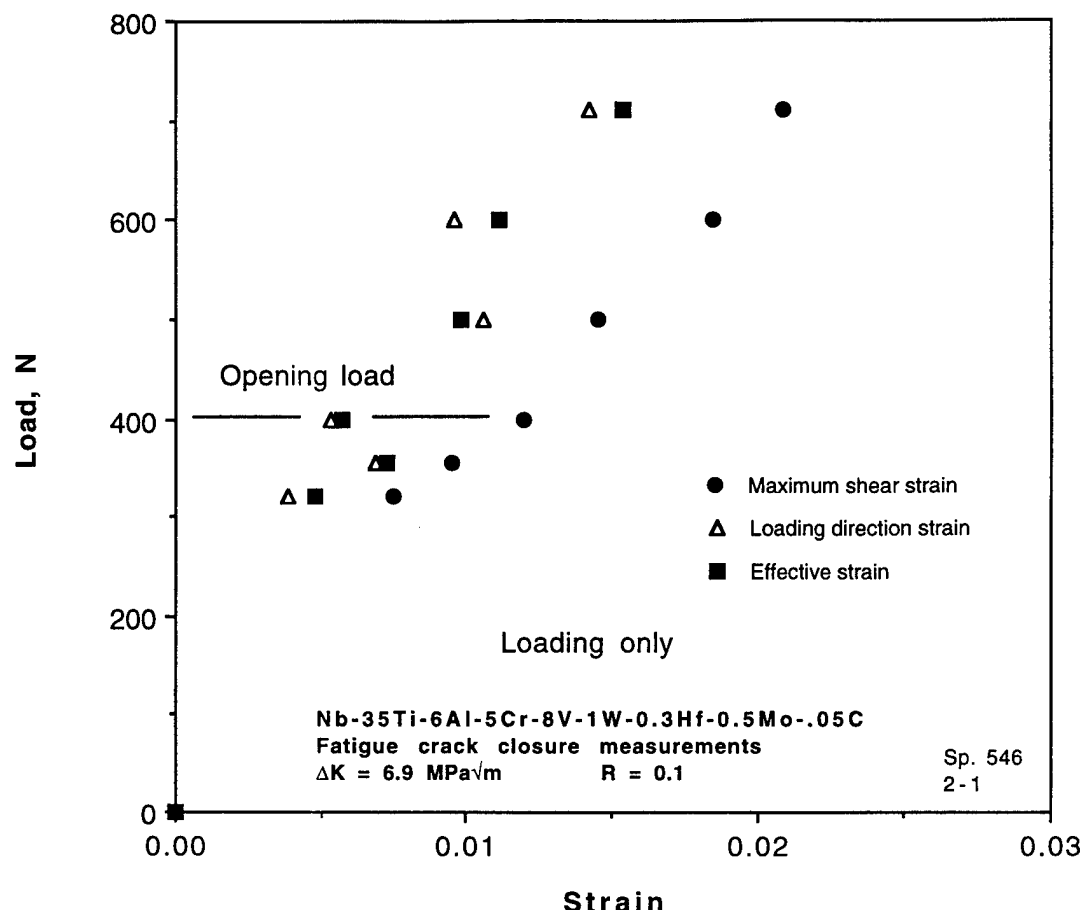


Fig. 6 Comparison of the crack tip response to load using 3 definitions of strain. Maximum shear strain should capture material response the best.

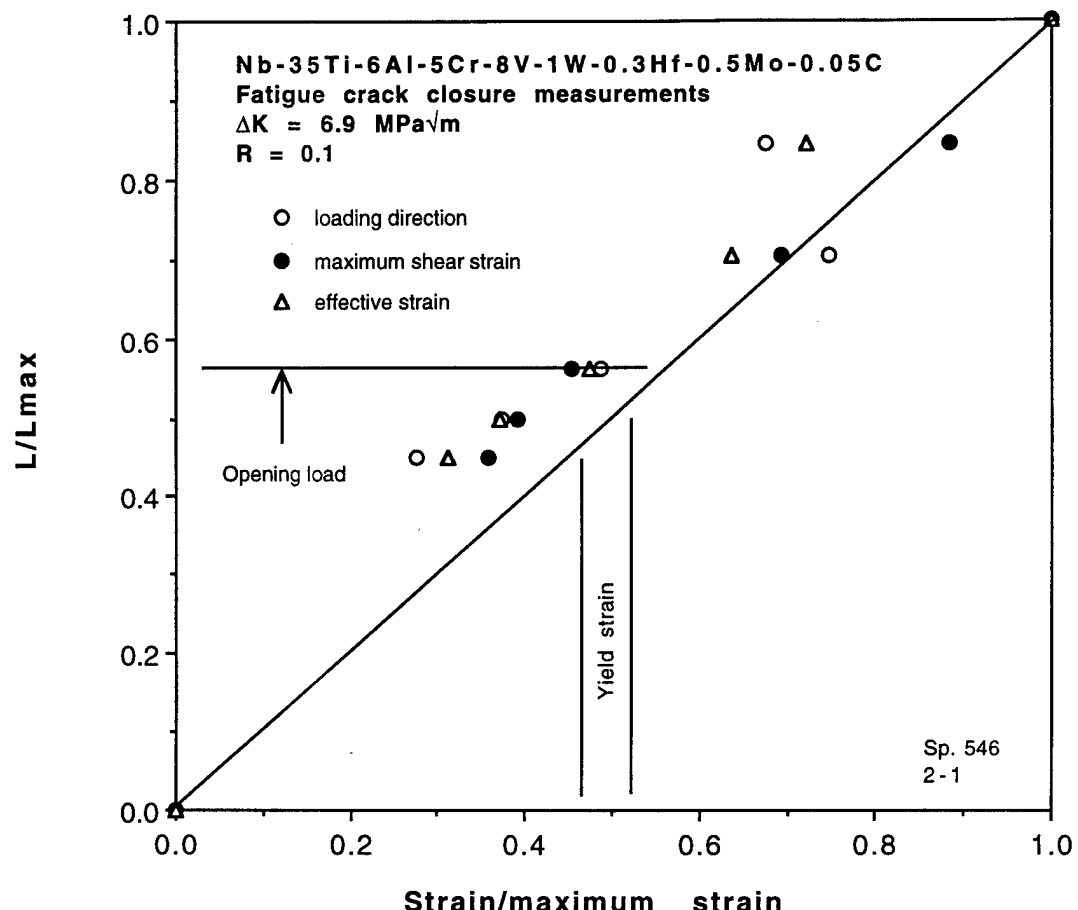
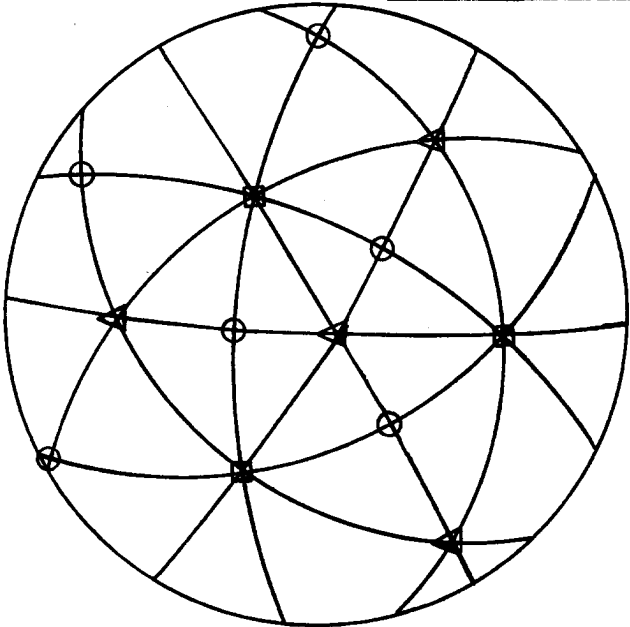
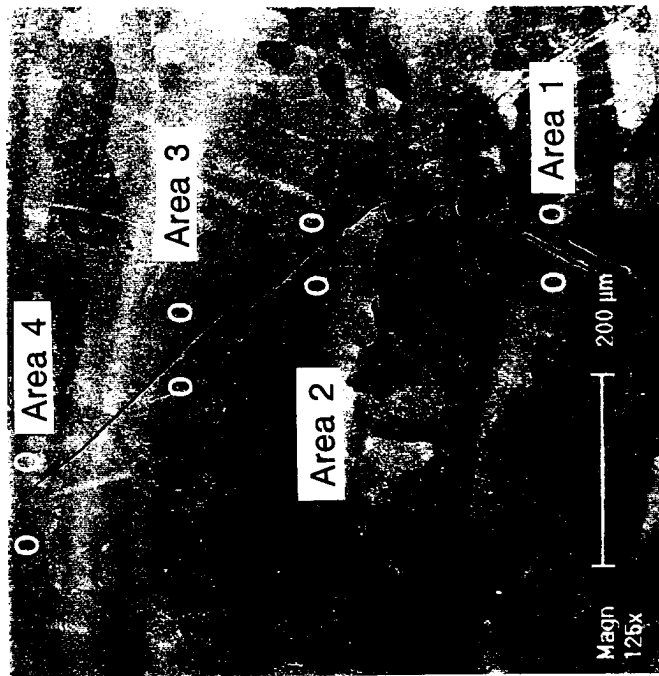
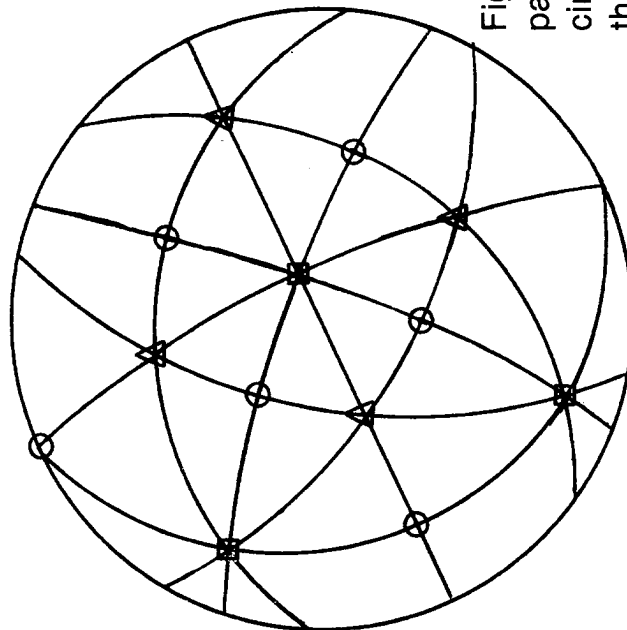


Fig. 7 Normalized load vs. normalized strain for the same data as shown in Fig. 6. Crack tip strain is nearly a linear function of load when considered on this basis. Strain at the crack tip approximates yield magnitude at opening load, which indicates that the compressive residual stress at the crack tip is approximately the yield stress.

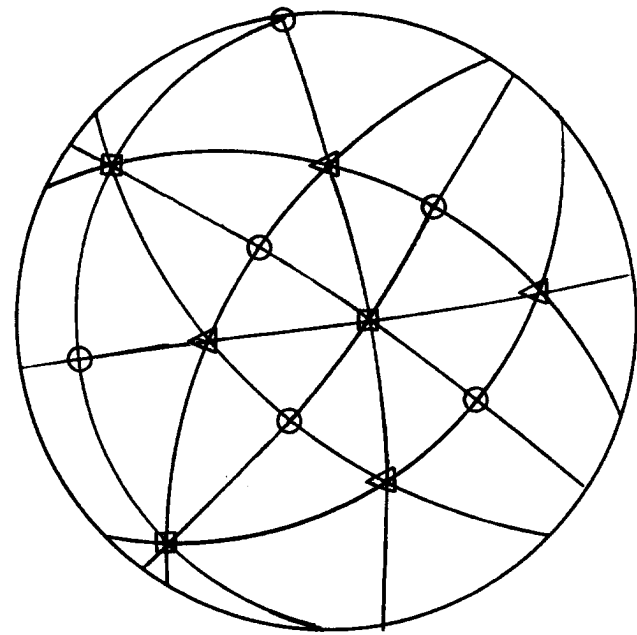
Area	Normal direction	Crack path plane
1	near $<112>$	near $\{112\}$
2	near $<115>$	near $\{112\}$
3	near $<112>$	near $\{112\}$
4	near $<112>$	near $\{112\}$



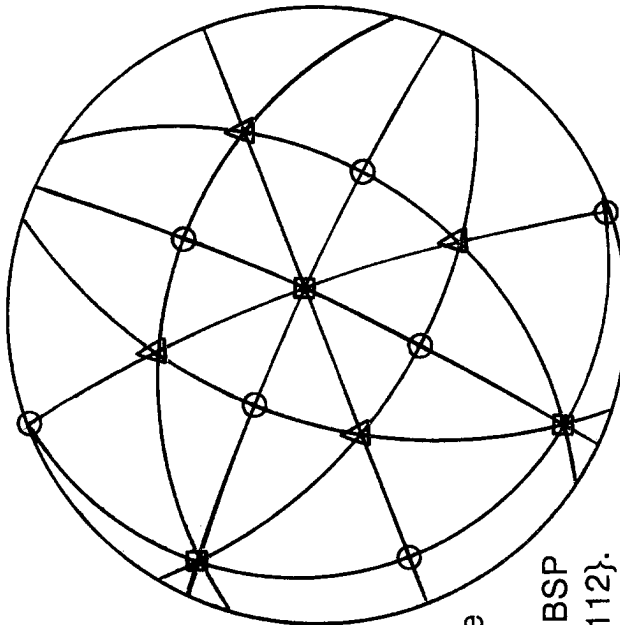
Area 1



Area 2



Area 4



Area 3

Fig. 8 A detailed view of the fast fracture path showing the effect of grain size. The circles show locations of orientations by EBSP that indicate the crack plane is probably  $\{112\}$ .

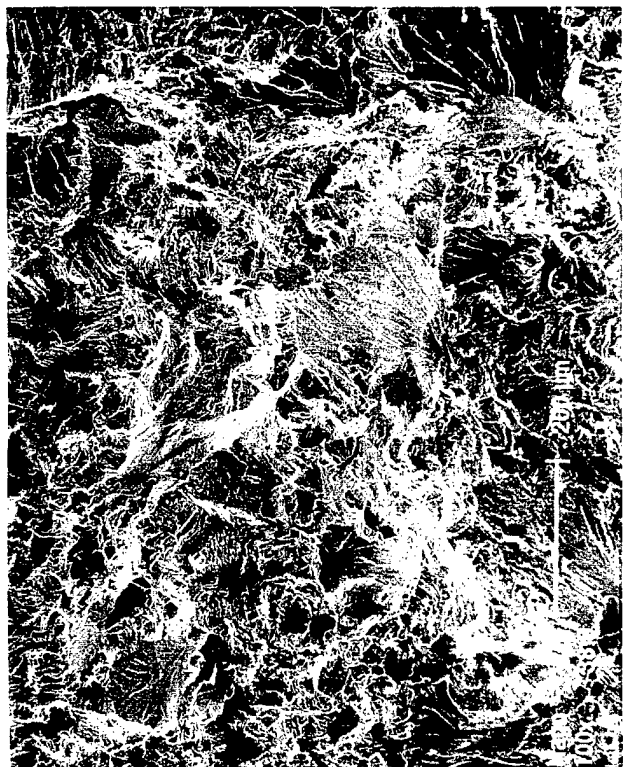


Fig. 9 Fractography of fatigue crack growth. General growth direction was from bottom to top. (a) A low magnification view showing transgranular cracking with some formation of flat facets. (b) At higher magnification, striations are visible in some areas. (c) Flat facets show river lines, and in this example, fine particles distributed systematically on the surface. (d) Very coarse structure on another relatively flat region that are similar to striations.

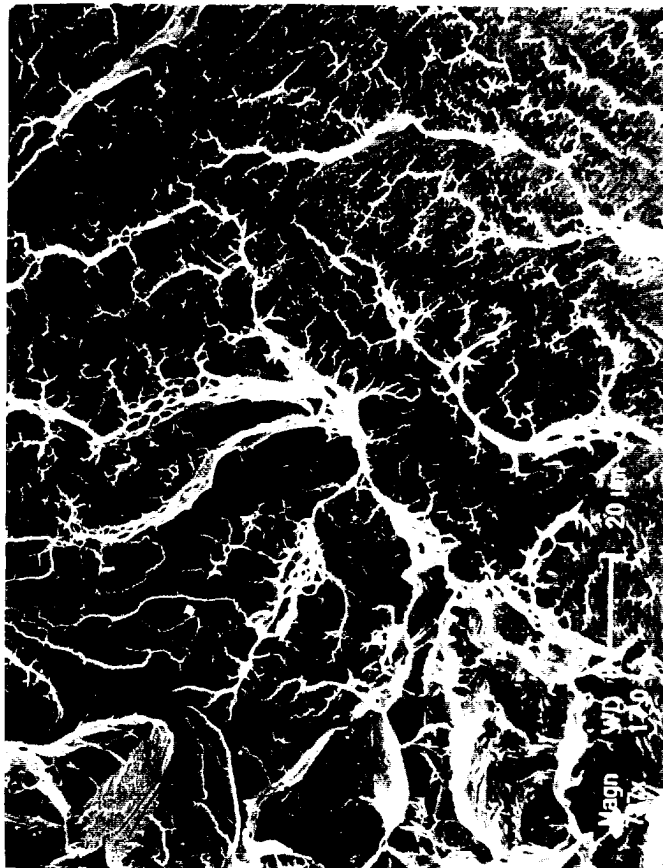


Fig. 10 Fractography of fast fracture. General growth direction was from bottom to top. No dimpled rupture was found. (a) A low magnification view shows much greater formation of flat facets than seen in fatigue. Some intergranular fracture in regions of small grains may be indicated. (b) Higher magnification views of flat facets shown features indicating considerable plasticity during fracture. (c) Another region of crystallographic cracking involving considerable plasticity.

## **The Fracture of Lamellar Composites**

**D. L. Davidson, K. S. Chan and T. P. Weihs**

## THE FRACTURE OF LAMELLAR COMPOSITES

D.L. Davidson and K.S. Chan  
Southwest Research Institute  
San Antonio, TX 78228

T.P. Weihs  
Johns Hopkins University  
Baltimore, MD

### ABSTRACT

The fracture characteristics of two Nb-based lamellar composites were evaluated. The composites were composed of an intermetallic layer ( $\text{Cr}_2\text{Nb}$  or  $\text{Nb}_5\text{Si}_3$ ) and a metallic layer (50Nb-13Cr-37Ti or pure Nb), and the composite bilayer dimensions were in the 1 to 3  $\mu\text{m}$  range. Problems were encountered in fabricating one composite that lead to void formation on heat treatment and very low fracture values, while the other composite was successfully fabricated and demonstrated reasonable fracture toughness values. Analyses of crack tip and crack bridging strains were made, and they indicated that plastic deformation occurred in this material, as did the fractography.

### INTRODUCTION

Because of the excellent fracture resistance of lamellar microstructures, principally formed from various titanium alloys, lamellar structures are being formed artificially. Lamellar structures have also been shown to deliver enhanced yield strengths. This enhancement has been attributed to retardation of dislocation motion caused by the small dimensions of the layers. This paper describes an effort to evaluate the fracture toughness characteristics of Nb-based layered composites, where one layer was a brittle intermetallic and the other layer a more ductile metal.

### MATERIALS

The lamellar composites evaluated were manufactured by two different techniques. The first material evaluate was fabricated at BIRL (Basic Industrial Research Laboratory), now a part of Northwestern University. The second composites evaluated were made at Johns Hopkins University.

The composites fabricated at BIRL were made using a Materials Research Corporation 902M in-line sputter deposition system. Two targets were used: one for  $\text{Cr}_2\text{Nb}$  and the other for the composition 50Nb-13Cr-37Ti. The picture frame shaped targets were divided into 64 sections or "tiles." The number of Ti,

Cr and Nb tiles were adjusted according to the composition desired and the sputter yield of the element. Sputter yields of Nb and Ti are approximately the same and about half that of Cr. Argon pressure and substrate bias voltage were varied during the deposition of each material to control stress in the layer. Deposition of material layers of 1  $\mu\text{m}$  each to form composites with a total thickness of at least 150  $\mu\text{m}$  each was the goal of the fabrication process.

Deposition of composites to the desired thickness proved to be difficult to achieve. Composites were deposited on Ti-6Al-4V substrates that had been very carefully polished to a surface roughness of approximately 0.2  $\mu\text{m}$ , as measured using a needle stylus instrument. This Ti alloy was chosen because its coefficient of thermal expansion approximately equaled that estimated for the composite. After significant effort, BIRL was able to deposit approximately 150 layers of alternating Cr<sub>2</sub>Nb and 50Nb-13Cr-37Ti approximately 1  $\mu\text{m}$  thickness each.

Microlaminate composites that came from Johns Hopkins were combinations of Nb and Nb<sub>5</sub>Si<sub>3</sub> layers that were fabricated using magnetron sputtering and high temperature anneals. The Nb layers were deposited using an elemental target (99.95% purity) and a DC power supply, and the amorphous Nb-37.5 at%Si layers were deposited using a polycrystalline Nb<sub>5</sub>Si<sub>3</sub> (99.95% purity) target and a RF power supply. The chamber base pressure prior to deposition was 1 x 10<sup>-7</sup> Torr and the pressure of the high purity Ar during deposition was 5.0 mTorr. The microlaminates were deposited onto polished <100> Si wafers that had been previously coated with an approximately 0.3  $\mu\text{m}$  thick layer of Ti followed by approximately 3.0  $\mu\text{m}$  of Cu. The wafers were neither heated nor cooled during the deposition. The total thickness of the microlaminate was approximately 50  $\mu\text{m}$  and the bilayer thickness was nearly 1  $\mu\text{m}$  with the Nb layers being 0.71  $\mu\text{m}$  thick and the silicide layer being 0.29  $\mu\text{m}$  thick.

After fabrication, the composite was removed from the substrate by submersion in a hydrochloric acid solution that did not attack either the composite or the substrate, or it could be peeled from the substrate mechanically without damage to the composite. Fracture experiments were performed on some pieces of composite as-fabricated and other pieces were heat treated to crystallize the amorphous as-deposited intermetallic after cutting into specimen configurations.

## EXPERIMENTAL METHODS

Special techniques were required for evaluating these composites, which were much thinner than the materials usually evaluated. Handling of the BIRL material indicated that the toughness was likely to be very low. While cutting into samples, it was discovered that the material debonded from the substrate in some places, but adhered strongly in other locations. A sample shaped as shown in **Fig. 1(a)** was the most successful of several attempts to find a specimen shape that would allow evaluation the BIRL material. This specimen had a double notched tapered tensile configuration in which the material between the notches had debonded, and from one of the notches, a crack had formed during machining, as seen in **Fig. 1(b)**. When this sample was loaded axially within the scanning electron microscope, the load applied to the substrate was transferred to the composite and the crack was extended in a controlled manner. This was a displacement controlled experiment, so the loads that caused crack extension were unknown. However, because of the high resolution of the SEM, photographs of the crack tip region were made at minimum load and the load required to propagate the crack. Thus, it was possible to measure the crack opening displacement (COD) using stereoimaging, and, from the analysis for an elastically loaded crack, the stress intensity factor was calculated. The crack was very sharp and there was no evidence of plasticity within several micrometers of the crack tip.

The free standing composite foils of the Johns Hopkins composite were cut into compact tension type specimens 25 mm on the side. For specimens this thin, antibuckling reinforcements were needed. A low modulus plastic was cut so that a strip extended along the periphery of the specimen, leaving the center open, as shown in **Fig. 2**. When this specimen was loaded within the SEM, the crack initiated and grew from the notch at extremely low loads, less than 10 N, which was below the resolution of the load cell. However, by careful loading and unloading, it was possible to extend a crack in a controlled manner in the heat treated material, and photograph it in the loaded and unloaded condition. As with the BIRL material, displacements were measured near the crack tip and along the crack flank, from which COD and strains at the crack tip were derived.

## RESULTS

**BIRL composites:** The stress intensity factor required to grow the crack shown in **Fig. 1** was derived from measuring the slope of the COD vs. distance behind the crack tip for a load near that which propagated the crack, and then using the

relation, derived from elasticity to compute  $K$ . Only one determination of  $K$  was made before the specimen broke, giving  $K = 0.32 \text{ MPa}\sqrt{\text{m}}$ . There was no evidence of any plasticity at the crack tip.

The fracture surface of the BIRL composite was examined, with the results shown in **Fig. 3**. Two regions were found at low magnification, Fig. 3(a), but no satisfactory explanation was found for the two different regions. A higher magnification photograph of the rougher region to the right in (a) is shown in Fig. 3(b), where the amorphous intermetallic layer is seen as smooth and the metallic layer exhibits a columnar grain structure. Reasons for the poor fracture characteristics of the composite were thought to be (1) the amorphous intermetallic, and (2) the columnar grain structure of the metal.

Heat treatments were conducted on the composite to recrystallize the metallic layers and to try to crystallize the amorphous intermetallic. The limit of our capability for heating in vacuum was  $1000^\circ\text{C}$ , so a 6 hr. heat treatment was used as a starting point. A cross section of material given this heat treatment is shown in **Fig. 4**. Images formed by secondary (SE) and backscattered electrons (BSE) are shown. From the SE image, it may be seen that strings of voids formed in one of the layers and that the other layer may have partially recrystallized. The BSE image indicates the same thing, but also shows that it was the metallic layer that voided. From these photographs, the bilayer thickness was measured as  $3.4 \mu\text{m}$ , with the voided region being about  $2 \mu\text{m}$  wide, meaning that the voided regions were about 60% of the total composite.

The formation of these voids is explained as follows: In the deposition process, the columnar grains grew from separate nuclei on the previous layer. Columnar grain growth did not occupy all of the space, especially near the nucleating layer, so that voids were left between the grains as they grew. Heating caused these vacant regions to spherodize due to diffusion. Thus, the problem was in the deposition conditions that resulted in intergranular voiding in the metallic layers.

No attempt was made to conduct fracture experiments on heat treated material. Soon after these results were obtained, BIRL ceased to function as a viable material supplier, and further efforts to develop these composites were abandoned.

Johns Hopkins composites: Experiments were conducted on three CT specimens of the Johns Hopkins composite: one in the as-received condition with

amorphous intermetallic, and two after heat treatment to crystallize the intermetallic. The first sample resulted in a crack length and load combination that gave a fracture toughness of about  $5 \pm 2$  MPa/m. The uncertainty in magnitude was caused by the very low loads required - approximately 10 N.

Crack growth results from the composite after heat treatment, with crystalline intermetallic, are shown in **Table 1**. This material was sufficiently tough that extension of the crack could be controlled, and it was possible to make several analyses of deformation of the crack growth processes. The crack tip region of one specimen is shown in **Fig. 5(a)** with an overlay of measured displacements, crack opening displacement is shown in (b), and a contour map of strains is shown in (c). As can be seen, substantial strain was developed at the crack tip, and the distribution of strain is about that expected for a crack of this type.

**Table 1**  
Johns Hopkins Composite

Load Sequence	Crack growth increment (mm)	Total crack length (mm)	Approximate load (N)
<b>CT-1</b>			
notch length		5.51	
1	0.23	5.54	10
2	4.25	9.99	9
3	4.49	14.48	-
4	1.34	15.82	-
<b>CT-2</b>			
notch length		6.17	
1	0.13	6.30	10
2	0.50	6.80	-
3	0.37	7.17	-
4	0.14	7.31	-
5	0.10	7.41	-

A region of material bridging the crack was found along the crack wake, and the strain was determined in this bridge. A photograph of the bridged region is shown in **Fig. 6(a)** with displacement overlays, in (b) is shown the COD, and in (c) a contour map of the strains. Similar to the crack tip analysis, substantial strains were developed in this bridged region, again indicative of significant deformation in this composite. The significance of the non-linear COD behind

one of the crack tips is that the bridge region alters the overall COD of the crack near the bridging location; the bridge "pinches" the crack together at that point. Thus, the bridge prevents the crack from fully opening, thereby enhancing the K level that the material can support.

The COD measurement shown in Fig. 5 was used to compute the K level experienced by the crack using the elastic relationship for COD as a function of K. Modulus of the composite was computed from the rule of mixtures as  $E_{comp} = 216$  GPa. The slope of the Mode I COD in Fig. 5 =  $0.146 \mu\text{m}$ , which gives  $K = 10.9 \text{ MPa}\sqrt{\text{m}}$ . Thus, the fracture toughness of the composite is estimated as at least this value. The crack bridging shown in Fig. 6 may have contributed some to the fracture toughness, but it was not accounted for in this calculation.

Fractography of the heat treated composite is shown in Fig. 7, where it may be seen that there is considerable evidence of deformation. The low magnification view of Fig. 7(a) shows uniform behavior across the entire material thickness. The higher magnification views of (b) and (c) show that considerable deformation has occurred in one of the layers, which is most likely the Nb layer. No columnar grain structure is evident. Stereoviews at higher magnification indicate that the surface is stair-stepped rather than the Nb layers exhibiting chisel-like reduction in thickness.

## DISCUSSION

This study contrasts the poor fracture behavior of a composite made with the inclusion of microvoided space in the columnar grain structure with the good fracture behavior of a composite deposited in the fully dense state. The fully dense composite (Johns Hopkins) with amorphous intermetallic resulted in a fracture toughness of approximately  $5 \text{ MPa}\sqrt{\text{m}}$  (estimated). When the intermetallic was converted from an amorphous to crystalline state without the formation of microvoids, a fracture toughness of  $\approx 11 \text{ MPa}\sqrt{\text{m}}$  resulted, which was the consequence of plasticity surrounding the crack tip and in a bridge behind the tip. Fractography also revealed evidence of plasticity on the fracture surface.

## CONCLUSIONS

A lamellar Nb-based composite with  $\text{Nb}_5\text{Si}_3$  at a level of 50 vol. % demonstrated a fracture toughness estimated to be approximately  $11 \text{ MPa}\sqrt{\text{m}}$ , which is as good, or better than other, similar materials containing this intermetallic [1].

## REFERENCES

1. R.M. Nekkanti and D.M. Dimiduk, Mat. Res. Soc. Proceedings, vol. 194, 1990, Mat. Res. Soc., Pittsburgh, PA, pp. 175-83.

## ACKNOWLEDGEMENT

Specimens were carefully preparation by Jim Spencer and Byron Chapa loaded them with great care. The research was funded by the Air Force Office of Scientific Research, Contract F49620-95-C-0043 at SwRI and Contract F49620-9X-C-00XX at Johns Hopkins University.

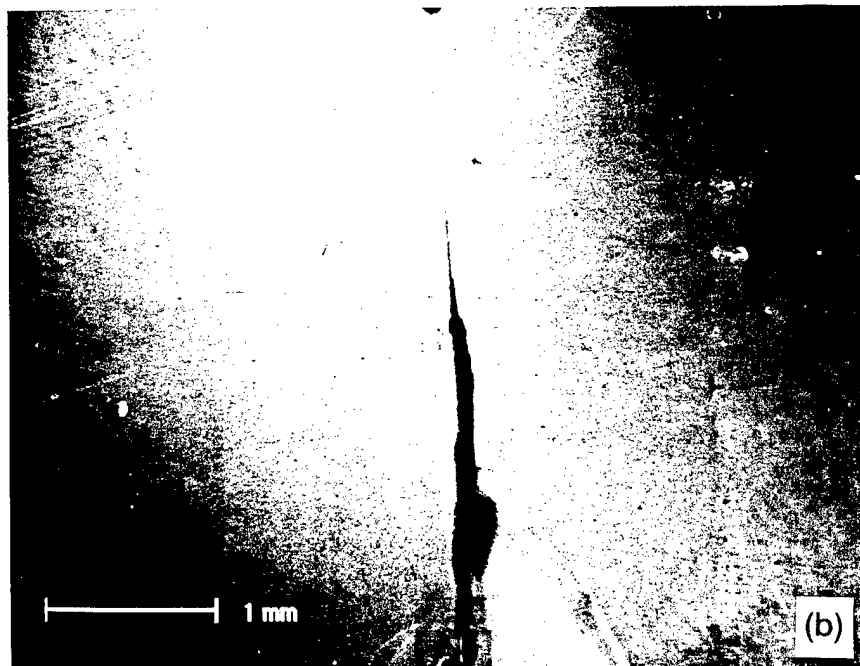
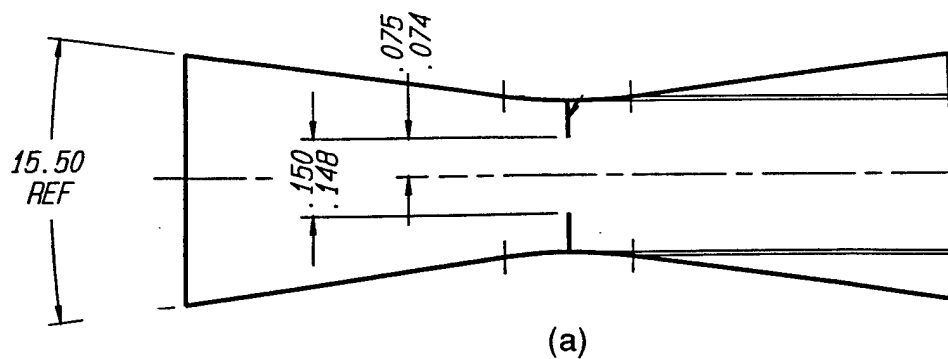


Fig. 1 (a) Specimen of the type used to evaluate BIRL lamellar composite.  
(b) Region between notches. The composite was debonded from the substrate in the region near the crack.

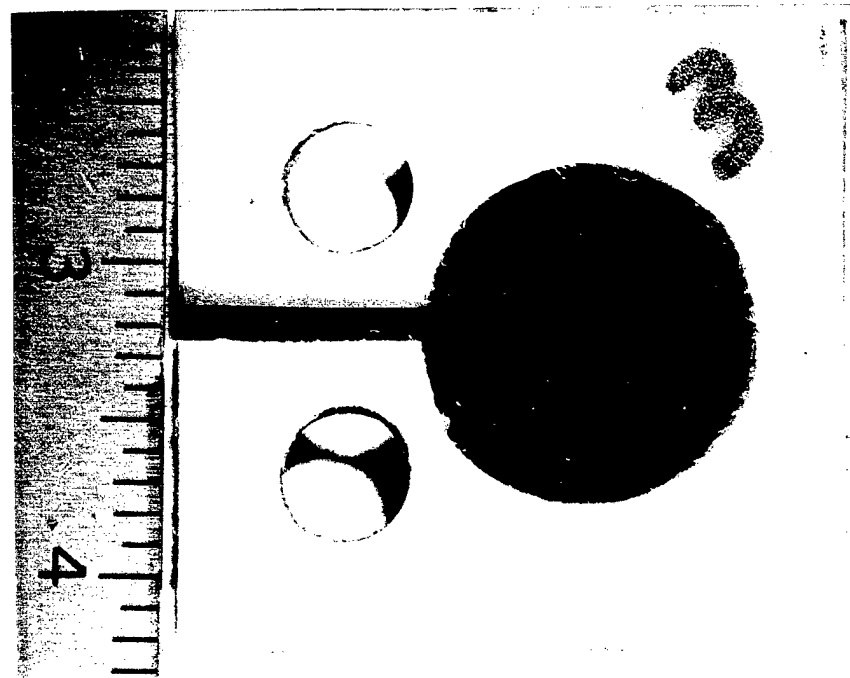


Fig. 2 Compact tension specimen used to evaluate the Johns Hopkins lamellar composite. The  $50 \mu\text{m}$  thick composite was reinforced along the edges to prevent buckling.

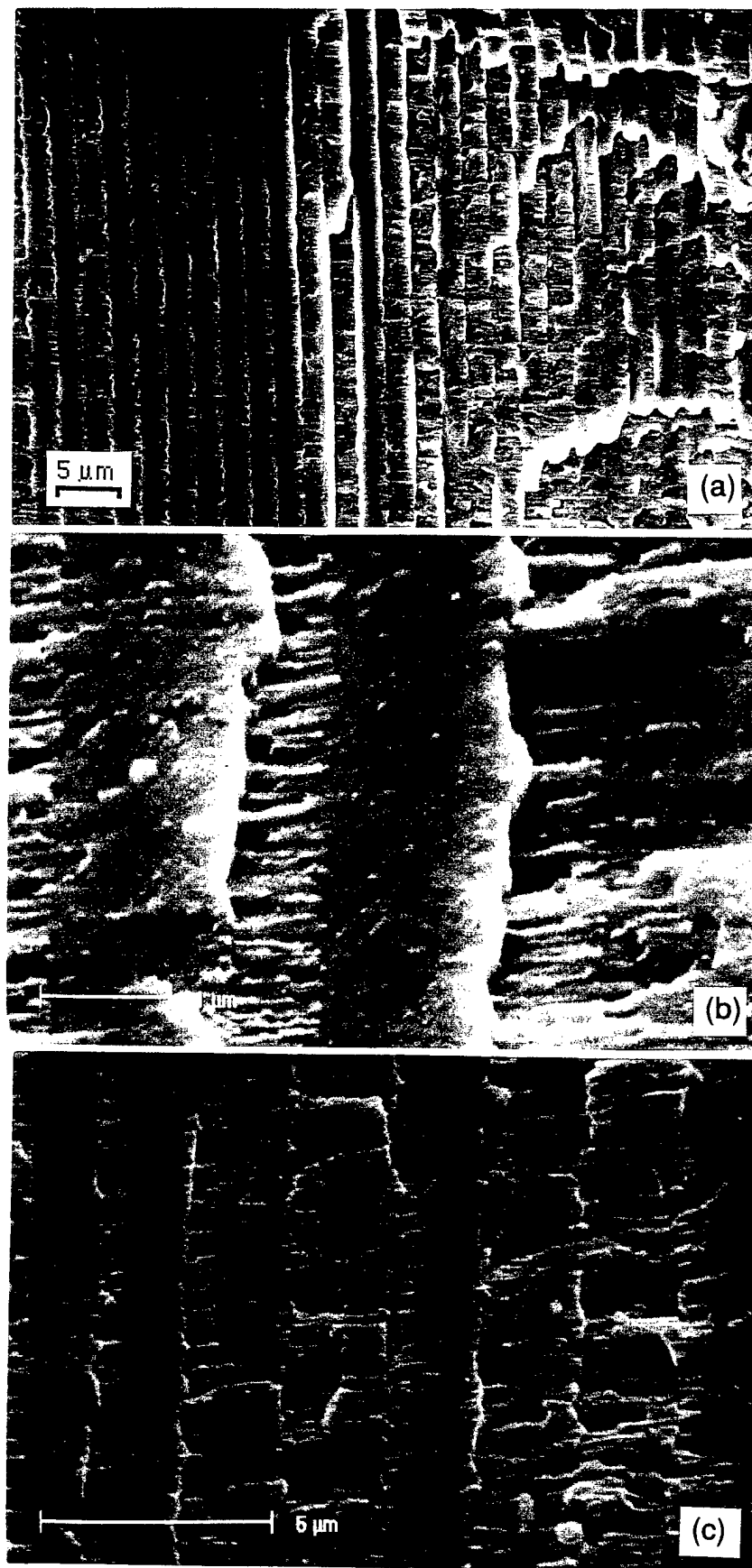


Fig. 3 Fracture surface of the BIRL composite. (a) Fracture to the left side is somewhat different than on the right. (b) Columnar grain structure of the Nb rich phase is evident. (c) The featureless regions of Cr<sub>2</sub>Nb are seen between the matrix regions where fracture has been through columnar grains.

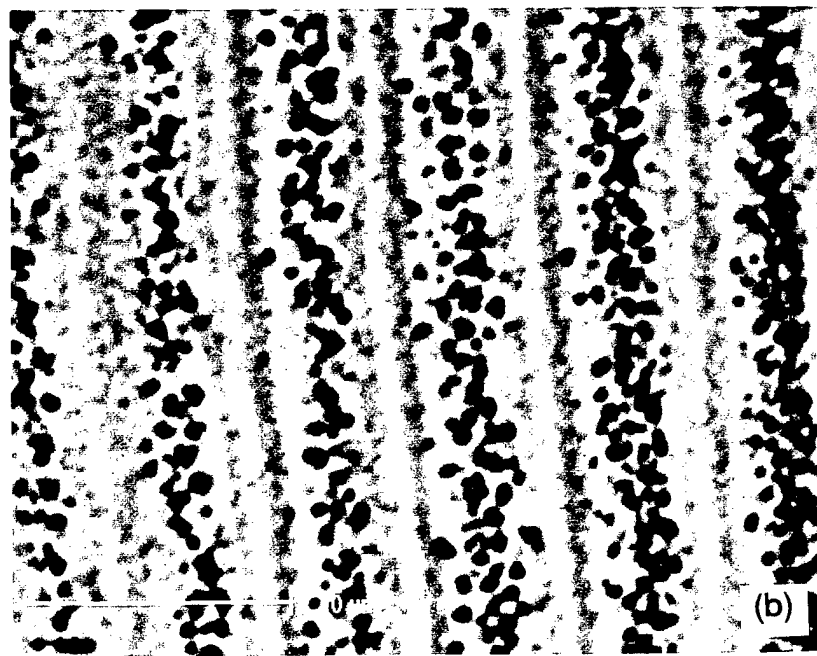
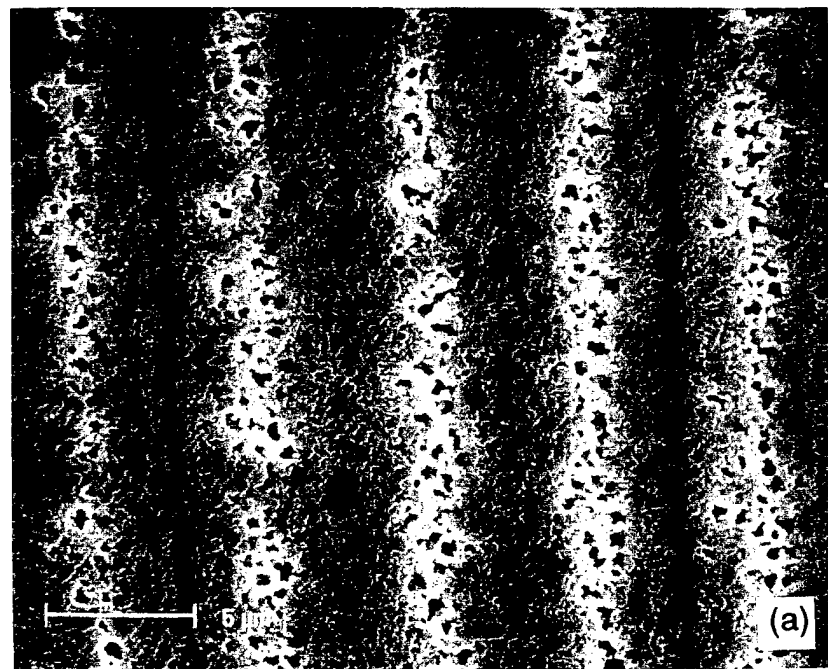


Fig. 4 Cross-section of BIRL composite held for 6 hrs. at 1000°C in vacuum.  
(a) Secondary electron image of a polished section. (b) Backscattered electron image of the section as seen in (a). Heat treatment caused the formation of pores as the columnar grain structure of the matrix alloy recrystallized. In (b), the compositional variation of the intermetallic was also imaged.

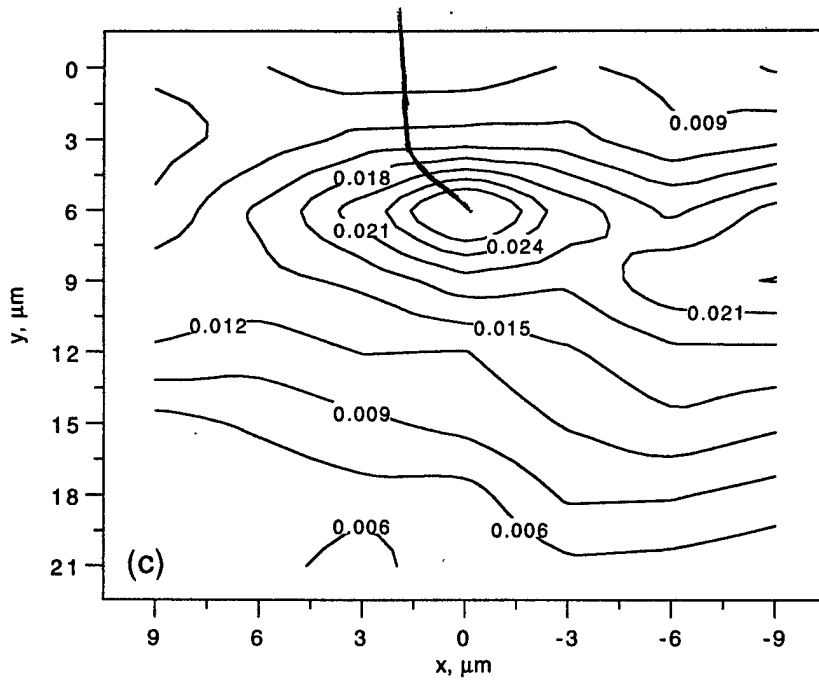
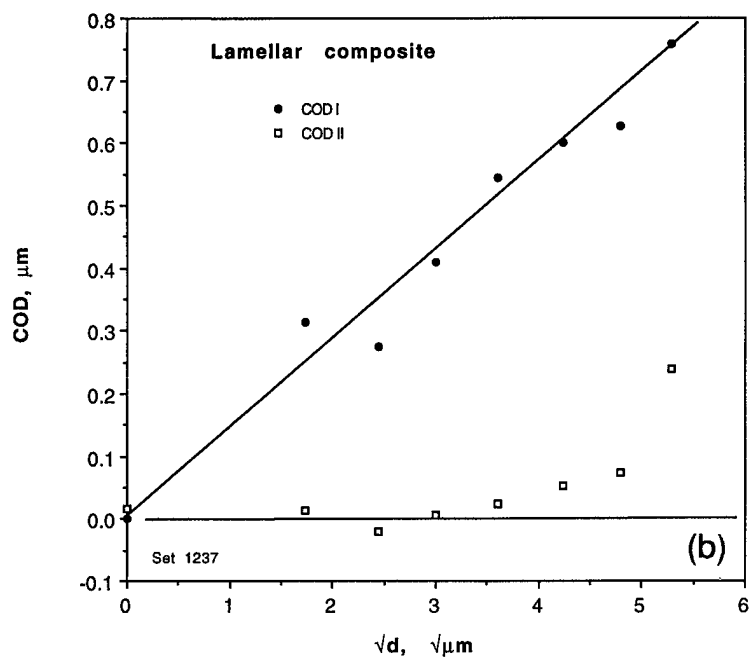
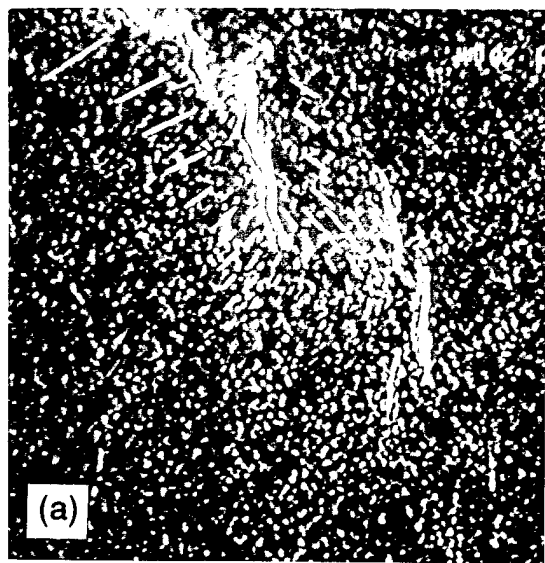


Fig. 5 (a) Crack tip region of a Johns Hopkins composite with overlay of measured displacements. Measurement increment was 3  $\mu\text{m}$ , and displacements are shown magnified 15X actual size. (b) Crack opening displacement as a function of distance behind the crack tip. (c) Contour map of maximum shear strain near the crack tip.

Set 1237

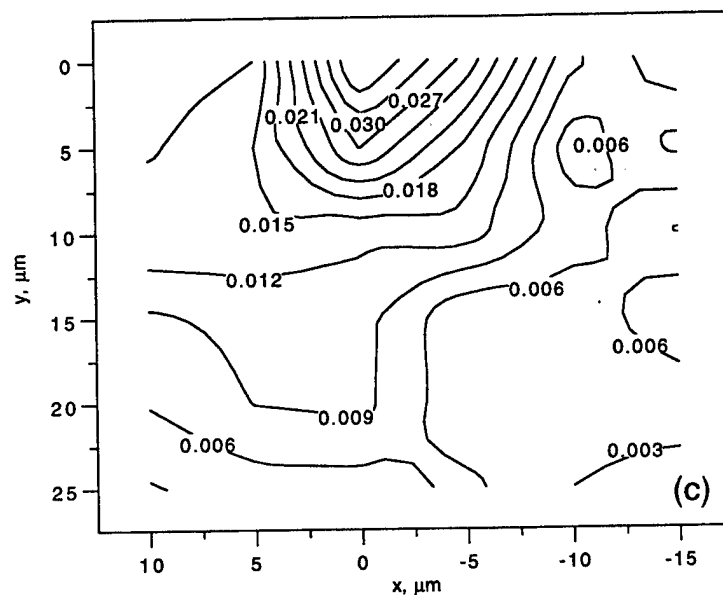
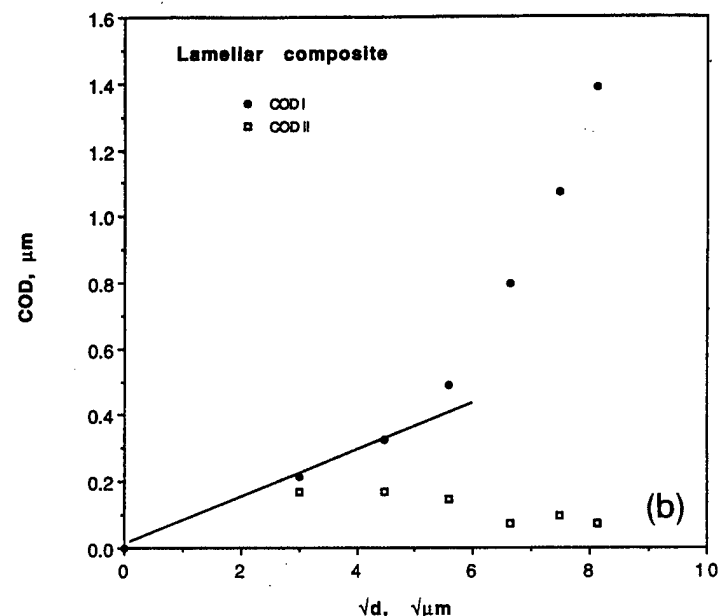
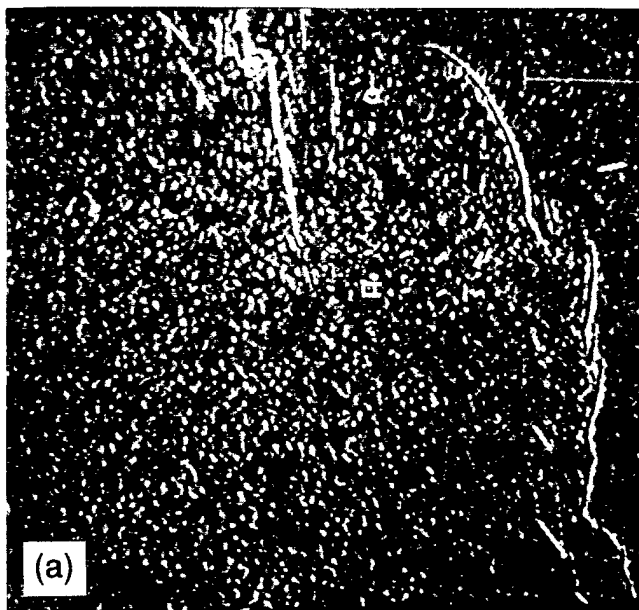


Fig. 6 (a) Material that has bridged the crack in the Johns Hopkins composite with an overlay of measured displacements. Measurement increment was 5  $\mu\text{m}$ , and displacements are shown magnified 15X actual size. (b) Crack opening displacement as a function of distance behind the crack tip for the upper crack. (c) Contour map of maximum shear strain within the bridged region. Set 1238

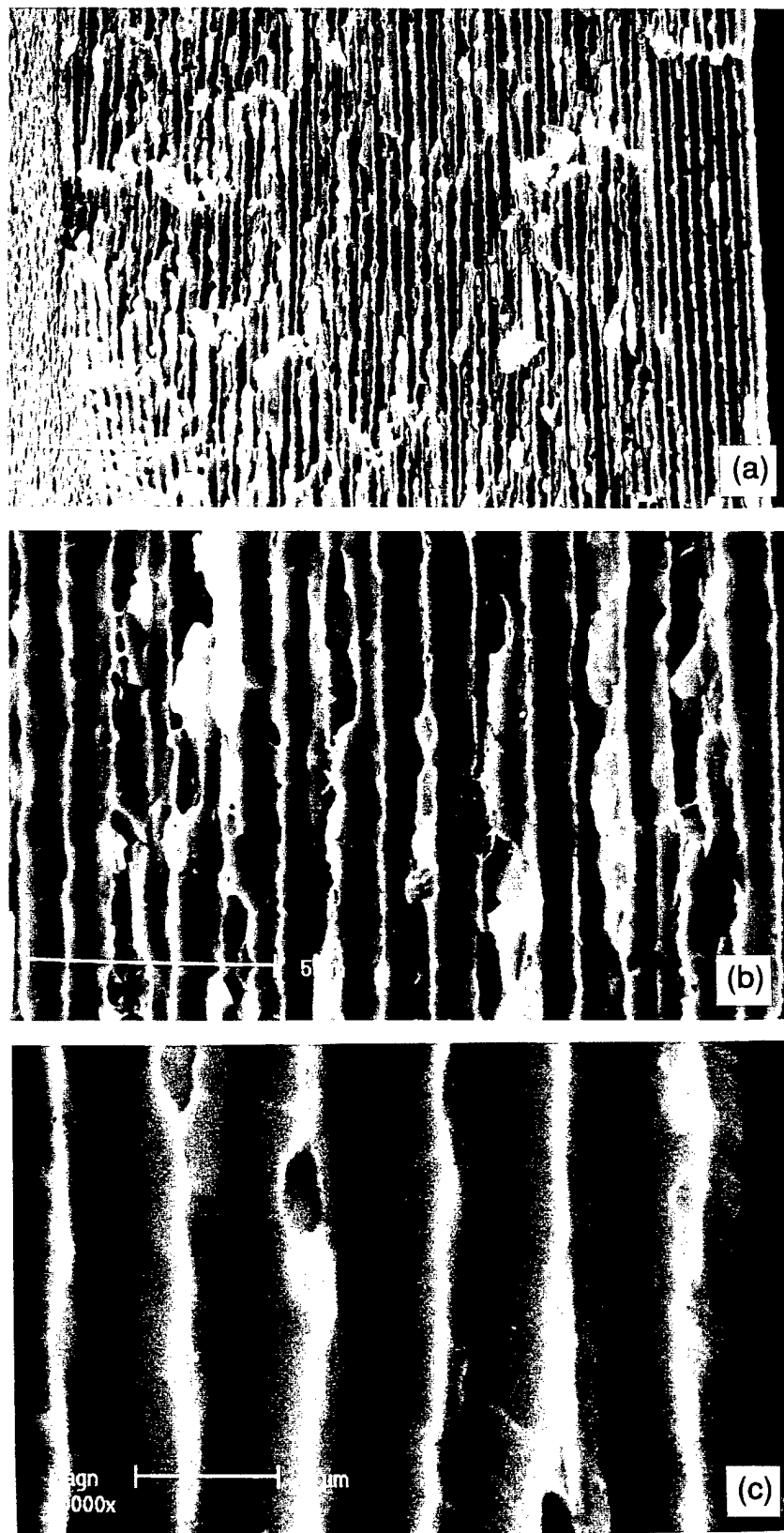


Fig. 7 Fracture surface of the heat treated Johns Hopkins composite.  
(a) Fracture is uniform across the specimen width, with evidence of considerable plasticity at many locations. (b) and (c) The fracture surface is stepped when viewed as a stereopair. Material on the left of the ridges is probably Nb because it evidences more deformation.

**Cluster Model for Calculation of Unstable Stacking Energy  
to Assist in the Alloying of Transition Metals**

**R. E. Beissner and D. L. Davidson**

## **CLUSTER MODEL FOR CALCULATION OF UNSTABLE STACKING ENERGY TO ASSIST IN THE ALLOYING OF TRANSITION METALS**

**R.E. Beissner and D.L. Davidson**  
Southwest Research Institute  
San Antonio, TX 78238

### **ABSTRACT**

The ductile or brittle nature of fracture in transition metal alloys has been related to the magnitude of the unstable stacking energy, which is an estimate of the energy barrier opposing the motion of dislocations, especially from crack tips. A model for computing this energy was developed to assist in transition metal alloy design by determining the effects of alloying on fracture properties. The lattice structure of the alloy or intermetallic compound is established as a cluster of atoms, and the electronic energy of the bonding electrons is computed through the density matrix approach, which induces a long range attractive term. The total energy computation is then completed by adding repulsive pairwise potentials that act near the atomic cores. The cluster is embedded in a much larger crystal that acts to impose boundary conditions on the cluster. The total energy of the crystal is computed again after shearing half the cluster by half the Burgers vector. The unstable stacking energy is the difference in energy between the sheared and original lattices. The energies thus computed are consistent with changes in fracture toughness values for Nb-Cr-Ti single phase alloys.

### **INTRODUCTION**

The design of alloys is mainly by empiricism. Phase diagrams greatly assist alloy design because composition can be used to predict the phases and compounds that are likely to be present in the alloy. The development of strength and damage tolerance are among the most important reasons for alloying, but the link between these properties and composition is not well understood. Damage tolerance is usually assessed through measurements of tensile ductility, or strain to fracture ( $\epsilon_F$ ), and fracture toughness ( $K_Q$ ).

Ductility measures the ability of a material to deform before it fractures. This parameter, although easy to measure, must be interpreted with care because it is often gage length dependent. An increase in fracture toughness usually relates to the work (W) expended during fracture. The work that is input to fracture = (load) x (crack opening displacement), and the material response is

work done under the stress strain curve within volumetric elements within the crack tip plastic zone. If the material tears, the toughness is equivalent to the work expended per unit area of newly formed crack. To increase  $K_Q$  usually requires that deformation within the plastic zone be increased, although there are also some other methods of increasing toughness. Since deformation within the crack tip plastic zone causes the crack tip opening to increase,  $W$ ,  $K_Q$ , and  $\epsilon_F$  are related.

To increase toughness, it is necessary to both emit dislocations from the crack tip and to move those dislocations away from the tip into the plastic zone. Fracture toughness can be restricted by either the ability to generate dislocations or move them away from the crack tip. Thus, a criteria is required for determining what conditions are required for generating dislocations at a crack tip. This issue has been the subject of considerable research. The continuum analysis by Rice and Thompson [1] developed a quantitative criterion for determining whether material behavior was likely to be brittle or ductile. More recently, there has been considerable analysis [2-7] of this problem by a number of investigators. Some of the more recent modeling suggests that it is not so much the emission of dislocations from crack tips that determines the toughness so much as it is the motion of dislocations within the crack tip plastic zone [8,9].

Most of the research on crack tip dislocation emission and motion has concentrated on pure elements. Alloying is often the technological solution required to enhance the properties of elements for engineering use, but the design of alloy composition has been empirical. More scientific methods are required to design new alloys. As one effort to design alloys, we have computed the "unstable stacking energy" (USE), or  $\gamma_{us}$ , as defined by Rice [2]: it is the difference in energy between a perfect lattice and after shearing half the lattice half a Burgers vector relative to the other half. Also of interest in the relation of fracture to alloy composition is the Peierls energy which controls the motion of dislocations in transition metal alloys once they have been emitted from the crack tip, but this requires a different computation.

Computation of both the USE and the Peierls stress for a dislocation has proved to be a difficult task. The most common method in current use requires interatomic potential functions that are derived from other known quantities, such as the vacancy formation energy, the elastic constants, etc. These quantities are all related to small atomic motions, whereas the core of a dislocation, the object of the modeling, is composed of large changes in atomic position. Therefore, the interatomic functions are of questionable validity, and

that is especially true for transition metals and alloys where part of the bonding is directional.

Several of the more recent fundamental analyses of fracture have used atomistic simulation rather than continuum analysis [4,7]. The work of Sun, et al. [4] results in expressions for mixed Mode I and II loading and indicates the importance of the tensile-shear coupling to dislocation emission. Another approach to determining the effects of dislocation motion on fracture toughness, has related  $\gamma_{us}$ , to  $\gamma_s$ , the surface energy, to derive a "shielding factor", defined as  $G_{far}/G_{tip}$ , the ratio of energy release rates in the far field (at the loading pins) compared to the crack tip energy release rate (according to the Griffith criteria) [4].

Regardless of which analysis is appropriate, the dislocation emission and motion criteria are dependent on the ability of the applied stress to generate dislocations at the crack tip and move them over the intrinsic energy barrier within the material, the Peierls energy barrier. Whereas the Peierls stress is small for face centered cubic metals, it is large for body centered cubic (bcc) metals and the more complex crystal structures of intermetallic alloys [4]. It is likely that dislocation motion through bcc metals, including emission from a crack tip, occurs by kink pair spreading. This process is also controlled by the magnitude of the Peierls barrier energy.

From what is currently understood about fracture, one of the factors that is required in the design of alloys is a method for assessing the change in the USE that occurs as the result of combining elements. Thus, a model is needed that allows for elemental substitution in the lattice and predicts the USE. The change in total energy of the crystal due to shearing by half a Burgers vector,  $\gamma_{us}$ , to a first approximation, will be indicative of the resistance of the lattice to dislocation generation at the crack tip and be one of the parameters controlling the magnitude of  $K_Q$ , and  $\varepsilon_F$ .

A model that allows for assessment of the effects of alloying on USE has the potential for being a screening technique in alloy design that would supplement other factors (e.g., microstructure) that must be considered. This paper describes a model that may be used to assess the effects of elemental additions on the magnitude of the USE. Recognition of the need for a physics-based approach to alloy design, along with the successes of other computer simulation studies, led to the development of this model.

## MODEL FORMULATION AND DESCRIPTION

To investigate the effects of alloying on ductility and toughness, a computational model for predicting the total energy of a solid as a function of atomic position and elemental constituents is needed. It was essential that the model be capable of handling three or more atomic species. To simulate the displacement of one part of the crystal relative to the other, it is also necessary that model treat arbitrary displacements in the direction of shear.

Thus, a model was developed that uses the wave functions of the individual atoms that constitute the alloy as basis functions in a 288 atom cluster of known lattice configuration and atomic separation. The atoms of the alloy were randomly placed in the cluster. To provide boundary conditions for the cluster so that the number of atoms was not a factor in the computation, the cluster was surrounded by 7000 atoms that had the characteristics of an "average" atom in the cluster.

With the model developed, we have computed the changes in the USE for Nb, and a series of solid solution alloys with additions of Cr and Ti for which fracture toughness was measured [10].

It is important to note that quantitative prediction of the USE is not required for the computational model to be useful; it is only necessary to determine if an atomic substitution, or atomic ordering, produces an increase or a decrease in USE as the lattice is sheared.

A cluster of atoms was used to represent an infinite solid. The cluster shown in **Fig. 1** was used to represent the bcc crystal structure. This lattice was sheared along the {110} and {112} slip planes in the <111> direction, which is the slip direction for the bcc structure. The size of the cluster used was limited by available computer resources to 288 atoms.

The electronic energy of the atom cluster was computed by the density matrix method using a superposition of neutral atom potentials for the electron potential energy. To simulate a much larger cluster, potential energies from a 7000 atom crystal, in which the small cluster was embedded, were included in the potential energy calculation.

The USE was defined as the difference in the total energy of the cluster deformed by one-half the Burgers vector ( $a[111]/4$ ) and the cluster before deformation. Following previous work [13-15], the total energy of the cluster

was determined by adding a sum of pairwise potentials to the electronic (band structure) energy. Thus

$$E_{\text{total}} = E_e + (1/2) \sum \sum \Phi_{ij}(R_{ij}) \quad (1)$$

where  $E_e$  is the total electronic energy of the cluster minus the corresponding free atom electronic energy,  $E_{\text{atom}}$ . Thus,  $E_e$  represents the change in energy that occurs when individual atoms are brought together into a solid and constitutes the attractive term that holds the crystal together.

Pairwise potentials  $\Phi_{ij}(R_{ij})$  represent the repulsive energy term and are summed over all nearest neighbors in the 7000 atom crystal. The method suggested by Baskes [16] was used to compute pairwise potentials by requiring agreement with the universal energy function of Rose, et al. [17], for reference crystals of each atom and each combination of atoms in the alloy. As a result

$$\Phi(R) = (2/Z)[E^u(R) - E_e(R)/N + E_{\text{atom}}] \quad (2)$$

where  $N$  = the number of atoms in the cluster,  $Z$  = the number of nearest neighbor atoms, and  $E^u$  is the energy per atom derived from the universal energy function. The universal energy function of Rose, et al., gives the total energy of the crystal as a function of the nearest neighbor distance. It contains parameters that are adjusted by requiring agreement with experimental values for the cohesive energy, bulk modulus, and lattice parameter. For pairwise interactions between atoms of the same element, the potential given by eq. (2) is used without adjustment of the universal energy function parameters, even though these atoms are now in the alloy environment. For unlike atoms, the parameters of Rose, et al., are taken as the averages of elemental values.

The electronic energy  $E_e$  is calculated by the density matrix method, described below, as a function of nearest neighbor distance for elemental crystals (to get the potential for like atoms) and for hypothetical binary alloys (to obtain the potentials for unlike atoms). These calculations are made for all the pairs of atoms of concern. Curve fits of these results are used in the final computation of pairwise potentials. Because the same method is used to calculate  $E_e$  in eq. (1), the end result is that pairwise potentials for like atoms fit the universal energy function for the like-atom crystal. However, for unlike atoms the potentials fit the approximate universal energy functions for hypothetical binary alloys obtained by averaging the parameters of Rose, et al. The potentials for unlike atoms are, therefore, subject to more uncertainty than those for like atoms.

## DENSITY MATRIX CALCULATIONS

The density matrix method [13,14,18] was used to compute the electronic energy  $E_e$ , following closely the work of Qui, et al. [14]. It is in this calculation that the hybridization of s and d electrons from the various alloy constituents is included. The electronic energy is given in terms of the density matrix by

$$E_e = \text{Tr}[\rho H] \quad (3)$$

where  $\rho$  is the density matrix,  $H$  is the same Hamiltonian matrix used in the traditional Local Combination of Atomic Orbitals (LCAO), or tight binding method [14], and  $\text{Tr}$  denotes the matrix trace.

The LCAO matrix elements used here were calculated directly from tabulated atomic wave functions [15] and overlapping free atom potentials. This is in contrast to the usual method of fitting matrix elements to experimental data or calculated band structures. The fitting method cannot be used in these calculations because we are working with new materials for which band structures and other data are unknown. Also, it should be noted that the final wave functions and electronic potentials obtained are not self consistent; the assumption is that this lack of self-consistency constitutes a minor error in the prediction of alloying effects. The density matrix is defined by minimizing the Gibbs free energy of all electrons in the cluster, subject to the constraint that

$$\text{Tr}[\rho] = N_e \quad (4)$$

where  $N_e$  is the total number of valence (d+s) electrons.

The Gibbs free energy  $G$  is minimized when  $\rho$  is defined through the relationship

$$G = \text{Tr}[\rho(H-E_F)] \quad (5)$$

where  $E_F$  is the Fermi energy, and is an unknown. Repeated variational calculations of eq. (5) were made with different assumed values of  $E_F$  until a value of  $\rho$  was found that satisfied eq. (4).

The density matrix calculation was performed for the cluster of 288 atoms

located near the center of the 7000 atom crystal. Electron potential energies, which are part of the Hamiltonian  $H$ , were computed by summing potentials over the full crystal. The only result used from the density matrix calculation is  $E_e$  = the average electronic energy per atom in the cluster. However, it is important that this number be correct since it constitutes the attractive (negative) part of the total energy, and is the part directly affected by hybridization effects.

Since  $\Phi(R)$  is being derived, it is also necessary to compute  $E_e(R)$ . A curve fit to  $E_e(R)$  derived from preliminary calculations, as described above, was used for calculating pairwise potentials.

### UNSTABLE STACKING ENERGY CALCULATION

How the procedure outlined above was used to compute the unstable stacking energy is summarized in **Fig. 2**. The computation begins with the definition of the undeformed lattice, followed by assignment of specific atomic species to each site in proportion to concentration in the alloy of interest. Site assignments can be based on either ordered arrays or random selection. Next, the electronic energy is determined by the density matrix method. This is followed by calculation of pairwise potentials, summed over all interacting pairs of atoms, which is then added to the electronic energy to obtain the total energy of the undeformed cluster. The lattice is then sheared and the energy calculations are repeated to obtain the total energy for the deformed cluster. The USE is the difference in total energy between the deformed and undeformed clusters.

Atomic positions in the undeformed cluster are determined from the average lattice constants. Thus far, lattice constants have been available from x-ray diffraction data for the alloys of interest. For alloys that have not actually been fabricated, an estimate of lattice parameter is required.

The positions for atoms along the slip plane in the sheared part of the crystal were obtained from a hard sphere calculation of atomic motion during slip. It was assumed that no force was exerted on an atom by a neighbor when the distance was greater than the nearest neighbor distance in the undeformed crystal. During slip, the atom was allowed to approach no closer than the equilibrium nearest neighbor distance; i.e., there was an infinite repulsive force at this distance. Thus, atoms were allowed to move normal to the slip plane as well as in it.

This "hard sphere" limitation is not consistent with the pairwise potentials

given by eq. (2), and so comprises another approximation used in the model. The significance of this approximation was explored by varying the distance across the slip plane and calculating the effect on the USE. The change in USE was small for changes in distance of 1 to 5 %. For some of the alloys, two computations of USE were made with two different randomizations of the alloys. The differences between these two calculations were larger than changes in interplanar distances across the slip plane, and are indicative of the importance of the specific atomic species that inhabit the plane of shear to the magnitude of the USE.

## RESULTS

Compositions of the Nb-based alloys for which the USE and Fermi energy were computed are given in **Table 1**. Direct comparison of USE with fracture toughness cannot be made because it is only one factor in controlling fracture and because only the tensile properties of the Jackson and Jones alloys [11] were measured.

The effect of Ti additions on computed values of the USE are shown in **Fig. 3(a)** for the Nb-Cr-Ti alloys [10]. All these materials were single phase.

Calculation of USE has been done for slip on the {110} and {112} because these are the most probable bcc crystal lattice slip planes. Titanium additions cause the USE to first decrease, then increase slightly for both slip planes. This is the same trend as followed by the fracture toughness for these materials, as shown in **Fig. 3(b)**, except that fracture toughness peaks at about 37 at.% while the USE is not much affected by additional Ti. Shown for comparison on the same graph are computed values of USE using a model by Rice [3] and the energy of the Peierls barrier [19]. These other energy factors decrease slightly with increasing Ti in contrast to the USE which is approximately independent of Ti; it increases slightly on the {110}.

Problems were encountered in computing the USE for the Jackson and Jones alloys and those of DiPasquale, et al. [12]. The problems encountered with these alloys appear to indicate one of the limitations of this computational approach. All these alloys contain Al, a non-transition metal having no d shell electrons. Thus, the inclusion of wave functions for Al requires additional assumptions.

Calculation with these compositions also identified an additional problem: the difference in energy level between the undeformed and deformed states was lowered to a level that the accuracy of the calculations became a problem.

Also, the differences in energy caused by different atoms in positions along the slip plane may limit the effectiveness of the calculation.

Change in Fermi energy caused by alloying is shown in Fig. 4. The changes in Fermi energy for the Nb-Cr-Ti alloys (DCA) [10] follow the same trends as seen in Fig. 3 due to Ti addition. This was expected because of the change in the number of bonding electrons caused by additions of Ti.

The Nb-Al-Ti-Cr alloys of Jackson and Jones [11] and the Nb-Al-Ti alloys of DiPasquale, et al. [12], continue the trend of the DCA alloys to lower atomic bonding electron numbers. The fit of the DCA and DiPasquale, et al. results is particularly smooth. The Jackson and Jones alloys contain both Cr and Al, and the fact that there is considerable scatter in computed values from these alloys may indicate that there is some problem in combining Al and Cr wave functions that was not a factor in the other calculations, or it has been found that ordering is caused by Al additions to transition metal alloys [20].

The Fermi level is determined by the total number of valence electrons and the density of states. For transition metals, the density of states changes very little from one element to another, which indicates that it is insensitive to details of the wave functions. Because of this insensitivity, it is expected that the density of states does not change much with addition of small amounts of Al, so that the total number of electrons is the only important factor. Therefore, calculation of the Fermi energy shift by the model given herein is less sensitive to the wave functions chosen for Al than is the computation of the USE because that computation is sensitive to interatomic interactions, which depend on the overlap integrals, which are sensitive to wave function details.

## DISCUSSION

This study was undertaken to find a tool to assist in alloy development; thus, wholly accurate computation parameters was considered as less important than rapidity and ease of computation. Alloy development requires an assessment of the effect of adding elements in many combinations. If this relative ease of use is to be maintained for the model, simplifying assumptions must be made.

The cluster size was limited to 288 atoms because of the computer facilities available and because the time requirements to perform the calculation were reasonable. However, from calculations described in the literature [18], the 285 atom cluster may be too small for a sufficiently accurate calculation of  $E_e$ .

The main limitations to more accurate computation of the USE are likely to be: (1) size of the cluster model, (2) assumptions made in the combinations of wave functions. The latter factor is the most important for the addition of elements that are non-transition metal; i.e., have no d-electrons. The smaller the cluster size, the more important is the location of the various atomic species relative to the slip plane. Thus, an alloy randomized differently gave different values of the USE, as would be expected. However, with the larger cluster size required to negate this effect, it would take longer to complete the computation. The effects of randomizing atomic distribution and ordering of the alloy can be viewed as limitations to the modeling process, or as a way to assess the effects of short and long range order on the mechanical properties of the material.

Determination of the mechanical properties of alloys for comparison with the modeling results also has its limitations, especially for experimental materials, such as used for comparison in this study. Experimental alloys are often made in small quantities, giving only enough material for one or two values of fracture toughness or elongation to fracture. When small specimens are used, accurate and repeatable measurements of a property may be compromised. Also, it is difficult to make materials in small quantities that are homogeneous, so there may be material variations from one to another specimen. All the alloys used for comparison in this study were thought to be single phase so that the complexities of multiple phase microstructure could be avoided. However, no specific determination of the single phase nature of the alloys was undertaken by Jackson and Jones. Nor was there any effort to determine the degree of ordering. The alloys of Davidson, Chan, and Anton are known to be single phase, but those of DiPasquale, et al, may well have contained an aluminide second phase.

Perhaps the best use of this cluster model computation is to predict changes in the Fermi level of an alloy, which can then be used to estimate density of states. The density of states (DOS) and integrated density of states (IDOS) curves are shown in **Fig. 5(a)** for Nb. Alloying will alter these curves, but not by much, as can be seen by comparing the curves for Nb and Mo; however, alloying does shift the Fermi levels, as shown in **Fig. 5(b)**. All the alloys examined in this work decrease the Fermi level except DCA alloy A, which raises it slightly. This effect is interpreted as follows: lowering the Fermi level decreases the number of d-electrons in bonding orbitals, thereby decreasing their level of covalent bonding. Alloying also decreases the melting temperature of these alloys, as can be seen from the phase diagram.

Pettifor diagrams have been explored for use in conjunction with these calculations. It might be possible to find trends in the effects of the alloying on ordering that would be of value in assessing the effects of randomizations made during the calculation.

The alloys investigated were plotted on a "pseudobinary AB" Pettifor diagram [21] to determine whether they may be near or within some of the regions known to contain ordered alloys. A similar approach was used by Smith, et al. [22], to examine Nb<sub>3</sub>Al alloys with other elemental additions. A portion of this diagram is shown in **Fig. 6** with the alloys located on it. As may be seen, the DCA alloys (A-G) are located well away from any region that might indicate ordering, while the Jackson and Jones alloys are closer to an ordered region. The DiPasquale, et al., alloys are closest to the ordered B2 region. This seems to indicate that there is an increasing tendency for these alloys to order as Al replaces Nb, Ti or Cr. In fact, the paper by Smith, et al., places the Nb-15Al-10Ti and Nb-15Al-40Ti alloys just in the edge of the B2 region, although the ordered region may be incorrectly positioned. As they point out, some evidence, obtained through TEM, does exist for ordering in these systems based on Nb<sub>3</sub>Al.

The conclusion from this analysis is that additional modeling work is necessary to understand the effects of alloying on USE and other characteristics of these alloys, especially in the presence of Al (Mendeleev No. 80). This approach would also indicate that similar issues would arise for alloys that contain Si (Mendeleev No. 85) and Be (Mendeleev No. 77).

## CONCLUSIONS

Computation of the unstable stacking energy by shear of the cluster of 288 atoms for random transition metal alloys correlates with trends in the mechanical properties of these alloys. More work is required, especially for additions of non-transition metals, but the model in its current state appears to provide assistance in improving alloy design from the perspective of metal physics.

**ACKNOWLEDGEMENT** Model development was funded by the Southwest Research Internal Research program, while application to the Nb-based alloys was funded by Air Force Office of Scientific Research (AFSC) under Contract F49620-95C-0043. The U.S. Government is authorized to reproduce and distribute reprints for governmental purposes notwithstanding any copywrite notation hereon.

**REFERENCES**

1. J.R. Rice and R. Thomson, Phil. Mag. A, v. 43, 1974, pp. 73.
2. J.R. Rice, J. Mech. and Phys. Solids, v. 40, 1992, p. 239.
3. J.R. Rice, G.E. Betz, and Y. Sun, in **Topics In Fracture and Fatigue**, A.S. Argon, ed., Springer, 1992, p. 1.
4. Y. Sun, G.E. Betz and J.R. Rice, Mat. Sci. and Eng., v. A170, 1993, pp. 67-85.
5. R. Thomson and A.E. Carlsson, Phil. Mag. A, v. 70, 1994, pp. 893-903.
6. S.J. Zhou, A.E. Carlsson, and R. Thomson, Phys. Rev. B, v. 47, 1993, pp. 7710-7719.
7. S.J. Zhou, A.E. Carlsson, and R. Thomson, Phys. Rev. Letters, v. 72, 1994, pp. 852-855.
8. M.H. Ashbury and J.D. Embury, Scripta metall. mater., v. 21, 1985, pp. 557.
9. P.B. Hirsch, S.G. Roberts, and J. Samuels, Scripta metall. mater., v. 21, 1987, p. 1523.
8. M.E. Eberhart, D.P. Clougherty, and J.M. MacLaren, J. Mat. Res., v. 8, 1993, p. 438.
9. C.L. Fu, M.H. Yoo, Acta metall. mater., 1992, v. 40, p. 703.
10. D.L. Davidson, K.S. Chan, and D.L. Anton, Met. and Mat. Trans., 1996, v. 27A, pp. 3007-3018.
11. M.R. Jackson and K.D. Jones in **Refractory Metals: Extraction, Processing and Applications**, K.C. Liddell, et al., eds., TMS, Warrendale, PA, 1990, pp. 311-320.
12. J. DiPasquale, D. Gahutu, D. Konitzer, and W. Soboyejo in **High Temperature Ordered Intermetallic Alloys VI**, J. Horton, et al., eds., Mat. Res. Soc. Symp. 364, 1995, p. 1347.
13. M.S. Daw, Phys. Rev. B, 1993, v. 47, p. 10895.

14. S.Y. Qiu, C.Z. Wang, K.M. Ho, and C.T. Chan, J. Phys: Condens. Matter., 1994, v. 6, p. 9153.
15. C.Z. Wang, C.T. Chang, K.M. Ho, Phys. Rev. B, 1989, v. 39, p. 8586.
16. M.I. Baskes, Phys. Rev. B, 1992, v. 46, p. 2727.
17. J.H. Rose, A. Banerjea, and J.R. Smith, Phys. Rev. Lett., 1981, v. 47, p. 675.
18. X.P. Li, R.W. Nunes, and D. Vanderbilt, Phys. Rev. B, 1993, v. 47, p. 10891.
19. D.L. Davidson "Transition metal alloys: elastic properties and Peierls-Nabarro stresses" Mat. Sci. and Eng., 1998 (in review).
20. Y.G. Li, P.A. Blenkinsop, M.H. Loretto, and N.A. Walker, Mat. Sci. and Tech., 1998, v. 14, pp. 732-737.
21. D.G. Pettifor, Mater. Sci. and Tech., 1988, v. 4, pp. 675-691.
22. L.S. Smith, D.K. Tappin, and M. Aindow, Scripta Met., Jan. 15, 1996, v. 34(2), pp. 227-234.

**Table 1**  
Alloy Characteristics and Fracture Properties

Alloy desig.	Composition				d+s	Elong- elect.	Fracture toughness	Lattice constant Å	Elastic Modulus GPa
	Nb	Al	Cr	Ti			MPa/m		

Davidson, Chan and Anton [10]

A	81	0	8	9	5.00		11	3.265	115
B	75	0	8	17	4.91		16	3.272	115
C	52	0	17	31	4.86		22-33	3.242	129
D	50	0	14	36	4.76		60-85	3.252	126
E	40	0	17	43	4.78		40	3.242	132
*F	40	10	10	40	4.66		23	3.245	118
G	100	0	0	0	5.00		8-12	3.302	100

Jackson and Jones Alloys [11]

1	35	14	7	44	4.57	0.11		3.249	113
2	45	10	0	45	4.50	0.33		3.289	104
*3	40	10	10	40	4.66	0.14		3.245	118
4	38	14	10	38	4.67	0.001		3.235	117
#5	48	12	0	40	4.54	0.26		3.282	103
6	46	12	5	37	4.64	0.13		3.261	110
7	50	12	6	32	4.55	0.12		3.255	110
8	50	10	10	30	4.78	0.001		3.242	117
9	52	10	6	31	4.71	0.04		3.227	110
10	57	9	0	34	4.63	0.18		3.288	103

DiPasquale, et al. [12]

11	75	15	0	10	4.88		19	3.266	97
22	65	15	0	20	4.71		20	3.271	99
#33	45	15	0	40	4.52		60-100	3.275	102

\* same composition

# nearly the same composition

atoms in slip plane

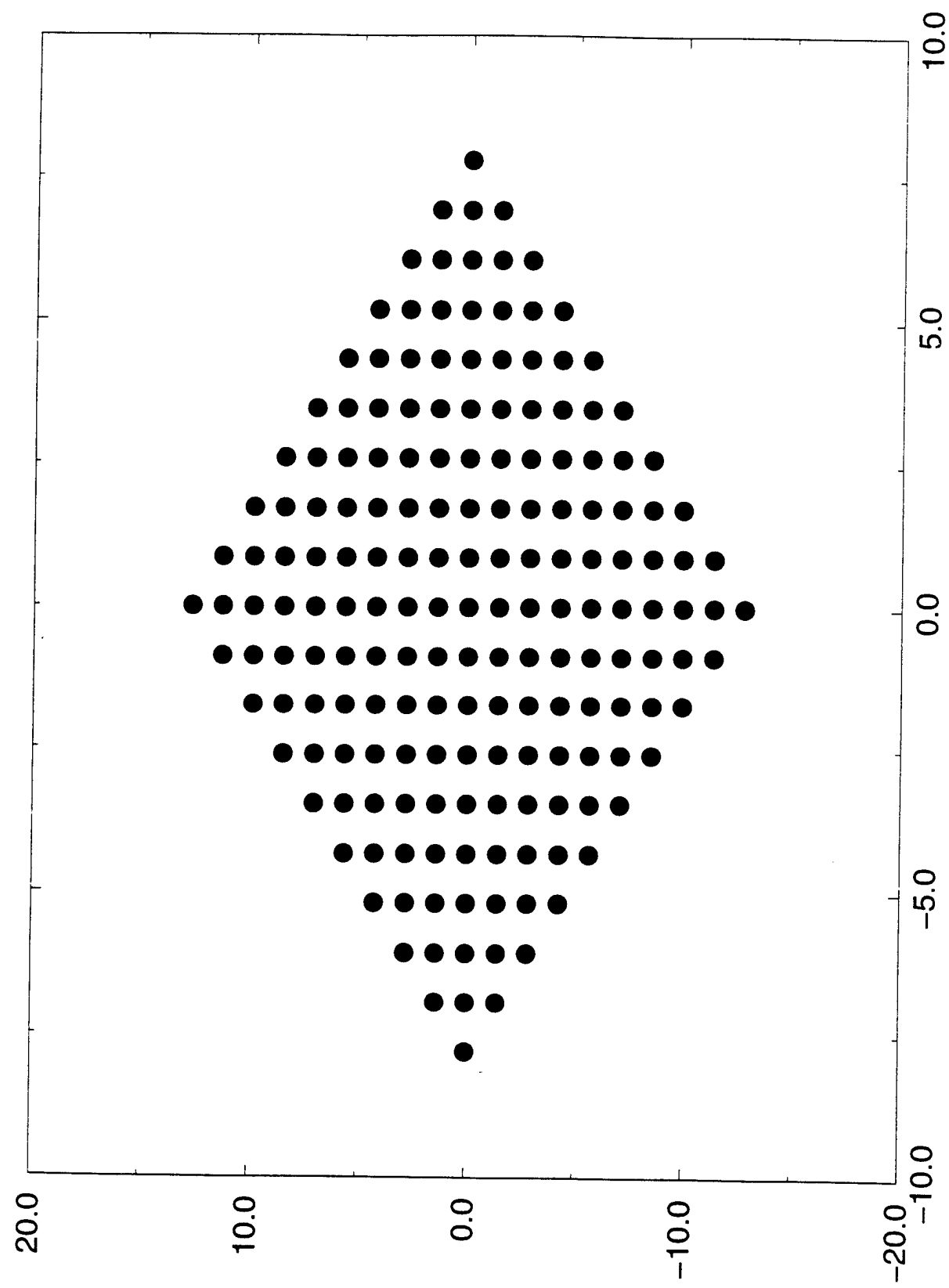


Fig. 1 Cluster of atoms used in USE computation

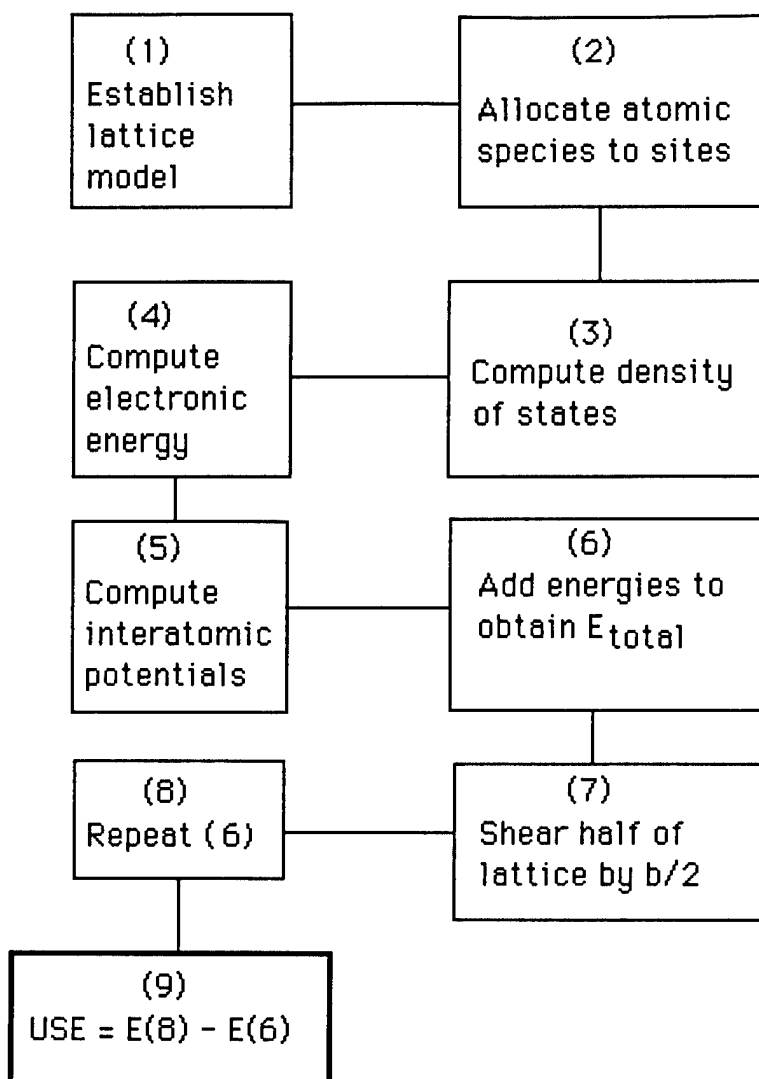


Fig. 2 Flow chart for the steps required in calculating the USE.

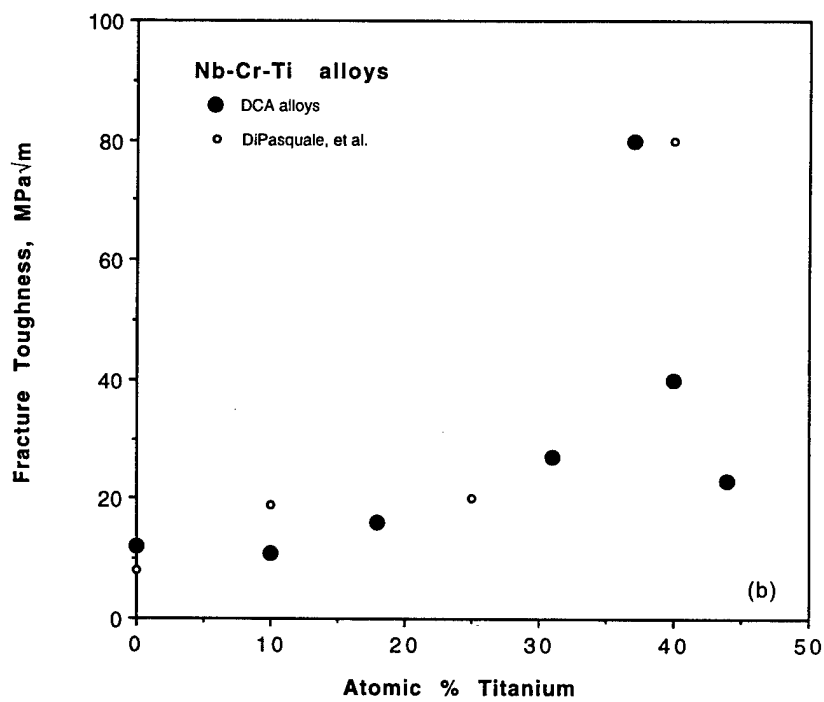
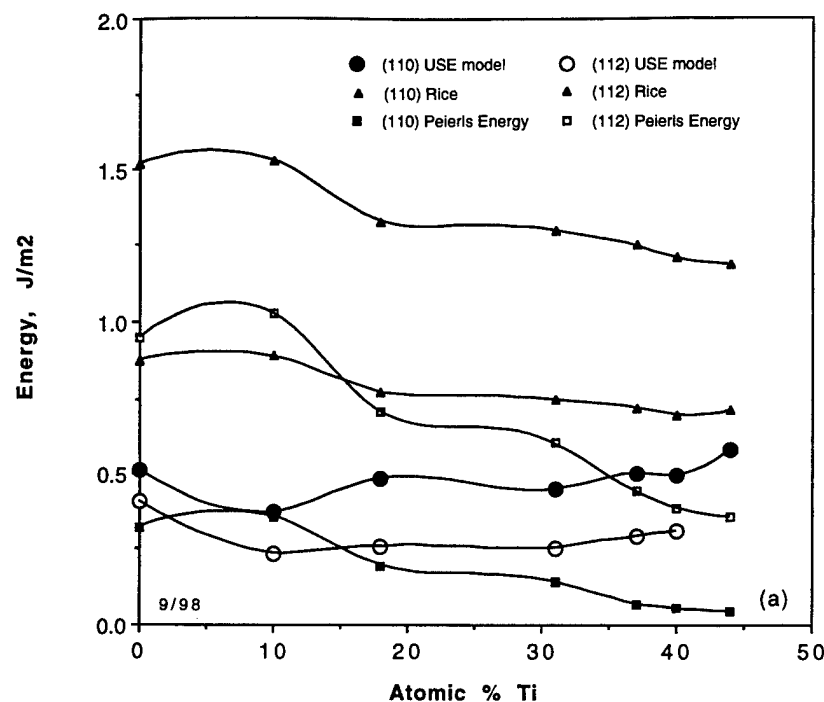


Fig. 3 (a) USE as computed by the atom cluster model compared to USE calculated from Rice's model and the Peierls barrier energy as a function of the concentration of Ti in Nb-Cr alloys. (b) Measured fracture toughness of Nb-Cr alloys (DCA) [10] and Nb-Al alloys (DiPasquale, et al.) [12], as a function of Ti concentration.

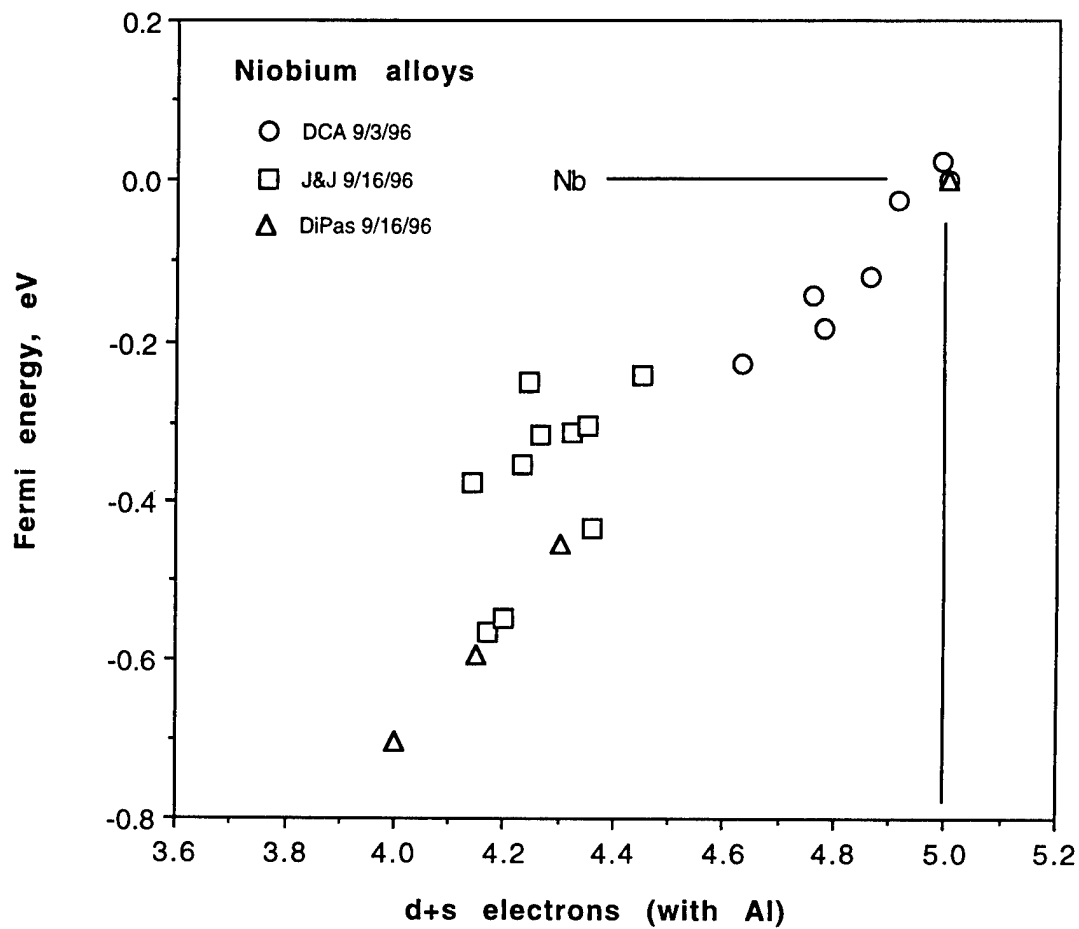


Fig. 4 Change in Fermi energy as a function of the number of bonding electrons for all the Nb-based alloys considered.

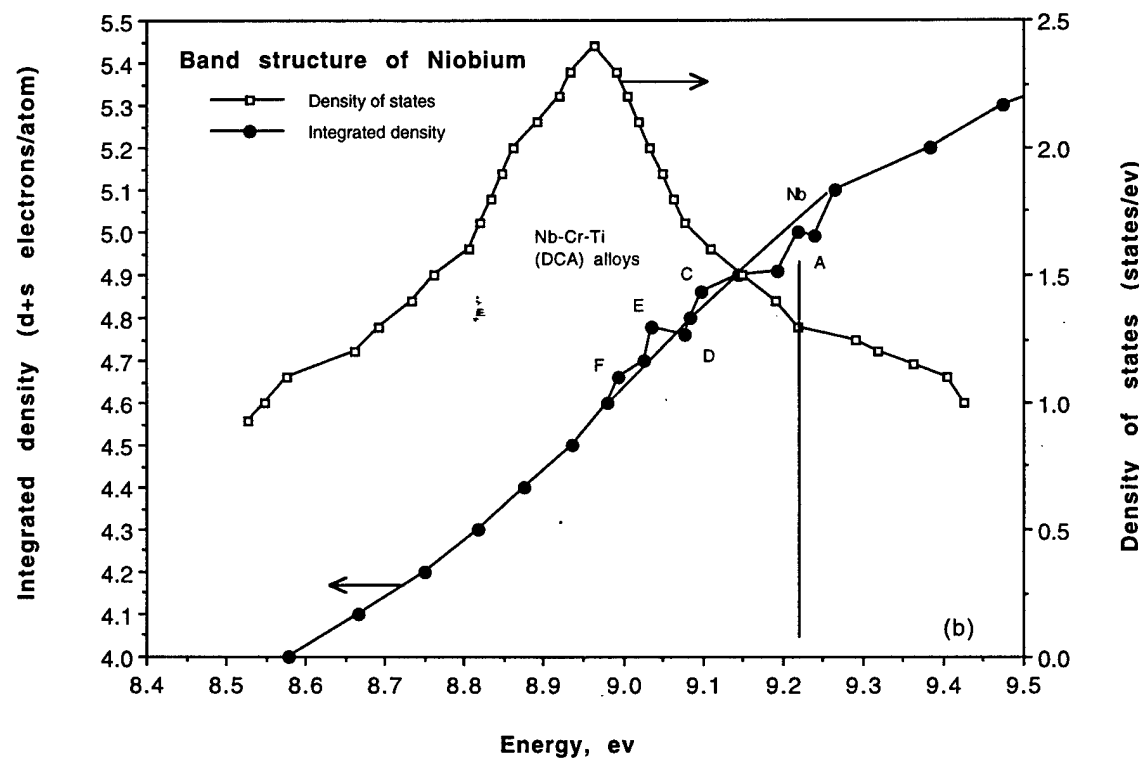
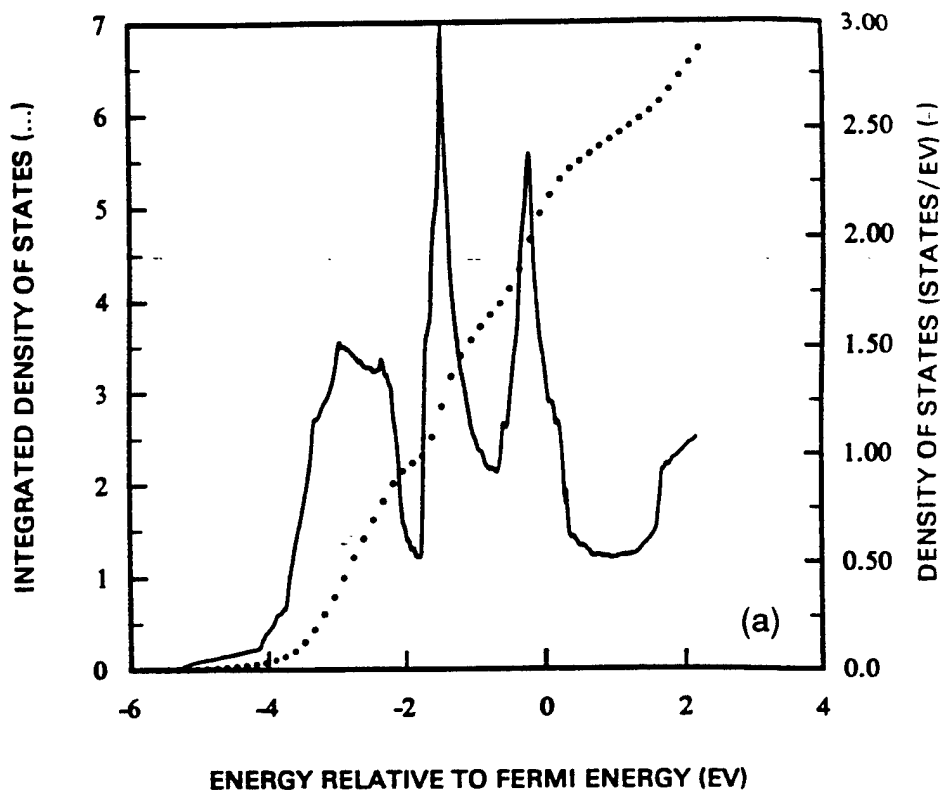


Fig. 5 (a) Density of states (DOS) and integrated density (IDOS) curves for Nb [ ]. The Fermi level of Nb is just below the minimum in DOS that indicates the complete filling of the bonding d-electron orbitals. (b) Superimposed on a limited part of the IDOS curve of (a) are the the DCA alloys. Alloying depletes the bonding d-orbitals of Nb.

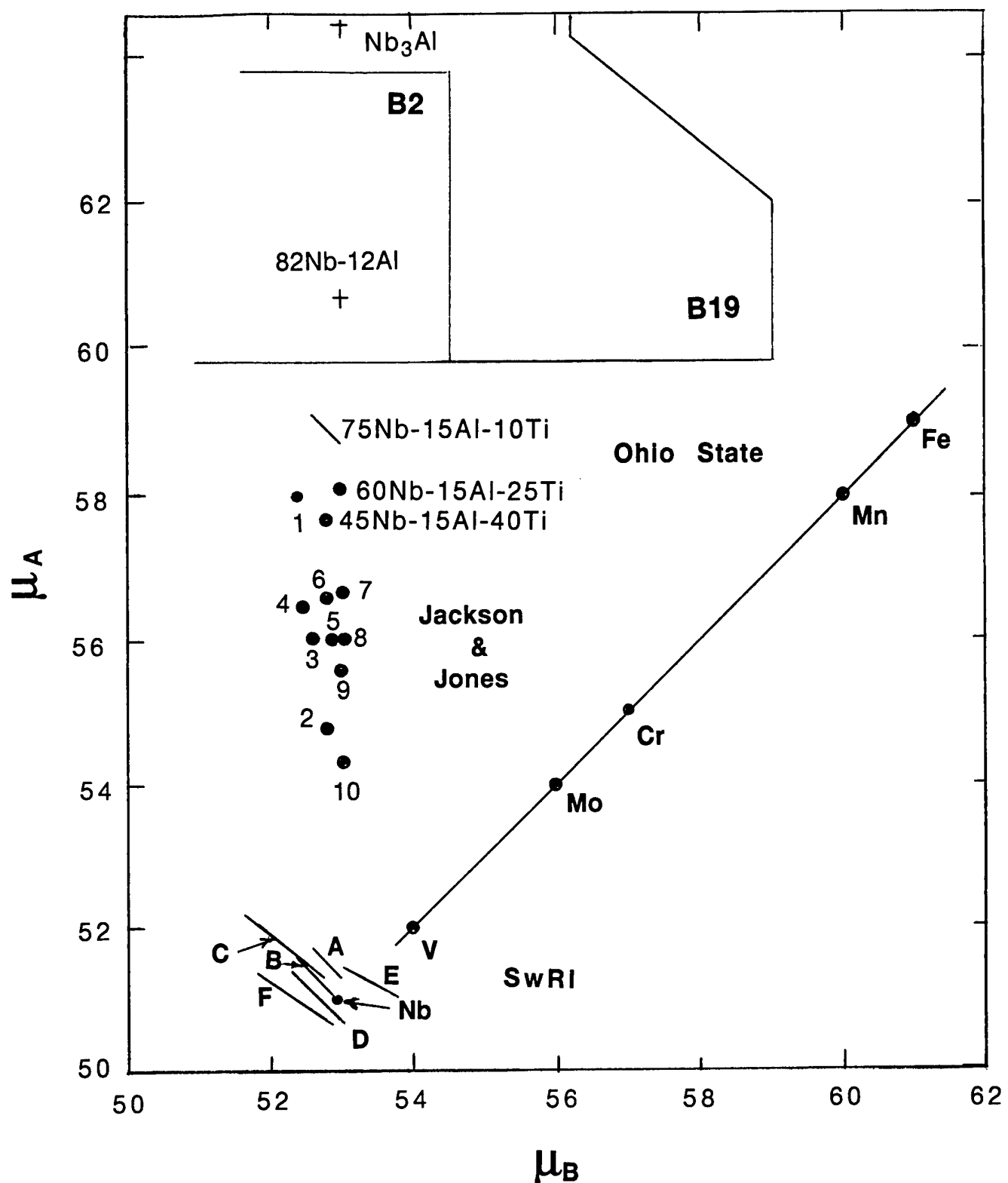


Fig. 6 A portion of the pseudo-AB Pettifor diagram showing the locations of the alloys relative to the ordered B2 structure.

# **Transition Metal Alloys: Elastic Properties and Peierls-Nabarro Stresses**

**David L. Davidson**

**Materials Science and Engineering**  
**(in review)**

## TRANSITION METAL ALLOYS: ELASTIC PROPERTIES AND PEIERLS-NABARRO STRESSES

David L. Davidson  
Southwest Research Institute  
San Antonio, TX 78228

### ABSTRACT

As an adjunct to alloying transition metals in the second long row of the Periodic Table with each other, published elastic properties have been analyzed and the Peierls-Nabarro (P-N) stresses computed. For binary alloys of Ti-Nb-Mo-Re, average tensile and shear elastic moduli, and Poisson's ratio were computed from the anisotropic elastic constants  $c_{ij}$ , which are also used to compute the energy factors for dislocations. From the latter, P-N stresses were computed for dislocation motion on the {110} and {112}. Computed values are compared to experimentally derived values for Nb and Mo. On the basis of measured values, the elastic constants are estimated for a series of Nb-Cr-Ti alloys of current interest.

### INTRODUCTION

Interest in transition metals has increased recently, as evidenced by research on high temperature materials for future use in gas turbines [1], space, and other applications. New materials based on Nb, Mo, Ta and W must have at working temperature a combination of high strength, low creep rates, good oxidation resistance, and at ambient temperature, reasonable ductility and fracture toughness. Density is always a factor in aerospace applications, so increases in operating temperature and stress must offset any density increase relative to alloys based on Ni, Co, and Fe.

The required combination of properties is not available from elemental metals, and alloying will be required to achieve the desired results. Although there is empiricism that assists some aspects of alloy development in the transition metals, mainly from research performed in the 1960's [2], there is very limited information that can be used for guidance in developing acceptable fracture properties. Plastic flow, e.g., dislocation multiplication, motion, and interaction, governs both ductility and toughness, if unwanted metallurgical factors can be avoided (e.g., grain boundary embrittlement). To achieve high fracture toughness, dislocations must be generated from a crack tip and moved away from it. Thus, dislocation multiplication and motion are the key issues in alloy development from the fracture perspective.

As an adjunct to developing new tough, ductile Nb-based alloys, the elastic properties of transition metals in the second row of the Periodic Table of the Elements have been gathered and analyzed. In this paper, those properties are reviewed and used to compute a variety of factors that may be helpful in transition metal alloy development.

## ELASTIC CONSTANTS

Elastic constants have been measured for a series of single phase alloys in the Ti-Cr [3,4], Nb-Mo [5], and Mo-Re [6] systems. Ideally, technicium (Tc) would be alloyed with Mo on the right side of this series, but Tc is rare, radioactive, and, therefore, impractical for engineering alloys. Values of the anisotropic elastic constants,  $c_{ij}$ , for those alloys are listed in **Table 1** and shown as a function of the number of bonding electrons in **Fig. 1**. On either end of this series, there are phase boundaries separating the body centered cubic (bcc) crystal structure of the transition metals from the hexagonal close packed (hcp) crystal structures.

Listed in **Table 1** are the lattice parameter ( $a$ ), measured by x-ray diffraction,  $C' = (c_{11} - c_{12})/2$ , which is a shear parameter related to the stability of the bcc structure [3], and the anisotropic factor  $A = c_{44}/C'$  ( $A = 1$  for isotropy). As the bcc-to-hcp boundaries are approached,  $C'$  decreases, which often correlates with deformation by twinning, and  $C'$  approaches zero at the phase boundaries. Also note that  $c_{11}$  follows the same trend as the melting point, and is a maximum at Mo. Because the Burgers vector of dislocations for the bcc structure ( $b = 0.866a$ ) is in the  $\langle 111 \rangle$ , this shear component is also tabulated as  $c_{\langle 111 \rangle} = (c_{11} - c_{12} + c_{44})/3$ , and is shown in **Fig. 2**.

Shown in **Fig. 1** are lines denoting the d+s electrons/atom for a series of Nb-based alloys containing Cr and Ti [7], denoted A through F, whose mechanical properties have been investigated. Compositions of these alloys are listed in **Table 2**. Data in **Fig. 1** were used to estimate the  $c_{ij}$  values for these alloys that are listed in **Table 1**.

## AVERAGE PROPERTIES

Average elastic moduli may be computed from  $c_{ij}$  using the Voight and Reuss averaging procedures [8]. Poisson's ratio was computed using the approach developed by Zener [9]. These average properties are given in **Table 1**. From  $E$  and  $\nu$ ,  $G = E/2(1+\nu)$  may be computed; numerically  $c_{\langle 111 \rangle}$  and  $G$  are similar.

## PEIERLS-NABARRO STRESS

Calculation of the P-N stress,  $\tau_p$ , using isotropic elasticity is made using the equation [13]

$$\tau_p = G/(1-\nu) \exp(-4\pi\zeta/b) \quad (1)$$

for the edge dislocation, and for the screw dislocation,  $(1-\nu)$  is replaced by 1, where  $\zeta = d/2(1-\nu)$ . Thus,  $\tau_p$  for screws is always greater than for edges. Dependence of  $\tau_p$  is dependent on the plane of slip through  $(d/b)$ , where  $d$  is the distance between planes. Therefore, planes with higher indices have larger Peierls stresses because of the smaller interplanar distance. To include anisotropy in the computation of Peierls stress, the preexponential factor is replaced by the appropriate anisotropic expression, or  $K$  factor, and the argument in the exponent is replaced by  $2\pi(d/b)(K/c)$  where  $c = c<111>$ .

The  $K$  values shown in **Table 3** can be used to compute the average energy of a dislocation line [10,11] as well as the stress required to move a dislocation over the Peierls barrier. These factors are dependent on the direction of the dislocation line and its angle to the Burgers vector. They have been derived analytically only for dislocations laying in the  $<100>$ ,  $<110>$ , and  $<111>$  directions; thus the edge dislocation moving perpendicular to  $b$  on the  $\{110\}$  must be derived from mixed dislocation solutions. The following expression has been used [10]

$$K_{\text{mixed}} = K_{\text{edge}} \sin^2\theta + K_{\text{screw}} \cos^2\theta \quad (2)$$

where mixed refer to  $K_3$  and  $K_7$ , which are values computed for dislocation lines in the directions  $<100>$  ( $\theta = 33^\circ$  to  $b$ ) and  $<110>$  ( $\theta = 77^\circ$  to  $b$ ). Equations for computing  $K_3$  and  $K_7$  may be found in [11], while for the  $<111>$  (screw), the equations are found in [12].

It should be noted that there is controversy as to whether eq. (1) is the correct equation to describe the Peierls stress in bcc metals. The main issue is whether 4 in the exponent should be replaced by 2, and there are other pre-exponential formulations available. Very recently, several papers have appeared that discuss various interpretations of models used to estimate the stress to move a straight dislocation [14,15,]. Equation (1), with 4 in the exponent, seems to adequately represent a wide range in experimental data, including the bcc metals. Thus, it appears to be the best form to use as an estimate of the P-N stress.

Many studies have identified overcoming the P-N stress for screw dislocations as the rate limiting factor for bcc metals being deformed at both low [14,16] and high temperatures [18,19]. Dislocation motion requires that a kink in the dislocation line be moved, and the rate limiting step may be the motion of two kinks away from one another. The description of the stress necessary for dislocation motion using eq. (1) is a greatly simplified model of the actual process, particularly since it was derived for pure metals, not alloys. The assumption made here is that calculation of the P-N stresses can provide a parameter useful in determining the expected effect of an alloying addition.

There is not currently an alternative to eq. (1) for computing the effect of alloying on the stress to move dislocation. Atomistic simulations of the core of a dislocation in transition metal alloys have not progressed to the point that such simulations have been made. The reasons for this are many, but include the problems of describing atom-atom interactions when the bonding is strongly influenced by partially filled d-shell electrons, i.e., is directional.

For dislocations on the {110} and {112}, P-N stresses were computed using the K factors of Table 3, and are listed in **Table 4**. Similar to  $c<111>$ , all the P-N stresses peak at Mo and decrease towards the phase transformation boundaries. P-N stresses are shown in **Fig. 3** as a function of both the alloy and d+s electrons/atom. Shown in **Fig. 4** are the P-N stresses for the Nb-Cr-Ti alloys as a function of Ti concentration.

Listed in **Table 4** are the energies computed for the P-N barrier using the equations given in Wang [13]. Similar to the shear coefficient  $c<111>$ , P-N energy barrier values peak at Mo and decrease towards the phase boundaries, as shown in **Fig. 5**, and as the concentration of Ti increases for the Nb-Cr-Ti alloys.

## COMPARISON OF COMPUTED vs. EXPERIMENTALLY DERIVED P-N STRESS

Peierls stress may be derived from experimental measurements of the flow stress ( $\tau_f$ ) as a function of temperature. Such measurements have been made only in single crystals of high purity elements. As temperature rises to  $T_0$ , the flow stress decreases to an athermal value ( $\tau_a$ ), which is defined as a slope that decreases about the same rate as the elastic modulus with temperature. Data are plotted as  $(\tau_f - \tau_a)/\tau_p$  vs.  $T/T_0$  where  $\tau_p$  is the value of  $(\tau_f - \tau_a)$  at  $T = 0^\circ\text{K}$ .

For comparison with the computed values, experimentally derived values of  $\tau_f$  are plotted in **Fig. 6** in the format described above using the Mo data of Aono, et al., as found in Suzuki, et al. [17], and for several Mo-Re alloys [20]. For Nb, the data of Takeuchi, et al, also found in Suzuki, et al. [17] was analyzed similarly.

Values of the parameters derived from the analysis are listed in **Table 5**.

Computed P-N stresses for a screw dislocation slipping on the  $\{110\}$  are larger than the values derived from experiment for Mo and the Mo-Re alloys. However, the magnitude of the computed values is critically dependent on the ratio (d/b), and the computation assumes no change of spacing between planes due to movement of the dislocation. For the  $\{110\}$ ,  $d/b = 0.8165$ , for Mo giving a P-N stress for the screw dislocation of 900 MPa, with a variation of 544 to 1490 MPa for change of  $\pm 10\%$  in d/b. For Nb, the P-N stress for a  $\{110\}$  screw is 380 MPa, and varies from 225 to 595 MPa for a  $\pm 10\%$  change in d/b. It is concluded that for Nb, the computed and experimentally determined P-N stresses are in close agreement, assuming that flow stress of Nb at low temperature is controlled entirely by motion of screw dislocations on the  $\{110\}$ . For Mo, experimental estimates of the P-N stress range from 550 to 730, which is on the low side of the theoretical estimates. Computed and measured values of the P-N stress for the Mo-Re alloys are in increasingly closer agreement as Re content increases.

## DISCUSSION

The estimation of measured elastic constants for alloys of interest, based on the number of bonding electrons, allows estimates of the tensile and shear moduli of those alloys, and that information is useful in alloy design. Clearly, alloying has a large influence on the moduli, Poisson's ratio, and the Peierls-Nabarro stresses. Computed P-N stresses and the energy of the Peierls barrier also correlate well with the number of bonding electrons. Values of P-N stress derived from experiment for Mo and Nb correlate reasonably well with those computed for screw dislocation motion on the  $\{110\}$ . However, the main usefulness of these estimates of P-N stress is believed to be the trends with alloying, not the absolute values.

There are a number of problems that limit the reality of this analysis. Yield stress and plastic deformation characteristics of these alloys are dependent on solid solution effects as well as the P-N stress. Derivation of eq. (1) is based only on the elastic properties of the materials and does not consider the influence of solute hardening. Deformation is strongly influenced by solute hardening, and a more useful theory would couple these two factors. There has been recent experimental work on dilute binary iron-based alloys [21] that explores the coupling of the P-N stress and solute effects.

Nabarro [15] has discussed a number of other problems in interpreting the P-N stress computation, such as the splitting of dislocations into partials, and the

fact that dislocations are most likely to move by the motion of kinks or kink pairs, that limit the value of computed P-N stresses. As Nabarro notes, the calculation is not very good for values of  $d/b < \approx 0.8$ . Although the computed P-N stresses for the movement of dislocations on the {112} is listed in Table 4, it may be a very poor estimate of the actual value, since  $d/b = 0.471$ .

Recent work by Duesbery and Vitek [22] using central interatomic force potentials computed the generalized stacking energy for slip on {110} and {112}. The maximum value of this factor is similar to the P-N barrier energy, listed in Table 4. For {110} slip in Mo, they computed  $0.908 \text{ J/m}^2$ , as compared to  $0.891 \text{ J/m}^2$  from the present computation. For {112} slip in Mo, they computed  $1.085 \text{ J/m}^2$  vs.  $2.74 \text{ J/m}^2$  from the present computation. The large difference in values obtained for the {112}, for which  $d/b \approx 0.477$ , appears to amplify Nabarro's concern about the accuracy of the P-N calculation for  $d/b < 0.8$ . Of course, the calculation using central interatomic force potentials also has its problems, but it may be more accurate than the simple P-N calculation.

The more complex calculation of the screw dislocation core structures [22] shows that the results of some restructuring of the core due to stress application can be observed in  $c<111>$ , which is listed in Table 1. This is reasonable since  $c_{ij}$  were used in construction of the potentials. Differences in the core structures between Nb and Mo indicate that their alloys would be expected to exhibit behavior that depends on electron concentration, as is shown by  $c<111>$ .

Remembering that screw dislocations move by the motion of kinks, or kink pairs, is important because the kink in a screw dislocation is a mixed dislocation; thus, a kink has some of the characteristics of an edge dislocation. Thus, a significant decrease in edge dislocation P-N stress may thus ease the motion of screw dislocations through the motion of kinks. In this way, a change in edge dislocation P-N stress would have more of an affect on screw dislocation motion than the calculation of the P-N stress for a straight screw would imply.

When transition metals are alloyed with each other, the present analysis should be useful in giving estimates of expected mechanical properties. However, a problem arises when non-transition metals such as Si and Al are added. How do adding those elements alter the number of bonding electrons? They may add or subtract from the number of bonding electrons available to the transition metal atoms, but, in general, their effects are not known.

## CONCLUSIONS

1. The elastic properties of transition metal alloys correlate systematically with the number of bonding (d+s) electrons.
2. For other alloys of interest, estimates of elastic moduli and the shear coefficient  $c_{111}$  may be made on the basis of the number of d+s electrons per atom.
3. Computed P-N stresses are in reasonable agreement with those derived from experiment.
4. Estimated values of P-N stress magnitudes, or at least the trends in P-N stress with alloying, can be derived on the basis of the number of bonding electrons per atom.

## ACKNOWLEDGMENT

This research was funded by the Air Force Office of Scientific Research (AFSC) under Contract No. F49620-92-0022, Dr. Charles H. Ward, Program Monitor. The United States Government is authorized to reproduce and distribute reprints for governmental purposes notwithstanding any copyright notion hereon.

## REFERENCES

1. P.R. Subramanian, M.G. Mendiratta, and D.M. Dimiduk "The Development of Nb-based Advanced Intermetallic Alloys for Structural Applications" JOM, 1996, v. 48, No. 1, pp. 33-38.
2. **Evolution of Refractory Metals and Alloys**, N.C. Dalder, T. Grobstein, and S. Olsen, eds., The Met. Soc., Warrendale, PA, 1994.
3. E.S. Fisher and D. Dever, Acta Met., 1970, v. 18, pp. 265-269.
4. E.S. Fisher and D. Dever in **The Science, Technology, and Application of Titanium** R.I. Jaffee and N.E. Promisel, eds., Pergamon Press, New York, 1968, pp. 373-381.
5. W.C. Hubbell and F.R. Brotzen, J. Appl. Phys., 1972, v. 43, pp. 3306-3314.
6. D.L. Davidson and F.R. Brotzen, J. Appl. Phys., 1968, v. 12, pp. 5768-5775.

7. D.L. Davidson, K.S. Chan, and D.L. Anton, Met Trans. A, 1996, v. 27A, pp. 3007-3018.
8. R.F.S. Hearmon **Applied Anisotropic Elasticity**, Oxford University Press, Oxford, 1961.
9. C.M. Zener **Elasticity and Anelasticity of Metals**, Univ. of Chicago Press, Chicago, 1948.
10. A.J.E. Foreman, Acta Met., 1955, v. 3, pp. 322-330.
11. Y.T. Chou and G.T. Sha, J. Appl. Phys., 1971, v. 42, pp. 2625-2631.
12. A.K. Head, phys. stat. sol., 1964, v. 6, pp. 461-465.
13. J.N. Wang, Acta mater., 1996, v. 44, pp. 1541-1546.
14. J.N. Wang, Mat. Sci. and Eng., 1996, v. A206, pp. 259-269.
15. F.R.N. Nabarro, Phil. Mag. A, 1997, v. 75, pp. 703-711.
16. K. Ohsawa, H. Hoizumi, H.O.K. Hirchner, and T. Suzuki, Phil. Mag. A, 1994, pp. 171- 181.
17. T. Suzuki, H. Koizumi, and H.O.K. Kirchner, Acta metall. mater., 1995, v. 43, pp. 2177-2187.
18. J.N. Wang and T.G. Nieh, Acta metall. mater., 1995, v. 43, pp. 1415-1419.
19. J.N. Wang and T.G. Langdon, Acta metall. mater., 1994, v. 42, pp. 2487-2492.
20. D.L. Davidson and F.R. Brotzen, Acta Met., 1970, v. 18, pp. 463-470.
21. K. Okazaki, J. Mat. Sci., 1996, v. 31, pp. 1087-1099.
22. M.S. Duesbery and V. Vitek, Acta mater., 1998, v. 46, pp. 1481-1492.

**Table 1**  
Elastic properties

Alloy	a Å	$c_{11}$ $\text{-- } 10^{12} \text{ dynes/cm}^2 = 10^5 \text{ MPa --}$	$c_{12}$	$c_{44}$	$C'$	$c<111>$	A	E	G	$\nu$
Ti(bcc)	3.33	1.086	1.085	0.427	0.001	0.143	---	71.3	25.6	0.500
Ti-7Cr	3.298	1.250	1.002	0.410	0.124	0.219	3.30	70.7	25.4	0.445
Ti-9.4Cr	3.288	1.331	0.951	0.427	0.190	0.269	2.25	90.4	30.9	0.417
Ti-13.8Cr	3.268	1.399	0.960	0.442	0.220	0.297	2.02	90.9	33.4	0.407
Ti-28.4Cr	3.202	1.591	0.941	0.477	0.325	0.376	1.47	110	40.9	0.372
Nb	3.302	2.516	1.320	0.297	0.598	0.491	0.497	110	39.5	0.344
Nb-23.3Mo	3.249	2.872	1.380	0.285	0.746	0.592	0.382	118	42.4	0.324
Nb-33.9Mo	3.229	3.159	1.389	0.319	0.885	0.696	0.360	135	48.7	0.305
Mo-48.7Nb	3.199	3.728	1.416	0.631	1.156	0.981	0.546	215	80.6	0.275
Mo-24.8Nb	3.169	4.318	1.494	0.902	1.412	1.242	0.639	282	108	0.257
Mo	3.146	4.757	1.609	1.112	1.574	1.420	0.706	330	128	0.253
Mo-16.1Re	3.137	4.758	1.852	1.257	1.453	1.388	0.865	345	133	0.280
Mo-27Re	3.130	4.721	2.021	1.350	1.350	1.350	1.00	351	135	0.300
Mo-35Re	3.125	4.550	2.120	1.390	1.215	1.273	1.14	344	132	0.318
A	3.260	2.55	1.32	0.282	0.610	0.500	0.458	108	38.8	0.341
B	3.272	2.36	1.33	0.285	0.515	0.438	0.553	105	36.2	0.360
C	3.252	2.26	1.285	0.309	0.488	0.428	0.634	103	37.1	0.362
D	3.246	2.00	1.14	0.381	0.430	0.414	0.886	110	40.0	0.363
E	3.242	1.95	1.14	0.391	0.405	0.400	0.965	109	39.6	0.368
F	3.226	1.76	1.00	0.428	0.380	0.396	1.13	110	40.8	0.362

$$C' = (c_{11} - c_{12})/2 \quad c<111> = (c_{11} - c_{12} + c_{44})/3 \quad A = c_{44}/C'$$

**Table 2**  
Alloy compositions  
atomic %

Alloy	Nb	Cr	Ti	Al	d+s electrons
A	84	10	6	0	5.04
B	75	8	17	0	4.91
C	53	16	31	0	4.85
D	50	13	37	0	4.76
E	40	17	43	0	4.74
F*	40	10	40	10	4.67

\* Al was not included in calculating d+s for this alloy

**Table 3**  
**Energy (K) factors**  
**Nb-Cr-Ti alloys**  
**GPa**

Alloy	d+s electrons/ atom	c<111>	K <sub>edge</sub> (110)	K <sub>edge</sub> (112)	K <sub>screw</sub> (H)
Ti(bcc)	4.00	14.3	1.13	46.1	0.83
Ti-7Cr	4.14	21.9	46.9	45.7	18.3
Ti-9.4Cr	4.19	26.9	53.2	51.5	24.7
Ti-13.8Cr	4.28	29.4	56.4	54.6	27.5
Ti-28.4Cr	4.57	37.6	64.9	63.4	36.8
Nb	5.00	49.8	60.8	63.8	46.7
Nb-23.3Mo	5.23	59.2	63.6	68.1	52.7
Nb-33.9Mo	5.40	69.6	71.1	76.7	61.0
Mo-48.7Nb	5.52	98.1	113	119	93.3
Mo-24.8Nb	5.75	124	147	153	121
Mo	6.00	142	173	178	140
Mo-16.1Re	6.16	139	186	188	138
Mo-27Re	6.27	135	193	193	135
Mo-35Re	6.35	127	192	191	127
G (same as Nb)	5.00	49.8	60.8	63.8	46.7
A	5.04	50.4	59.5	62.7	46.6
B	4.91	43.8	57.1	59.3	41.9
C	4.85	42.8	58.6	60.3	41.7
D	4.76	41.4	62.9	63.4	41.3
E	4.74	40.0	62.9	63.0	40.0
F	4.67	39.6	63.9	63.4	39.5

**Table 4**  
 Peierls Stress  
 Nb-Cr-Ti alloys  
 MPa

Alloy	$\tau_{\text{edge}}(110)$	$\tau_{\text{screw}}(110)$	$\tau_{\text{edge}}(112)$	$\tau_{\text{screw}}(112)$	$E_p(110)$	$E_p(112)$
	----- MPa -----				---- J/m <sup>2</sup> ----	
Ti(bcc)	13.1	5	25	43	0.004	0.002
Ti-7Cr	0.8	108	95	947	0.002	0.063
Ti-9.4Cr	2.1	146	177	1276	0.006	0.117
Ti-13.8Cr	3.0	163	221	1422	0.008	0.144
Ti-28.4Cr	9.2	218	427	1904	0.025	0.274
Nb	115	276	1433	2417	0.322	0.947
Nb-23.3Mo	258	312	2264	2725	0.712	1.47
Nb-33.9Mo	376	361	2935	3153	1.03	1.90
Mo-48.7Nb	305	552	3302	4824	0.830	2.11
Mo-24.8Nb	334	714	3987	6243	0.898	2.53
Mo	334	825	4344	7218	0.891	2.74
Mo-16.1Re	193	818	3401	7155	0.514	2.13
Mo-27Re	127	798	2805	6980	0.337	1.76
Mo-35Re	82	751	2260	6568	0.218	1.41
G (same as Nb)	115	276	1433	2417	0.322	0.947
A	139	276	1571	2412	0.358	1.03
B	71.5	248	1080	2167	0.198	0.707
C	51.9	246	927	2155	0.143	0.601
D	25.7	244	678	2135	0.071	0.441
E	19.9	237	595	2070	0.055	0.386
F	16.2	234	552	2044	0.044	0.356

**Table 5**  
**Peierls stresses**  
**Derived experimentally vs. computed**

Alloy	(110) screw Peierls stress ( $\tau_p$ ) derived	Peierls stress ( $\tau_p$ ) MPa computed	Athermal stress, $\tau_a$ MPa	Athermal temp. $T_o$ °K	Reference
Mo	630	825	15	475	Aono, et al.[17]
Mo	550	825	40	460	[20]
Mo-8Re	515	821	80	375	[20]
Mo-16Re	450	818	140	425	[20]
Mo-25Re	900	800	200	500	[20]
Nb	415	276	23	290	Takeuchi [17]

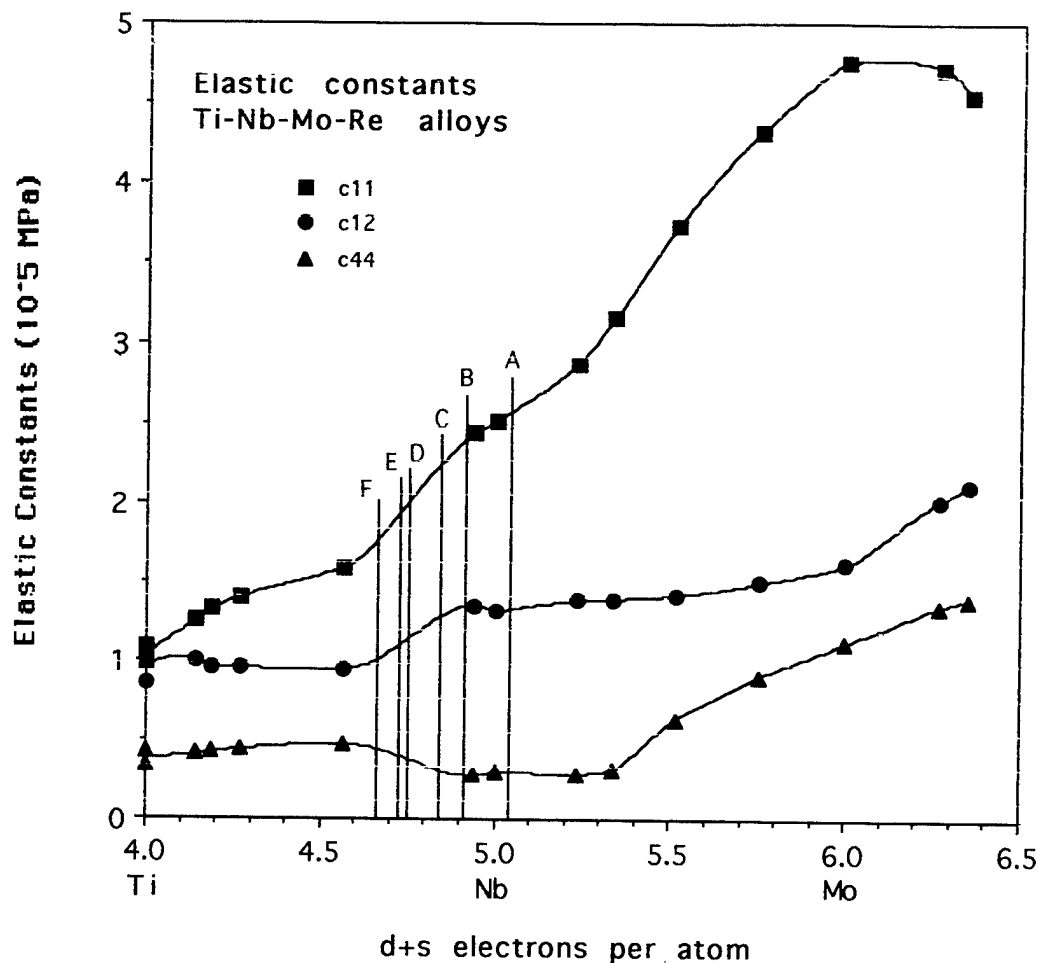


Fig. 1 Elastic constants  $c_{ij}$  correlated with the number of d+s bonding electrons per atom for transition metal alloys. Shown as A-F are other alloys of interest.

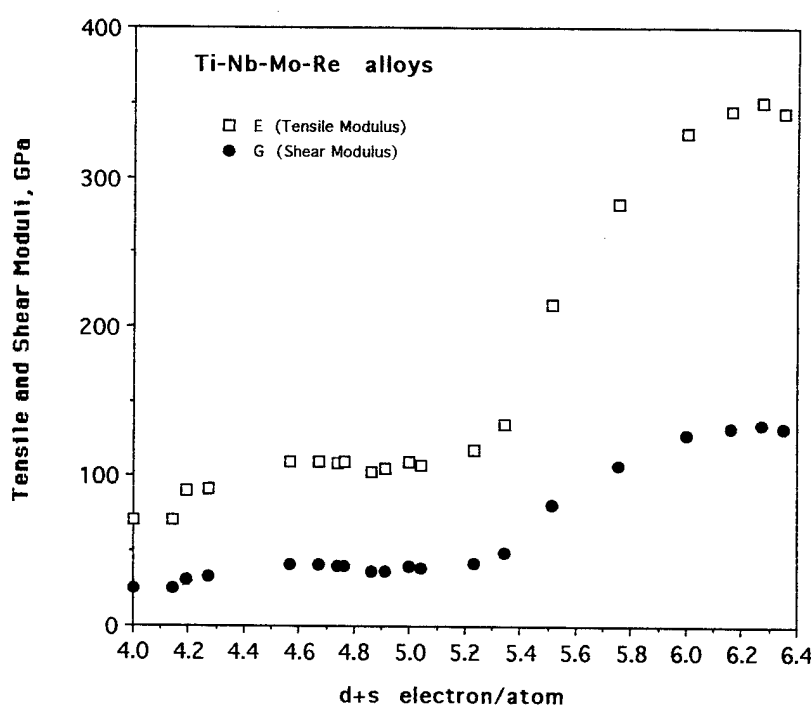
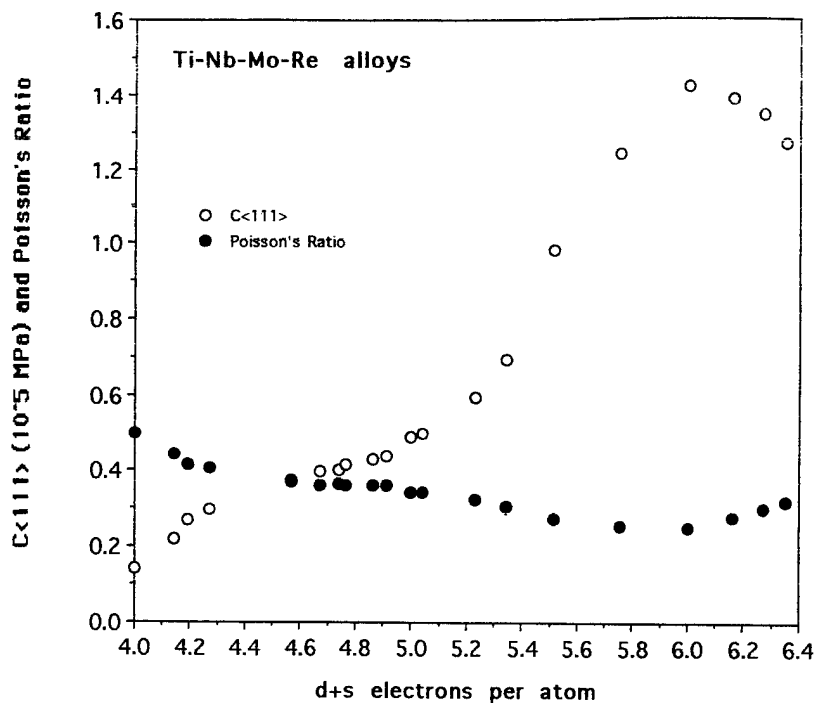
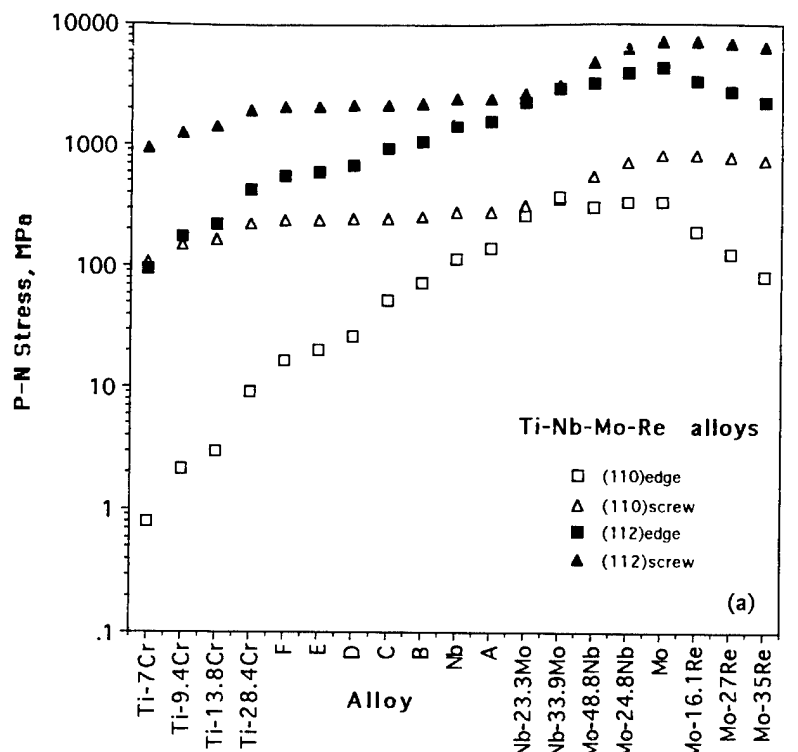
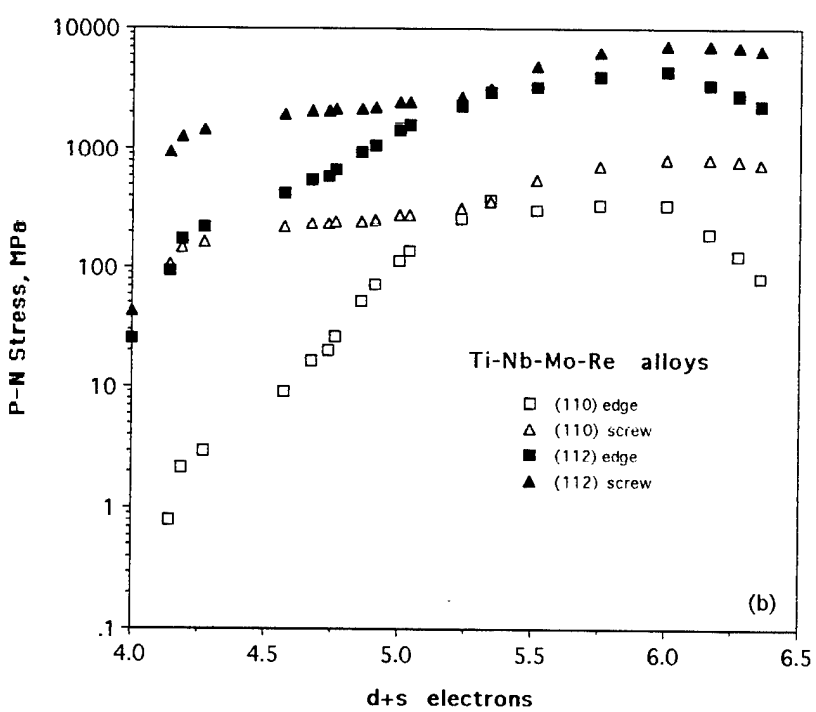


Fig. 2 Shear constant in the [111] correlated with the number of d+s bonding electrons per atom.



(a)



(b)

Fig. 3 (a) Peierls-Navarro stresses computed for all the alloys. (b) P-N stresses correlated with the number of d+s bonding electrons per atom.

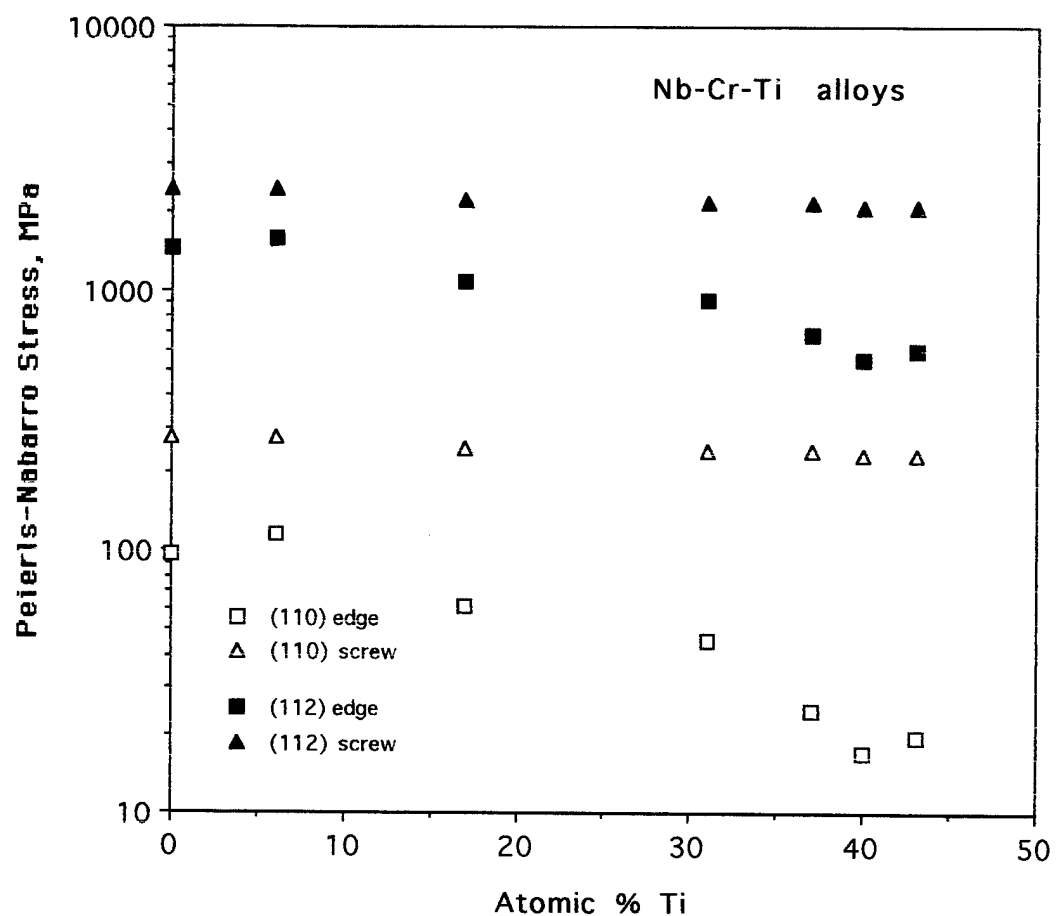


Fig. 4 Peierls-Navarro stresses vs. atomic % Titanium for the alloys A-F.

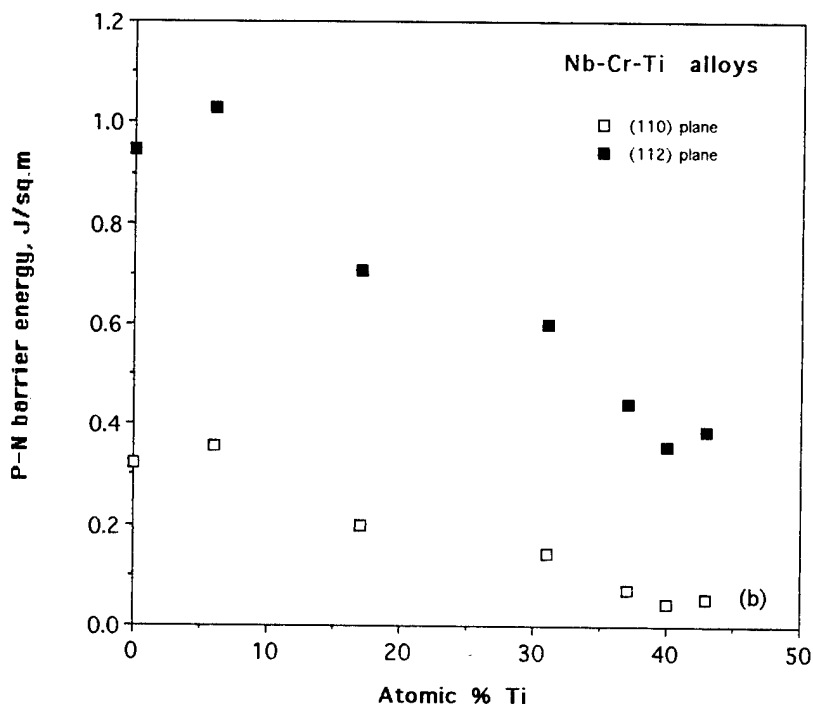
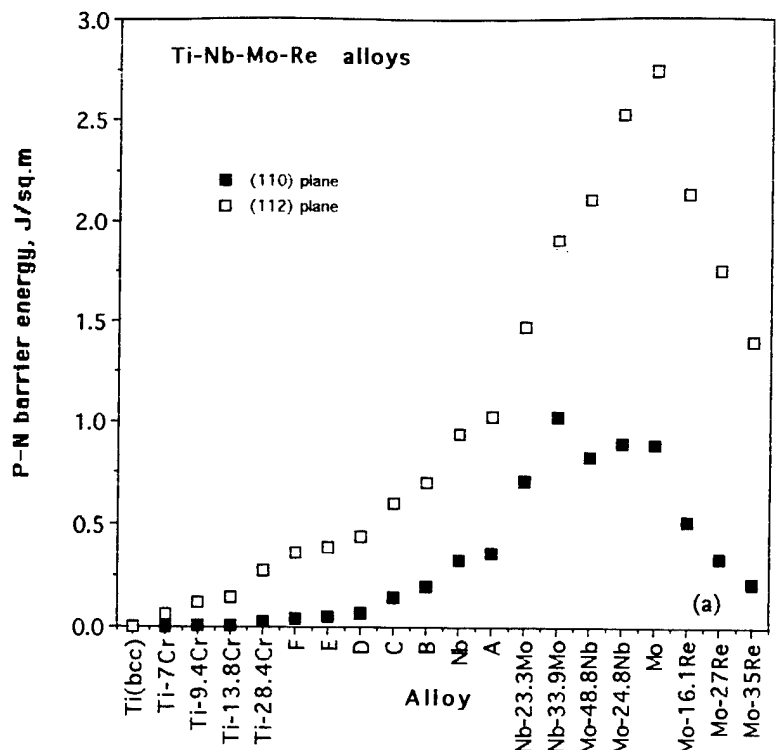


Fig. 5 Peierls barrier energies computed for dislocation motion on the {110} and {112} planes: (a) for all the alloys, and (b) as a function of atomic % Titanium for alloys A-F and Nb.

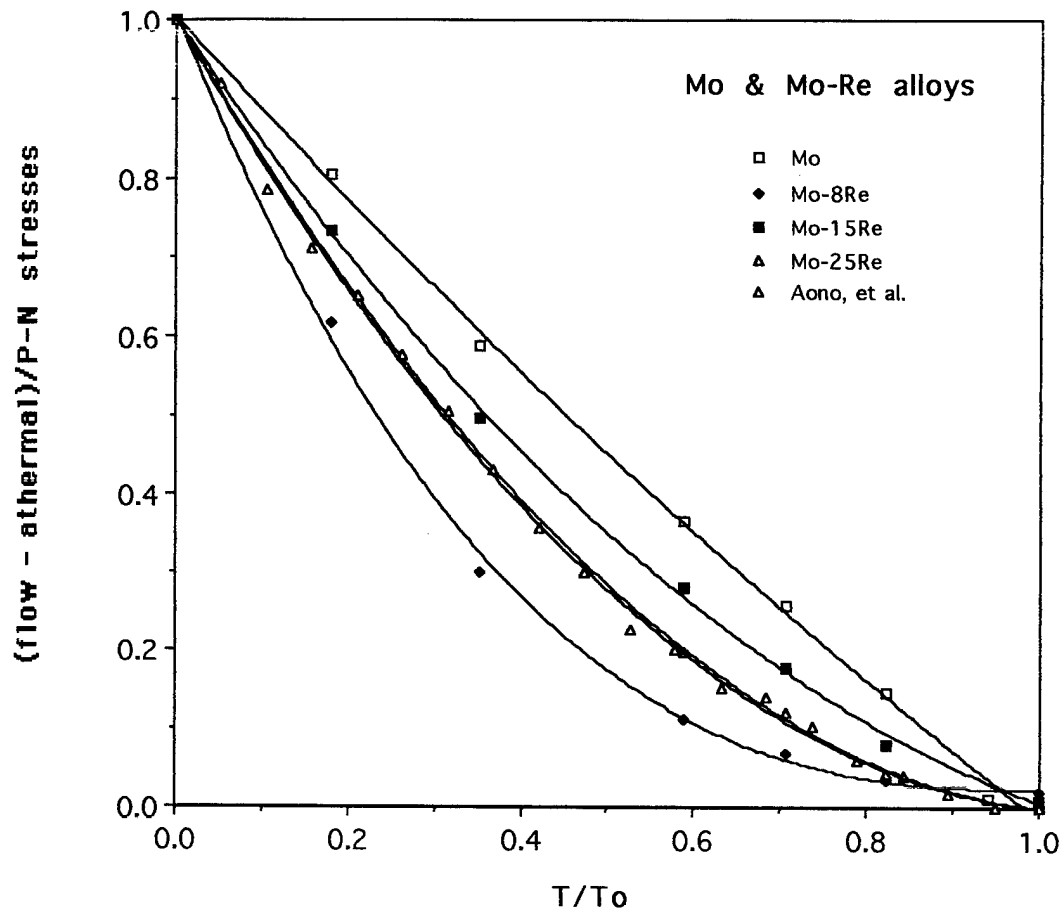


Fig. 6. Comparison of the reduced stress ( $\tau_f - \tau_a$ ) normalized by  $\tau_p$ , the P-N stress, as a function of the normalized temperature, where  $T_o$  corresponds to  $\tau_a$ . Data shown are from refs. 17 and 20. The lines are least squares fit through the data using a third order polynomial. The Mo data of Aono, et al., and the Mo-25Re data approximately fit the theoretical models of Suzuki, et al. [17].

**Effects of Ti Addition on Cleavage Fracture in Nb-Cr-Ti  
Solid Solution Alloys**

**Kwai S. Chan and David L. Davidson**

**Metallurgical and Materials Transactions A**  
**(in press)**

# Effects of Ti Addition on Cleavage Fracture in Nb-Cr-Ti Solid Solution Alloys

Kwai S. Chan and David L. Davidson  
Southwest Research Institute  
San Antonio, TX 78238

## ABSTRACT

The fracture toughness of Nb-Cr-Ti solid solution alloys has been shown to be greatly improved by Ti addition, but the mechanism of toughness enhancement has not been established. In this study, critical experiments were performed on the tough Nb-Cr-Ti alloy to characterize the crack-tip fracture process and to investigate the origin of fracture toughness. In addition, theoretical calculations of the unstable stacking energy (USE) and the Peierls-Nabarro (P-N) energy and stress were performed as a function of Ti content in the Nb-Cr-Ti alloys. The experimental results indicate that the fracture toughness in the tough Nb-Cr-Ti alloy originates from extensive dislocation emission that suppresses cleavage crack propagation from the crack tip. The theoretical calculation indicates that Ti addition lowers the P-N energy and stress, but has little effect on the unstable stacking energy. These results are used to elucidate the effects of Ti addition on cleavage fracture in Nb-Cr-Ti alloys by considering the influence of the P-N energy and stress values on (1) dislocation mobility, (2) crack-tip dislocation emission, (3) fracture toughness, and (4) brittle to ductile fracture transition. It is concluded that dislocation emission in the Nb-Cr-Ti alloys appears to be controlled by the P-N energy, which influences dislocation mobility, rather than by the USE, which influences dislocation nucleation. Ti increases the fracture toughness of Nb-Cr-Ti alloys by increasing dislocation mobility and dislocation emission from the crack tip through a reduction of the P-N energy and stress.

## INTRODUCTION

Recent investigations based on the Nb-Cr-Ti system have demonstrated that Ti addition is beneficial for improving the fracture toughness of solid solution alloys and in-situ composites [1-3]. This beneficial effect, which is illustrated in **Figure 1**, is manifested as a marked increase in fracture toughness in alloys containing 30-40 a/o% Ti [2,3]. The amount of toughness improvement by Ti addition is more modest in the in-situ composite, and the maximum toughness value appears at a Ti content of about 30 a/o%. While the enhancement is well documented, the mechanism by which Ti improves the fracture resistance in these materials is not fully understood. Correlation of fracture and flow properties revealed a complex relationship between fracture toughness and yield stress, Table I. A plot of fracture toughness against yield stress shows a maximum toughness value at  $\approx 765$  MPa, which corresponds to the alloy with 37 a/o% Ti and a tensile ductility greater than 6.5%.

The lack of understanding is the result of the complex fracture process in the Nb-Cr-Ti alloys. In most of these alloys, the fracture toughness increases with Ti content even though the observed fracture mode is entirely or mostly cleavage, as illustrated in **Figure 2** which shows the fracture appearances of Nb-Cr-Ti alloys as a function of Ti contents and fracture toughness [2,3].

In the 30-40 at.-% Ti range where the maximum toughness occurs, several fracture modes including slipband decohesion, grain boundary cracking, cleavage, and dimpled fracture were observed [1]. The fractographic result therefore does not provide an unambiguous explanation for the toughness enhancement by Ti addition. Neither the controlling fracture mechanism nor the source of toughness has been fully established. For example, it remains unclear which is the toughness limiting mechanism among the observed fracture processes which include slipband decohesion, grain boundary cracking, cleavage, and dimpled fracture. Although dimpled fracture is present in Nb-Cr-Ti alloys, the size of the microvoids are small and they cover only a small percent of the fracture surface [1]. Therefore, the microvoids should have a negligible influence on toughness. The implication is that the toughness increase in the Nb-Cr-Ti alloys is due to the deformation accompanying the other aforementioned fracture processes.

An experimental correlation revealed that the fracture toughness of both the Nb-Cr-Ti solution alloys and in-situ composites increase with decreasing number of d+s electrons per atom in the material system [2]. This correlation is illustrated in Figure 3, which shows a log-log plot of fracture toughness versus the sum of the d and s electrons per atom in the alloys [2]. The result suggests that Ti addition affects the fracture toughness by changing the atomic bonding condition, thereby changing the lattice resistance to dislocation motion in the Nb-Cr-Ti alloys. In particular, it seems plausible that the enhancement of fracture toughness in Nb-Cr-Ti alloys by Ti addition is a manifestation of the influence of Ti atom on the crack-tip slip processes. To the authors' knowledge, there have been no detailed studies of the role of Ti addition in the crack-tip slip process in Nb alloys and its effect on fracture toughness.

The objective of this paper is to present results of an investigation whose goals were to determine: (1) the sequence and the relative importance of the slip originating from the crack-tip and non-tip fracture processes including slipband decohesion, grain boundary cracking, and cleavage in Nb-Cr-Ti alloys; (2) the factors that limit fracture toughness; and (3) the role of Ti addition in the fracture of the Nb-Cr-Ti solid solution alloys. To achieve these goals, the fracture processes in the tough Nb-Cr-Ti matrix alloy were studied by micromechanical testing in an SEM equipped with a loading stage. The observed slip and fracture processes were then correlated with the stress intensity factor to determine the onset of a particular failure mode and the associated fractographic features. In addition, theoretical modeling was performed to calculate the influence of Ti addition on the unstable stacking energy [4], Peierls-Nabarro (P-N) stress [5,6], and P-N barrier energy for the experimentally observed slip systems. The experimental and theoretical results were then correlated to elucidate the role of Ti addition in (1) emission of dislocations from the crack tip, (2) dislocation motion in the plastic zone, and (3) the onset of cleavage fracture. The results indicate that Ti addition improves fracture resistance by reducing the energy barrier for dislocation emission, improving dislocation mobility, and suppressing cleavage crack propagation from the crack tip. Substantial near-tip plastic flow led to non-tip fracture processes that include slipband decohesion, grain boundary cracking, dislocation pileup-induced cleavage, and dimpled fracture.

## BACKGROUND

Cleavage fracture in metals has been classified as Cleavage I, II, and III according to the amount of plasticity accompanied fracture [7]. In Cleavage I, fracture occurs in the absence of general plasticity at a fracture stress that is less than the yield stress of the material. In Cleavage II, fracture is preceded by microplasticity, induced by slip or twining, and is accompanied by negligible ductility (< 1%). In Cleavage III, substantial plastic strain (1-10%) precedes fracture. The common cleavage planes for bcc metals and alloys, including Nb and Nb alloys, are the (001), (011), (112), and, occasionally, (111) planes [8].

The prevailing view on cleavage fracture is that there is a competition between the emission of dislocations and the propagation of a Griffith crack from the crack tip [4,9-20]. The limiting stage in the dislocation emission process can either be the nucleation of dislocations at the crack tip [4,9-20] or once nucleated, the mobility of the dislocations propagating away from the crack tip [21-23]. In both cases, dislocation emission leads to shielding of the crack tip that results in an enhancement of fracture resistance. A recent model by Rice [4] has suggested that the nucleation of a dislocation from a crack tip requires overcoming the unstable stacking energy, which is defined as the maximum energy encountered in a block like sliding of one half of a crystal relative to the other by half of a Burgers vector along a slip plane. The ratio of the surface energy to the unstable stacking energy is hypothesized as a measure of the propensity for the onset of ductile fracture. If nucleation of dislocations at the crack tip is relatively easy, the mobility of dislocations moving away from the crack tip, which is controlled by the lattice resistance and assisted by thermal activation, dictates the mode of fracture [21-23]. Cleavage fracture limited by dislocation mobility has been modeled by Hirsch and Roberts [21-23], who showed that the brittle-to-ductile fracture transition in brittle materials, such as TiAl, Si, and Ge is the consequence of increasing dislocation mobility at higher temperatures.

Recent work by Gerberich, et al. [18] showed that dislocation emission and shielding of the crack tip increased the fracture toughness of Fe-3 wt. % Si single crystal crystals from 3 to 60 MPa $\sqrt{m}$  in the 100-260 K temperature range, despite the fact that fracture occurred entirely by cleavage. To account for the experimental observations, they proposed a cleavage fracture model that postulated the existence of dislocation emission and cleavage fracture surfaces in a three-dimensional space (K-space) of the local mode I, II, and III stress intensity, K, factors [18]. These surfaces represent the local K conditions for dislocation emission from the crack tip and the onset of cleavage fracture, respectively. Furthermore, Gerberich, et al. [18] envisioned that dislocation emission from the crack tip results in a ductile fracture behavior when the loading path representing the local applied stress intensity factors intersects the dislocation emission space before the cleavage fracture surface. In contrast, cleavage fracture results if the local loading line encounters the cleavage fracture surface before the dislocation emission surface. A ductile-to-brittle fracture transition occurs when dislocation emission leads to the expansion of the dislocation emission surface so that it intersects the cleavage surface. Using a dislocation emission criterion due to Lin and Thomson [24] and a cleavage fracture criterion due to Griffith [25], Gerberich and his coworkers investigated the role of dislocation emission in cleavage fracture of Fe-3 wt.% Si single crystals [18], Mo single crystals [18], and 3 wt. % Si steel [19] by computer simulation and analytical modeling. Their result showed that the plane strain fracture

toughness associated with plasticity-induced cleavage depends on the local Griffith stress intensity factor and the yield stress [18].

In addition to dislocation emission from the crack tip, slip in the plastic zone might also induce cleavage ahead of and away from the crack tip. At least two cleavage fracture models [12,13,26,27] have been proposed for explaining this type of cleavage fracture; one is based on the existence of an elastic field embedded within a plastic field [12,13] and the second [26,27], motivated by experimental observations, considers plasticity-induced cleavage to occur as the result of the elastic stress field of a dislocation pileup by the Stroh mechanism [28]. In other studies, the effects of temperature, loading rate, and the triaxial state of stress on cleavage fracture and fracture toughness in Nb-Si alloys were examined [29]. These investigations demonstrated that the fracture toughness of Nb-Si alloys could be relatively high, even though fracture occurred entirely by cleavage as assessed from fractography. Cleaving fracture in steel has been shown to obey a critical fracture stress by Ritchie, Knott, and Rice (RKR) [30]. A critical fracture stress for cleavage was recently reported for Nb alloys [31]. Thus, there is ample evidence in the literature that a high fracture toughness can accompany cleavage fracture in Nb-based alloys. None of these previous studies, however, address the effect of alloying on cleavage fracture, the roles of near-tip and non-tip slip, and their relationship to fracture resistance.

## EXPERIMENTAL PROCEDURES

The material studied was a Nb-Cr-Ti solid solution alloy with the composition of Nb-13Cr-37Ti (in atomic percent). The Nb-Cr-Ti alloys were nonconsumably arc cast into a 75 mm<sup>2</sup> water cooled copper hearth in an atmosphere of argon gettered with titanium. The ingots were then cut into quarters and heat-treated in helium gettered by titanium first for 8 hours at 1500°C, then for 48 hours at 1200°C. The microstructure was single phase bcc (determined by x-ray diffraction) with a grain size of approximately 1500  $\mu$ m. Compact-tension specimens were prepared by electrodischarge machining to the size of 19.9 mm in width, 19.1 mm in height, and 4.8 mm in thickness. A thinner (1 mm thickness) specimen was also used to determine whether or not cleavage could be prevented by a reduction in specimen thickness. Cleavage fracture was present in both the thin and thick specimens. A notch was introduced to the specimens by cutting with a diamond wheel cutter. Subsequently, the surfaces of the specimens were mechanically polished, followed by fatigue precracking, and then ion etched. Fatigue precracking was conducted at a stress intensity range of 8 MPa $\sqrt{m}$  under a stress ratio, R, of 0.1. The crystallographic orientation of the surface grains around the crack tip was determined by the Laue back-reflection technique [32]. This result was used to identify the slip or fracture planes using the two-surface analysis technique [32].

Fracture toughness testing was performed in an SEM equipped with a loading stage [33]. The load was applied manually at a relatively slow loading rate, but the actual loading rate was not measured. At each load increment, the near-tip region was photographed as a function of the stress intensity, K, levels in increments of 2-3 MPa $\sqrt{m}$ , starting at 15 MPa $\sqrt{m}$  and continuing until the specimen failed. The photographs were used to determine the amount of crack extension, the level of strain in the fracture process zone, and to identify the near-tip fracture processes. The K-resistance curve was generated by plotting the stress intensity, K, as a function

of crack extensions and fracture toughness was calculated using the peak load and the crack length at fracture. Micrographs of the loaded and unloaded crack-tip region were analyzed using a machined-vision-based stereoimaging technique [34] to obtain the near-tip displacement and strain fields. The fracture surfaces of the specimens were examined using SEM fractography. The traces of the slip and fracture planes were obtained and used to identify the slip and/or fracture planes using the two surface analysis.

## THEORETICAL CALCULATIONS OF UNSTABLE STACKING ENERGY AND THE PEIERLS BARRIER ENERGY AND STRESS

### A. Unstable Stacking Energy

The unstable stacking energy,  $\gamma_{us}$ , is the maximum energy encountered in a block-like sliding of one half of a crystal over another half by half of a Burgers vector on a slip plane. Introduced first by Christian and Vitek as the gamma surface [35], Rice [4] later termed the maximum value as the unstable stacking energy ( $\gamma_{us}$ ). This parameter is hypothesized as a measure of the energy required to nucleate and emit a dislocation from a stressed crack tip. The applied stress intensity factor required for dislocation nucleation has been shown by theoretical analysis to be proportional to  $\sqrt{\gamma_{us}}$ . Estimates of the unstable stacking energy have been reported by Rice for a number of metals including Nb [4]. Two types of estimates were given; one was based on a sinusoidal relation of the shear stress and shear displacement of the periodic lattice and the other calculated using the embedded-atom approach. Using these estimates, Rice suggested that the ratio of the surface energy to the unstable stacking energy ( $\gamma_s/\gamma_{us}$ ) can be used as a measure of the propensity for brittle fracture and also as a criterion for the brittle-to-ductile transition. The analysis concludes that, for bcc metals, if  $\gamma_s/\gamma_{us} > 6.3$  for pure mode I loading, then dislocation motion will precede cleavage fracture. If the material response results in some mode II crack tip behavior, then  $\gamma_s/\gamma_{us} > 3.5$  will result in dislocation emission [4]. For the Nb-Cr-Ti alloys, two methods were used to estimate  $\gamma_{us}$ . In the first method, the equation given by Rice for calculating USE was used, which is [4]

$$\gamma_{us} = \frac{\mu b^2}{2\pi^2 d} \quad (1)$$

where  $b$  is the Burgers vector and  $d$  is the planar separation distance. Values of the Burgers vector and planar separation distance for the Nb-Cr-Ti alloys were determined from the lattice parameter [2]. The parameter  $\mu$  is usually the shear modulus, but Rice used the shear modulus in the Burgers vector direction [111], leading to  $\mu_{\text{slip}} = (c_{11} - c_{12} + c_{44})/3$ . This factor ( $\mu_{\text{slip}}$ ) was computed from estimates of the elastic compliance  $c_{ij}$  made for each alloy [36]. The surface energies were estimated using the method proposed by Reynolds et al., [37] on the basis of the melting temperature and lattice constant. Reynolds, et al, [37] used values of surface energy derived by others, some of which may have been near the melting point. Nonetheless, surface energy estimates based on the Reynolds correlation are applicable to ambient temperature since surface energy does not change much with temperature. On the other hand, the Reynolds correlation was derived using pure elements, not alloys. As a result, there is likely to be error in the value of the surface energy computed for alloys using this method, but no other method was

found to make this estimate. The application of the Reynolds correlation to alloys is valid as long as changes in the surface energy due to alloying are reflected as changes in the melting point of the alloys. Melting temperatures for the alloys were estimated from the work of Thoma [38]. Values of  $\mu_{\text{slip}}$ ,  $b$ ,  $\gamma_s$ , and  $\gamma_{\text{us}}$  for slip on the (110) plane are listed in Table II.

In the second method, a quantum mechanics approach was used to estimate the unstable stacking energy for these alloys using a three-dimensional cluster of 288 atoms embedded in a crystal of approximately 7000 atoms to provide boundary conditions for the cluster. The effect of grain boundaries was not considered in the cluster model. Wave functions for the  $s$  and  $d$  bonding electrons of each of the elements of an alloy were combined to compute the electronic energy of the cluster. Half the cluster was then moved relative to the other half by  $b = \frac{a}{2}[111]$ ,

and the energy was again computed. The difference in the two energies is denoted as  $\gamma_{\text{us}}^*$ , the value of  $\gamma_{\text{us}}$  determined from the cluster computation [39]. Computed  $\gamma_{\text{us}}^*$  values for slip on the (110) and (112) planes are listed in Table II where they may be compared to those calculated using Rice's equation, Eq. 1. For (110) slip, the USE from the cluster model and Rice's estimate are in reasonable agreement, with  $\gamma_{\text{us}} \approx 1.6\gamma_{\text{us}}^*$ . However, for slip on the (112) plane, there is a large difference between  $\gamma_{\text{us}}$  and  $\gamma_{\text{us}}^*$  with  $\gamma_{\text{us}} \approx 5\gamma_{\text{us}}^*$ . All the results for  $\gamma_{\text{us}}$  are presented as a function of Ti content in Fig. 4, which also includes the computed Peierls-Nabarro barrier energy,  $U_{\text{P-N}}$ , for comparison, since this factor may also be thought of as a measure of the same thing. An important observation in Table II is that for slip on both the (110) and (112) planes, increasing the Ti content reduces both  $\gamma_s$  and  $\gamma_{\text{us}}$  leading to a slight increase in  $\gamma_s/\gamma_{\text{us}}$  in all but one case ((110) slip in Alloy A). This result may be interpreted as indicating that alloying increases the ease by which dislocations may be generated at a crack tip.

The calculated values of the  $\gamma_s/\gamma_{\text{us}}$  ratio based on Rice's estimate range from 2.66 to 3.10 for the (110) plane and from 1.55 to 1.81 for the (112) plane. On the other hand, the calculated  $\gamma_s/\gamma_{\text{us}}^*$  values based on the cluster model range from 3.66 to 6.36 for the (110) plane and from 5.90 to 9.96 for the (112) plane. According to Rice's analysis, dislocation motion will precede cleavage fracture when  $\gamma_s/\gamma_{\text{us}} > 6.3$  for mode I loading and when  $\gamma_s/\gamma_{\text{us}} > 3.5$  for mixed mode I and II loading. Using these criteria, cleavage fracture on the (110) and (112) planes is expected on the basis of the  $\gamma_s/\gamma_{\text{us}}$  values (Rice's estimate), while ductile fracture is expected according to the  $\gamma_s/\gamma_{\text{us}}^*$  values (cluster model). Thus, neither the  $\gamma_s/\gamma_{\text{us}}$  nor the  $\gamma_s/\gamma_{\text{us}}^*$  values appear to provide an obvious explanation for the high toughness observed in the alloys containing a high Ti content. The discrepancies between the Rice estimate and the cluster model might be partly due to the approximate nature of both methods and perhaps partly due to the fact that the Nb-Cr-Ti alloys might lie at the boundary between a truly brittle and a true ductile material. An alternate interpretation, which is adopted here, is that the cluster calculation gives reasonable estimates of the USE, but dislocation nucleation at the crack tip, which the USE is presumed to measure, is not the limiting step in the fracture process. Because of this rationale, the influence of Ti addition on the P-N energy and stress in the Nb-Cr-Ti alloys has been examined as a function of Ti content.

## B. The Peierls-Nabarro Barrier Energy and Stress

In the absence of thermal activation, the minimum stress required to move a dislocation rigidly and irreversibly through a periodic lattice is the Peierls-Nabarro (P-N) or the Peierls stress. The P-N stress can therefore be viewed as the maximum resistance of the discrete lattice to dislocation motion and used as a measure of dislocation mobility. Calculation of the lattice resistance was first made by Peierls [5] and Nabarro [6], with subsequent modifications by a number of investigators [40-42], with the most recent refinement by Wang [43,44]. For isotropic materials, the P-N stress in shear,  $\tau_p$ , is given by [44]

$$\tau_p = \frac{\mu}{f(\nu)} \exp\left\{-\frac{4\pi\zeta}{b}\right\} \quad (2)$$

with

$$\zeta = \frac{d}{2(1-\nu)} \quad (3)$$

where  $\mu$  is the shear modulus,  $d$  is the interatomic spacing between the slip planes, and  $b$  is the Burgers vector; the function  $f(\nu) = 1$  for screw dislocations and  $f(\nu) = (1 - \nu)$  for edge dislocations. The barrier energy, i.e., the P-N energy,  $U_{P-N}$ , is given by Wang [44] as

$$U_{P-N} = \frac{\mu b^3 \zeta^2}{4\pi^2 d} (\Sigma_B + \Sigma_T) \quad (4)$$

where

$$\Sigma_T = \frac{\pi}{b\zeta} \left[ \frac{\sinh\left(\frac{2\pi\zeta}{b}\right)}{\cosh\left(\frac{2\pi\zeta}{b}\right) + \cos\pi\alpha} \right] \quad (5)$$

and

$$\Sigma_B = \frac{\pi}{b\zeta} \left[ \frac{\sinh\left(\frac{2\pi\zeta}{b}\right)}{\cosh\left(\frac{2\pi\zeta}{b}\right) - \cos\pi\alpha} \right] \quad (6)$$

which are functions of  $\zeta$ ,  $b$ , and a variable  $\alpha$  which represents the fraction of the Burgers vector,  $b$ , by which the dislocation is displaced.

For anisotropic solids, the Peierls stress is obtained from Eq. (2) by replacing the pre-exponential factor by the dislocation line energy factor,  $\kappa$ , of a mixed dislocation and the argument in the exponent is replaced by  $2\pi\kappa/bc$ , leading to [45]

$$\tau_p = \kappa \exp\left[-\frac{2\pi d\kappa}{bc}\right] \quad (7)$$

with

$$\kappa = \kappa_{edge} \sin^2 \theta + \kappa_{screw} \cos^2 \theta$$

$$c = \frac{c_{11} - c_{12} + c_{44}}{3} \quad (8)$$

where  $\kappa_{edge}$  and  $\kappa_{screw}$  are the line energies for the edge and screw dislocations, respectively;  $\theta$  is the angle of the dislocation axis and  $b$  for dislocations of mixed character. Calculation of the P-N barrier and energy and stress requires knowledge of the lattice parameter and the elastic properties of the alloy system, i.e., some of the same inputs as those used in computing the unstable stacking energy using Rice's equation [4]. The calculated P-N barrier energies for slip on the (110) and (112) planes are shown in Figure 4 and tabulated in Table II.

## EXPERIMENTAL RESULTS

The K-resistance curve of the tough Nb-Cr-Ti alloy tested in 4.8 mm thick specimens is presented in **Figure 5**, which shows that the material exhibits a high resistance against crack growth. Initiation of crack extension occurs at  $K = 50 \text{ MPa}\sqrt{\text{m}}$ , followed by a rising resistance curve that reaches a K level as high as  $114 \text{ MPa}\sqrt{\text{m}}$  before fracture occurs. The near-tip deformation and fracture processes observed in the tough Nb-Cr-Ti alloy are complicated and vary with the K level. Emission of slip from the crack tip, was first observed at  $K = 50 \text{ MPa}\sqrt{\text{m}}$ , **Figure 6(a)**. The corresponding strain distribution in the near-tip region is presented in **Figure 6(b)**. Further increases in the K level led to continued emission of dislocations from the crack-tip, resulting in extensive crack tip blunting, but without crack extension. Subsequent crystallographic analysis indicated that slip occurred primarily on the (110) plane. This test was stopped at  $K = 55 \text{ MPa}\sqrt{\text{m}}$  when the capacity of the loading stage was exceeded.

The fracture toughness test was repeated using the same specimen with a longer crack length introduced by fatigue. The K-resistance curve of the duplicate test is presented in **Figure 5**. As observed previously, there was substantial crack-tip blunting due to emission of dislocations deformation at the crack tip. At  $K = 82 \text{ MPa}\sqrt{\text{m}}$ , a small extension of the crack occurred, identified as being on the (011) zone, **Figure 7(a)**. The emission of dislocations (as evidenced by slip traces) on three inclined slip planes from the crack-tip, however, prevented the further propagation of this crack, as shown in **Figure 7(b)**. The slip planes were identified as being in the (101), (211), and (121) zones. The slip planes in the (211) and (121) zones were probably (211) and (121) because they were the only slip planes within those zones.

Dislocation emission from the crack tip, as implied by the evidence of the slip traces, facilitated extensive crack tip blunting and suppressed further extension of the main crack. Instead, crack extension occurred at  $K = 98 \text{ MPa}\sqrt{\text{m}}$  by decohesion of a grain boundary located ahead of the crack tip. This resulted in the formation of an intact ligament between the grain boundary microcrack and the previous main crack tip. A further increase in the K level led to plastic fracture of the ligament and extensive blunting of the grain boundary crack due to crack-tip slip (or dislocation) emission, as shown in **Figure 8**. At this point, a fairly large process zone had developed ahead of the crack tip due to non-tip plastic deformation, as shown in **Figure 9**, which shows many microcracks residing within the process zone. Detailed examination of these microcracks indicated that most were grain boundary cracks, but some were slipband cracks and

slip-induced cleavage cracks. As reported earlier [1], the slipband cracks were formed as the result of decohesion of localized slipbands along the active slip planes, which, in turn, led to cleavage crack formation via the Stroh mechanism [28]. Experimental evidence of the Stroh mechanism was presented earlier in Figure 5 of Ref. [1], which shows a series of micrographs depicting the formation of a localized slipband at a crack tip, decohesion along the slipband, and the formation of a cleavage crack ahead of the decohered slipband crack at the Stroh's angle [28]. As an illustration, **Figure 10(a)** shows a slipband crack formed by decohesion along an active (112) plane in the same alloy, which was reported earlier [1]. Impingement of a slipband or a shear crack on the grain boundary led to slip-induced cleavage in a neighboring grain, **Figure 10(b)**. In both cases, some slipbands were found to have fractured and showed the presence of small, shallow, poorly formed voids within the slipbands. Void nucleation, growth, and coalescence within the planar slipbands resulted in the formation of dimples on fracture surfaces which failed at extremely high stress intensity factors ( $>114 \text{ MPa}\sqrt{\text{m}}$ ). The final fracture surfaces, therefore, contained a mixture of slipband decohesion, grain boundary cracking, slip-induced cleavage, and dimpled fracture, which gave a brittle fracture appearance when viewed at a low magnification because of the featureless facets associated with slipband decohesion, grain boundary cracking, and cleavage. Dimpled fracture in this alloy, which constituted only a small fraction of the fracture surfaces only and had little influence on the fracture toughness, involved microvoid nucleation and growth along planar slipbands. Details of this fracture process are the subject of another paper [46].

## CALCULATED P-N STRESSES

Values of the P-N stress for [111] edge and screw dislocations on both the (110) and (112) planes were calculated as a function of Ti content, and the results are presented in **Figure 11**. For (110) and (112) screw dislocations, the P-N stress decreases slightly with increasing Ti content, but the decrease is small so that the P-N stress appears to be a constant in a log-log plot. In contrast, the P-N stress values for edge dislocations on the (110) and (112) planes show significant decreases with increasing Ti content when the Ti addition is larger than 18 a/o%. The most important result is thought to be the large decrease in the P-N stresses of edge dislocations at high Ti contents. ( $> 30 \text{ a/o\%}$ ). The P-N stresses are higher for screw dislocations when compared to edge dislocations. For example, the P-N stress is considerably higher for the screw dislocation on the (112) plane, when compared to edge dislocations on the (112) plane and to edge and screw dislocations on the (110) plane. This result indicates that cross slip would be relatively easy on the (110) plane, but is expected to be quite difficult on the (112) plane. Thus, planar slip on the (112) plane would be expected.

## DISCUSSION

Recent Work has indicated that the addition Ti improves the fracture toughness of Nb-Al-Ti alloys. A direct comparison of the fracture toughness of Nb-Cr-Ti and Nb-Al-Ti alloys was made earlier [2]. Two important differences exist between the Nb-Cr-Ti and Nb-Al-Ti systems, which are that (1) the Nb-Al-Ti solid solution is ordered while the Nb-Cr-Ti system is not, and (2) Al is not a transition element while Cr is. An ordered structure has not been considered in the current cluster model or the computation methods for the P-N energy and stress. Applying the

cluster model to the Nb-Al-Ti system also requires bonding of the P electrons; such a method is subject of current research. For these reasons, a comparison of the Nb-Cr-Ti and Nb-Al-Ti systems is premature and not very meaningful at this time.

The fracture toughness values in Table I were obtained under the plane strain condition except for that of Alloy D. Because of the high toughness, the ASTM thickness criterion for plane strain fracture was not satisfied at the peak loads in Alloy D. On the other hand, the onset of crack extension in Alloy D occurred at 34 to 55 MPa $\sqrt{m}$ . The plane strain condition was met at 34 MPa $\sqrt{m}$ . Thus, the plane strain initiation toughness of Alloy D is 34 MPa $\sqrt{m}$ , which is still significantly higher than the fracture toughness of alloys with lower Ti contents. After the initiation of crack extension, substantial crack tip deformation led to a resistance-curve behavior before final fracture occurred. Neither the formation of shear lips nor a reduction in specimen thickness was observed. Thus, while fracture of the tough Nb-Cr-Ti alloy was not fully plane strain, it was not truly plane stress either. The ability of Alloy D to transit from plane strain fracture to a less constrained fracture appears to derive from the alloy's intrinsic ductility, which allowed the development of a large crack-tip plastic zone.

The number of grains per specimen thickness was small ( $\approx 3$ ) in Alloy D, which is too few to satisfy the condition for polycrystalline behavior. Nonetheless, the fracture toughness value remains valid and its relationship to the Ti addition and crack-tip slip behavior is meaningful. Neither the specimen thickness nor the number of grains per specimen thickness provides an explanation for the beneficial effects of Ti addition on fracture toughness. Instead, it appears that the origin to the observed Ti effects on fracture toughness is in the influence of Ti addition on the crack-tip slip process.

#### A. Slip Emission from the Crack Tip

A significant observation made in this study is the extensive slip emission, which implies dislocation emission, from the crack tip in the tough Nb-Cr-Ti alloy. Emission of slip from the crack can be dictated either by the nucleation of dislocations at the crack tip or the propagation of dislocations away from the crack tip. A measure of the barrier to dislocation nucleation from the crack tip is the USE [4], while the appropriate measures for dislocation mobility are the P-N barrier energy and the P-N stress [5,6]. Results of the cluster atom calculation indicate that the values of the USE [4] for the Nb-Cr-Ti alloys are low compared to the surface energy for (111) edge dislocations on the (110) and (112) planes, suggesting that crack-tip nucleation of dislocations on two these slip systems should be relatively easy. The insensitivity of the USE to Ti content indicates that the dislocation nucleation process is approximately the same in the various Nb-Cr-Ti alloys. The nucleated dislocations, however, must overcome the P-N barrier in order to propagate slip away from the crack tip. On this basis, it can be concluded that dislocation emission from the crack tip in the Nb-Cr-Ti alloys is controlled by the mobility rather than the nucleation of dislocations.

The calculated P-N energy and stress values are reduced when the Ti content is greater than 18%, Figures 4 and 11. The implication is that the dislocation mobility is enhanced by Ti addition in excess of 18%. The extensive slip emission observed in the tough Nb-Cr-Ti alloys

can, therefore, be attributed to an increased dislocation mobility due to the reduction in the P-N barrier energy and stress values for edge dislocations on the (110) and (112) planes. The high P-N barrier energy and stress values indicate that screw dislocations on the (112) plane are not easily mobilized. This result implies that (112) slip will be very planar, while (110) slip is likely to be wavy because of a greater propensity for cross-slip. Both wavy (110) and planar (112) slip are indeed observed in the Nb-Cr-Ti alloys, as shown in Figures 6 and 7. Planar slip on (112) planes also led to slipband decohesion and induced cleavage crack nucleation [1]; both are consistent with the notion of difficult cross-slip as represented by a high P-N stress for screw dislocations on (112) planes.

### B. Source of Fracture Toughness

It is evident from Figures 5 and 6 that extensive dislocation emission from the crack tip contributes to the high fracture resistance observed in the tough Nb-Cr-Ti alloys. Dislocation emission results in not only extensive blunting of the crack tip, but also prevents the propagation of a cleavage crack. Crack-tip shielding due to dislocations moving away from a crack tip has been modeled by Hirsch and Roberts [23]. Their analysis showed that the local stress intensity at the crack tip,  $K_{tip}$ , is lower than the applied stress intensity,  $K$ , because of the shielding effect of the emitted dislocations and their corresponding image dislocations. The microscopically-shielded Griffith criterion model proposed by Gerberich and coworkers [18] predicts the fracture toughness to increase with  $\exp(E_{[hkl]}\gamma_s/\sigma_{ys})$ , where  $E_{[hkl]}$  is the elastic modulus in the  $[hkl]$  direction,  $\gamma_s$  is the surface energy, and  $\sigma_{ys}$  is the yield stress. This fracture criterion does not agree with experimental observation for the Nb-Cr-Ti alloys because the fracture toughness does not increase with decreasing yield stress, Table I.

Correlation of fracture toughness and USE revealed the absence of an obvious or simple relation. In contrast, correlation between fracture toughness and the P-N energy indicated that the fracture toughness of Nb-Cr-Ti alloys generally increases with decreasing values of the P-N energy for both (110) and (112) slip. This is illustrated in Figures 12 (a) and (b), which shows plots of fracture toughness values as a function of the P-N energy for (110) and (112) slip, respectively. Plane strain fracture toughness values are shown in Figure 12 together with fracture toughness values for the two cases for which the plane strain condition was not satisfied (labeled as non-plane strain). The correlation of increasing plane strain fracture toughness to decreasing P-N energy is self-evident in Figure 12. Since dislocation mobility decreases with increasing P-N energy, the result suggests that the enhancement of fracture toughness in Nb-Cr-Ti alloys is the consequence of increasing dislocation mobility and, hence, dislocation emission from the crack tip. It should also be noted that in Figure 12, the plane strain fracture toughness (23 MPa $\sqrt{m}$ ) of Alloy F was obtained on a commercial material that contained a relatively high interstitial content [47], while the higher fracture toughness value (65 MPa $\sqrt{m}$ ) was obtained on a laboratory sheet material with a lower interstitial content [48].

### C. The Effect of Alloying on Fracture Toughness

An alternative approach to modeling the effect of dislocation mobility on fracture toughness is to consider how the work expended by the applied load is spent in creating crack

surface energy and in dissipating plastic work at the crack tip. A fracture analysis based on the J-integral, which is presented in the appendix, gives

$$J_{IC} = W_o h e^{-\frac{\Delta F - v^* \tau}{kT}} \quad (9)$$

where  $W_o$  is given in Eq. (A8), and  $h$  is the size of the process zone. This analysis is based on the thermal activation of dislocations past the P-N barrier and does not consider, explicitly, the solute hardening present in alloys. For the transition metal alloys in general, and the Nb-Cr-Ti alloys in particular, solute strengthening provides a large component of the measured flow stress, i.e.,

$$\tau_{applied} = \tau_{P-N} + \tau_{solution \ strengthening} \quad (10)$$

Thus, the stress needed to activate dislocations past P-N barriers is only a fraction of the remotely applied stress.

Another factor to be considered is that dislocation motion is dependent disproportionately on the stress needed to activate edge dislocations because screw dislocations move by the motion of kinks that are of edge orientation, or of mixed dislocation orientation that has some edge character [49]. When alloying allows edge dislocations to move at a lower stress, screw dislocations also become easier to move. However, only when the P-N stress of screw dislocations is lowered does cross-slip become easier. Since the P-N stress of the (112) screw is not lowered significantly by Ti addition, cross-slip on the (112) plane remains difficult at high Ti contents, hence explaining the planar (112) slip in those materials.

The fracture behavior of the Nb-Cr-Ti alloys can be rationalized qualitatively on the basis of the critical fracture stress criteria postulated in the RKR theory [30] and using Eq. (9) and the computed P-N barrier energy and stress values. According to the RKR theory, cleavage fracture occurs when the stress at a characteristic distance ahead of the crack tip reaches the cleavage fracture stress [30]. When the Peierls energy is high, the exponent in Eq. (9) is small. For a large P-N stress, Eq. (7) implies that the applied stress must also be large. In other words, the applied stress reaches a critical level of the cleavage stress [30] before sufficient thermal activation can occur to allow dislocations to move. The value of the cleavage fracture stress may vary with crystallographic plane and grain boundary. This condition is illustrated in **Fig. 13** as point "p." This situation is made worse because in this circumstance the P-N stress is also high, as illustrated in **Fig. 13(b)**, allowing few dislocations to move, causing  $v^*$  to be small. The consequence of this combination of high P-N stress and low  $v^*$  is that cleavage crack growth occurs with little plastic dissipation, **Fig. 13(c)**. This is the condition found for Nb-Cr alloys with little Ti (alloy A). For intermediate values of the P-N barrier energy and P-N stress magnitude, some of the dislocations that are emitted from the crack tip move along various slip planes and plastic work occurs, particularly at low strain rates. This condition, applicable to Nb-Cr alloys with intermediate Ti content (alloys B and C) is shown in Figs. 11 as point "q."

A ductile fracture behavior results when the P-N barrier energy and stress values are low. Under this circumstance, dislocation emission from the crack tip, which is easy, suppresses cleavage crack propagation and shifts the fracture process from the crack tip to a region further ahead of and away from the crack tip. This shift from a crack tip to a non-tip fracture process increases the size of the slip/fracture process zone [50] and the amount of the plastic dissipation

accompanies fracture increases accordingly. A combination of fracture modes (slipband decohesion, grain boundary cracking, and dimpled fracture) can occur in the presence of cleavage when the near-tip stress exceeds the critical stress level for cleavage after a substantial amount of plastic flow. The fracture behavior of the tough Nb-Cr-Ti alloy with 37% Ti (Alloy D) appears to fall into this category. The experimental results from Alloy D indicate that there are two possible cleavage mechanisms; one that results from an extension of the crack tip, Fig 7(a), and the other as a consequence of non-crack tip deformation, Fig. 9 and 10(b). When the cleavage crack nucleation process is suppressed by crack tip deformation, the process zone (h in Eq. 9) and the plastic zone sizes increase also, thereby further increasing the fracture toughness. Also, the fracture process can be shifted to non-crack tip events that include slipband and grain boundary decohesion. Fracture toughness in this alloy would have been even higher had these non-crack tip processes been suppressed by microstructural manipulation, such as by grain size reduction. If the critical cleavage stress is never exceeded, then a pure (100%) ductile fracture behavior results, as illustrated by point "r" in Figure 13. This fracture behavior has not been observed in the Nb-Cr-Ti alloys since cleavage is always present even in the toughest alloy (Alloy D). A possible explanation for the lack of extensive ductile dimpled fracture in the tough alloy is that the critical cleavage fracture stress is met before void nucleation, growth and coalescence can be fully developed. The absence of hard particles, which act as void nucleation sites, might have also contributed to delaying the onset of dimpled fracture.

The use of a critical stress as a failure criterion for cleavage is justified on the basis of prior work by RKR [30], who demonstrated that a critical cleavage stress criterion is applicable for predicting the fracture toughness of steels. The result of this paper suggests that the critical stress criterion is consistent with the experimental observations and P-N energy and stress calculations for Nb-Cr-Ti alloys. Conceptually, the critical cleavage stress criterion is equivalent to the cleavage fracture surface postulated by Gerberich, et al. [18]. Furthermore, Eq. (9) can be considered as the limiting condition where the cleavage surface intersects the dislocation emission surface. In the case of the tough Nb-Cr-Ti alloy, the dislocation emission surface is dictated by the mobility of dislocation, and not by the nucleation of dislocations at the crack tip.

Most, if not all, cleavage fracture observed in the Nb-Cr-Ti alloys occurs after substantial dislocation emission from the crack tip has occurred; hence, this fracture falls into the category of Cleavage III [7]. The occurrence of non-crack tip cleavage and slipband and grain boundary decohesion can be explained on the basis of the relaxation of elastic stresses and constraint that develops in the region ahead of a blunted crack. Loading a sharp crack tip results in triaxial stresses that increase the stress near the crack tip to levels approaching the cleavage stress. Since dislocation nucleation is not the limiting step, lowering the P-N barrier stress and P-N stress allows dislocations to leave the crack tip, causing plastic relaxation of the constraint, which lowers the triaxial stress state, thereby preventing stresses from reaching cleavage stress level. Non-crack tip cleavage, such as that illustrated in Fig. 10(b), occurs because the cleavage stress is exceeded in the grain or grain boundaries that are highly stressed possibly due to the Stroh mechanism [28], or have low strength due to an unfavorable misorientation.

The strain rate sensitivity of the brittle-to-ductile transition in transition metal alloys can be understood in terms of the changes in P-N barrier and P-N stress as illustrated in Fig. 13, and

this is supported by the experimental observations of crack tip deformation herein presented. Cleavage on the (100) plane is suppressed by crack tip deformation on the (110) plane, and slipband decohesion on the (112) plane. As Ti content is increased, deformation on the (110) plane becomes easier as a consequence of the lower P-N barrier energy and P-N stress, thereby blunting the crack tip, while decohesion of the (112) plane occurs as a consequence of the higher values of P-N barrier energy and P-N stress relative to the (110) plane.

Based on the previous discussion, it is evident that Ti addition to Nb-Cr alloys results in large improvements in fracture toughness that are probably the result of reductions in the P-N barrier energy and P-N stresses. Shown in **Fig. 14** is a correlation of the alloy Ti content to (a) the number of d+s bonding electrons/atom calculated based on the number of d and s electrons in individual elements in the alloys; (b) the P-N energy barrier for (110) dislocations; (c) and the elastic anisotropy factor  $A = 2c_{44}/(c_{11}-c_{12})$  ( $c_{ij}$  being the elastic compliances). This correlation reveals two important findings: (1) there is a parallel decrease in the number of d+s electrons per atom and the P-N barrier energy with increasing Ti content, and (2) the alloys become increasingly elastically isotropic ( $A = 1$ ) with Ti addition. Lowering the number of d+s electrons results in a weakening of the atomic bonding of the alloys, particularly the covalent bonds, which decreases both the P-N barrier energy and the P-N stresses, especially the P-N stress for edge dislocations on the (110) plane. The correlation of fracture toughness to the number of d+s electrons in Figure 3 can, thus, be explained on the basis of the reduction of the Peierls Energy with increasing numbers of d+s electrons per atom in the Nb-Cr-Ti alloys. With regard to the influence of the A parameter on  $U_{P-N}$ , it must be remembered that screw dislocations move mostly by the action of kinks that are either edge dislocations or are mixed dislocations of partial edge character [49]. Increasing isotropy enhances dislocation motion as the P-N barrier energy of edge dislocations is reduced by increasing elastic isotropy. The net result is that more dislocations that are emitted from the crack tip move into the plastic zone as the Ti content is increased, leading to increased fracture toughness when the elastic anisotropy factor approaches unity (i.e., isotropy).

In summary, correlations of fracture toughness and Ti content to the number of d+s electrons, the P-N barrier energy, and the elastic anisotropy parameter, shown in Figures 3, 12, and 14, can be understood on the basis that Ti addition to Nb-Cr alloys changes the atomic bonding of the alloys, which, in turn, alters the elastic moduli, the P-N barrier energy, the dislocation mobility, the crack-tip slip process, and eventually the fracture properties. These various phenomena are all interconnected as they are influenced primarily by the underlying atomic bonding forces, which vary with Ti addition in the alloys.

## CONCLUSIONS

1. The fracture toughness of Nb-Cr alloys is greatly enhanced by additions of Ti, because it leads to extensive crack tip deformation that is the result of both the emission and motion of dislocations from the crack tip.
2. Brittle cleavage crack propagation (Cleavage I) is suppressed in Nb-Cr-Ti alloys by a sufficient Ti addition, because of the extensive dislocation emission from the crack tip. This results in a change of fracture morphology from brittle cleavage (Cleavage I) to a combination of non-tip slip-induced cleavage (Cleavage III), slipband decohesion, grain boundary cracking, and dimpled fracture.
3. The propensity for nucleation for dislocations from the crack tip, as measured by the unstable stacking energy, is not altered very much by Ti additions to Nb-Cr alloys. Thus, the fracture characteristics of these alloys are not controlled by changes in crack tip dislocation nucleation characteristics. Crack-tip dislocation motion is enhanced by a high Ti content, because the P-N energy and stress are reduced.
4. The computed values of the Peierls-Nabarro barrier energy and the Peierls-Nabarro stress for both edge and screw dislocations are lowered considerably by Ti additions. The P-N barrier energy of the least tough alloy is five times greater than that for the highest toughness alloy, and the P-N stress for the (110) edge for the toughest alloy is about 1/5 that for the least tough alloy.
5. Slip band decohesion on the (112) can be attributed to the high Peierls-Nabarro barrier energy and stresses.
6. The brittle-to-ductile transition can be rationalized by a crack-tip dislocation shielding process that results in a reduction of the triaxial stress state at the crack tip, thereby limiting the maximum stress to below the cleavage stress value.

## REFERENCES

1. K.S. Chan: *Metall. Mater. Trans. A*, 1996, vol. 27A, pp. 2518-31.
2. D.L. Davidson, K.S. Chan, and D.L. Anton: *Metall. Mater Trans A*, 1996, vol. 27A, pp. 3007-18.
3. K.S. Chan and D.L. Davidson: *JOM*, 1996, vol. 48, (9), pp.62-68.
4. J.R. Rice: *J. Mech. Phys. Solids*, 1992, vol. 40, pp. 239-271.
5. R.E. Peierls: *Proc. Phys. Soc.*, 1940, vol. 52, pp. 34-37.
6. F.R.N. Nabarro: *Proc. Phys. Soc.*, 1947, vol. 59, pp. 236-394.
7. M.F. Ashby: *Advances in Applied Mechanics*, 1983, vol. 23, pp. 117-177.
8. W.R. Tyson, R.A. Ayres, and D.F. Stein: *Acta Metall.*, 1973, vol. 21, pp. 621-627.
9. J.R. Rice and R.M. Thomson: *Phil. Mag.*, 1974, vol. 29, pp. 73-97.
10. V. Shastry and P.M. Anderson: *Phil. Mag. A*, 1997, vol. 75, pp. 771-789.
11. T.C. Wang: *Phil. Mag. A*, 1998, vol. 77, pp. 31-53.
12. D.M. Lipkin and G.E. Beltz: *Acta Mater.*, 1996, vol. 44, pp. 1287-91.
13. G.E. Beltz, J.R. Rice, C.F. Shih, and L. Xia: *Acta Mater.*, 1996, vol. 44, pp. 3943-54.
14. W. Zielinski, M.J. Lii, and W.W. Gerberich: *Acta Metall. Mater.*, 1992, vol. 40, pp. 2861-71.
15. H. Huang and W.W. Gerberich: *Acta Metall. Mater.*, 1992, vol. 40, pp. 2873-81.
16. P.G. Marsh, W. Zielinski, H. Huang, and W.W. Gerberich: *Acta Metall. Mater.*, 1992, vol. 40, pp. 2883-94.
17. Y. Katz, R.R. Keller, H. Huang, and W.W. Gerberich: *Metall. Trans. A*, 1993, vol. 24A, pp. 343-350.
18. W.W. Gerberich, H. Huang, W. Zielinski and P.G. Marsh: *Metall. Trans. A*, 1993, vol. 24A, pp. 535-543.
19. P.G. Marsh and W.W. Gerberich: *Acta Metall. Mater.*, 1994, vol. 42, pp. 613-619.

20. H. Huang and W.W. Gerberch: *Acta Metall. Mater.*, 1994, vol. 42, pp. 639-647.
21. P.B. Hirsch and S.G. Roberts: *Phil. Mag. A*, 1991, vol. 64, pp. 55-80
22. S.G. Roberts and A.S. Booth: *Acta Meter.*, 1997, vol. 45, pp. 1045-53.
23. P.B. Hirsch and S.G. Roberts: Cleavage Fracture, Proceedings of George R. Irwin Symposium, Kwai S. Chan, ed., TMS, Warrendale, PA, 1997, pp. 137-145.
24. I.H. Lin and R. Thomson: *Acta Metall.*, 1980, vol. 34, pp. 187-206.
25. A.A. Griffith: *Phil Trans. R.. Soc.*, London A, 1920, vol. 221, pp. 163-197.
26. K.S. Chan: Micromechanics of Advanced Materials, S.N.G. Chu, P.K. Liaw, K.S. Chan, R.J. Arsenault, K. Sadananda, K.S. Chan, W.W. Gerberch, C.C. Chau, and T.M. Chung, eds., TMS, Warrendale, PA, 1995, pp. 113-120.
27. K.S. Chan: Cleavage Fracture, Proceedings of George R. Irwin Symposium, Kwai S. Chan, ed., TMS, Warrendale, PA, 1997, pp. 207-220.
28. A.N. Stroh: *Proc. Roy. Soc. A.*, 1954, vol. 223, pp. 597-606.
29. M.G. Medira, R. Goetz, D.M. Dimiduk, and J.J. Lewandowski: *Metall. Trans. A*, 1995, vol. 26A, pp. 1767-1776.
30. R.O. Ritchie, J.F. Knott and J.R. Rice: *Intl. J. Mech. Phys. Solids*, vol. 21, pp. 395-410.
31. A.V. Samant and J.J. Lewandowski: *Metall. Trans. A*, 1997, vol. 28A, pp. 389-399.
32. B.D. Cuthill: Elements of X-Ray Diffraction, Addison-Wesley, 1967, pp. 215-229.
33. D.L. Davidson and A. Nagy: *J. Phys. E*, 1978 vol. 11, pp. 207-10.
34. E.A. Franke, D. Wenzel, and D.L. Davidson: *Rev. Sci. Instrum.*, 1991, vol. 62, pp. 1270-79.
35. J.W. Christian and V. Vitek: *Rep. Prog. Phys.*, 1970, vol. 33, pp. 307-411.
36. D.L. Davidson: Transition Element Alloys: Elastic Properties and Peierls-Nabarro Stresses, manuscript in preparation, 1998.
37. C.L. Reynolds, P.R. Couchman, and F.E. Karasz: *Phil. Mag.*, 1976, vol. 34, pp. 659-661.
38. D.J. Thoma: Ph.D. Dissertation, University of Wisconsin, 1992, available from university microfilms.

39. D.L. Davidson and R.E. Beisner: Computation of the Unstable Stacking Energy for Transition Element Alloys, unpublished work, SwRI, 1997.
40. A.J. Foreman, M.A. Jaswon, and J.K. Wood: *Proc. Phys. Soc.*, 1951, vol. 64A, pp. 156-163.
41. H.B. Huntington: *Proc. Phys. Soc.*, 1955, vol. 68B, pp. 1043-1048.
42. K. Ohsawa, H. Koizumi, H.O.K. Kirchner, and T. Suzuki: *Phil. Mag. A*, 1994, vol. 69A, pp. 171-181.
43. J.N. Wang: *Mat. Sci. & Eng. A*, 1996, vol. A206, pp. 259-269.
44. J.N. Wang: *Acta Mater.*, 1996, vol. 44, pp. 1541-1546.
45. A.J.E. Foreman: *Acta Metall.*, 1955, vol. 3, pp. 322-330.
46. K.S. Chan and D.L. Davidson: *Metall. Transactions A*, 1998, (submitted).
47. E.A. Loria: Proceedings of the 2<sup>nd</sup> Intl. Conf. On Heat-Resistance Materials, Gatlinburg, TN, 11-14 September, 1995, pp. 613-619.
48. M.R. Jackson: In Tungsten and Refractory Metals, Proceedings of APMI Conference, edited by A. Bose, MPIF Publications, Princeton, New Jersey, 1994, pp. 657-664.
49. T. Suzuki, H. Koizumi, and H.O.K. Kirchner: *Acta Metall. Mater.*, 1997, vol. 43, pp. 2177-2187.
50. K.S. Chan, M.-Y. He, and J.W. Hutchinson: *Mater. Sci. Eng.*, 1993, vol. A167, pp. 57-64.
51. G.R. Irwin: Fracture Dynamics, ASM, Cleveland, OH, 1948, pp. 147-166.
52. E. Orowan: Welding Journal Res. Sup., 1995, vol. 34(3), pp. 1575-1605.
53. J.R. Rice: *J. Appl. Mech.*, 1968, pp 379-386.
54. G.B. Gibbs, *Physica Status Solidi*, 1965, vol. 10, pp. 507-512.

## APPENDIX

For a crack tip under small-scale yielding, the J-integral at fracture,  $J_{IC}$ , can be considered to be comprised of two terms as given by [51,52]

$$J_{IC} = J_S + J_D \quad (A1)$$

where  $J_s = 2\gamma_s$  is the surface energy term, and  $J_D$  is the plastic work expanded per unit crack extension. By considering a counterclockwise contour around the crack tip surface, it has been shown by Rice that [53]

$$J_D = \sigma\delta = \sigma\epsilon h \quad (A2)$$

where  $\delta$  is the crack-tip opening displacement,  $\epsilon$  is the crack-tip strain, and  $h$  is the size of the crack tip process zone. The process zone is the region of intense deformation surrounding the crack tip.

From the theory of thermally activated dislocation motion, the plastic strain rate for material being deformed at the crack tip is [54]

$$\dot{\gamma} = \dot{\gamma}_o e^{-\Delta G/kT} \quad (A3)$$

$$\Delta G = \Delta F - v^* \tau \quad (A4)$$

where  $F$  is the energy of the intrinsic barrier to dislocation motion, which for the bcc metals is the P-N barrier energy;  $\tau$  is the applied shear stress;  $v^*$  is the activation volume;  $k$  is Boltzmann's constant; and  $T$  is absolute temperature. The pre-exponential factor is [54]

$$\dot{\gamma}_o = NAbv \quad (A5)$$

where  $N$  = number of points per unit volume where activation is occurring,  $A$  = area swept out by the activated dislocation,  $b$  = Burgers vector, and  $v$  = the attempt frequency for dislocation activation, which is proportional to the Debye frequency.

The activation volume is given by  $v^* = b\ell x$ , where  $\ell$  is the length of dislocation line, and  $x$  is the activation distance. If  $\tau = \tau(t)$  or  $x = x(t)$ , then (A3) can be integrated, giving

$$\gamma = \left( \dot{\gamma}_o kTt / \tau b\ell \right) e^{-\frac{\Delta F - v^* \tau}{kT}} \quad (A6)$$

Combining (A2) and (A6) with  $\sigma = \sqrt{3} \tau$  and  $\epsilon = \gamma / \sqrt{3}$  gives for the fracture toughness

$$J_{IC} = W_o h e^{-\frac{\Delta F - v^* \tau}{kT}} \quad (A7)$$

with

$$W_o = \dot{\gamma}_o kTt / bl \quad (A8)$$

From (A2), and (A6) it can be seen that the fracture toughness is strongly influenced by (1) the magnitude of the P-N barrier strength, (2) the activation parameters,  $v^* \tau$ , and (3) assumptions about the size of the process zone,  $h$ . However, fracture toughness is more sensitive to the P-N barrier energy and the activation parameters than to the size of the process zone because  $J$  is linearly proportional to  $h$  (A2) but varies exponentially with the P-N energy and the activation parameters.

Table I. A Summary of the Composition, Fracture Toughness, and Yield Stress of Nb-Cr-Ti Solid Solution Alloys

Alloy	Composition in Atomic Percent	Fracture Toughness (Plane Strain)	Yield Stress
	Nb-Cr-Ti-Al	MPa $\sqrt{m}$	MPa
G	100-0-0-0	12	539.6*
A	81-9-10-0	11	624.8*
B	74-8-18-0	16	594.0*
C	53-16-31-0	27	881.5*
D	50-13-37-0	34, 80 <sup>+</sup>	765.0*
E	40-17-43-0	40	826.2*
F	40-10-40-10	23, 65 <sup>+</sup> [48]	655 [47]

\* Calculated from Vicker hardness values and calibrated by tensile tests.  
+ Non-plane strain

Table II. A Summary of Calculated Values of Shear Modulus ( $\mu_{\text{slip}}$ ) in the Slip Direction, Burgers Vector (b), Peierl Energy (PE) Surface Energy ( $\gamma_s$ ), and unstable stacking energy. The unstable stacking energy value obtained, based on Rice's model (Eq. 1), is reported as  $\gamma_{us}$  and  $\gamma_{us}^*$  is the corresponding value computed from the atomic cluster model.

Alloy	$\mu_{\text{slip}}$ (GPa)	b (Å)	$\gamma_s$ (J/m <sup>2</sup> )	(110)				(112)			
				PE (J/m <sup>2</sup> )	$\gamma_{us}$ (J/m <sup>2</sup> )	$\gamma_{us}^*$ (J/m <sup>2</sup> )	$\frac{\gamma_s}{\gamma_{us}}$	PE (J/m <sup>2</sup> )	$\gamma_{us}$ (J/m <sup>2</sup> )	$\gamma_{us}^*$ (J/m <sup>2</sup> )	$\frac{\gamma_s}{\gamma_{us}}$
G	49.1	2.859	2.42	.322	0.871	0.512	2.78	4.73	.947	1.56	0.410
A	50.4	2.841	2.36	.358	0.888	0.371	2.66	6.36	1.03	1.51	0.237
B	43.8	2.834	2.31	.198	0.770	0.485	3.00	4.76	0.707	1.33	0.260
C	42.8	2.816	2.25	.143	0.747	0.448	3.01	5.02	0.601	1.30	0.255
D	41.4	2.810	2.19	.071	0.721	0.502	3.04	4.36	0.441	1.26	0.292
E	40.0	2.807	2.15	.055	0.696	0.494	3.09	4.35	0.386	1.20	0.310
F	39.6	2.794	2.13	.044	0.686	0.582	3.10	3.66	0.356	1.18	0.320

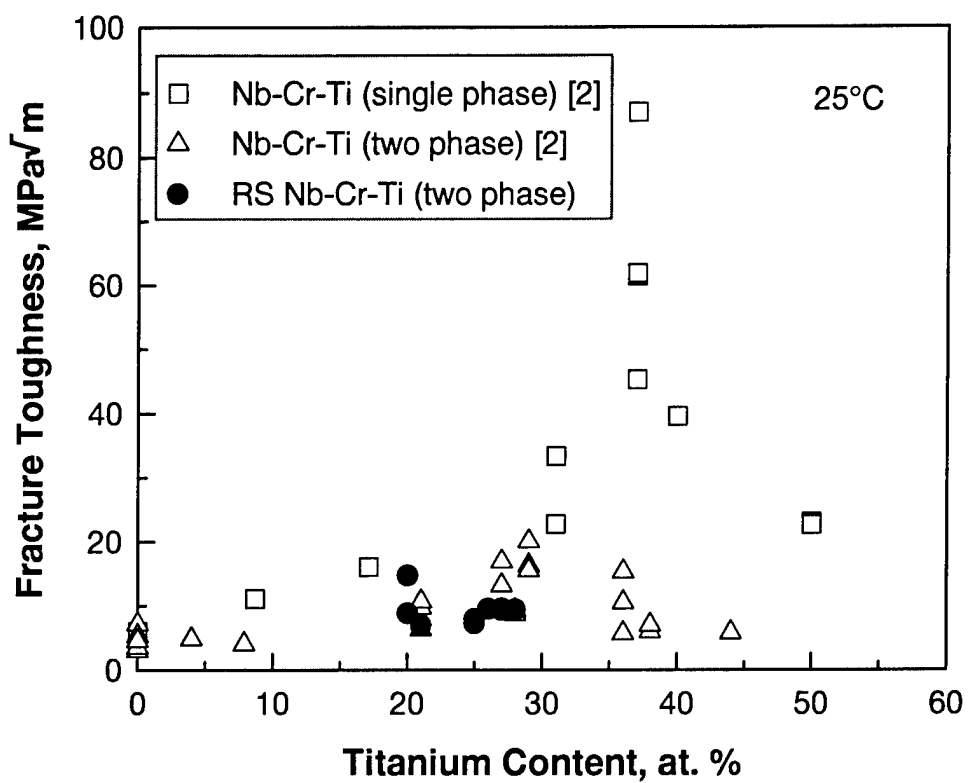
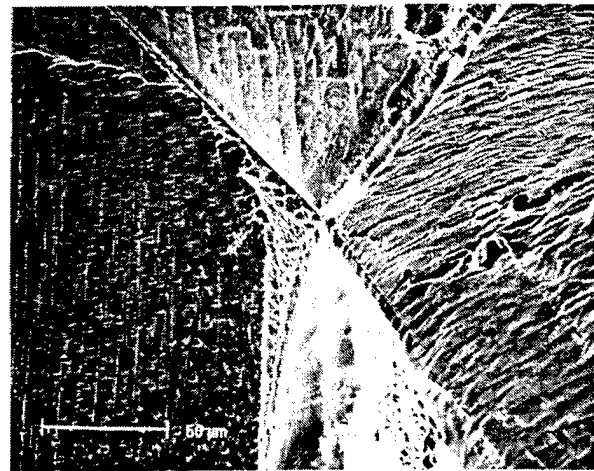


Figure 1. Dependence of fracture toughness of Nb-Cr-Ti solid solution alloys and in-situ composites on Ti content. From Davidson, et al. [2].



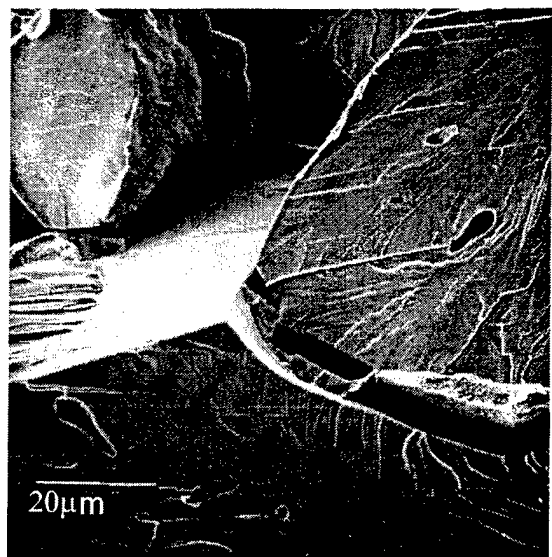
(a).  $K_c = 11 \text{ MPa}\sqrt{\text{m}}$

8.7% Ti



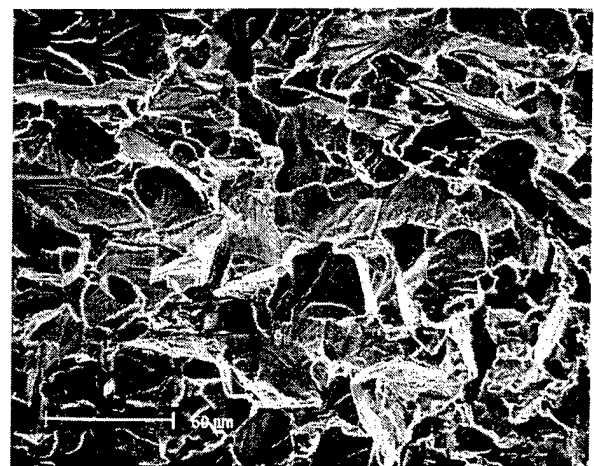
(c).  $K_c = 34 \text{ MPa}\sqrt{\text{m}}$

37% Ti



(b).  $K_c = 16 \text{ MPa}\sqrt{\text{m}}$

17% Ti



(d).  $K_c = 23 \text{ MPa}\sqrt{\text{m}}$

50% Ti

Figure 2. Correlation of fracture toughness and fractographic features with Ti contents: (a) cleavage at  $K_c = 11 \text{ MPa}\sqrt{\text{m}}$  and 8.7% Ti, (b) cleavage at  $K_c = 16 \text{ MPa}\sqrt{\text{m}}$  and 17% Ti, (c) cleavage, slip band decohesion, intergranular and dimpled fracture at  $K_c = 34 \text{ MPa}\sqrt{\text{m}}$  and 37% Ti, and (d) cleavage at  $K_c = 23 \text{ MPa}\sqrt{\text{m}}$  and 50% Ti. All compositions are in atom pct.

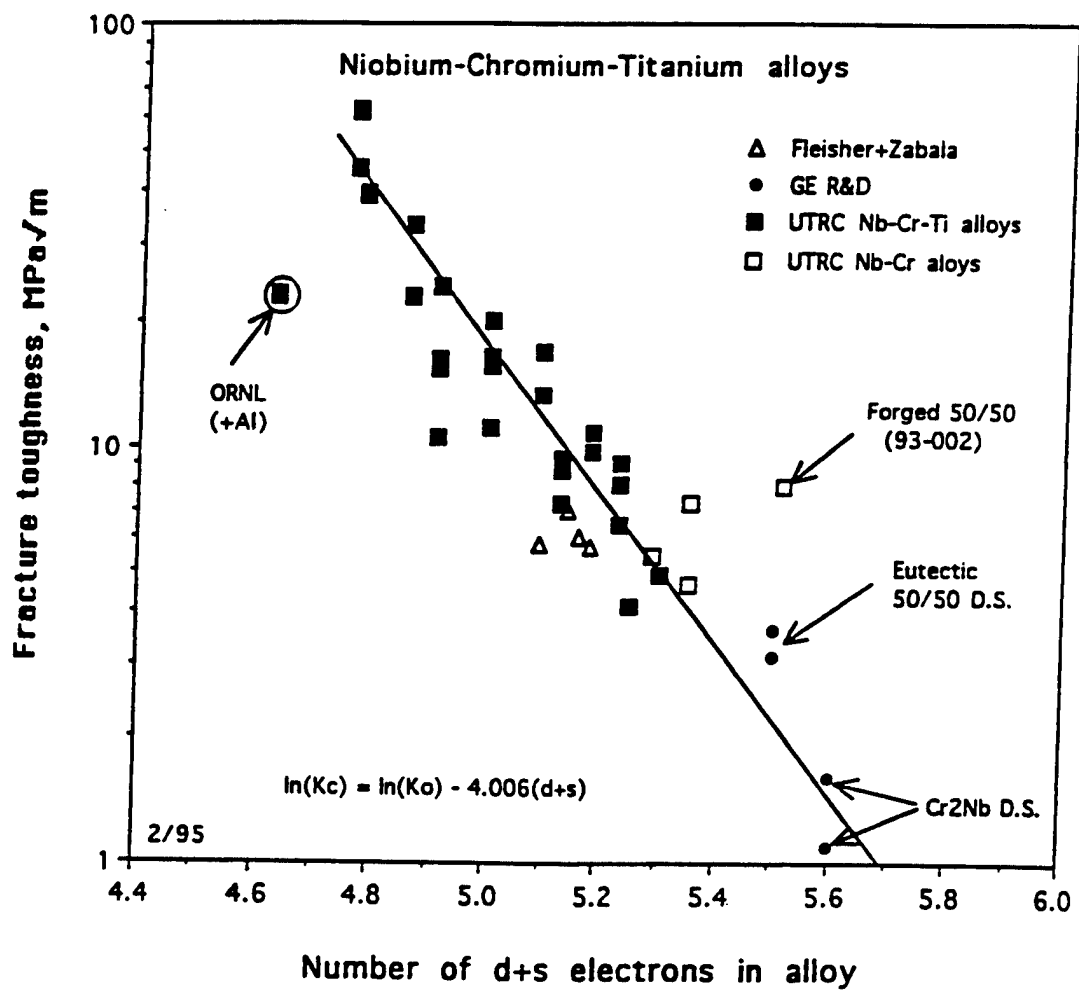


Figure 3. Correlation between fracture toughness and the number of  $d+s$  bonding electrons per atom in the alloys [2].

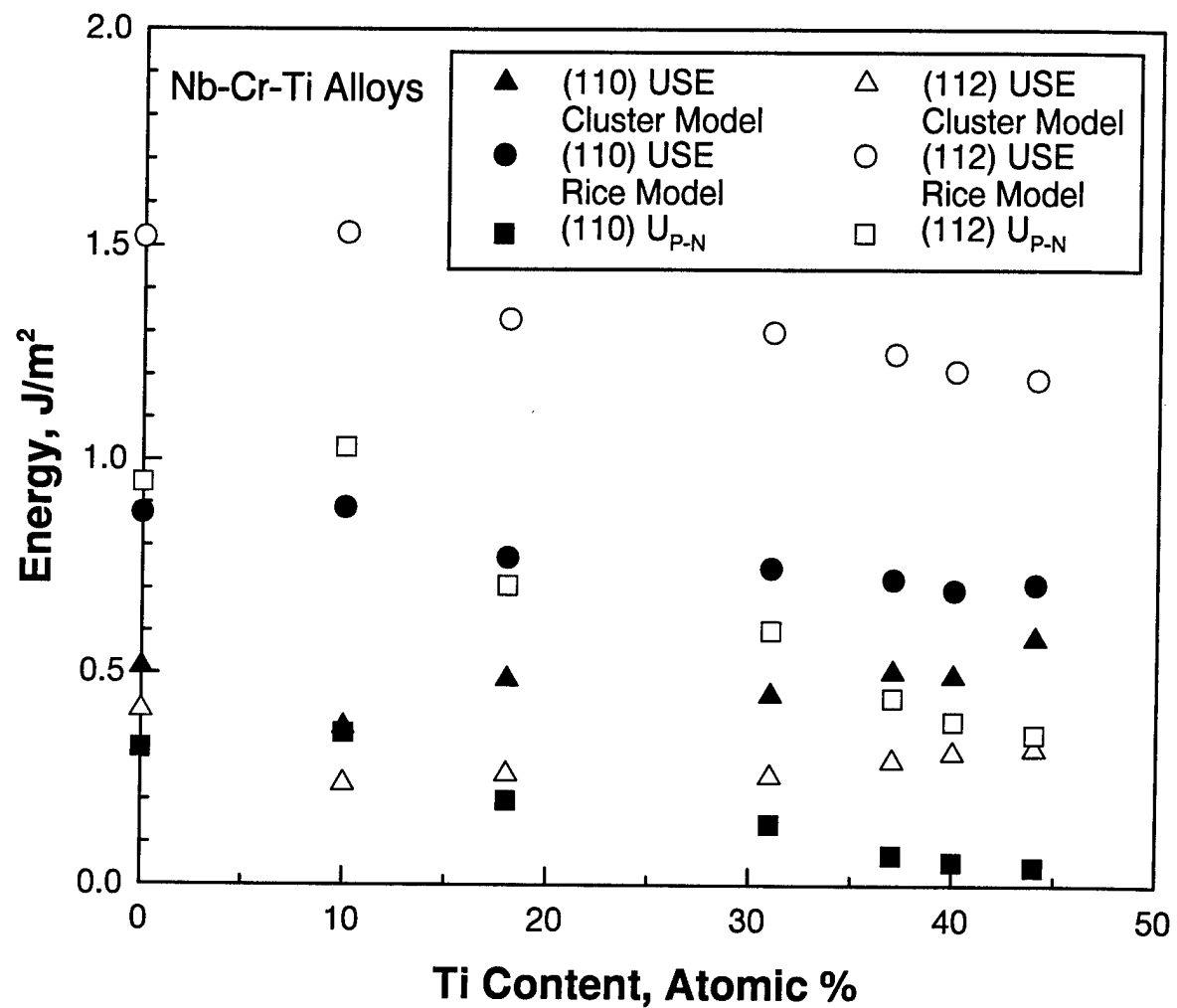


Figure 4. Comparison of unstable stacking energy (USE) calculated based on the cluster model and Rice equation against Peierls barrier energy ( $U_{P-N}$ ) as a function of Ti content.

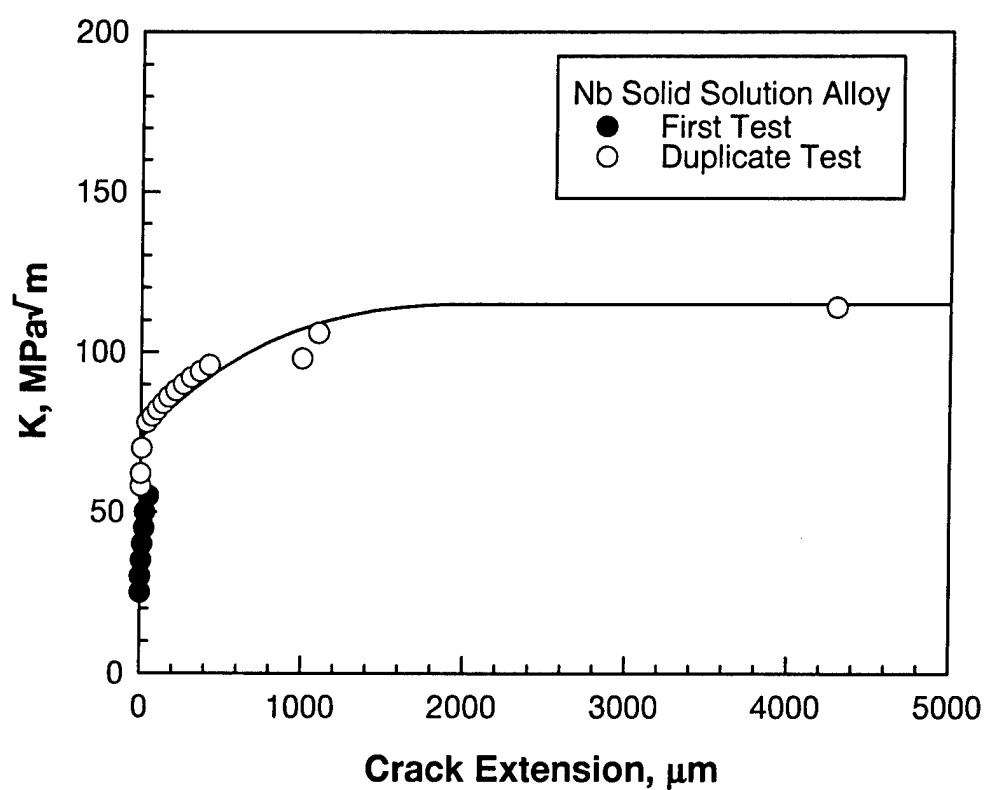


Figure 5. K-resistance curve of Nb-13Cr-37Ti at 25°C.

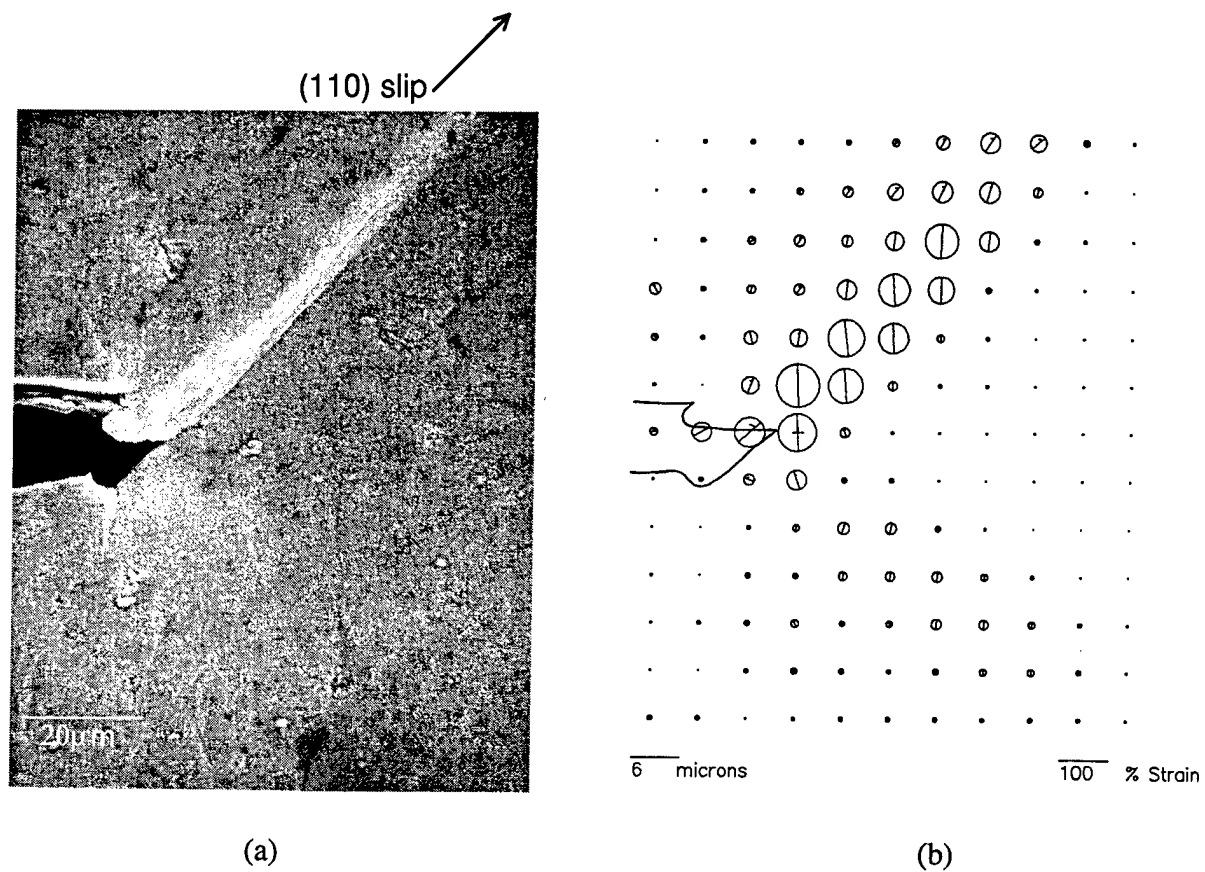


Figure 6. Near-tip slip behavior in Nb-13Cr-37Ti at 25°C: (a) slip emission from the crack tip at  $K = 50 \text{ MPa}/\text{m}$ , and (b) near-tip strain distribution presented in terms of Mohr's circle of strain shows strain concentration along the slip band.

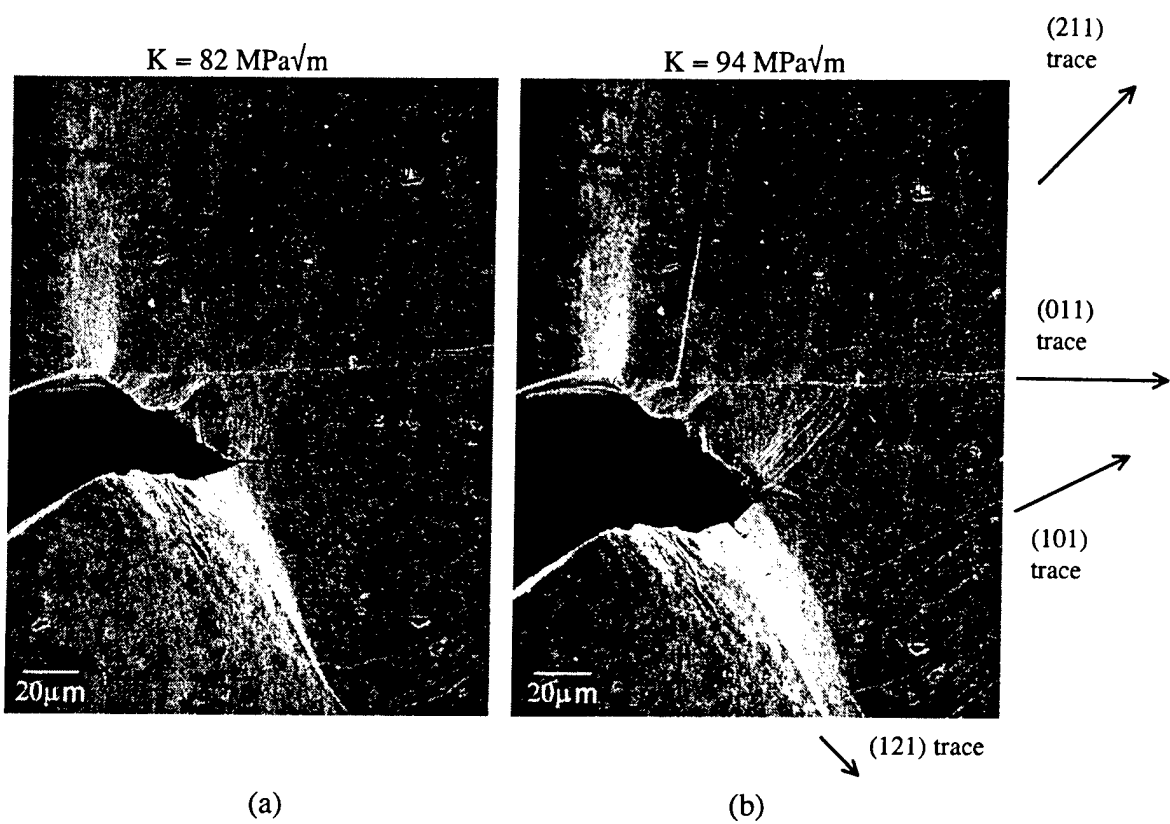


Figure 7. Observations of near-tip slip and fracture process in the Nb-Cr-Ti alloy at 25°C:  
 (a) small extension of the main crack on a plane in the (011) zone at  $K = 82 \text{ MPa}\sqrt{\text{m}}$ , and (b) emission of slip on three planes in the (101), (211), and (121) zones suppressed further propagation of the main crack at  $K = 94 \text{ MPa}\sqrt{\text{m}}$ .

$K = 98 \text{ MPa}\sqrt{\text{m}}$



(a)

$K = 100 \text{ MPa}\sqrt{\text{m}}$



(b)

Figure 8. Non-tip fracture process in the Nb-Cr-Ti alloy at 25°C: (a) grain boundary decohesion ahead of the main crack at  $K = 98 \text{ MPa}\sqrt{\text{m}}$ , and (b) ligament tearing at  $K = 100 \text{ MPa}\sqrt{\text{m}}$ .

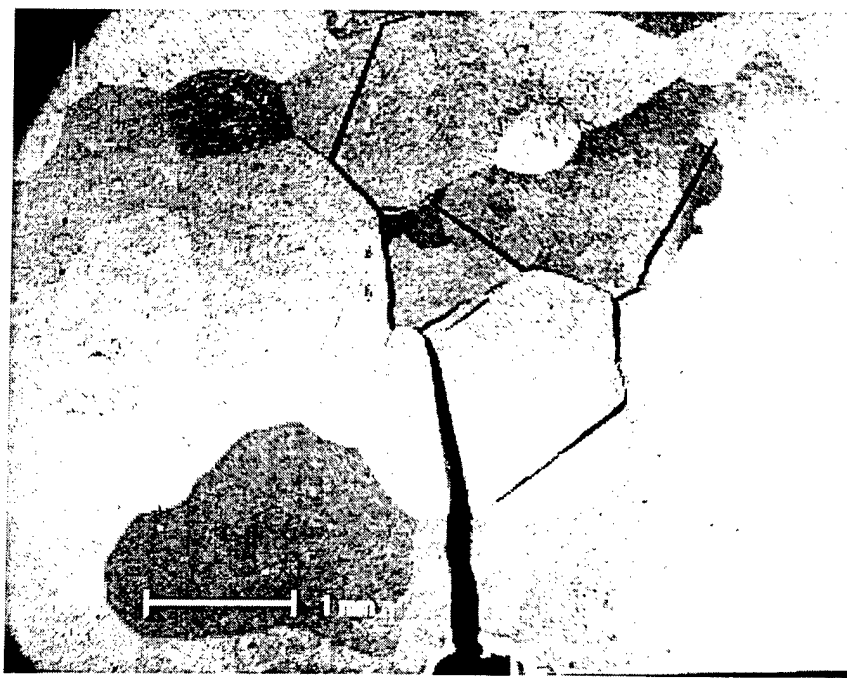
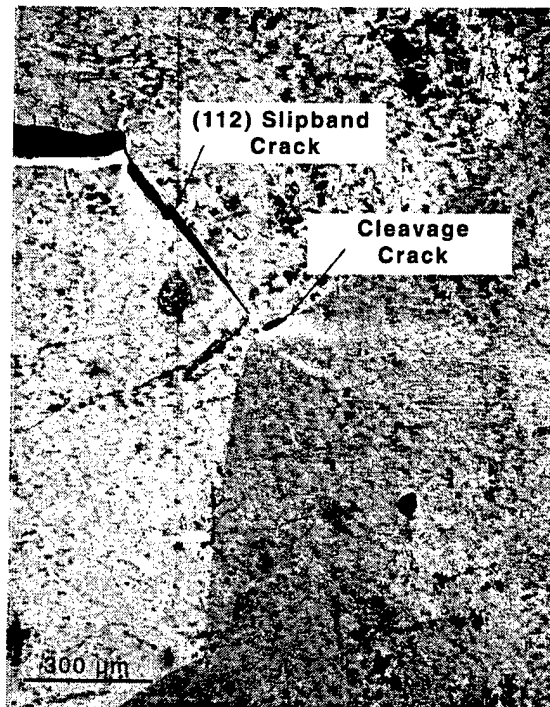
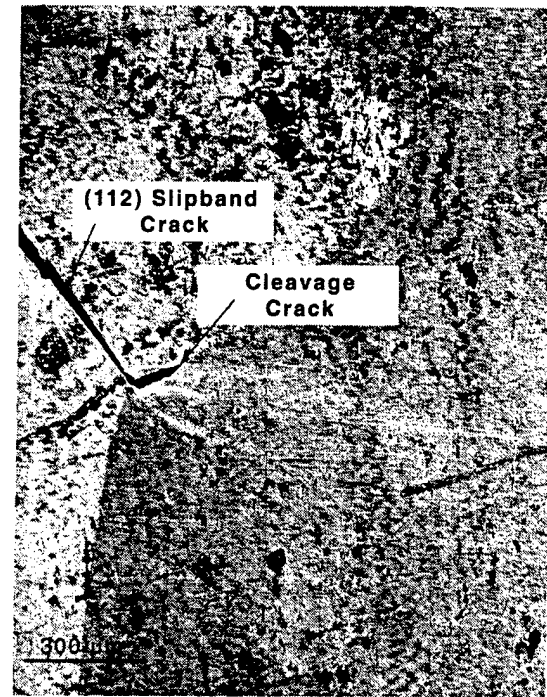


Figure 9. A macroscopic view of the extent of the fracture process zone in the Nb-Cr-Ti alloy, which shows grain boundary cracks, cleavage cracks, and slip band cracks within the near-tip plastic zone.



(a)



(b)

Figure 10. Planar slip on a (112) plane and slip-induced cleavage fracture by the Stroh mechanism in the Nb-Cr-Ti alloy at 25°C: (a) initiation of a cleavage crack ahead of the planar (112) slip, and (b) linkage of cleavage slip band cracks at  $K = 82 \text{ MPa}/\text{m}$ .

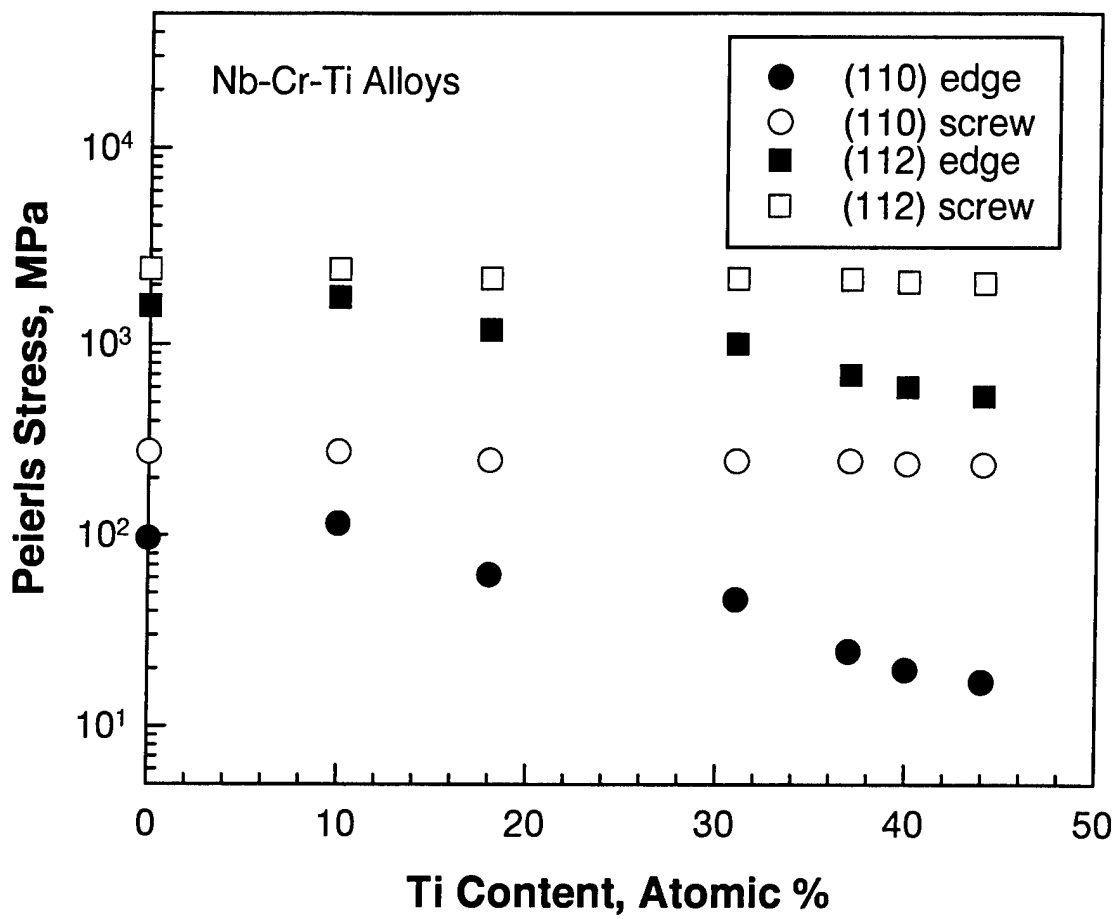
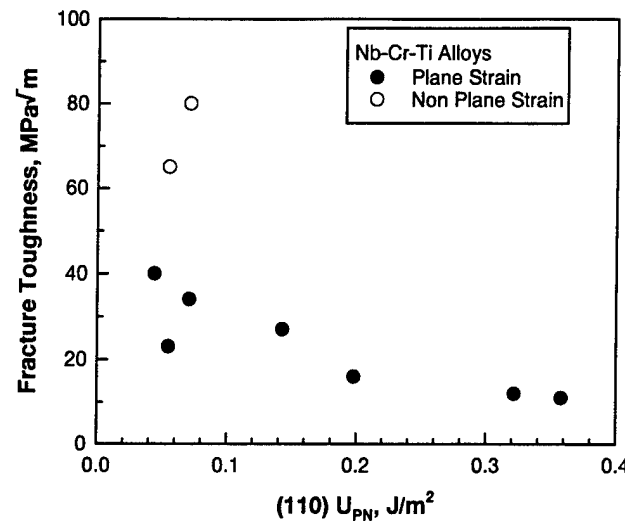
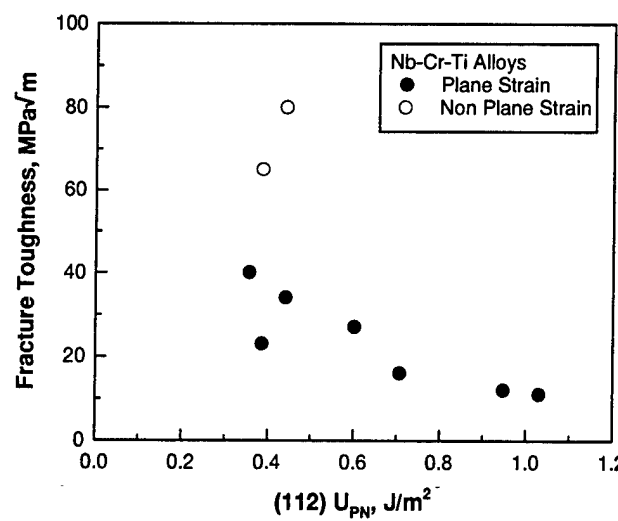


Figure 11. Peierls stress values for edge and screw dislocations on the (110) and (112) planes as a function of Ti content show decreasing lattice resistance for edge dislocations with increasing Ti contents and high lattice resistance for (112) screw dislocations.



(a)



(b)

Figure 12. Correlation of fracture toughness against the P-N energy values: (a) P-N energy for (110) slip, and (b) P-N energy for (112) slip. In both cases, the trend is increasing fracture toughness with decreasing values of the Peierl-Nabarro energy barrier,  $U_{P-N}$ .

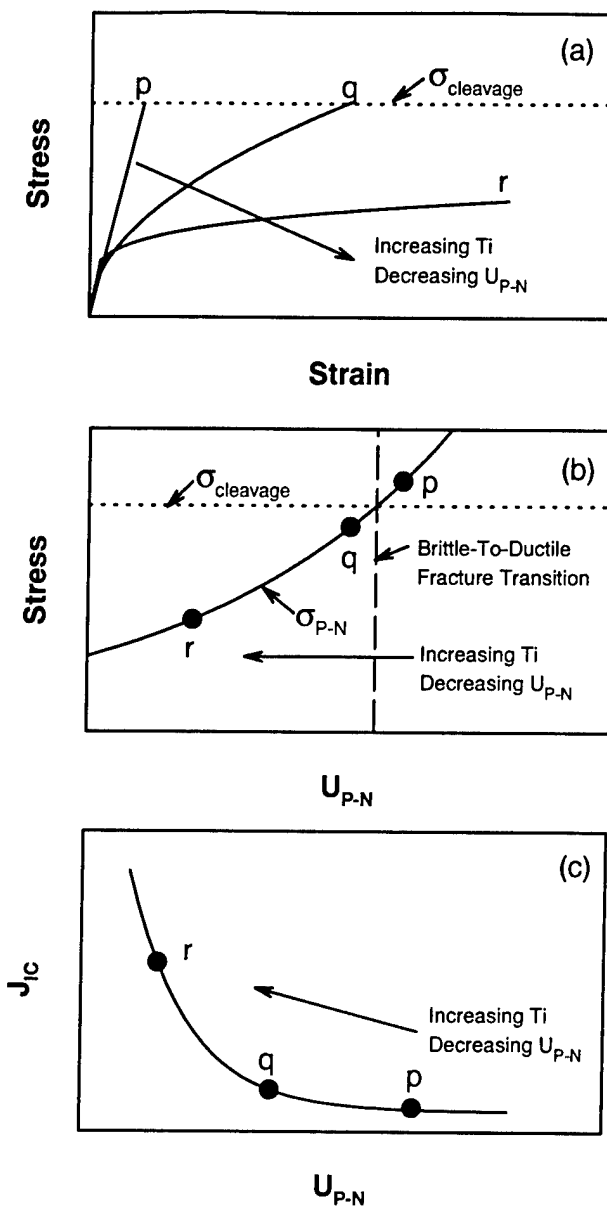


Figure 13. Schematics illustrate the effects of Ti addition on the P-N barrier energy, cleavage fracture, and fracture toughness in Nb-Cr-Ti solid solution alloys: (a) increasing Ti content leads to lower P-N energy barrier, greater crack-tip plastic deformation and relaxation of crack-tip stress buildup to values below the cleavage fracture stress; (b) a brittle-to-ductile fracture transition occurs when Ti addition reduces the P-N energy barrier sufficiently to prevent the crack-tip stress from exceeding the critical stress for cleavage fracture, and (c) Ti addition enhances fracture toughness by decreasing the P-N barrier energy which in turn promotes plastic dissipation in the near-tip plastic zone.

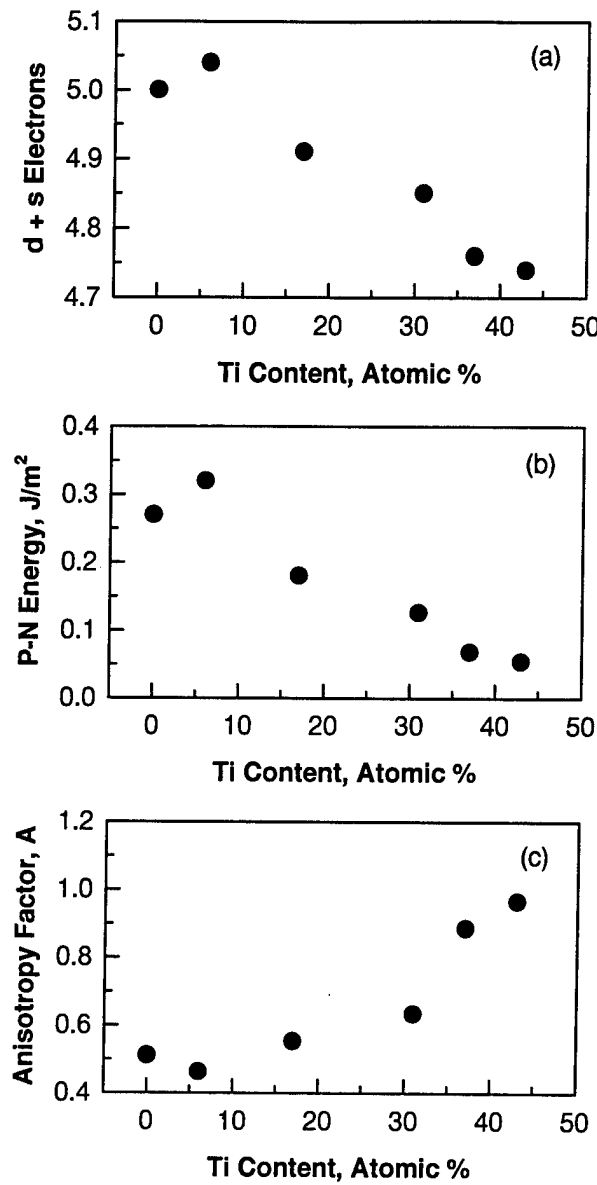


Figure 14. A summary of correlations of d+s electrons per atom, P-N barrier energy, and the elastic anisotropy parameter  $A = 2c_{44}/(c_{11}-c_{22})$  with Ti content in the Nb-Cr-Ti alloys: (a) decreasing number of d+s electrons per atom with increasing Ti contents, (b) increasing P-N barrier energy with increasing Ti contents, and (c) decreasing elastic anisotropy ( $A = 1$  for elastically isotropic materials) with increasing Ti contents.

**Optimizing the Design of Particulate Composites for  
Maximum Fracture Resistance Through Modeling**

**D. L. Davidson**

**International Journal of Fracture**  
**(in press)**

## OPTIMIZING THE DESIGN OF PARTICULATE COMPOSITES FOR MAXIMUM FRACTURE RESISTANCE THROUGH MODELING

D.L. Davidson  
Southwest Research Institute  
San Antonio, TX 78228

### ABSTRACT

The failure modes of particulate reinforced metallic alloys are reviewed with special emphasis on *in situ* intermetallic particle reinforced niobium alloys, but information derived from ceramic reinforced aluminum alloys is also included. Constraint of plastic deformation by particles is emphasized as one of two very important factors in controlling fracture behavior. The other factor is particle fracture toughness. Models are proposed for describing the fracture toughness, from which several methods of enhancing toughness are envisioned. This modeling of fracture toughness is intended to help optimize the design and processing of these materials for enhanced fracture resistance.

### INTRODUCTION

Particulate reinforced composites, such as the SiC and  $\text{Al}_2\text{O}_3$  reinforced aluminum alloys, have the benefit of enhanced modulus and reduced coefficient of thermal expansion, but often are lacking in fracture resistance, specifically, fracture toughness. Several reviews of the characteristics of these materials have been published (Nair, et al., 1985, Friend, 1989, and Roebuch and Lord, 1990). Some of the reasons for reduced fracture toughness have been identified in these materials. More recently, ductile phase toughened intermetallic alloys have been produced that are similar in many ways to the ceramic reinforced aluminum and magnesium alloys. These composites with intermetallics, often termed *in situ* composites, are designed to demonstrate ambient temperature fracture resistance while maintaining high temperature strength, creep and oxidation resistance. Some of these composites are based on niobium-chromium, niobium-aluminum and niobium-silicon binary systems, but with a number of other elements included. The synthesis of these materials is still evolving.

The objective of this paper is to examine what is known about the failure modes of particulate reinforced composites and to model those materials so that they may be designed to produce optimum fatigue crack growth and fracture toughness resistance. The hypothesis is that if the failure modes can be modeled, then it may be possible to alter composite formulation and processing conditions to optimize fracture resistance. Furthermore, it should be possible

to determine which of the variables, e.g., matrix ductility, particle size, particle fracture toughness, etc., is likely to have the greatest effect on fracture resistance so that effort can be focused on those parameters.

The crack growth resistance for large cracks will also be enhanced by a high fracture toughness, since the slope of the crack growth rate vs. cyclic stress intensity factor ( $da/dN-\Delta K$ ) curve is dependent on fracture toughness.

## FAILURE MODES AND MECHANISMS

Fracture of these composites is not always by the same mode; in fact, several fracture modes have been identified as being important for specific composites. It is important to recognize which mode of fracture is applicable to which composite when attempting to model fracture processes and improve the resistance to fracture of these materials.

**Ductile Fracture Modes:** Microvoid initiation, growth, and coalescence is a very work intensive fracture mode. If microvoids are large and deep and cover a large fraction of the fracture surface, it is possible to use micromechanics models that relate fracture toughness to material parameters that can be easily measured. See the literature (Ritchie and Thompson, 1992, and Somerdøy and Gangloff, 1994) for examples of this modeling process. However, if microvoids cover only a small proportion of the fracture surface, or if they are shallow and small, then the work done in their formation is low, and the contribution of this mode to fracture toughness is small.

**Particle Fracture:** Fracture of the reinforcing particles is generally recognized as being detrimental to the fracture resistance of these composites. For this reason, strong particles, e.g., alumina and silicon carbide single crystals, are used in their manufacture. There is a relationship between particle fracture and their size; the larger the particle, the easier they break. Since flaw sizes in particles should be proportional to their size, this behavior is expected. During fracture of these materials, particle fracture usually occurs just ahead of the crack tip in locations that are antishielding. Thus, particle fracture is to be avoided. When the composite is made using particles of low fracture toughness, particle sizes should be small to avoid fracture.

**Crack Bridging:** The formation of regions of unbroken matrix behind a crack tip usually results in strong shielding of the crack tip from the applied stress; thus, fracture toughness is greatly enhanced by this mechanism. Composites of Co cemented WC provide an excellent example of the importance of this fracture

enhancing mechanism. Reasonably accurate models of crack bridging have described the fracture toughness of WC/Co composites with accuracy (Ravichandran, 1994). Lamellar microstructures, such as the TiAl/Ti<sub>3</sub>Al "composites" also sometimes exhibit crack bridging (Chan, 1995). Although bridging has an important influence on fracture, it is unknown as to how to design composites to incorporate this fracture mechanism.

Constraint: Macroconstraint does not affect the fracture toughness of particle reinforced composites (Somerday and Gangloff, 1994). Notches in homogeneous materials have been used to vary the level of constraint, and it is well known that fracture stress and strain are related to notch configuration. For particulate composites, limits on matrix deformation occur not from the macroconstraint of the notch, but from the microconstraint of the particles. Particle induced microconstraint has recently been measured experimentally for several composites (Davidson and McClung), and it was shown that the fracture strain at the crack tip is inversely proportional to the level of microconstraint in the matrix. A number of modeling studies (Christman, et al., 1989, Llorca, et al., 1991, and Lloyd, 1991) have also identified increased triaxiality of stresses within composites as a factor in their behavior. High triaxiality is another way to express increased constraint. Constraint is influenced by particle shape, size, and location relative to adjacent particles (Christman, et al. 1989, Llorca, et al., 1991, and Heness, et al., 1997).

Particles also have the effect of increasing the flow stress in composite matrix. There is a new model for the stress elevation due to large particles (Hutchinson, 1993) and there are the detailed models originated by Orowan for the elevation of flow stress due to small particles (Martin, 1980)

Brittle Fracture: Many composite systems either do not evidence microvoid type fracture, or if they are found, the fraction of the surface covered is small, and the microvoids are small and shallow, and do not account for the levels of fracture toughness measured. Matrix fracture appears brittle, with no microvoids at all. This is especially true for many composites with body centered cubic alloys for a matrix. Yet, large crack tip strains have been measured (Chan, 1996, Davidson, 1997). There exist few models for fracture of composites with brittle matrices.

To illustrate the effect of some of the failure mechanisms listed above, fracture toughness as a function of volume fraction of particulate is shown in **Fig. 1** for a niobium-based alloy with Cr and Ti additions (Davidson, Chan, and

Anton, 1996). The experimentally measured values are shown together a line based on combining the fracture toughness of the two constituents according to the rule-of-mixtures, and the rule of mixtures modified by elastic modulus. Measured fracture toughness values drop severely from the fracture toughness of the matrix when the intermetallic is introduced. The question is, why does introduction of the particulate intermetallic cause this severe reduction in toughness, and what can be done to realize more of the inherent toughness exhibited by the matrix? The rule-of-mixtures values serve as measures of the fracture toughness values that might be possible if microstructure were optimized.

Examination of the fracture surfaces of these composites indicates that some microvoids do form, but they are small and the coverage of the fracture surface is very low. Thus, very little of the toughness can be attributed to this fracture mechanism. Strains at the tips of cracks in some of these composites have been measured (Chan, 1996, and Davidson, 1997), and the strains were found to be well above the expected elastic values, indicating that considerable plastic flow was occurring within the fracture process zone. It is this plasticity that accounts for the fracture toughness values measured. But, crack tip strains in the matrix material of the composites was found to be considerably below those of crack tips in the unreinforced matrix, indicating that the particles were limiting plasticity in the matrix of the composite. A method was then devised to evaluate the level of constraint within the matrix alloy, with and without particles, and these measurements indicated that fracture strain was inversely proportional to the level of constraint (Davidson and McClung, 1997).

## DESCRIPTION OF THE MODEL

A number of models for fracture of particle reinforced composites have been examined. For materials that leave a high proportion of the fracture surface covered with microvoids, existing models will probably be helpful in understanding fracture (Ritchie and Thompson, 1985; Manoharan and Kamat, 1991; Manoharan and Lewandowski, 1990). But there is an absence of models for materials that fracture without the benefit of microvoid formation; thus, there is the need for new models to assist in an understanding of fracture for these materials.

A high fracture toughness requires that matrix deformation occur within the crack tip process zone. This process requires that dislocations be formed at the crack tip and move into the material, thereby lowering the stress intensity at the crack tip by blunting while dissipating the work expended in opening the crack tip. Or, alternatively, dislocations already within the process zone can be activated, thereby dissipating the work of crack opening. The more work dissipated by plastic deformation, the higher will be the fracture toughness.

The presence of particles near a crack tip can alter the formation and motion of dislocations in a number of ways. Particles elevate the yield stress of the matrix, thereby requiring a higher load to activate crack tip dislocation sources. This elevation in flow stress might also be considered as being the result of constrained plasticity. The elevation in yield stress is relatively minor for large particles unless the volume fraction is at least 50% (Hutchinson, 1993). In aluminum alloys, the dispersoids, which are a low volume fraction of very small particles, cause dislocation motion to occur on many crystallographic planes, thereby dispersing, or diffusing or homogenizing, deformation throughout the fracture process zone. The presence of larger particles, as used in composites, tends to block dislocation motion rather than diffuse it, thus lowering the strain that a crack tip can sustain before fracture (Davidson and McClung, 1997).

The key effects to model in the fracture of these materials appears to be constraint. There are actually two effects of constraint. The first is the increase in stress within the fracture process zone just ahead of the crack tip, and the second is the decrease in strain that the crack tip can sustain at fracture.

It is likely that the two effects of constraint, one on strain and the other on stress, are physically linked, but they have not been for the purpose of this modeling process.

Particle shape, size ( $r$ ), and volume fraction ( $f$ ) are the characteristics that contribute to constraint, assuming the particles deform only elastically before fracture. Particle shape is neglected at this point, and all particles are considered as spherical and well dispersed. The concept of a mean free path (MFP) for dislocation motion within a particle field has been adopted here as capturing the main effect of constraint on fracture strain because MFP is a function of both particle diameter and volume fraction:

$$\text{MFP} = 4r(1-f)/3f \quad (1)$$

As particles become larger and volume fraction decreases, MFP increases, while constraint is lowered. Thus, constraint is proportional to the inverse of MFP. Constraint should be a dimensionless quantity, but the appropriate length scale by which to normalize MFP has not been found.

If MFP is normalized by particle diameter, then the resulting function is proportional to  $(1-f)/f$ , and the inverse of this function + 1 is

$$C_\sigma = 1+f/(1-f) \quad (2)$$

which is very similar to a function derived for stress elevation using an asymmetric cellular model (Hutchinson, 1993). In this case,  $C_\sigma$  is defined as the ratio of flow stress to yield stress.

As particle size is reduced, the Orowan mechanism of particle looping by dislocations is more likely to result in an increased flow stress. The effect of the Orowan mechanism on flow stress was examined using the following function (Martin, 1980, eq. 2.28)

$$\Delta\sigma = 1.62 Gb \ln(2r/r_0)/[2\pi(\lambda_s - d)(1-\nu)^{1/2}] \quad (3)$$

where  $r$  = particle radius,  $G$  = shear modulus,  $\nu$  = Poisson's ratio,  $r_0 \approx$  Burgers vector  $b$ , and  $\lambda_s$  = the mean planar surface separation of particles (Martin, 1980, eq. 1.32). Small particles begin to significantly increase the flow stress when size is approximately less than about 1  $\mu\text{m}$ .

The various methods for estimating the elevation of the flow stress due to particles is shown in **Fig. 2**. Shown in the figure are the Hutchinson model, the addition of stress from the Orowan mechanism to that model, and the approximation derived from mean free path, eq. (2). In the models developed here, the approximation embodied in eq. (2) is used to compute the stress elevation due to particles, and no difference is recognized between the constraint that elevates stress and that which decreases fracture strain. The reason eq. (2) was chosen to represent stress elevation is that the effects of smaller particles are being modeled, and that approximation accounts gives a better approximation than the Hutchinson model, which was developed for larger particles.

Large particles fracture at a lower stress than small particles because the flaw size in a particle is proportional to its size. Here it will be assumed that flaw size ( $d$ ) is a fraction ( $x$ ) of the particle diameter ( $2r$ ), and that the particle fracture stress is given by

$$\sigma_p^f = K_p^f / \sqrt{2\pi d} \quad (4)$$

where  $K_p^f$  is the fracture toughness of the intermetallic or ceramic particle.

**Model 1** (Particle fracture model): The first approach to modeling this process computes the stress to fracture particles using eq. (4) and treats the effect of constraint through the empirically observed relationship between strain to fracture of the matrix ( $\epsilon_f$ ) and constraint ( $C$ ).

$$\varepsilon_f = \varepsilon_0 C^{-q} \quad (5)$$

where  $\varepsilon_0$  is the matrix strain with no particles, and  $q \approx -1$ .

The relationship between crack tip opening displacement ( $\delta$ ) (in micrometers) and crack tip fracture strain has been determined for composites through measurement (Davidson, 1997) to be

$$\delta (\mu\text{m}) = 8 \varepsilon_f^{1.3} \quad (6)$$

Fracture toughness of the material is then related to these parameters through the familiar relationship used to compute  $J$

$$K_C = \sqrt{E \sigma_x \delta} \quad (7)$$

where  $\sigma_x = \sigma_p^f$ , the stress to break particles.

Model 2 (Matrix fracture model): Stress within the process zone at fracture could be considered to be stress in the matrix when fracture occurs in the particle. Therefore, in eq. (7)

$$\sigma_x = \sigma_m = C \sigma_{yield} \quad (8)$$

when stress at the crack tip is limited by deformation in the matrix, even when the particle fracture stress is above this value. The model tests  $\sigma_x$  and uses the lower of the two possible values of stress.

Model 3 (Characteristic distance model #1): When particles break, another method can be used for calculation of the fracture toughness

$$K_C = \sigma_p^f \sqrt{2\pi l^*} \quad (9)$$

where  $\sigma_p^f$  is the stress at the crack tip when a particle breaks at a distance of  $l^*$  from the crack tip, where  $l^* = \text{MFP}$ . Thus, stress within the process zone is elevated to the stress needed to break the particle, and particle size and volume fraction enters through the MFP.

Model 4 (Characteristic distance model 2): The concepts are the same as model 3, except stress used in eq. (9) is the stress in the matrix, as given by eq. (8), so

that regardless of the stress needed to break particles, matrix stress is elevated only by constraint.

**RESULTS** - With models that result from the reasoning given above, it is possible to consider the effects of the following variables:

1. Matrix ductility and yield strength.
2. Particle size, volume fraction, and fracture toughness.

This number of variables (5) makes it difficult to convey the results of the models in a readily comprehensible way. The best way thus far found has been to determine the effect of each variable changed independently, then to determine the values of each variable that, when taken together, maximize the level of fracture toughness that might be obtained under "best-case" conditions.

The model is based mainly on a composite consisting of particles of the brittle intermetallic  $\text{Cr}_2\text{Nb}$  in a ductile matrix alloy of 50Nb-37Ti-13Cr, as shown in Fig. 1. The fracture toughness of these constituents are approximately 1.5 MPa $\sqrt{\text{m}}$  for the intermetallic particles and at least 65 MPa $\sqrt{\text{m}}$  for the matrix (fracture toughness values of up to nearly 100 MPa $\sqrt{\text{m}}$  have been measured). Another material for which some data are available are the aluminum alloy matrix - SiC particulate composites. Measured values of fracture toughness vs. volume fraction of particles are shown in Fig. 3 for both types of composites together with some results for the models.

The measured values shown in Figs. 3 and 4 should be taken as general trends for the composite because there are likely to be factors other than volume fraction that affect fracture toughness. For example, the distribution of particles is an important influence that has been considered as being uniform. However, the increase in volume fraction of particles is thought to be, by far, the dominant cause for the decrease in fracture toughness.

The data shown in Fig. 3 for the Nb-based composites are from experimental materials, so there is likely to be a wide variation in the toughness values if enough material existed for repeated values to be measured. Likewise, the particles in these materials were not all spherical or evenly distributed, as assumed by the model. Volume fractions of particles were estimated from the phase diagram, from x-ray diffraction line intensities, and by metallography.

The data shown in Fig. 4 for the Al/SiC composites (Goolsby and Austin, 1986) are for fracture toughness values known to be obtained under plane strain conditions in composites with a variety of aluminum alloy matrices having a wide range in strength. The SiC particle volume fractions were as

manufactured, not measured, and the particle sizes ranged from 0.5 to 20  $\mu\text{m}$ . Clumping of particles in these composites has a significant effect on fracture toughness; the level of clumping for these materials was not reported.

For the Nb-based composites, the results indicate that either Model 3, or perhaps Model 1, fit the available data better than either Model 2 or Model 4.

For the Al-based composites, Model 1 appears to be the most descriptive, Model 3 is the least, and Models 2 and 4 giving poor results. Toughness values for Al-based composites are actually closer to the ROM values than for the Nb-based composites, possibly because the differences in matrix and particle fracture toughness values is less for these materials than for the Nb-based composites.

Thus, considering both composite systems, Model 1 best conforms to the limited data. It is recognized that more extensive data might change this perception, and that is one reason for including the results of all the models on the figures.

The models predict rather different levels of composite fracture toughness when particle size is reduced, as shown in **Fig. 5**. If the data were available, it might be possible to discern which model fits the composite of interest better by examining the effects of particle size.

## OPTIMUM COMPOSITE DESIGN

Values of the material characteristics were altered in the models, searching for values that will provide a maximum fracture toughness. One objective for using these models to find the optimal microstructure is to give guidance to future research that would seek composite processing procedures that could achieve the optimum microstructures identified. Some of the questions that are addressed are: (1) How important is increasing the fracture toughness of the particles? (2) What is the optimum size of the particles? (3) What relationship between volume fraction of particles and their size gives maximum fracture toughness? (4) How important is matrix yield strength to fracture toughness?

Optimum composite design has been considered only for the Nb alloy matrix composite with  $\text{Cr}_2\text{Nb}$  particles because these composites are formed *in situ*. Thus, there is more opportunity to manipulate the microstructures of these materials than there is for a system like aluminum alloys with SiC particles. In addition, more micromechanics data have been measured for these composites than for the aluminum matrix materials.

One of the reasons for making composites is to increase the material modulus; thus, it is desirable that the volume fraction of intermetallic should be as high

as possible. The effect of decreasing particle radius from 7.5  $\mu\text{m}$  diameter to half that (3.7  $\mu\text{m}$ ) at a particulate loading of 40% is an increase in fracture toughness from 15.3 to 18.9 MPa $\sqrt{\text{m}}$  by Model 1, or from 13.9 to 14.8 MPa $\sqrt{\text{m}}$  as predicted by Model 3. Neither of these increases is dramatic. The number of particles is increased from about 226 to 1885 per cc by this change in particle diameter at constant volume fraction.

If the particle loading is lowered from 40% to 10%, and the particle diameter is decreased from 15 to 7.5  $\mu\text{m}$ , the particle density decreases from 1885 to 471 per cc. Fracture toughness is increased from 13.8 to 36.3 MPa $\sqrt{\text{m}}$  by Model 1, or from 15.3 to 26.7 MPa $\sqrt{\text{m}}$  by Model 3. Clearly, decreasing volume fraction is much more important to increasing fracture toughness than is decreasing particle size, but if both are decreased, a factor of 2 increase in fracture toughness is expected.

The above results are for a particulate fracture toughness of 1.5 MPa $\sqrt{\text{m}}$ . The effect of increasing particle toughness to 3.0 MPa $\sqrt{\text{m}}$  is that the fracture toughness increases by a factor of 2 (from 13.8 to 27.6 MPa $\sqrt{\text{m}}$ ) by Model 1, or from 15.3 to 21.6 MPa $\sqrt{\text{m}}$  by Model 3, both for a 40% loading of particles of 7.5  $\mu\text{m}$  radius. The effect of lowering particulate loading to 10% and the size to 3.7  $\mu\text{m}$  radius is to increase fracture toughness to 38 MPa $\sqrt{\text{m}}$  by Model 1 and to 73 MPa $\sqrt{\text{m}}$  by Model 3. Thus, the full potential of the composite could be realized, if Model 3 is applicable. If Model 1 is applicable, then a sizable increase in fracture toughness could be realized, but to a value still far below that of the matrix alone.

## DISCUSSION

The modeling procedures used here were derived to account for two factors that have been found to limit the fracture toughness of particle reinforced composites. Particles constrain the deformation of matrix material within the process zone, and that elevates stress within the process zone and limits the strain that can be sustained at the crack tip at the point of fracture. The other composite toughness limiting factor is the fracture toughness of the particles. The low toughness of particles can be partially accommodated by decreasing the particle size, but for a given volume fraction, that increases the number of particles. The only way to compensate for low crack tip fracture strain is to decrease the volume of particles and increase their size; thus, lowering constraint.

Using the model to examine what might be the effect of changing particle size, particle toughness, and volume fraction indicates that these can have a large effect on the fracture toughness of the composite. But only if volume fraction

of the particles is decreased to levels that may be unacceptably low from a modulus perspective (and perhaps others; e.g., creep), can the full potential of the matrix toughness be approached. Increasing fracture toughness of the particulate is a very potent method for increasing fracture toughness of the composite.

The validity and reasonableness of the four models postulated is difficult to assess. The assumptions associated with models 2 and 4 appear to be the most reasonable because they postulate that it is the stress within the process zone that is appropriate in describing the fracture toughness of the matrix, rather than the particle stress, which is generally much higher. Model 1 fits the data the best, which uses the particle stress in the computation of fracture toughness.

One major difficulty in modeling fracture has been finding a way to compute the stress elevation that is due to the constraint caused by particles. The fact that the two models that use matrix stress in the computation for fracture toughness predict lower values than when the particle stress is used may indicate that constraint is underestimated by eq. (2). This function depends only on volume fraction, rather than on both volume fraction and particle size. When particle size is further considered in the stress elevation when Orowan hardening was included, but for the particle sizes of interest in these composites, Orowan hardening is of little consequence.

Other problems in the modeling are the relationships between fracture strain and constraint, eq. (5), and CTOD and fracture strain, eq. (6). Both relations were empirically derived for Nb matrix composites, but used also to model the Al-SiC composites. A better theoretical basis is required for these functions.

Yet to be modeled is the effect of having shearable particles, such as those found in the nickel based superalloys, instead of unyielding particles. If strong, but shearable, intermetallic particles were used in the niobium matrix composites, then it is more likely that the full toughness of the matrix could be achieved.

## **SUMMARY AND CONCLUSIONS**

Several models for the fracture processes in composites have been derived that account for the effects of particle fracture and volume fraction in a matrix that is not forming microvoids during fracture. For a given fracture toughness of particles, the composite fracture toughness is maximized when the particles are as few and large as possible so that they do not break in the elevated stress field of the crack tip. Thus, increasing particle fracture toughness has a larger effect than increasing fracture toughness of the matrix. Although these models

indicate that substantial increases in fracture toughness can be achieved by microstructural manipulation, it is probably not possible to realize the full potential of the matrix material toughness for a given volume fraction of particulate, due mainly to the constraint imposed on the matrix deformation by the particles.

## ACKNOWLEDGEMENT

The research that lead to this modeling effort was sponsored by Office of Naval Research, Dr. Steven Fishman, project monitor, and by Air Force Office of Scientific Research, under various project monitors. Many colleagues have stimulated thought, questioned the concepts used in these models, and suggested ideas, and the author is pleased to acknowledge those interactions.

## REFERENCES

Chan, K.S. (1995) Evidence of shear Ligament Toughening, Metallurgical and Materials Transactions A, **26A**, 1407-18.

Chan, K.S. (1996) The fracture toughness of niobium-based in situ composites Metallurgical and Materials Transactions A, **27A**, 2518-31.

Christman, T., Needleman, A., and Suresh, S. (1989) An experimental and numerical study of deformation in metal-ceramic composites, Acta metallurgica, **37**, 49-61.

Davidson, D.L. (1997) Fatigue crack growth through alloyed niobium, Nb-Cr<sub>2</sub>Nb and Nb-Nb<sub>5</sub>Si<sub>3</sub> in situ composites, Metallurgical and Materials Transactions A, **28A**, 1297-1314.

Davidson, D.L., Chan, K.S., and Anton, D.L. (1996) The effects on fracture toughness of ductile phase composition and morphology in Nb-Cr-Ti and Nb-Si in situ composites, Metallurgical Material Transactions A, **27A**, 3007-18.

Davidson, D.L. and McClung, R.C. (1997) Local constraint near fatigue cracks in alloys and particulate composites, International Journal of Fracture **84**, 81-98.

Friend, C.M. (1989) Toughness in metal matrix composites, Materials Science and Technology, **5**, pp. 1-7.

Goolsby, R.D. and Austin, L.K. (1989) Fracture toughness of discontinuous SiC reinforced aluminum alloys, Advances in Fracture, ICF-7, v. 4, K. Salama, et al., eds., Pergamon Press, New York, pp. 2423-35.

Heness, G.L., Davidson, D.L., Gan, L.H. and Mai, Y-W. (1998) "Constraint and matrix flow in metal matrix composites" (in press).

Hutchinson, J.W. (1993) Continuum models for deformation: discontinuous reinforcements, in **Fundamentals of Metal-Matrix Composites**, S. Suresh, A. Mortensen, and A. Needleman, eds, Butterworth-Heinemann, Chap. 6, pp. 158-173.

Llorca, D., Needleman, A., and Suresh, S. (1991) Acta metallurgica and materialia, **39**, 2317-35.

Lloyd, D.J. (1991) Aspects of fracture in particulate reinforced metal matrix composites, Acta metallurgica and materialia, **39**, pp. 59-71.

Martin, J.W. (1980) **Micromechanisms in particle-hardened alloys**, Cambridge University Press, Chapters 1, 2, and 3.

Manoharan, M., and Kamat, S.V. (1991) On the fracture toughness of particulate reinforced metal matrix composites, Scripta Metallurgica et Materialia, **25**, 2121-2125.

Manoharan, M., and Lewandowski, J.J. (1990) Crack initiation and growth toughness of an aluminum metal matrix composite, Acta metallurgica et materialia, **38**, 489-496.

Nair, S.V., Tien, J.K., and Bates, R.C. (1985) SiC-reinforced aluminum metal matrix composites, International Metals Reviews, **30**, pp. 275-290.

Ravichandran, K.S. (1994) Fracture toughness of two phase WC-Co Cermets, Acta metallurgica and materialia, **42**, 143-50.

Ritchie, R.O., and Thompson, A. W. (1985) On macroscopic and microscopic analyses for crack initiation and crack growth toughness in ductile alloys, Metallurgical Transactions A, **16A**, 233-48.

Roebuch, B. and Lord, J.D. (1990) Plane strain fracture toughness test procedures for particulate metal matrix composites, Materials Science and Technology, **6**, pp. 1199-1209.

Somerd़ay, B.P. and Gangloff, R.P. (1994) Global constraint-insensitive fracture in SiC particulate reinforced AA2009, Metallurgical Transactions A, **25A**, 1471-79.

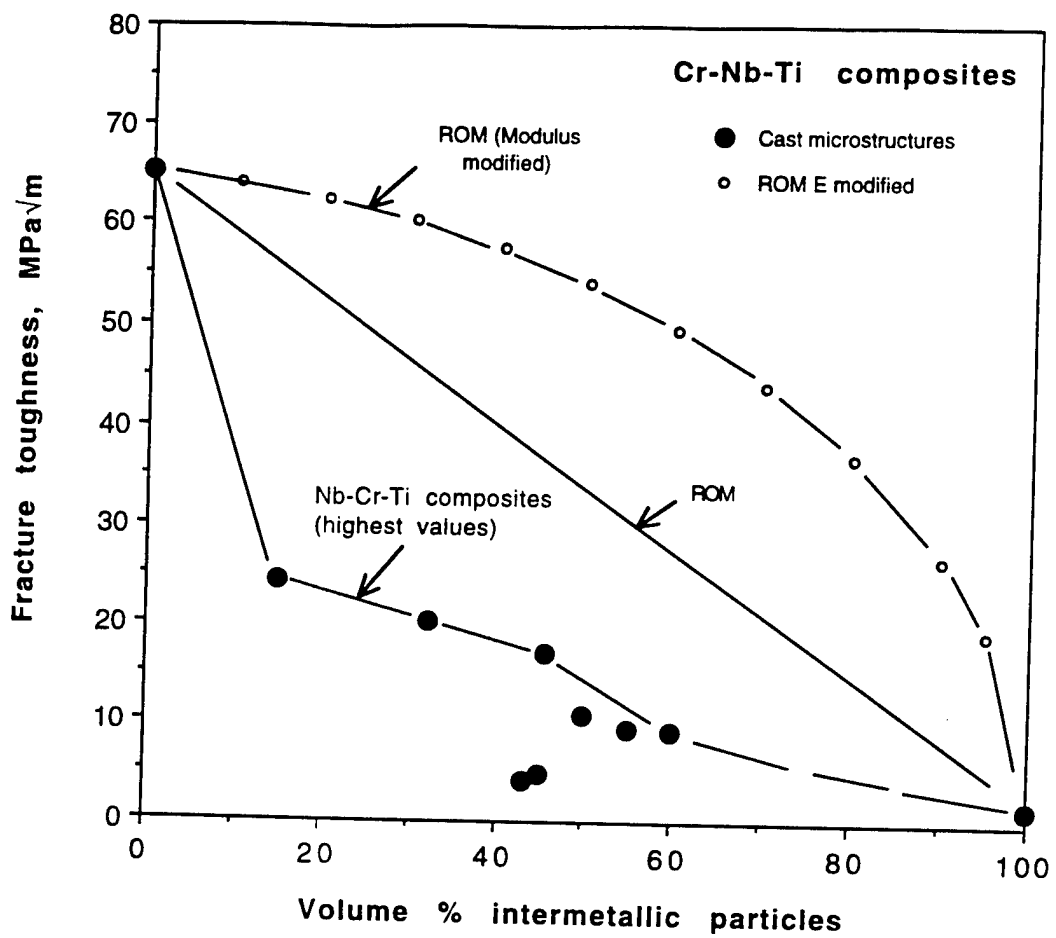


Fig. 1 Fracture toughness of composites containing particles of the intermetallic  $\text{Cr}_2\text{Nb}$ . Also shown are the rule of mixture (ROM) and modulus modified ROM estimates of fracture toughness.

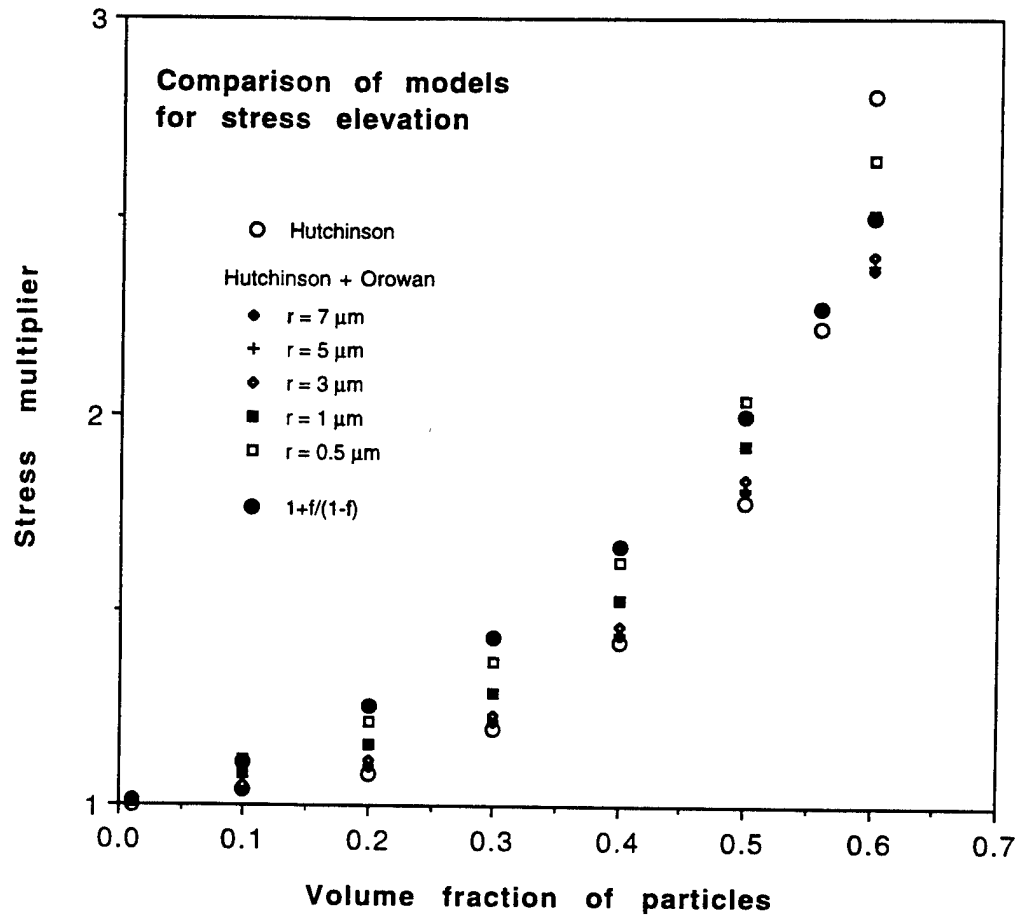


Fig. 2 The effect of volume fraction of particles on the stress increase in the matrix of composites. The models that have been used to estimate this stress elevation are compared.

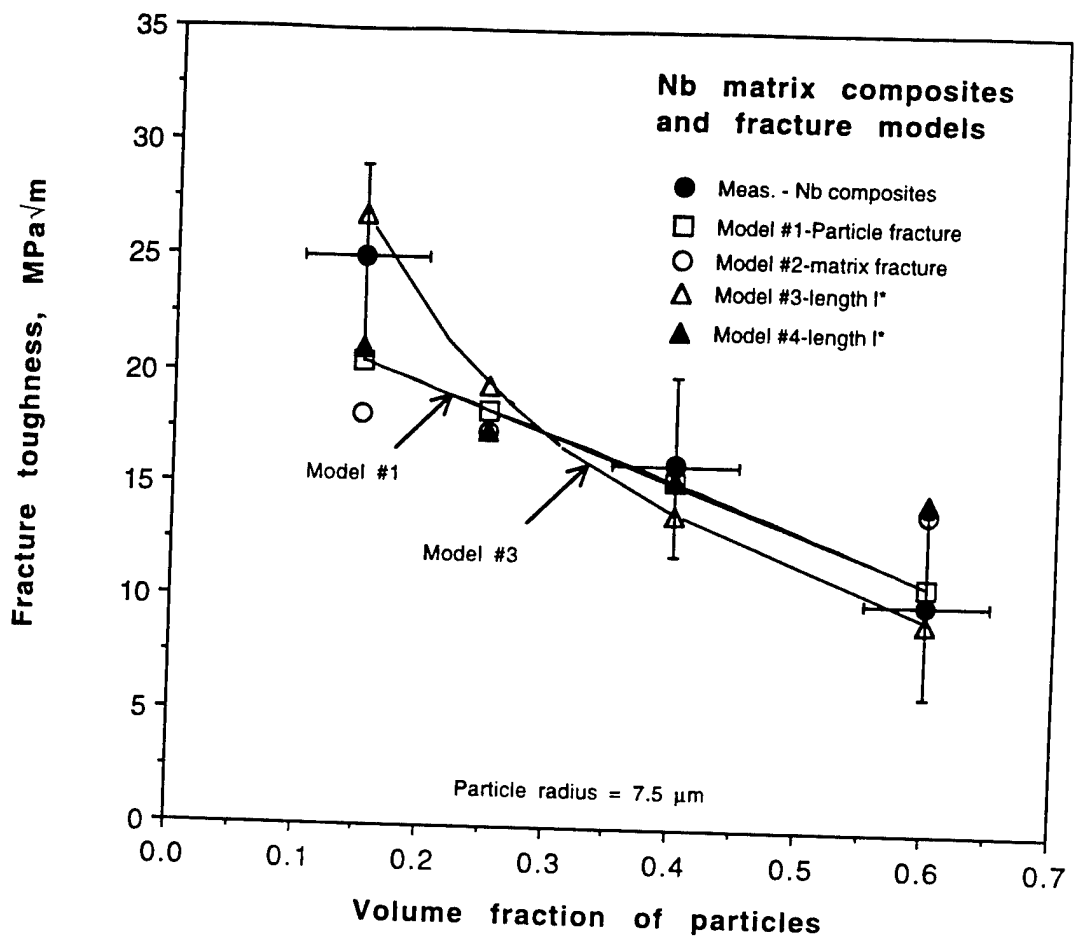


Fig. 3 Comparison between measured values of fracture toughness and the model predictions for Nb-alloy matrix composites with  $\text{Cr}_2\text{Nb}$  particles.

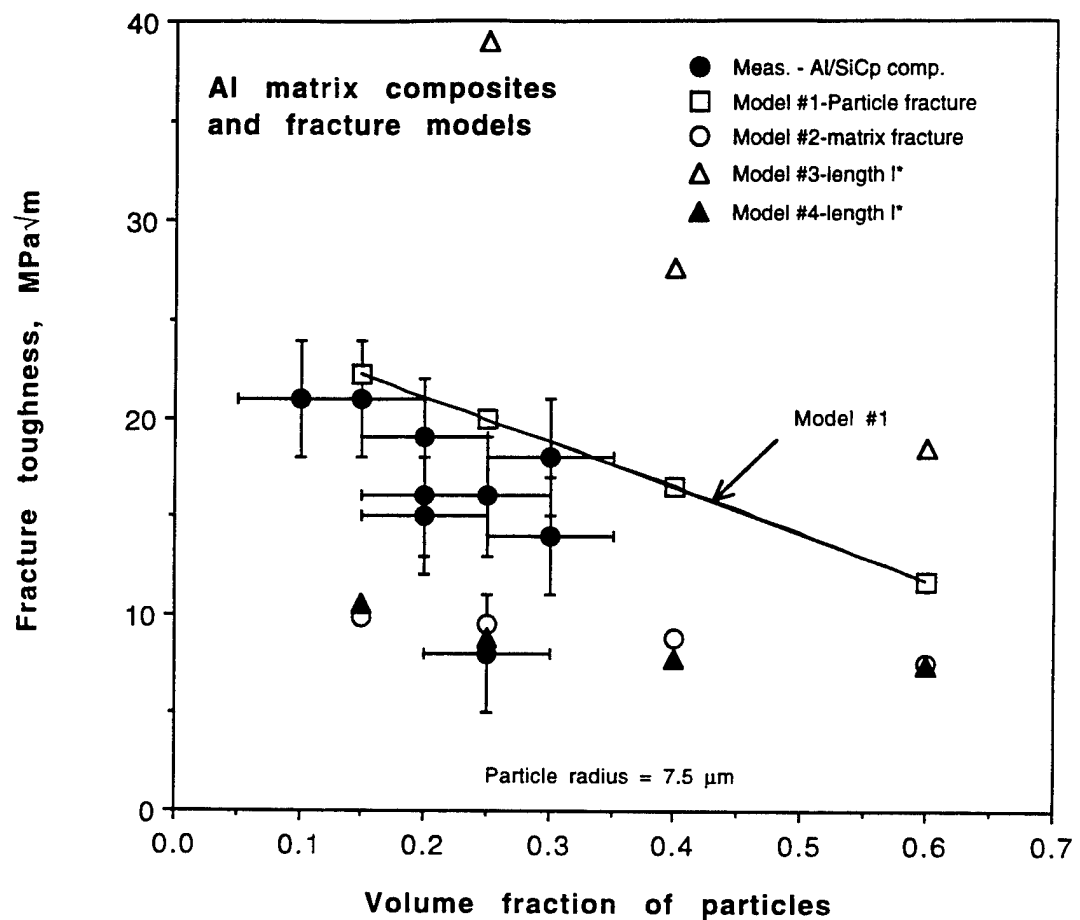


Fig. 4 Comparison between measured values of fracture toughness and the model predictions for Al-alloy matrix composites with SiC particles.

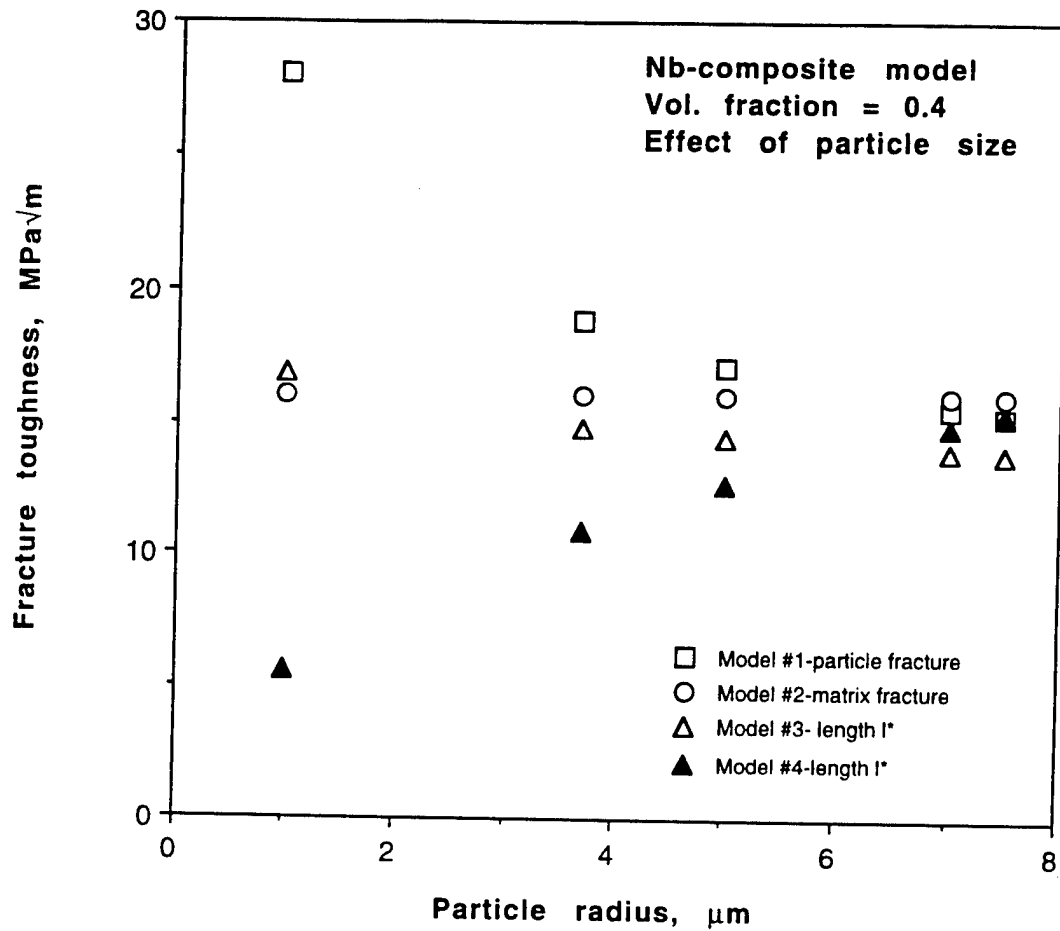


Fig. 5 The effect of particle size on fracture toughness. If particle toughness controls, as described by Model 1, then reduction of size will nearly double the fracture toughness of the composite.

**Tensile Experiments with a High Toughness Niobium Alloy  
at Ambient Temperature**

**D. L. Davidson and K. S. Chan**

## **TENSILE EXPERIMENTS WITH A HIGH TOUGHNESS NIOBIUM ALLOY AT AMBIENT TEMPERATURE**

**D.L. Davidson and K.S. Chan**  
Southwest Research Institute  
San Antonio, TX 78228

### **ABSTRACT**

Tensile deformation experiments have been conducted on the high fracture toughness alloy 50Nb-13Cr-37Ti at ambient temperature. Stress-strain curves were measured in a laboratory servohydraulic loading machine, with strain gages used to obtain the strain. Specimens were also deformed inside the scanning electron microscope where a strain gage was used to measure macroscopic strain and stereoimaging was used to measure microscopic strains within several grains that formed slip lines. One of the specimens deformed was subsequently used for transmission electron microscopy.

### **INTRODUCTION**

Tensile properties are important in evaluating the mechanical characteristics of materials and provide an important adjunct to the evaluation of fracture properties. Consequently, tensile experiments were conducted on an alloy that had been found to have very high fracture toughness [1] in order to study its deformation characteristics. These detailed tensile experiments complement detailed fracture toughness experiments conducted on this material.

### **MATERIAL AND EXPERIMENTAL PROCEDURES**

The alloy was cast onto a cold Cu hearth at United Technologies Research Center (UTRC) into a billet approximately 50 mm square by 6 mm thick [2]. No intermetallic was found in the alloy either by x-ray diffraction or metallography. The casting was cut into a number of specimens that were used to evaluate the fatigue crack growth resistance and fracture toughness of the material. Several tensile samples with uniform gage sections and tapered ends for loading were cut in the plane of the billet using electric discharge machining (EDM). These specimens were hand polished with SiC papers and diamond paste to remove any residual damage from machining.

Two tensile loading experiments were conducted on this material, one in a servohydraulically controlled laboratory loading frame (specimen 1) and the other in a special loading stage for the scanning electron microscope (SEM) (specimen 2). Grain structure was revealed in this specimen by ion etching. The SEM loading system allowed high resolution photographs to be made of the specimen at various stages of deformation so that the strains could be determined subsequently using the stereoimaging technique [3]. For both specimens, the macroscopic displacements were measured with strain gages having a 1.6 mm gage length. Width and thickness of each specimen is listed in Table 1.

## RESULTS

The stress strain curves for these specimens are shown in **Figs. 1 and 2** and the measured values of modulus, proportional limit and yield stress are listed in Table 1. Specimen 1 deformed with load drops and serrations. The two large load drops just before and after yield were accompanied by clicking sounds thought to be the formation of twins or slip lines. Loading was partially removed and then reapplied to measure modulus. The rate of deformation was approximately  $10^{-4}$ /sec. The load drop that occurred at the largest strain was accompanied by the formation of a visible crack, and the specimen was unloaded prior to fracture. The substructure of this specimen was subsequently examined using transmission electron microscopy.

**Table 1**  
Tensile modulus and yield

Width	Thick- ness	Modulus			Yield stress		Maximum
mm	mm	Initial ----	mid ----	end ----	proportional limit -----	0.2% offset strain -----	strain %
<b>Specimen 1</b>							
3.76	1.33	111	92.9	102	877	933	2.8
<b>Specimen 2</b>							
2.40	1.40	93.0	83.8	--	811	856	6.4

The loading of specimen 2 in the SEM was applied manually. Periodically,

loading was stopped while photographs were being made, and during these periods, the specimen continued to elongate by creep, as may be seen in Fig. 2. The load was partially removed and reapplied to measure modulus, and finally unloaded without fracture.

The creep rates measured in specimen 2 were correlated with stress, as shown in **Fig. 3**. The line shown indicates that the stress exponent  $n' = 51.4$  in the equation

$$\dot{\epsilon} = \dot{\epsilon}_0 \sigma^{n'} \quad (1)$$

The grain structure of the gauge section of the specimen deformed in the SEM is shown in the drawing and photograph of **Fig. 4**. The orientations of these very large grains 1 - 3 were obtained using the Laue back reflection technique and are listed in **Table 2**.

Strain in grains 1-3 were measured by the stereoimaging of photographs. Strain was relatively uniform in grains 1 and 2, but a slip line formed in grain 3, disrupting the uniform strain field. The strain fields in grain 3 at the same location are shown as a function of increasing stress in **Figs. 5, 6 and 7**. The relatively uniform strain field seen in Fig. 5 is seen to become quite inhomogeneous upon the formation of slip lines in Fig. 6, but homogeneous strain is restored upon subsequent deformation, as shown in Fig. 7.

**Table 2**  
Grain orientations

Grain No.	Size mm	Normal	Tensile axis
1	2	[201]	[102]
2	1	5° from [103]	16° from [011]
3	1.2	15° from [001]	13° from [010]

The maximum shear strain distribution in grain 3 at 750 MPa, just before slip line formation, shown in **Fig. 5**, had a maximum value of approximately 0.0135, with a average axial strain of about 0.002. The macroscopic axial strain was 0.0108 as measured by the strain gage.

Slip lines formed at about 825 MPa, with a macroscopic axial strain of about 0.0133. The proportional limit for this specimen was approximately 811 MPa, so the slip lines formed just above the proportional limit stress. The

distribution of strain shown in **Fig. 6** had average microscopic axial values of between 0.0039 and 0.0058, but maximum shear strains along the slip lines ranged from 0.022 to 0.025. Thus, the concentration of shear strain in the slip lines is about 6 times the average axial strain. These strains are based on a measurement interval of 15  $\mu\text{m}$ . If the discontinuity in displacements across the slip lines are divided by the width of the slipline, as measured from the photograph (1.7 to 2.1  $\mu\text{m}$ ) then the strains across the sliplines are increased to between 0.12 and 0.14, or 29 times the average axial strain.

After further loading raised the stress to 920 MPa, holding relaxed the stress to 910 MPa. The macroscopic axial strain at that condition was approximately 0.031. The average axial strain measured in grain 3, **Fig. 7**, was 0.025, and 0.036 was maximum shear strain measured. As seen in the figure, the strain has become much more homogeneous, indicating that additional strain has taken place in locations other than within the slip lines.

The strains measured for these three stresses are summarized in **Table 3**.

**Table 3**  
Summary of measured strains

Stress MPa	Average strains macroscopic	microscopic	Strain in slip line
750	0.0108	0.002	--
825	0.0133	0.0045	0.13
920	0.031	0.030	--

Finally, values of stress and strain were measured from the curves of Figs. 1 and 2, in order to exclude the stress changes caused by slip line formation and the strains due to creep. The resulting curves are plotted in **Fig. 8**, where comparison is made to the tensile stress-strain curves of Adams, et al. [4] for pure Nb and one stress-strain curve for Nb-5Cr measured at UTRC. From the lines fit to these data, as shown in **Fig. 8**, the workhardening coefficient ( $n$ ) and stress coefficient ( $\sigma_0$ ) may be determined for the equation

$$\sigma = \sigma_0 \varepsilon^n \quad (2)$$

that can be used to describe these stress-strain curves. The values derived

from the curves of Fig. 8 are listed in **Table 4**.

**Table 4**  
Parameters that describe stress-strain curves

Material	grain size mm	yield stress MPa	n	$\sigma_0$ MPa
Nb [4]	0.024	165	0.12	280
Nb [4]	0.700	147	0.066	190
Nb-5Cr	~1	545	0.013	590
50Nb-13Cr-37Ti #1	1.5	933	0.041	1200
50Nb-13Cr-37Ti #2	1.5	856	0.056	1275

From these data, it can be concluded that the work hardening coefficient for this alloy is about what would be expected from the available data on pure Nb, and that work hardening is likely to be a strong function of grain size. These data also show the large effect of solid solution strengthening caused mainly by Cr additions to Nb, although some effect of Ti also would be expected.

Specimen 1 was examined by transmission electron microscopy (TEM) through the SHARE program at Oak Ridge National Laboratory. The complete results of the TEM work are reported elsewhere [4], but shown in **Fig. 9** is one example of the dislocation structure and slip lines observed. The slip lines in the figure are seen impinging on each other, unlike the slip lines shown in Figs. 6 and 7. The width of the slip lines as seen in TEM are about the same as measured from the photographs of Fig. 6. The dislocation structure within the slip lines is a dense tangle of dislocations, whereas the dislocations in between are of much lower density and confined to only a few planes. The slip planes on which the dislocations lie are thought to be {110}.

## DISCUSSION

Analysis of the stress-strain curves from this alloy indicate that the strain hardening exponent is not much different from that of large grained pure Nb. The main effect of alloying is to strongly increase the yield stress through solid solution strengthening.

Niobium has not been reported as forming localized deformation through the formation of slip lines, as observed in these experiments, and it is not understood why massive slip occurs in some alloys and not in others. The slip

lines that do form result in strains of  $\approx 0.13$ , and cause load drops in the stress-strain curve, but subsequent straining of the material does not cause more localized deformation in these slip lines. In other words, additional straining of the specimen resulted in homogeneous deformation, rather than concentration of strain in the slip lines.

This alloy has been found to have high fracture toughness [1], and this characteristic of slip homogenization after the formation of highly localized slip is probably one reason for high toughness in that a large plastic zone forms at the tip of the crack. In Figs. 6 and 7 considerable deformation has occurred on multiple slip planes, probably {110} as identified by TEM.

The room temperature creep observed in this alloy probably is related to the formation of slip highly localized into slip lines. From the perspective of structural alloy development, room temperature creep is a disturbing characteristic. In addition, the stress exponent of the creep rate is large, meaning that a small change in stress resulted in a large increase in creep rate.

## ACKNOWLEDGEMENT

Technical assistance was furnished by Jim Spencer and Byron Chapa. Funding for this research was from Air Force Office of Scientific Research, Contract F48620-95-C-0043.

## REFERENCES

1. K.S. Chan, Met. and Mat. Trans. A, 1996, v. 27A, pp. 2518-2531.
2. D.L. Davidson, K.S. Chan, and D.L. Anton, Met. and Mat. Trans. A, 1996, v. 27A, pp. 3007-3018.
3. D.R. Williams, D.L. Davidson, and J. Lankford, Exper. Mech., 1980, v. 20, pp. 134-139.
4. M.A. Adams, A.C. Roberts, and R.E. Smallman, Acta. Met., 1960, v.8, pp. 328-337.

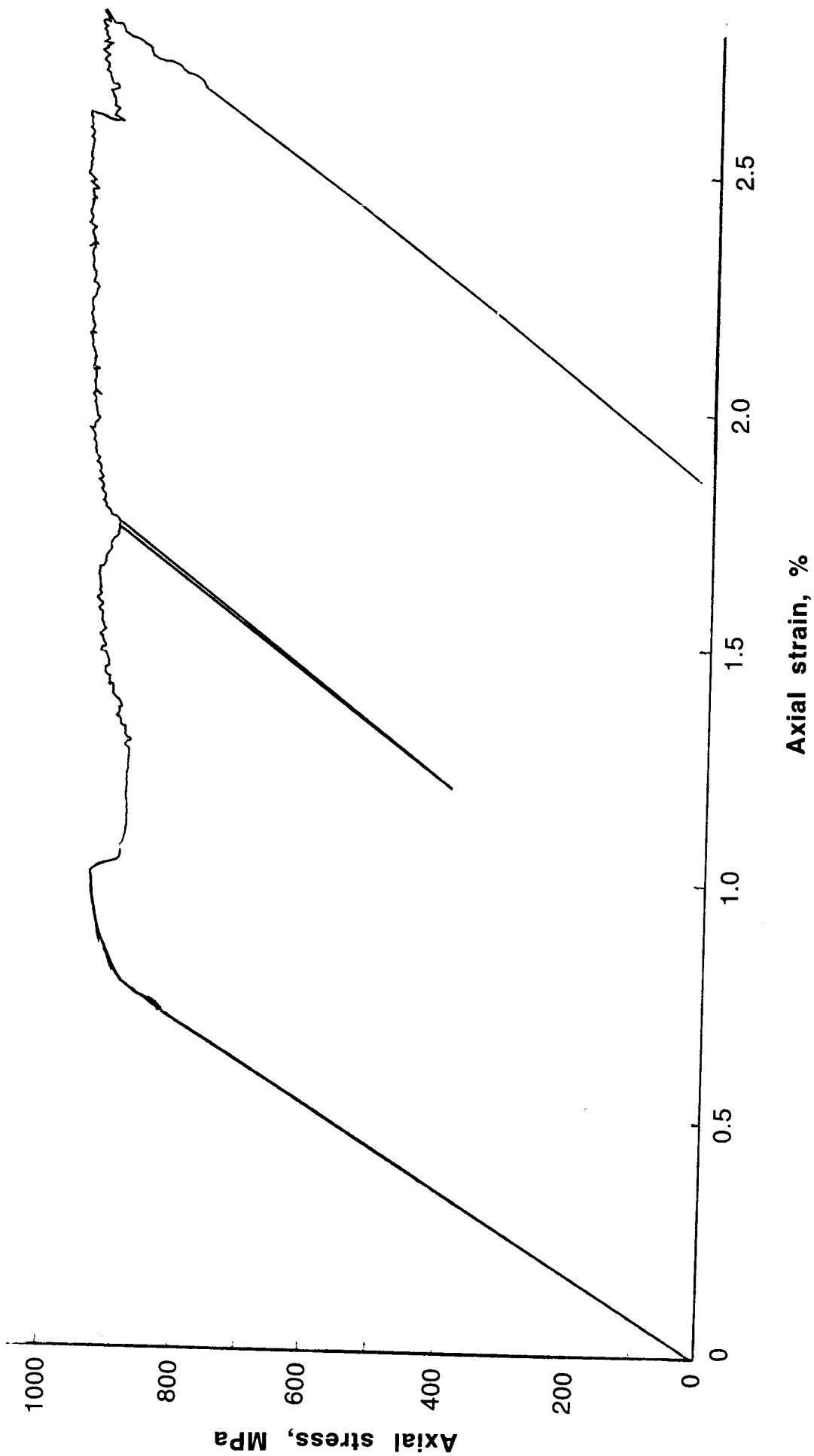


Fig. 1 Tensile deformation curve for specimen 1 in the laboratory machine. An audible "click" was heard at the load drop near yield, but no crack was visible. Modulus was measured during the partial unloading half way to maximum strain. The load drop near maximum strain resulted in a visible crack, and the experiment was halted.

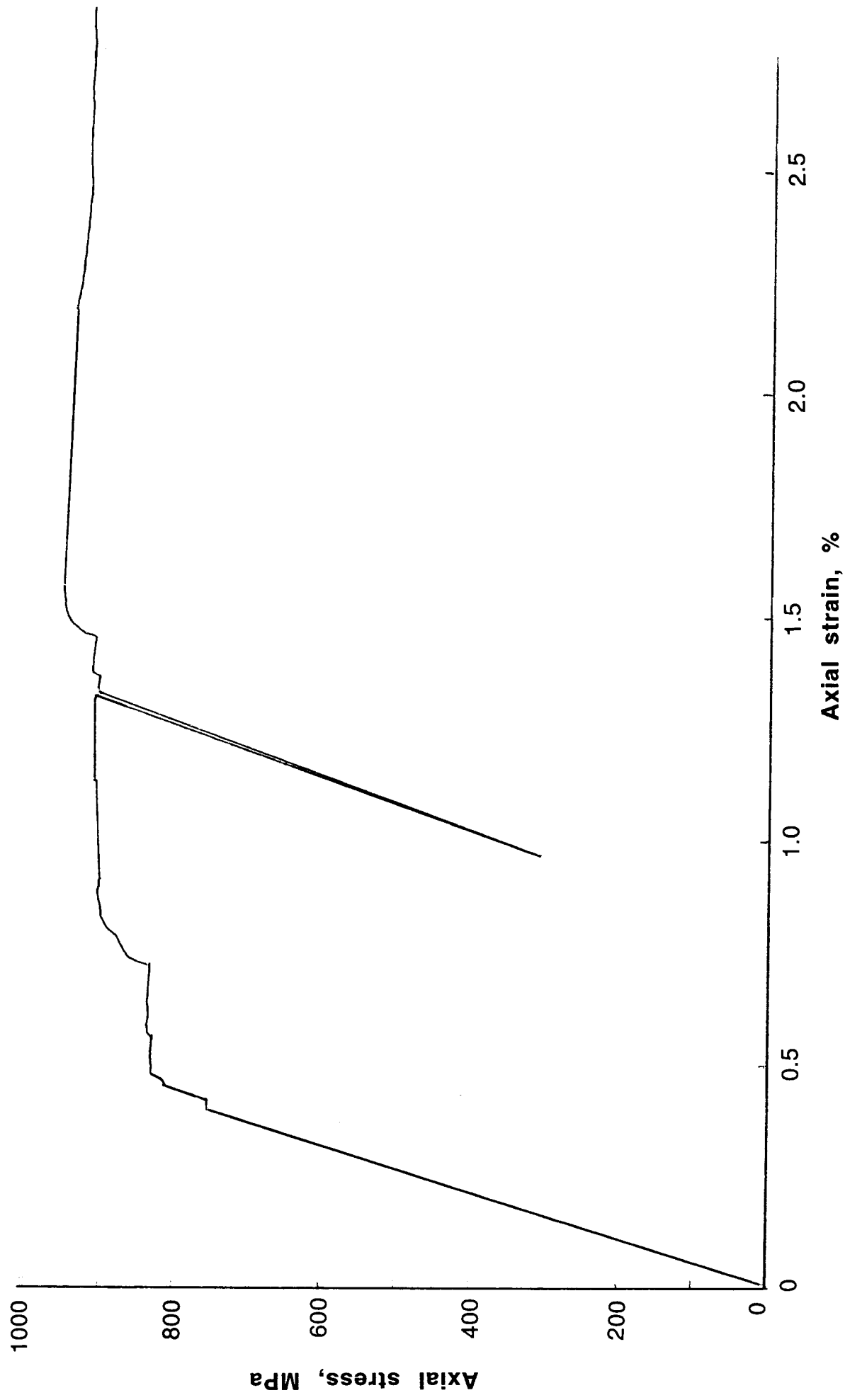


Fig. 2 Tensile deformation curve for specimen 2 in the SEM loading system. Loading was periodically halted to make photographs, during which creep occurred. Partial unloading at about half maximum strain was used to measure modulus. The experiment was stopped with the specimen unbroken.

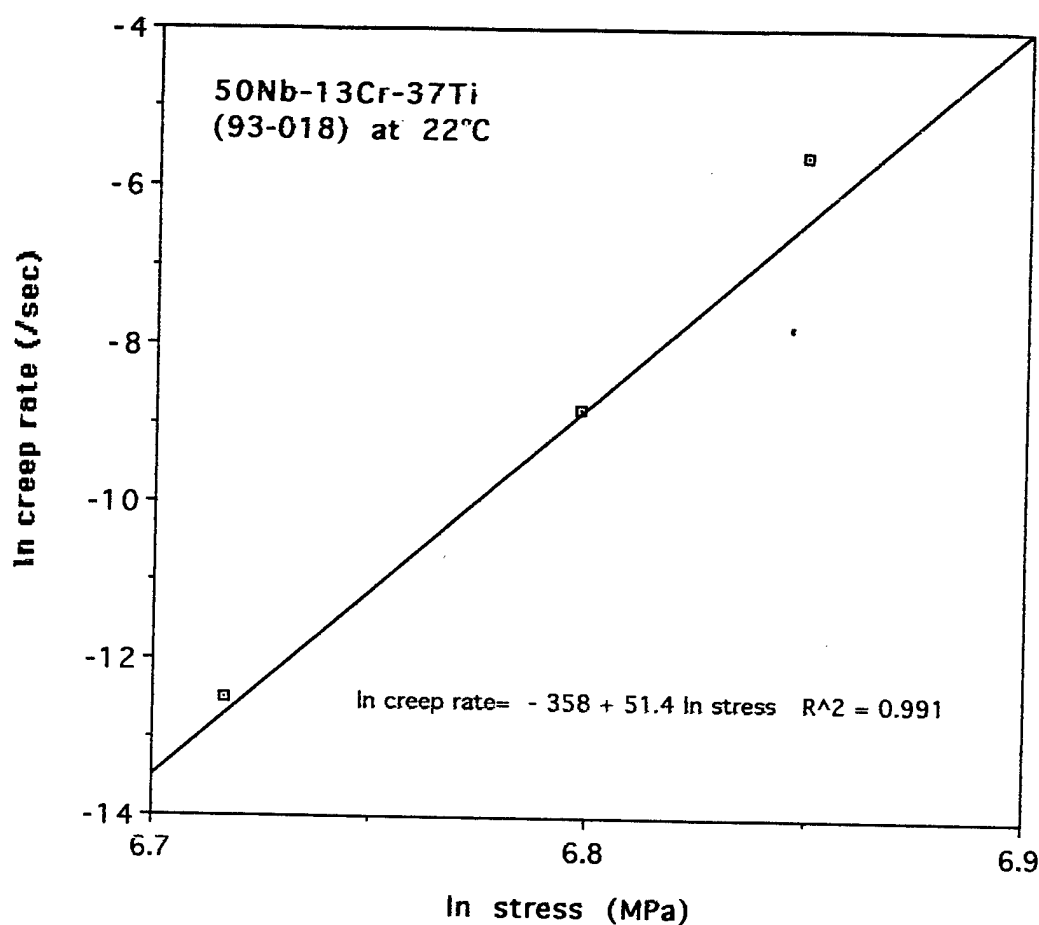
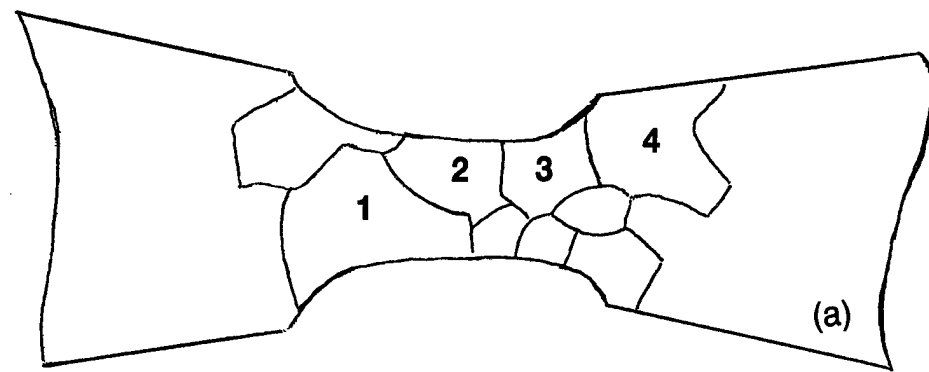
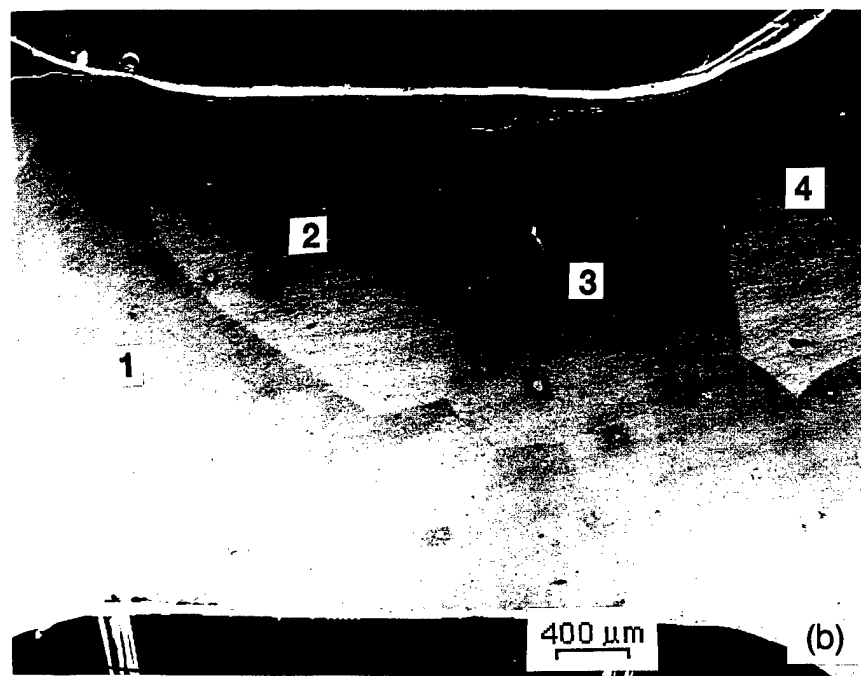


Fig. 3 Creep rate vs. stress, from specimen 2 (SEM).

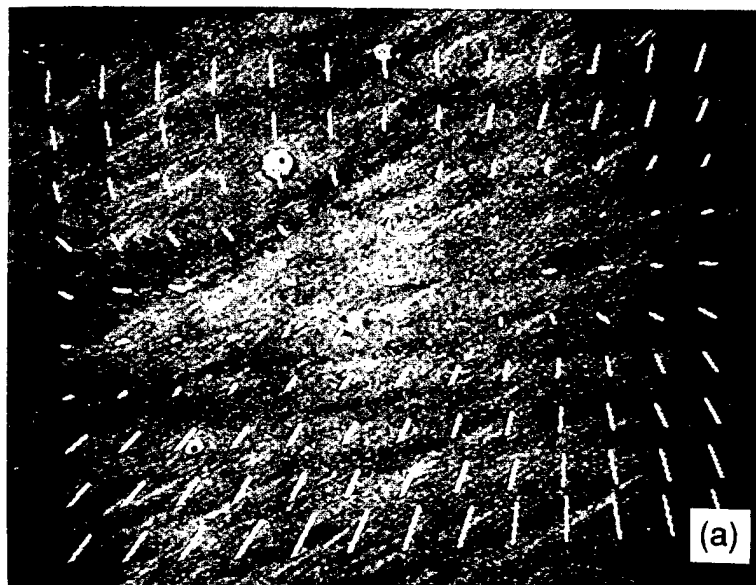


(a)

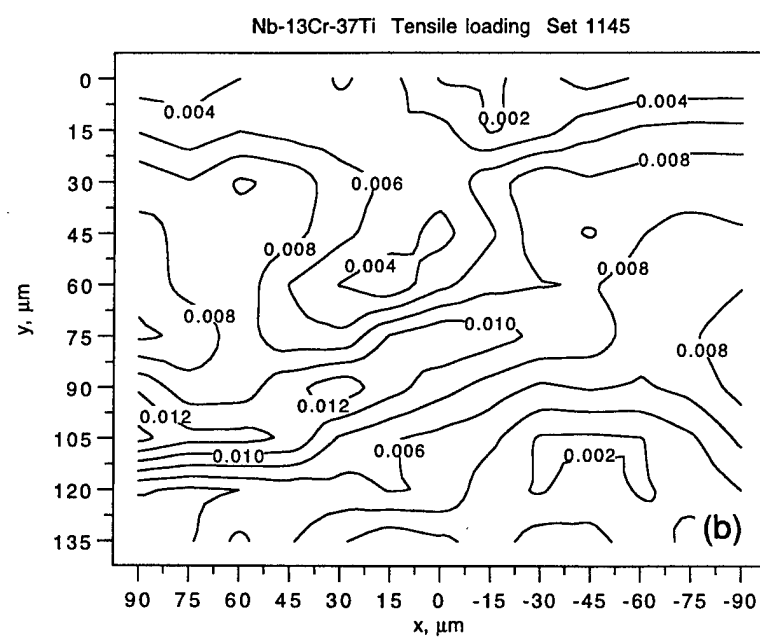


(b)

Fig. 4 (a) Drawing of grains in specimen 2 (SEM) showing grains that were oriented by Laue back reflection x-rays. (b) Photograph of specimen gage section showing grain structure.

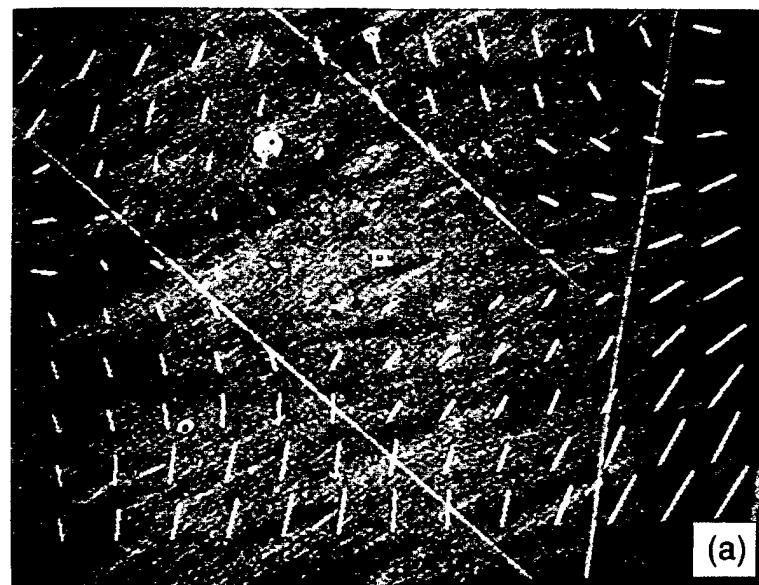


(a)



(b)

Fig. 5 SEM secondary electron image of Grain 4, stress = 750 MPa, with overlay of displacements each 15 μm. Displacement magnification is 15X actual. Also shown is a contour map of the maximum shear strains. Set 1145



Nb-13Cr-37Nb Tensile loading Set 1146

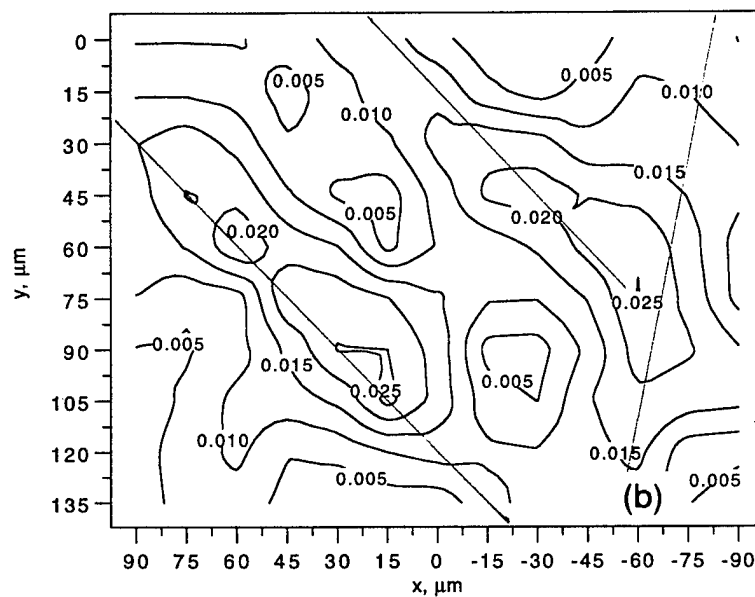


Fig. 6 SEM secondary electron image of Grain 4, stress = 825 MPa, with overlay of displacements each 15  $\mu\text{m}$ . Displacement magnification is 15X actual. Also shown is a contour map of the maximum shear strains. Strain has concentrated along the slip lines.

Set 1146

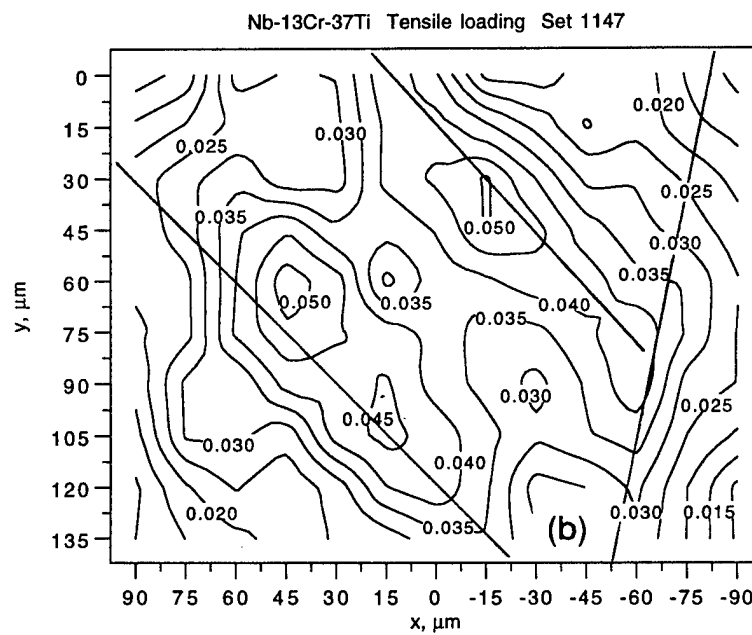
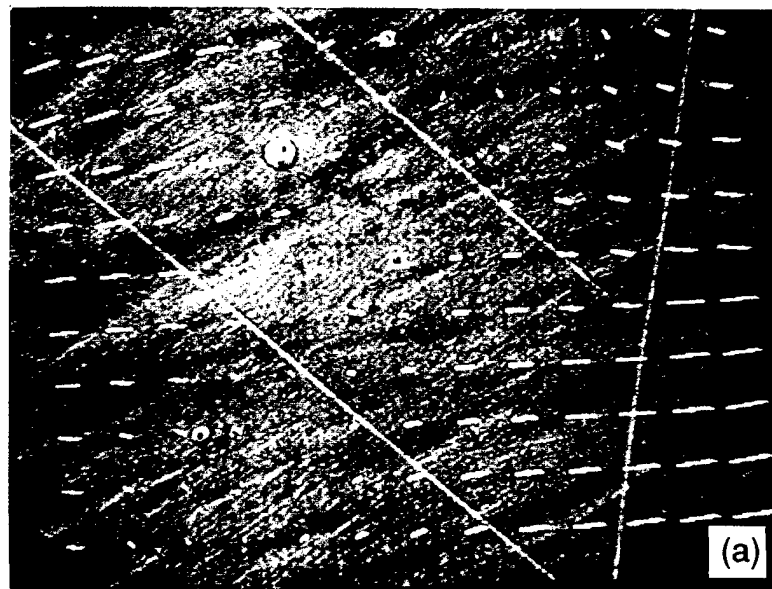


Fig. 7 SEM secondary electron image of Grain 4, stress = 910 MPa, with overlay of displacements each 15  $\mu\text{m}$ . Displacement magnification is 3X actual. Also shown is a contour map of the maximum shear strains that shows further concentration of strain at the slip lines, but also increased strain throughout the deforming region.

Set 1147

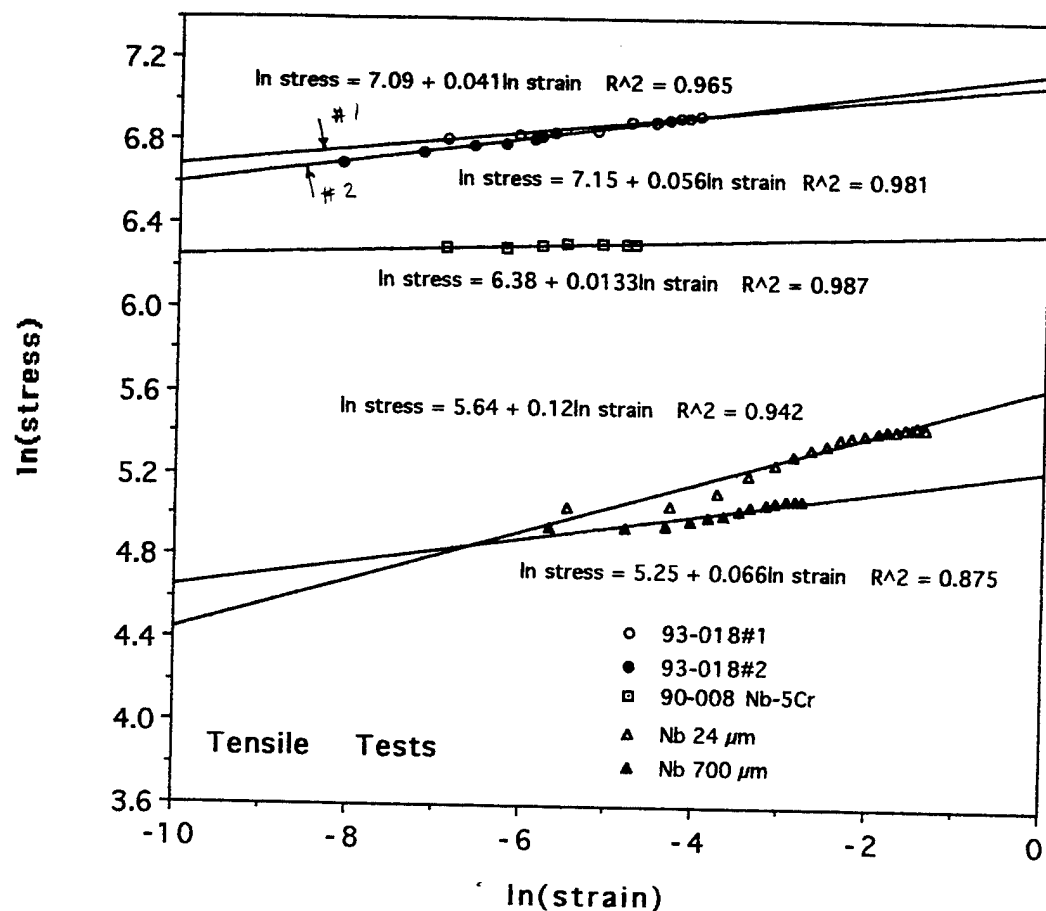


Fig. 8 Stress vs. strain for Nb and Nb alloys - derivation of work hardening coefficient.



Fig. 9 TEM photo of slip lines and dislocations

## TRANSMISSION ELECTRON MICROSCOPY OF Nb-BASE ALLOY AND COMPOSITE

D.L. Davidson and K.S. Chan  
Southwest Research Institute  
San Antonio, TX 78228

P.X. Maziasz  
Oak Ridge National Laboratory  
Oak Ridge, TN

### ABSTRACT

The dislocation structure of a high fracture toughness single phase niobium alloy ( $K_c = 60$  to  $100$  MPa $\sqrt{m}$ ) was investigated as were the dislocation structure and precipitate morphology of an *in situ* composite that has the high toughness alloy as the matrix, according to the phase diagram. The matrix alloy had a dominance of long, straight screw dislocations mostly on  $\{110\}$ , while the composite matrix had dense tangles and curved dislocations. Precipitates in the composite were on planes with 3-fold symmetry, probably the  $\{111\}$ . From measurement of the lattice parameter of the composite matrix, the dislocation structure seen can be reconciled with that of pure Nb.

### INTRODUCTION

To understand the deformation of metals and alloys, several experimental techniques are required. The stress-strain curve is fundamental to a knowledge of plasticity, and this is readily measured using laboratory loading equipment and strain gages. But dislocation motion is responsible for plastic deformation, so an understanding of how dislocations move and interact is also necessary, and that requires the use of transmission electron microscopy (TEM). Observation of the dislocation structure is not only difficult because of specimen preparation and interpretation of the structures and diffraction patterns, but TEM allows only minute quantities of material to be investigated, so caution must be used when these results are correlated to other deformation experiments, such as the stress-strain curve.

When the material has precipitates, it is useful to know the crystallography of the precipitates and how dislocations interact with them. During the 1960s, there were many fundamental studies of deformation behavior and dislocation morphology in the body centered cubic (bcc) transition metals, and there were a few studies in transition metal alloys. Most of the studies were of single crystals of high purity. An example of one deformation study of Nb is that of

Duesbery and Foxhall [1] and an example of a TEM study is that of Taylor and Christian [2]. Interstitials (C, O, and N) have a very strong influence on the deformation behavior of bcc metals; thus for fundamental studies, single crystals were used because it was otherwise difficult to obtain materials that were substantially free of interstitial effects. The main variables investigated were temperature and the effects of differences between the stress axis and the crystal axis.

One of the principal results that emerged from all the work on transition metals was the realization that there is an "athermal temperature" below which the motion of screw dislocations controls the deformation process. It was found that there was a large difference between the friction stress, or Peierls-Nabarro stress, required to move edge and screw dislocations. Hirsch [3] was the first to recognize that screw dislocations had a high friction stress because the core of these dislocations was dissociated onto several slip planes.

This paper reports a TEM investigation into the substructure of a composite and an alloy of nearly the same composition. A single phase material is the matrix alloy for the composite. The TEM work supplements the measurement of stress-strain curves on macroscopic specimens and detailed stress-strain information determined using a loading stage for the SEM and the stereoimaging technique [4]. The chemical composition of these two materials was very similar: The solid solution alloy had the composition 50Nb-13Cr-37Ti and the composite had the composition 48Nb-15Cr-37Ti. The alloy was produced by casting and the composite was produced by consolidating powders that were mechanically alloyed.

The objectives of this work were as follows: For the 50Nb-13Cr-37Ti alloy (1) to determine the morphology of the dislocation structure and (2) plane(s) slip of the dislocations, (3) look for dislocations separated by stacking faults, (4) find if any twinning or antiphases were formed, and (5) examine the the degree of ordering, if any. For the 48Nb-15Cr-37Ti material that had been heat treated to precipitate the  $\text{Cr}_2\text{Nb}$  phase, the examination was designed to determine (1) the amount of intermetallic present, (2) the size and shape of submicron particles not visible by ordinary metallography, (3) the habit planes, if any, (4) the level of structural defects, and (5) the interrelationship between the dislocation morphology and the intermetallic.

## SPECIMEN PREPARATION

The TEM specimens were prepared at Oak Ridge National Laboratory. Samples of the materials to be examined were cut using electric discharge machining (EDM) from the bulk that had been deformed in tension. The alloy was deformed to a tensile strain of approximately 2.8 % and the composite was deformed about 1.5%. Specimen blanks were ground with silicon carbide papers to a thickness of 125  $\mu\text{m}$  and selectively thinned further with a Gatan dimpling device using 6  $\mu\text{m}$  diamond paste. Jet polishing was then used for final thinning and perforation. Perchloric acid in methanol with butal alcohol added was used at -25°C on the plateau at 16 vdc, 60 mA current. An oxide was found to be forming on the specimens containing higher amounts of intermetallic, so the thinning method was modified to minimize this artifact. The specimen was removed from the jet polisher each 20 secs. and dipped in a 5 % solution of hydrogen peroxide. After perforation, the sample was soaked in the hydrogen peroxide solution for about 2 min. Some oxide remained on these samples even after this cleaning treatment, so the samples were ion milled for 15 min. at 6 keV with the beam at an angle of 16° to the plane of the specimen. This grazing angle was used to minimize ion damage in the specimen. After removal of the oxide, the specimen was cleaned further by ion exposure for 20 min. with a beam voltage of 3 keV at an 11° angle.

## MICROSCOPY

The specimens were examined using a Philips CM 30, 300 keV electron microscope equipped with a double tilting stage. Standard magnifications of 1600, 3000 and 19000X were used for all specimens, with a few other magnifications used as needed. A cold finger was used to avoid contamination. A Hitachi 4100 FEG SEM was used at 5 keV to image the surfaces of the specimens at the same magnifications, after TEM examination.

## RESULTS

Single phase alloy (50Nb-13Cr-37Ti): Grains that contained slip bands were found to be electron transparent. Within the slip bands, there were dense tangles of dislocations, as is shown in Fig. 1. In the regions outside the slip bands, "matrix" dislocations were found that were long and straight, but showed no evidence of splitting. In other words, dislocations separated by stacking faults were not found. Antiphase boundaries were not found. No

intermetallic particles were found within the grains, within slip bands, nor within the grain boundary examined. The matrix exhibited a strange "mottled" look that had the appearance of small cellular regions. This mottled appearance was probably an artifact of specimen preparation. No ordering was found in any diffraction pattern. When the slip band was tilted so that the view was perpendicular to the beam axis, two regions of dense dislocations could be seen separated by a narrow region of low dislocation density in the middle.

The dislocation pattern caused by deformation before slip band formation was evidently interrupted by the slip band, as shown in **Fig. 2**, where long, straight screw dislocations with the same orientation can be seen on both sides of the slip band. On the right side, dislocations with 3 orientations are seen. Only dislocations close to the slip band are seen in one orientation. The angle between the dislocations is consistent with the dislocations lying along 3  $\langle 111 \rangle$  directions. On the right side of the slip band, the angle between the 2 of dislocation directions that show the longest segments is close to  $70^\circ$ , which is consistent with the plane of the thin foil and the plane on which these dislocations are lying being the  $\{110\}$ .

The region seen in **Fig. 3** is oriented so that dislocations of one orientation only can be seen. Numerous jogs in these dislocations are visible, and there are some mixed dislocations as well as edge segments. Dislocations in two orientations approximately  $90^\circ$  apart are seen in **Fig. 4**; this pattern is consistent with screw dislocations on the  $\{110\}$ . Some curved dislocation segments are also visible. Three dislocation directions are again seen in **Fig. 5**, and the angles between these directions are consistent with screw dislocations lying on  $\{110\}$ .

Two phase mechanically alloyed material (48Nb-15Cr-37Ti): The thinned regions were in three adjacent grains. Regions just next to grain boundaries were not very electron transparent. A thin layer was found in the grain boundaries that was likely to be an oxide because it is more electron transparent than the surroundings. Within the matrix, there was a high density of intermetallic particles that are lens or plate shaped, as illustrated in **Fig. 6**. The thickness of these particles is submicrometer ( $0.1 - 0.6 \mu\text{m}$ ) and there is a large distribution of lengths. The particles are oriented to one another in some specific way; i.e., there is a habit plane for these intermetallics. The long axis of the precipitates shows 3 fold symmetry, which would indicate that the long axis is along the  $\langle 111 \rangle$  of the matrix.

Individual dislocations in the matrix between the particles were curved, **Fig. 7**, and loops were seen, as shown in **Fig. 8**, but there was no evidence that they were split. In **Fig. 8**, the large dark regular shape are particles, but the other dark areas are thought to be dense tangles of dislocations. No antiphase regions or stacking faults were seen in the matrix. Diffraction patterns did not indicate any ordering of the matrix.

Dislocations intersecting precipitates can be seen in **Fig. 9**, and it appears that these dislocations are attached to the particles on one end. The origin of the background texture effects is unknown. It could be contrast from braids of dislocations, or it might be an artifact of the thinning process. In places, it appears to be numerous short dislocation segments.

A dark field view of the  $\text{Cr}_2\text{Nb}$  particles is shown in **Fig. 10**, which shows their internal structure. Nothing can be seen that would indicate twinning or other planar faults were present as have been seen within large particles in materials that were slowly and rapidly solidified from the melt [4].

## DISCUSSION

50Nb-13Cr-37Ti single phase alloy: The dislocation morphologies illustrated in Figs. 1-5 have been compared to photographs of dislocation structures, and descriptions of dislocation structures, in pure Nb and alloys of Nb. Dislocation structures in pure Nb single crystals deformed at low temperatures and up to ambient were reported by Taylor and Christian [2]. At ambient temperature, dislocations formed dense tangles, often on the  $\{112\}$ , at lower strains, and these evolved into cell structures at higher strains. Crystals deformed at 77 and 158°K evidenced long, straight primary screw dislocations. The dislocations in 50Nb-13Cr-37Ti at ambient temperature, large strain, look more like the description of Nb at low temperature, which is an indication that the difference in edge and screw velocities caused by decreasing temperature in Nb was caused by alloying in 50Nb-13Cr-37Ti.

Foxall and Statham studied the deformation of several alloys of Nb [6]. Dislocations found in Nb-16Mo deformed at ambient temperature to a low strain look similar to those seen in 50Nb-13Cr-37Ti, i.e., long, straight screws. However, with increasing strain, the dislocation distribution becomes more homogeneous. In Nb-9Re deformed at ambient temperature, the dislocations arrangement at low strain is again similar to 50Nb-13Cr-37Ti, except there are more edge dislocation segments. Deformation at 77°K resulted in many long

screw dislocations, but with more cusps and loop ends than seen in 50Nb-13Cr-37Ti.

Low and Turkalo studied dislocation arrangements in Fe-3wt.%Si deformed to a 0.01 strain in compression [7]. They saw long, straight screw dislocations, some with jogs and cusps, and some without. Some edge dislocations were also seen as parts of dislocation loops. Dislocations in their photographs look similar to those from 50Nb-13Cr-37Ti, and similar to those in Nb-Mo and Nb-Re at low temperatures.

The observation of long, straight screw dislocations in this alloy are in agreement with calculations that indicated the Peierls-Nabarro (P-N) barrier energy and stress would be higher for screw dislocations than for edge dislocations on the {110} and {112}. The higher P-N energy and stress means that screw dislocations are less mobile than edge dislocations. This higher mobility for edge dislocations means that they can move farther and escape the foil, leaving behind long segments of screw dislocations that are straight because they are so immobile.

48Nb-15Cr-37Ti mechanically alloyed composite: The matrix of this material, according to the phase diagram, should have about the same composition as the single phase 50Nb-13Cr-37Ti alloy. However, the dislocation arrangements are entirely different than seen in the unreinforced material. Dislocations seen in Figs. 7-9 are generally curved, and the few loops that can be seen are approximately smoothly ovular. Some cusps are evident. These dislocation shapes are so markedly different from those seen in 50Nb-13Cr-37Ti that they would seem to be from another alloy.

The lattice parameter of 50Nb-13Cr-37Ti is 3.228 Å [5], and the lattice parameter of the matrix of the composite is 3.224 to 3.245 Å in the as-received condition, increasing to  $\approx$  3.310 Å with the precipitation of  $\approx$  20 v/o  $\text{Cr}_2\text{Nb}$  [8]. An estimate of the area fraction of precipitates seen edge on in Fig. 7 is  $\approx$  5%. When this is multiplied by 3 to include the precipitates on the 2 other habit planes, the estimate of volume fraction of precipitate in this region of material is about 15%. An estimate of the lattice parameter with 15%  $\text{Cr}_2\text{Nb}$  is about the same as for pure Nb = 3.302 Å, so the matrix of this composite may be closer to pure Nb than to the 50Nb-13Cr-37Ti alloy, which would be consistent with the high density regions of tangled dislocations and the curved individual dislocations that can be seen in Figs. 7-9. There is also a lack of long screw

dislocations as were seen in the matrix alloy. Examination of the matrix of this material by Auger Electron Spectroscopy has shown that there are regions of high Ti concentration that appear as a consequence of heat treatment, and this would lead to depletion of the matrix in Ti content. Formation of  $\text{Cr}_2\text{Nb}$  would deplete the matrix of Cr. The result of this de-alloying of the matrix would be to increase the lattice parameter as the Nb content of the matrix increased.

## CONCLUSIONS

1. The alloy composition 50Nb-13Cr-37Ti is a single phase, solid solution material that contains no  $\text{Cr}_2\text{Nb}$  and is not ordered. Dislocations are not split, exhibiting no stacking faults or antiphase boundaries.
2. Dislocation arrangements in 50Nb-13Cr-37Ti consist primarily of screws on  $\{110\}$  with some evidence of edges. Some jogs and cusps are seen on the screws, but the number per unit length is small relative to photographs of similar dislocations in Nb, Nb-Mo, and Nb-Re alloys found in the literature.
3. The dislocation arrangements in 50Nb-13Cr-37Ti indicate a large difference in mobility between edges and screws, with the screw mobility being the least. By comparison with [2], the mobility difference between edges and screws is smaller in Nb.
4. The screw/edge dislocation mobility ratio difference between Nb and Nb-13Cr-37Ti is similar to the effect of lowering the temperature on the ratio in Nb, Nb-Mo and Nb-Re alloys.
5. The matrix of the 48Nb-15Cr-37Ti in situ composite showed no evidence of ordering, dissociated dislocations, stacking faults, or antiphase boundaries.
6. Precipitates in the 48Nb-15Cr-37Ti composite were found on planes with 3-fold symmetry, probably the  $\{111\}$ , and have a plate-like shape. The average thickness was measured as 0.02 to 0.06  $\mu\text{m}$  thick by 0.15 to 1.25  $\mu\text{m}$  long in the plane of the foil, with a volume fraction estimated to be  $\approx 15\%$ .
7. Dislocations in the 48Nb-15Cr-37Ti composite are very different than those found in the 50Nb-13Cr-37Ti matrix alloy. Tangles of dislocations and curved individual dislocations are seen in contrast to the long, straight screw dislocations seen in the matrix alloy.

8. An estimate of the volume fraction of  $\text{Cr}_2\text{Nb}$  seen in the composite, from which the lattice parameter of the matrix of this composite can be derived, indicates that the matrix may be closer to Nb in composition than 50Nb-13Cr-37Ti, which would correlate better with the dislocation pattern seen in Nb than those seen in the matrix alloy.

**ACKNOWLEDGEMENT** The assistance of the SHARE program at Oak Ridge National Laboratory made this research possible. Funding of work on the Nb materials was furnished by Air Force Office of Scientific Research under contract F49620-95-C-0043. Mr. Wade Jones prepared the specimens. The specimens were deformed at SwRI technical assistance of Byron Chapa.

## REFERENCES

1. M.S. Duesbery and R.A. Foxhall, Phil. Mag., 1969, v. 20, pp. 719-751.
2. G. Taylor and J.W. Christian, Phil. Mag., 1967, v. 15, pp. 893-
3. P.B. Hirsch as quoted by J.W. Christian, **Second International Conf. on Strength of Metals and Alloys**, v. 1, Am. Soc. for Metals, Metal Park, OH, 1970, pp. 31-53.
4. See Chapter 10 on tensile experiments.
5. K.S. Chan, D.L. Davidson, and D.L. Anton, Met. and Mat. Trans. A, 1997, v. 28A, pp. 1797-1808.
6. R.A. Foxall and C.D. Statham, Acta Met., 1970, v. 18, pp. 1147-1158.
7. J.R. Low and A.M. Turkalo, Acta Met., 1962, v. 10, pp. 215-227.
8. See Chapter 3 for lattice parameters.

**FEM Simulation of Effects of Microstructure, Stress State,  
and Interface Strength on Flow Localization and Constraint  
Development in Nb/Cr<sub>2</sub>Nb *In-Situ* Composites**

**Kwai S. Chan and Guoyu Lin**

**Metallurgical and Materials Transactions A  
(submitted)**

# **FEM Simulation of Effects of Microstructure, Stress State, and Interface Strength on Flow Localization and Constraint Development in Nb/Cr<sub>2</sub>Nb *In-Situ* Composites**

**Kwai S. Chan<sup>1</sup> and Guoyu Lin<sup>2</sup>**

<sup>1</sup> Southwest Research Institute, San Antonio, TX 78238

<sup>2</sup> GKSS Research Center, Geesthacht, Germany (currently at ANSYS, Canonsburg, PA)

## **Abstract**

The effects of microstructure, stress state, and interface strength on the yield strength, flow localization, plastic constraint and damage development in Nb/Cr<sub>2</sub>Nb *in-situ* composites have been investigated by the finite-element method. The microstructure of the *in-situ* composite was represented in terms of a unit rectangular or square cell containing Cr<sub>2</sub>Nb particles embedded within a solid solution alloy matrix. The hard particles are considered to be elastic and isotropic, while the matrix is elastic-plastic obeying the Ramberg-Osgood constitutive relation. The FEM model was utilized to compute the composite strength, local hydrostatic stress and plastic strain distributions as functions of volume fraction of particles, stress state, and interface strength. The results were used to elucidate the influence of microstructure, stress state, and interface property on the development of plastic constraint and damage in Nb/Cr<sub>2</sub>Nb composites.

## **Introduction**

Many emerging material systems for high temperature aerospace applications are *in-situ* composites that are comprised of a two-phase microstructure containing hard intermetallic particles embedded in a solid solution matrix [1-19]. Examples of these *in-situ* composites include Nb-Ti-Hf-Cr-Al-Si [2-5], Nb-Cr-Ti-Al [9,10], Nb-Cr-Ti [11-16], Nb-Al-Ti [7,8], and Mo-Si-B [17-19] systems. The main characteristics of these *in-situ* composites are: (1) a large volume fraction of intermetallic particles that are intended to provide high-temperature strength, creep strength, and oxidation resistance, and (2) a ductile solid solution alloy matrix that is intended to provide tensile ductility and fracture resistance at ambient temperatures. None of the current *in-situ* composites exhibit all the desired mechanical properties for applications at or above 1200°C, but the Nb-Ti-Hf-Cr-Al-Si system is near the target as it is by far the most developed *in-situ* composite system.

The fatigue and fracture characteristics of many *in-situ* composites have been identified. Some of the important features associated with fracture of Nb-Cr-Ti *in-situ* composites are particle fracture and flow localization in the ligament between cracked particles or microcracks [12-14]. This is illustrated in Figure 1, which depicts the concentration of strain in a ligament located between the tip of the main crack and a cracked particle in Nb-Cr-Ti that contained 38% Cr<sub>2</sub>Nb particles in a ductile matrix of Nb solid solution [12]. It is evident from Figure 1 that the plastic strain localized within a small deformation zone. Because of strain localization, the ligament fractured relatively easily and did not provide sufficient bridging force or plastic dissipation to improve fracture resistance. For fracture toughness consideration, it would thus be desirable to eliminate or delay particle fracture in *in-situ* composites containing hard particles.

Qualitatively, both particle fracture and flow localization in the matrix ligament can be explained on the basis of a high plastic constraint due to a buildup of the triaxial tensile stress arising from maintaining compatibility between the non-deformable particles and the deformable matrix. Experimental measurements of local strains in *in-situ* composites indicated a high constraint near the hard particles [20]. This understanding, however, is insufficient for devising a means for reducing the plastic constraint to eliminate particle fracture, to reduce flow localization, and to enhance plastic dissipation in the ligament prior to failure. To improve the fracture resistance of *in-situ* composites, it is necessary to develop a fundamental understanding of the roles of the microstructure and the interface strength in the buildup of plastic constraint that lead to particle fracture and flow localization.

The development of plastic constraint in particle-reinforced metal-matrix composites has been investigated extensively via finite-element analyses of representative composite microstructures idealized as a unit cell containing a whisker, a square particle, or a sphere in a ductile matrix [21-24]. The whisker has been shown to be most effective in increasing composite strength and plastic constraint when compared to other particle shapes such as cylinder, cube, and sphere [21-23]. Regions of high plastic constraint in the matrix are prone to void nucleation and growth, while those in the particle are prone to brittle fracture [22,24]. In addition to particle shape, plastic constraint also depends on the volume fraction and spatial distribution of particles, as well as on the void nucleation and growth at the interface [22-24]. Most, if not all, of the prior studies were limited to small volume fractions (< 20%) of particles with a strong particle/matrix interface. There is little work on composite microstructures with particle contents in excess of 20%. The effects of the global stress state, cracked particle, and the interface strength have not been examined for either MMC or *in-situ* composites.

The objective of this paper is to present results of an FEM investigation whose goals were: (1) to determine the plastic constraint in the *in-situ* composites as a function of volume fraction of spherical particles, the external stress state, and the interface properties; (2) to develop a basic understanding of the flow localization process in the ligament; and (3) to devise a means to improve the fracture resistance of the *in-situ* composite by mitigating flow localization in the ligament and increasing the plastic dissipation in the near-tip process zone. The paper will first present results that establish the influence of microstructure and stress state on the local plastic constraint in the

matrix. The influence of cracked particles and the interface strength (or toughness) on the local constraint will then be examined. The FEM results are then compared against experimental data to establish a fundamental understanding of the relationships between volume fraction of particles, matrix constraint, and interface strength on the macroscopic strength and damage development in Nb/Cr<sub>2</sub>Nb *in-situ* composites. Particle size is not considered in this paper since the continuum model does not provide information concerning this effect.

## The Finite Element Model

The present study emphasizes on the plastic constraint on the local deformation in the ductile matrix as a result of the presence of hard, brittle spherical particles in the microstructure. Spherical particle is chosen because it produces a plastic constraint that is lower than those for particle shapes such as whisker, cylinder, cube or cornered particles [21-24]. The microstructure of the *in-situ* composite is modeled via a unit cell containing Cr<sub>2</sub>Nb particles in a Nb solid solution matrix. Two typical unit cells with different particle configurations are used, as shown in Figure 2. The rectangular unit, shown in Figure 2(a), represents a periodic hexagonal array packing arrangement [25]. The square unit cell, shown in Figure 2(b), corresponds to the configuration where particles are located at the edge of the square or equivalently, at the center of the square, i.e., the so-called square edge-packing [25]. The finite element analyses are performed within the context of the 2D generalized plane strain formulation. Finite element program ABAQUS [26] were used for performing the analysis.

The Cr<sub>2</sub>Nb particle is assumed to be elastic and isotropic with Young's modulus E<sub>p</sub> and Poisson's ratio v<sub>p</sub> (E<sub>p</sub> = 216 GPa; v<sub>p</sub> = 0.333). The elastic constants for the Nb solid solution matrix are E = 123 GPa and v = 0.333, where E and v are the Young's modulus and Poisson's ratio of the matrix, respectively. The stress-strain behavior of the Nb matrix is assumed to be obey the Ramberg-Osgood constitutive relationship given by

$$\varepsilon = \frac{\sigma}{E} \left[ 1 + \alpha \left( \frac{\sigma}{\sigma_o} \right)^{n-1} \right] \quad (1)$$

where  $\sigma$  is the stress,  $\sigma_o$  is the reference yield stress, n is the inverse of the strain hardening exponent, and  $\alpha$  is an empirical constant. For the Nb solid solution alloys investigated,  $\sigma_o$  = 900 MPa, n = 30, and  $\alpha$  = 0.435 based on fitting the Ramberg-Osgood equation to the uniaxial tensile stress-strain data.

The boundary conditions of the unit cell are imposed under the generalized plane strain condition in the manner described as follows. The low edge and left edge of cell are fixed on the X<sub>2</sub> and X<sub>1</sub> direction, respectively. The constraint has been also enforced on the top edge and right edge of the cell such that the rectangular cell retains the rectangular shape during deformation. As a result of the generalized plane strain assumption, the boundary conditions include also strains and stresses that are constant in

the out-of-plane direction (normal to the unit cell plane). Both the volume fraction and the external stress are varied. The volume fraction of the Cr<sub>2</sub>Nb particle is altered by changing the radius of the particle with respect to the width of the unit cell. The stress state is varied by prescribing the stress ratio,  $\lambda$ , which is the ratio of  $\Sigma_2$  to  $\Sigma_1$ , where  $\Sigma_1$  and  $\Sigma_2$  are the principal applied stresses. For uniaxial loading condition, displacement is applied on the top edge, and the load is calculated by summing the reaction force of nodes on the top edge. For the biaxial loading condition, the biaxial force is applied on the top edge and right edge of the model, Figure 2, to ensure a constant stress ratio is applied. The RIKS technique, provided by ABAQUS [26] for the case where the solution is sought for a proportional loading problem, was used to perform the calculation when the force was applied. Figure 3 shows a typical mesh used in the present study for the rectangular unit cell. In order to capture the high strain and stress gradient across interface, very fine meshes have been put on the region near the interface. The meshes consist of about 2000 eight-node, isoparametric elements and 4000 nodes depending on the particle sizes. This meshing scheme is also used for the square unit cell model.

The overall average stress is calculated

$$\Sigma_{ij} = f \int_{V_p} \sigma_{ij} dV + (1-f) \int_{V_m} \sigma_{ij} dV \quad (2)$$

where  $f$  is the volume fraction of particles and the applied strain is defined as

$$E_i = \ln(1 + U_i / L_i) \quad (3)$$

where  $U_i$  and  $L_i$  are the edge displacement and length, respectively. In this paper, global stresses are represented by  $\Sigma_{ij}$ , while local stresses are represented by  $\sigma_{ij}$ .

Perfect bonding, representing strong interface, between the matrix and the particle is assumed for the most of the calculations. For comparison, a few calculations have been also conducted for the cases of very weak interface by assuming that there is not bonding strength between matrix and particle, and cracked particle by freeing the nodes on the lower edge of the particle. All the results presented in this paper are based on the rectangular cell, unless stated otherwise.

## Effects of Volume Fraction of Particles

The influence of the volume fraction,  $f$ , of hard Cr<sub>2</sub>Nb particles on the strength of the *in-situ* composite was examined by computing the stress-strain curves. The volume fraction,  $f$ , of particles considered ranged from 0 to 0.8, where  $f = 0$  for a solid solution matrix without particles and  $f = 0.8$  for a composite with 80% volume fraction of particles. Figure 4(a) shows the results for the calculated stress-strain curves for  $f = 0.2, 0.4, 0.6, 0.7$ , and  $0.8$  under uniaxial tension,  $\lambda = 0$ . The stress-strain curves are presented in terms of the global Mises effective stress,  $\Sigma_e$ , normalized by the uniaxial tensile yield stress,  $\sigma_o$ , versus the true strain,  $E_2$ , in the  $X_2$  direction. The stress-strain curve shows a

moderate increase in the flow stress with increasing volume fraction of particles. The largest increase of the flow stress occurs at  $f = 0.8$ . The corresponding global hydrostatic stress,  $\Sigma_H = \Sigma_{kk}/3$ , is shown as a function of true strain in Figure 4(b), which indicates increasing hydrostatic stress values with increasing volume fraction of particles.

The distribution of the plastic strain within the matrix under uniaxial tension for  $f = 0.2$  is presented in Figure 5(a), which shows the contour plot of the effective plastic strain normalized by the yield strain,  $\epsilon_0 = \sigma_0/E$ . The particles are elastic, while the matrix is plastic. The plastic strain is concentrated at the interface between the particle and the matrix as well as in the matrices on the upper and lower planes of the unit cell. The corresponding contour plot of the local hydrostatic stress,  $\sigma_H$ , is shown in Figure 5(b), which indicates that the highest hydrostatic stress occurs at the poles of the particles. The hydrostatic stress is lower in the matrix and it occurs in the ligament linking the poles of the particles.

At  $f = 0.4$ , the plastic strains intensify at the interface between the particles and the matrix as well as in the matrices on the upper and lower planes of the unit cell, Figure 6(a). The corresponding contour of the local hydrostatic stress, shown in Figure 6(b), indicates both the particles and the matrix exhibit high values of hydrostatic stresses compared to those at  $f = 0.2$ . As in the case for  $f = 0.2$ , the highest hydrostatic stress also occurs in the matrix near the poles of the particles for  $f = 0.4$ . The results in Figure 5 and 6 reveal that the particle/matrix interfaces sustain both high plastic strains and high hydrostatic stresses. In contrast, the highly strained region in the matrix exhibits a low hydrostatic stress, while the highly stressed region exhibits a low plastic strain.

The distributions of the equivalent plastic strain and the local hydrostatic stress along the particle/matrix interface are shown in Figures 7 (a) and 7(b), respectively for  $f = 0.2, 0.4, 0.6, 0.7$ , and  $0.8$ . The results indicate that concentrations of the plastic strain and hydrostatic stress do not occur at the same location. The highest plastic strain occurs at  $\vartheta = 45^\circ$  for  $f = 0.2$ , but the locations shifts to lower angles with increasing  $f$  values. In contrast, the maximum hydrostatic stress occurs at  $\vartheta = 70^\circ$  for  $f = 0.2$  and it shifts toward a lower angle as the volume fraction,  $f$ , increases. At  $f = 0.8$ , compressive hydrostatic stresses occur at  $\vartheta < 10^\circ$ . The region near the poles of the particle, i.e.,  $\vartheta > 45^\circ$ , are always under tensile hydrostatic stresses.

## EFFECTS OF STRESS STATE

The influence of the global stress state on the stress-strain curves of the *in-situ* composite is shown in Figure 8 for  $f = 0.2, 0.4, 0.6$ , and  $0.8$  and  $\lambda = 0, 0.5, 0.7$ , and  $0.8$ . At  $f = 0.2$ , the effective stress-strain curves are only slightly dependent on the stress state. The dependence on the stress state, however, increases with increasing values of volume fraction of particles. The global hydrostatic stress also increases with increasing values of  $\lambda$ , with the largest increase occurring at  $f = 0.8$ .

Contour plots of the local equivalent plastic strain and local hydrostatic stress distributions are shown in Figure 9 (a) and (b), respectively, for  $f = 0.2$  and  $\lambda = 0.5$ . The corresponding results for  $f = 0.4$  and  $\lambda = 0.5$  are shown in Figure 10 (a) and (b). In both cases, the plastic strain distributions are similar to those for  $\lambda = 0$  under identical volume fractions of particles.

The locations of the maximum local hydrostatic stress are independent of  $\lambda$ . The magnitude of the local hydrostatic stress, however, increases with increasing values of  $\lambda$ . This is demonstrated in Figure 11, which shows the distributions of plastic strain and local hydrostatic stress along the particle/matrix interface. Compared to  $\lambda = 0$ , the local hydrostatic stress for  $\lambda = 0.5$  is a factor of  $\frac{1}{2}$  to 2 higher at an identical volume fraction of particles. The increase in the local hydrostatic stress reflects mainly a higher global hydrostatic stress signified by a higher  $\lambda$ .

## **EFFECTS OF INTERFACE STRENGTH AND CRACKED PARTICLES**

The calculated effective stress-strain curve with a strong interface and an intact particle is compared against those for a weak interface and a broken particle in Figure 12. The results for both  $f = 0.2$  and  $0.4$  are shown. A weak interface reduces the flow stress of the composite significantly, while a broken particle is less damaging compared to a weak interface, but the reduction in strength is still significant. The degradation in strength increases with increasing volume fraction of particles. This is expected since most of the load is carried by the particles.

Contour plots of local equivalent plastic strain and local hydrostatic stress for  $f = 0.4$  are presented in Figures 13 (a) and (b), respectively. The weak interface leads to detachment of the particles from the matrix. As a result, plastic deformation localized in the matrix ligament, Figure 13 (a), without a buildup of hydrostatic stress, Figure 13(b). When a biaxial stress of  $\lambda = 0.5$  is applied, the entire particle is detached from the matrix. The plastic flow is localized in a very small channel in the matrix, Figure 13(c), and the local hydrostatic occurs in the least deformed regions of the matrix, which are located near the poles of the detached particles, Figure 13(d).

The microcrack associated with a cracked particles tends to localized plastic flow in the matrix ligament, as shown in Figure 14(a) for  $f = 0.4$  and  $\lambda = 0$ . In addition, a high hydrostatic stress also occurs at the tip of the microcrack in the particle, Figure 14(b). Increasing the biaxial stress ratio from 0 to 0.5 results in little change in the distribution of plastic strain in the matrix ligament, Figure 14(c). The hydrostatic stress region ahead of the tip of the microcrack is, however, enlarged significantly to engulf much of the particle/matrix interface, 14(d). Thus, the interface of a cracked particle still maintains its load carrying capacity and is subjected to a high hydrostatic tensile stress.

## DISCUSSION

Contour plots of effective plastic strain and hydrostatic stress for MMC reinforced with spherical particles subjected to uniaxial tension have been presented by Christman et al. [21], Shen et al. [22], Llorca et al. [23], and Song et al. [24]. All of these results are for volume fraction of particles less than 0.2. Qualitatively, the present results for  $f=0.2$  are in agreement with those reported earlier for the distributions of effective plastic strain and hydrostatic stress. All showed a high concentration of effective plastic strain at the particle/matrix interface at the angle  $\vartheta$  of about  $45^\circ$ , Figures 5(a) and 7(a). The location of the maximum strain concentration site at the interface, however, is shifted toward a lower angle of  $\vartheta$  when the volume fraction of particles is increased, Figure 7(a). The regions near the poles of the particles are always under high hydrostatic stresses, whose value increases with increasing volume fraction of particles, Figure 7(b). For uniaxial tension, increasing the volume fraction of the particles expands the size of the highly constrained matrix.

Calculated effective stress-strain curves as a function of volume fraction indicated very little strengthening due to spherical particles can be obtained when the volume fraction of particles is less than 0.6, Figure 4(a). Similar results have been reported by Lloca et al. [22] for calculated stress-strain curves of 2124Al-SiC sphere-reinforced composites with  $f = 0.2$  or less. A measure of the strengthening effect is the ratio of the effective stress,  $\Sigma_e$ , of the composite to the flow stress,  $\sigma_o$ , of the matrix at a given strain. Results of the ratio  $\Sigma_e/\sigma_o$  for  $E_2 = 0.095$  are compared against the experimental data in Figure 15. The experimental data were obtained based on microhardness measurements of the composite and the matrix alloy. In measuring the microhardness of the *in-situ* composites, the indentor indented on both the particles and the matrix so the composite hardness values were obtained. In contrast, single-phase solid solution alloys were used to obtain the hardness for evaluation of  $\sigma_o$ . The hardness values were then used to compute the strengthening ratio. Comparison of the calculated and measured results in Figure 14 indicates that fair agreement, but the model calculation tends to underpredict the strengthening effect. The calculated results also depend on the geometric arrangement of the particles in the unit cell. The discrepancy between model calculation and experimental data is thought to arise from the highly idealized assumption of a uniform distribution of spherical particles in the *in-situ* composite. In the actual composites, the particle distribution is not truly uniform and the particle shape is not exactly spherical. Any non-uniformity in the particle distribution or deviation from the spherical morphology is likely to increase the composite strength due to clustering or particle shape effects [21-23].

The location of the maximum plastic strain occurs at both the particle/matrix interface and in the matrix. If fracture occurs at a critical plastic strain, then the fracture initiation site can be either the interface or the matrix. Increasing the global constraint increase the size of the region where the maximum plastic strain resides, but does not alter the location of the maximum plastic strain, as illustrated by the contour plots shown in Figures 9 and 10. If fracture obeys a critical fracture strain criterion, the critical fracture strain would be reached under the same nominally strain value, regardless of the

difference in the global plastic constraint. This phenomenon has been observed in SiC particulate-reinforced MMC and referred to as global-constraint insensitive fracture by Somerday and Gangloff [27]. If the critical fracture strain value itself depends on the plastic constraint, then the fracture of the composite should also be sensitive to the global stress state.

Unlike the plastic strain distribution, increasing the global constraint leads to increases in the local hydrostatic stress, as illustrated in the stress contours shown in Figures 9 and 10. If fracture is controlled by a critical fracture stress, then fracture would be sensitive to the global constraint since the local triaxial tensile stress depends directly on the external stress state. To prevent a stress controlled fracture phenomenon such as particle fracture or cleavage in the matrix, it is necessary to lower the local hydrostatic stress. This can be accomplished by either reducing the volume fraction of particles or using particles with low interface strength. In both cases, the strength of the *in-situ* composite will be reduced. The strength reduction is more severe in the case of strong particles with weak interface than that realized by reducing the volume fraction of particles.

Cracked particles with a strong interface tend to localize plastic strain in the matrix and induce a high hydrostatic stress in the particles. The calculated localized deformation zone shown in Figure 14 is reminiscent of the localized deformation zone observed in the matrix of the Nb/Cr<sub>2</sub>Nb *in-situ* composite shown in Figure 1. To mitigate strain localization in the matrix, cracking in the particle need to be avoided. A weak interface can reduce the hydrostatic stress concentration in the cracked particle, but the strength of the composite would be lowered also.

It is evident that the local plastic constraint in *in-situ* composites is likely to be high because of the high volume fraction of particles. This would be the case even if the particles can be made to be spherical and uniformly distributed. To overcome the inherent plastic constraint in the microstructure, the second phase particles must be very strong and do not fracture under the imposed constraint. In addition, the fracture mechanism in the matrix should not be dictated by a stress-controlled process such as cleavage. A weak interface relaxes the constraint in the matrix as the expense of the composite strength. As a results, a weak interface is not desirable if composite strength is essential.

## CONCLUSIONS

The conclusions obtained in this study are as follows:

1. The strengthening effect that can be achieved via uniformly distributed spherical particles is predicted to be quite modest for volume fractions of particles up to 60%. The predicted strengthening effect is lower than that observed in the experimental data for Nb/Cr<sub>2</sub>Nb *in-situ* composites.

2. The maximum effective plastic strain occurs at the particle/matrix interface and in the matrix. The maximum local plastic constraint (local hydrostatic tensile stress/flow stress) occurs in the matrix near the poles of the spherical particles.
3. The particles in the composites are highly stressed. A cracked particle leads to flow localization in the matrix located directly ahead of the crack and a high hydrostatic stress in the particle and along the particle/matrix interface.
4. A weak interface relaxes the plastic constraint within the matrix at the expense of the composite strength. The composite damage mechanism changes from particle fracture for a strong interface to interface debonding and void growth for a weak interface.
5. The local hydrostatic stress increases with the global constraint but the effective plastic strain distribution does not. As a result, fracture controlled by a critical stress criterion is sensitive to the global constraint, while one that is dictated by a critical strain criterion is insensitive to the global constraint.
6. There is no effective ways of mitigating plastic constraint in the composite microstructure without reducing composite strength. One means of preventing localized flow in the matrix is to have strong particles with strong interface.

## Acknowledgements

The contribution of Kwai Chan was supported by the Air Force Office of Scientific Research through Contract No. F49620-95-0043, Dr. Spencer Wu, Program Manager. Part of this work was performed while Kwai Chan was a visiting scientist at the Institute of Materials Research, GKSS Research Center under the sponsorship of Deutsche Forschungsgemeinschaft (SFB371). The contribution of Guoyu Lin was supported by Deutsche Forschungsgemeinschaft (SFB371). The clerical assistance provided by Ms. Lori Salas at SwRI in the preparation of this manuscript is appreciated.

## References

1. M.G. Medira, R. Goetz, D.M. Dimiduk, and J.J. Lewandowski: *Metall. Trans. A.*, Vol. 26A, 1995, pp. 1767-1776.
2. P.R. Subramanian, M.G. Mendiratta, and D.M. Dimiduk: *JOM*, Vol. 48, January 1996, pp. 33-38.
3. P.R. Subramanian, M.G. Mendiratta, D.M. Dimiduk, and M.A. Stucke, *Mat. Sci. Eng.*, 1998 (in press).
4. M.R. Jackson, B.P. Bewlay, R.G. Rowe, D.W. Skelly, and H.A. Lipsitt: *JOM*, Vol. 48, January 1996, pp. 39-43.

5. B.P. Bewlay, M.R. Jackson, and H.A. Liptsitt: *Metall. Mater. Trans. A*, Vol. 27A, 1996, pp. 3801-3808.
6. M.R. Jackson and K.D. Jones: Refractory Metals: Extraction, Processing and Applications, eds. K. Nona, C. Kiddell, D.R. Sadoway, and R.G. Bautista, TMS, Warrendale, PA, 1990, pp. 311-319.
7. R.L. Fleischer, and R.J. Zabala: *Metall. Trans. A*, Vol. 21A, 1990, pp. 2149-2154.
8. J. Dipasquale, D. Gahutu, D. Konitzer, and W. Soboyejo: *Materials Research Society Proceedings*, Materials Research Society, Pittsburgh, PA, Vol. 364, 1995, pp. 1347-52.
9. V.K. Sikka, S. Viswanathan, and E.A. Loria: Superalloys 1992, S.D. Antolovich, R.W. Strusrud, R.A. MacKay, D.L. Anton, T. Khan, R.D. Kissinger, and K.L. Klarstrom, eds., TMS, Warrendale, PA 1992, pp. 423-431.
10. V.K. Sikka and E.A. Loria: *Mat. Sci. Eng.*, Vol. 239-40, 1997, pp. 745-751.
11. D.L. Anton and D.M. Shah: *MRS Symp. Proceedings*, Vol. 194, 1990, pp. 175-82.
12. K.S. Chan: *Metall. Mater. Trans. A*, 1995, Vol. 27A, pp. 2518-31.
13. D.L. Davidson, K.S. Chan, and D.L. Anton: *Metall. Mater. Trans. A*, 1996, Vol 7A, pp. 3007-18.
14. K.S. Chan and D.L. Davidson: *JOM*, 1996, Vol. 48 (9), pp. 62-68.
15. K.S. Chan, D.L. Davidson, and D.L. Anton: *Metall. Mater. Trans. A*, Vol. 28A, 1997, pp. 1797-1808.
16. K.C. Chen, D.J. Thoma, P.G. Kotula, F. Chu, C.M. Cady, G.T. GrayIII, P.S. Dunn, D.R. Korzekwa, C. Mercer, and W. Soboyejo: Proc. Third Pacific Rim Intl. Conf. on Advanced Materials and Processing, M.A. Iman, R. NeNale, S. Hanada, Z. Zhong, and D.N. Lee, eds., TMS, Warrendale, PA, 1998, pp. 1431-1436.
17. High Temperature Materials Workshop, Wright-Patterson Air Force Base, September 12, 1997, Dayton, OH.
18. R. Saidja, H. Sieber and J.H. Perepezko: presented at TMS Symposium on Molybdenum and Molybdenum Alloys, TMS Annual Meeting, San Antonio, TX, February 14-19, 1998.
19. M.G. Mendiratta and P.R. Subramanian: Presented at TMS Symposium on Molybdenum and Molybdenum Alloys, TMS Annual Meeting, San Antonio, TX, February 14-19, 1998.
20. D.L. Davidson and R.C. McClung: *Int. J. Fracture*, Vol. 84, 1997, pp. 81-98.
21. T. Christman, A. Needleman, and S. Suresh: *Acta Metall.*, Vol. 37, 1989, pp. 3029-3050.
22. J. Llorca, A. Needleman, and S. Suresh: *Acta Metall. Mater.*, Vol. 39, 1991, pp. 2317-2335.
23. Y.-L. Shen, M. Fniot, A. Needleman, and S. Suresh: *Acta Metall. Mater.*, Vol. 43, 1995, pp. 1701-1722.

24. S.G. Song, N. Shi, G.T. Gray III, and J.A. Roberts: *Metall. Mat. Trans. A*, Vol. 27A, 1996, pp. 3739-3746.
25. J.R. Brockenbrough and S. Suresh: *Scripta Metal. Mater.*, Vol. 24, 1990, pp. 325-330.
26. ABAQUS/Standard, User's Manual, Version 5.4, 1994, Providence, RI.
27. B.P. Somerday and R.P. Gangloff: *Metall. Mat. Trans. A*, 1994, Vol. 25A, pp. 1471—1479.

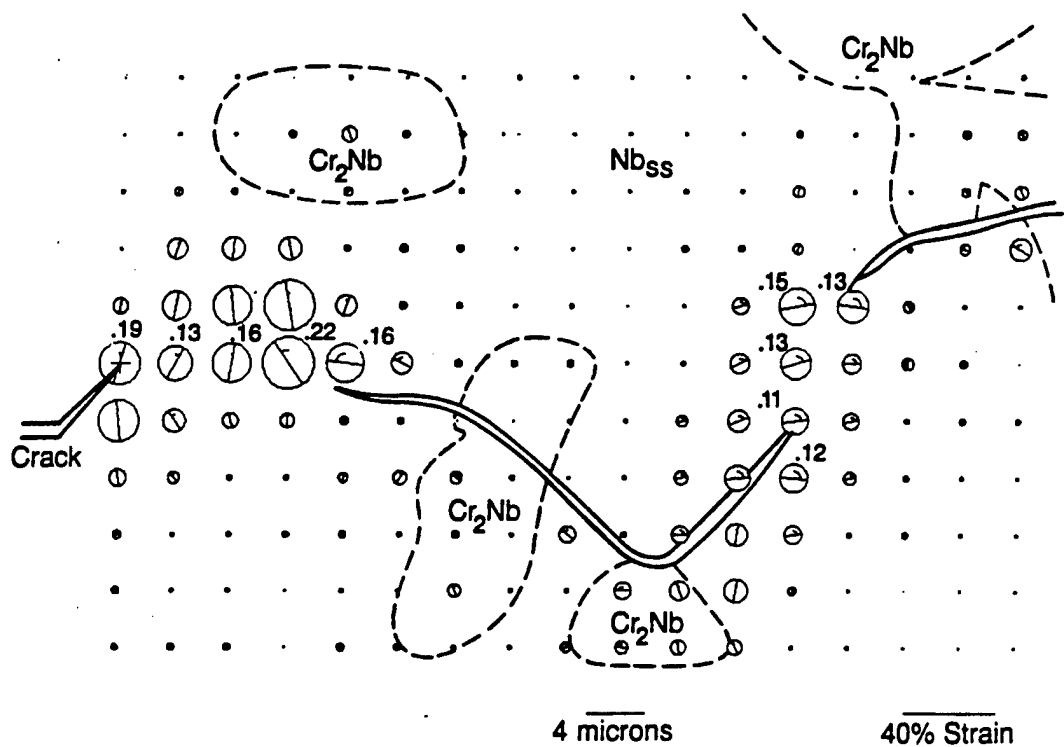


Figure 1. Near-tip strain distribution obtained by the stereomicrography technique for the *in situ* composite, Nb-36Cr-27Ti. The strains are presented in terms of Mohr's circles of strains at various locations in the near-tip process zone. The Mises effective strains are indicated at locations of high strain concentration. From Chan [12].

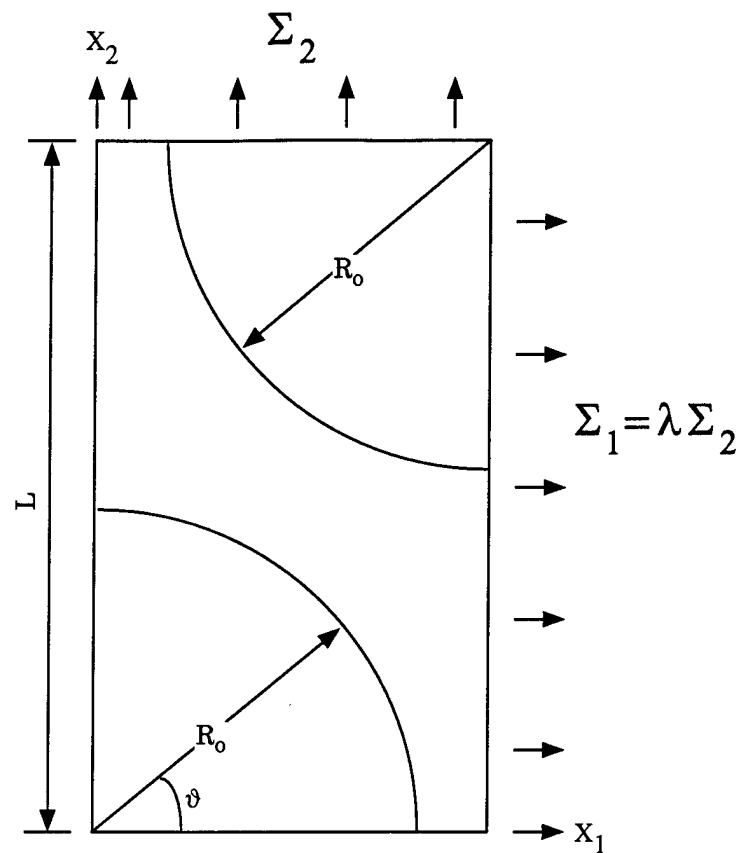


Figure 2(a). Schematic of a unit cell of hexagonal packaging.

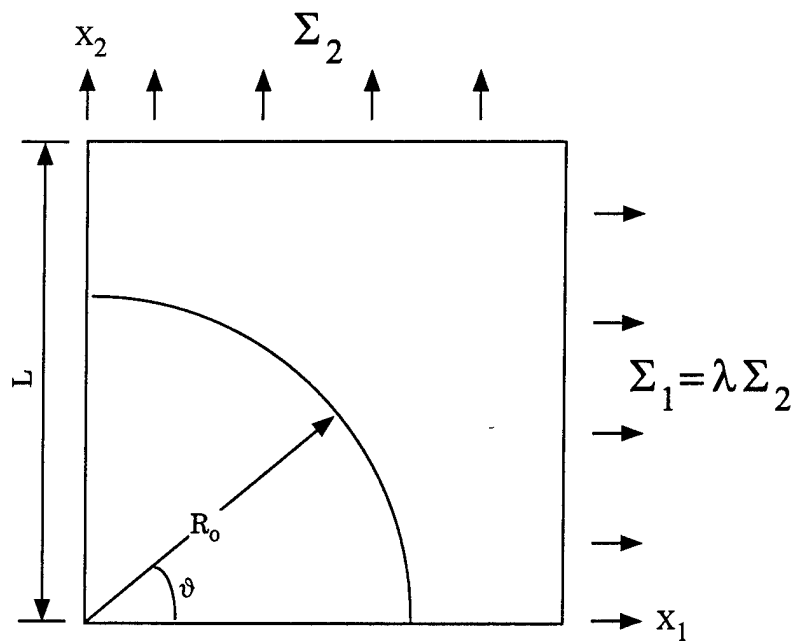


Figure 2(b). Schematic of a unit cell of square edge packing.

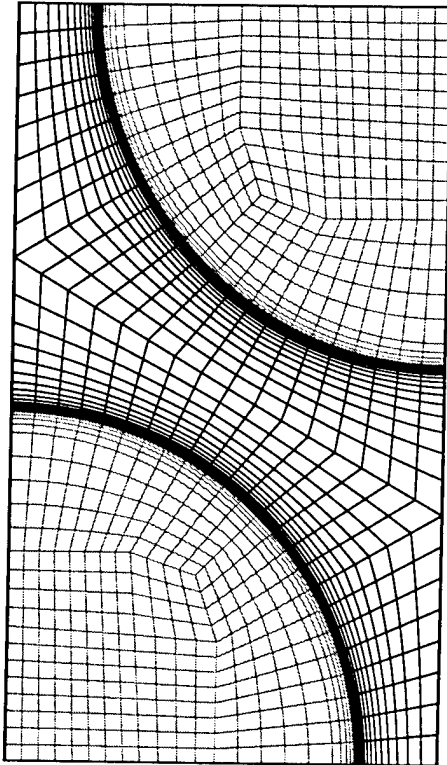


Figure 3. A finite element mesh of a hexagonal unit cell.

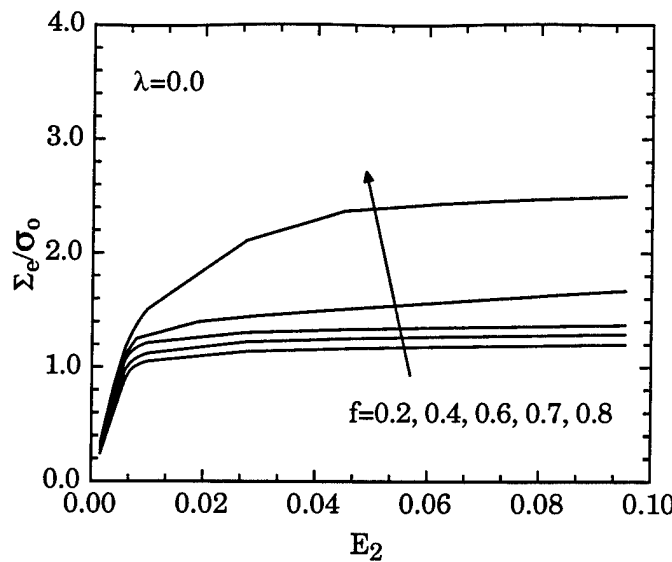


Figure 4(a). Stress-strain curves for various ratios of volume fraction of particles under uniaxial loading.

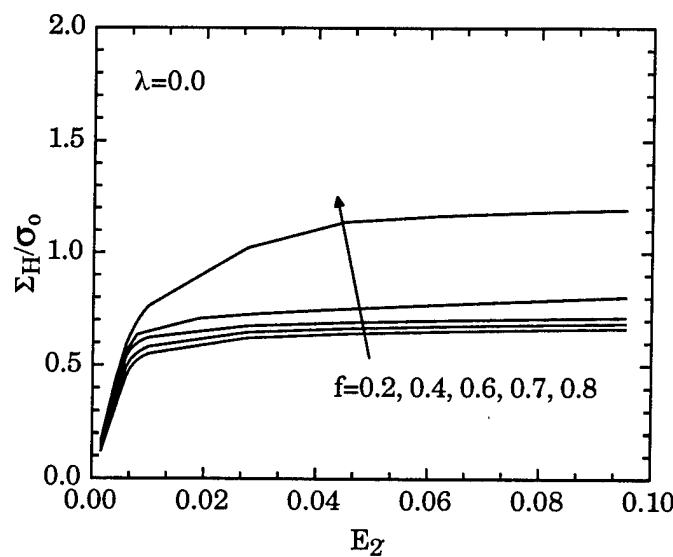
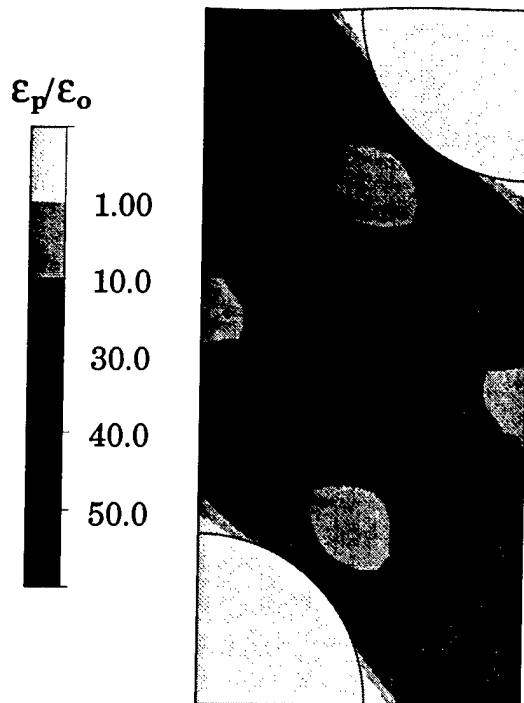


Figure 4(b). Global hydrostatic stress normalized by the reference yield stress,  $\sigma_0$ , versus the applied strain for various values of volume fraction of particles under uniaxial loading.



5(a). Contour plot of equivalent plastic strain under uniaxial tension,  $f = 0.2$  and  $\lambda = 0.0$ .

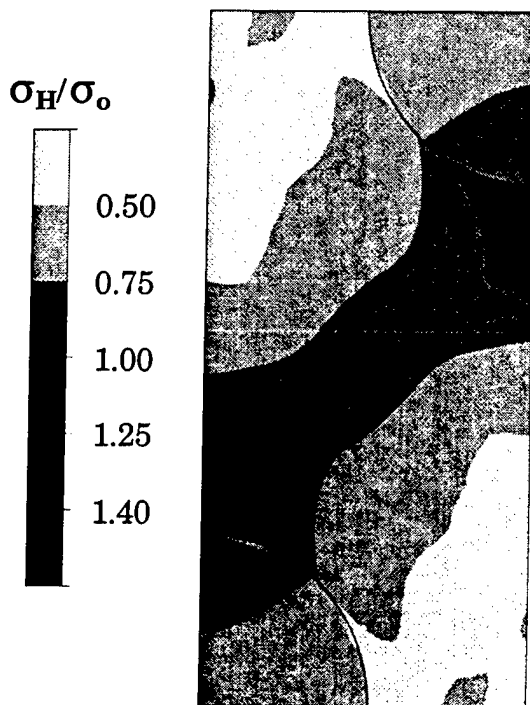


Figure 5(b). Contour plot of hydrostatic stress  $\sigma_H$  under uniaxial tension,  $f = 0.2$  and  $\lambda = 0.0$ .

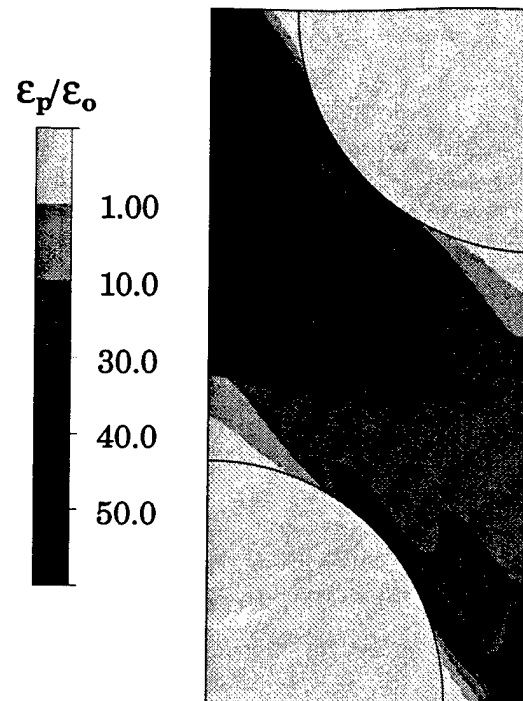


Figure 6(a). Contour plot of equivalent plastic strain under uniaxial tension,  $f = 0.4$  and  $\lambda = 0$ .

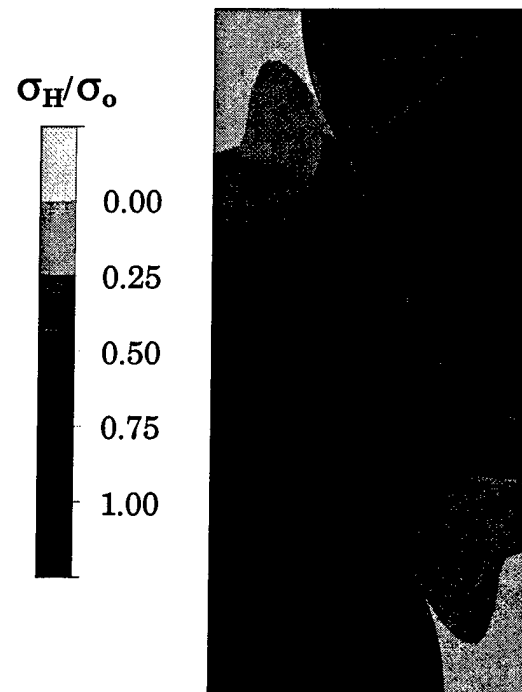


Figure 6(b). Contour plot of hydrostatic stress  $\sigma_H$  under uniaxial tension,  $f = 0.4$  and  $\lambda = 0$ .

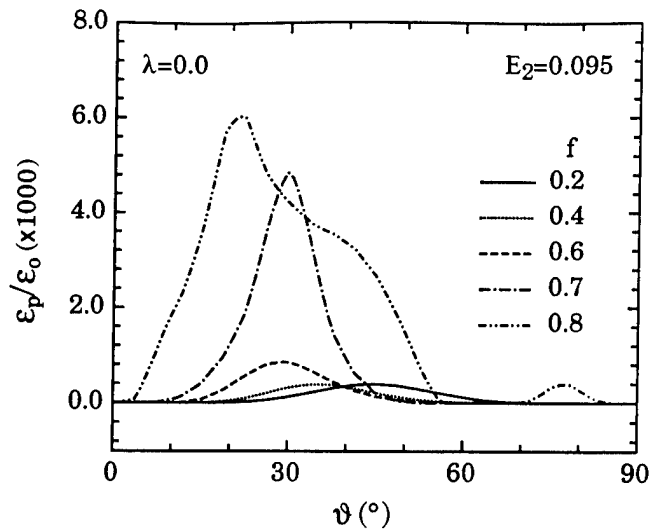


Figure 7(a). Distribution of equivalent plastic strain in Nb matrix at interface for various ratios of volume fraction of particles under uniaxial tension.

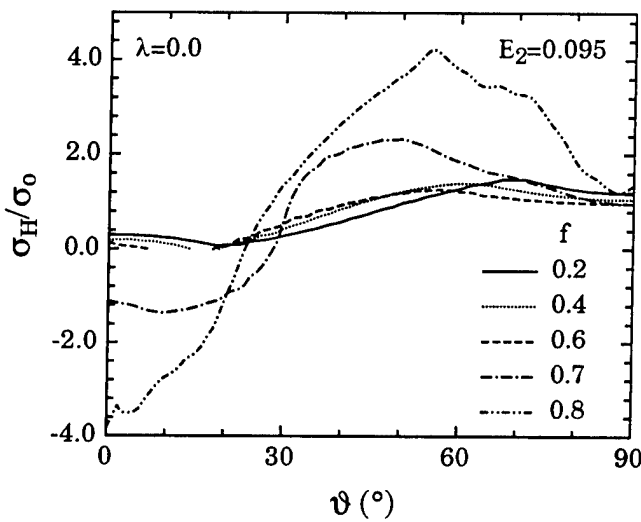


Figure 7(b). Distribution of hydrostatic stress in Nb matrix at interface for various ratios of volume fraction of particles under uniaxial tension.

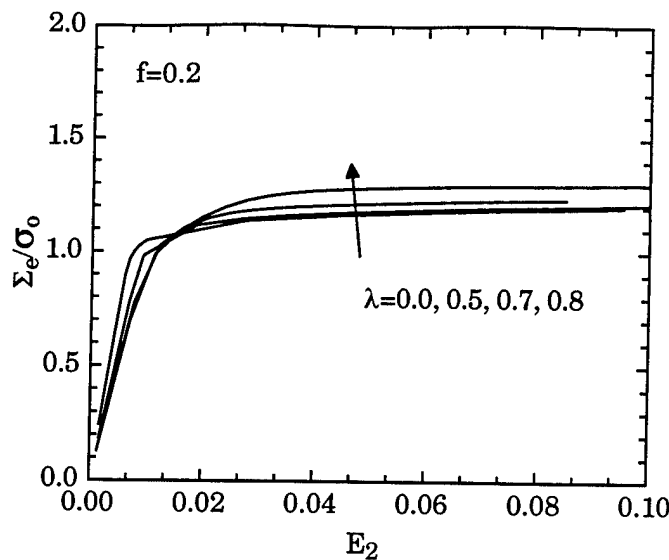


Figure 8(a). Stress strain curves for various ratios of biaxial loading,  $f = 0.2$ .

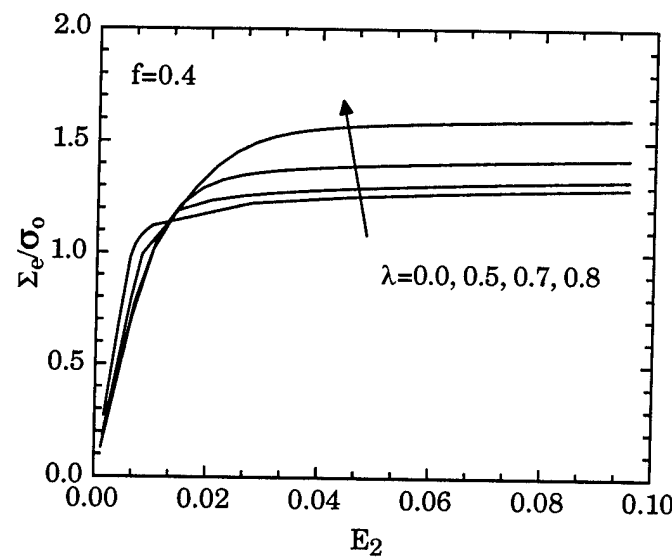


Figure 8(b). Stress strain curves for various ratios of biaxial loading,  $f = 0.4$ .

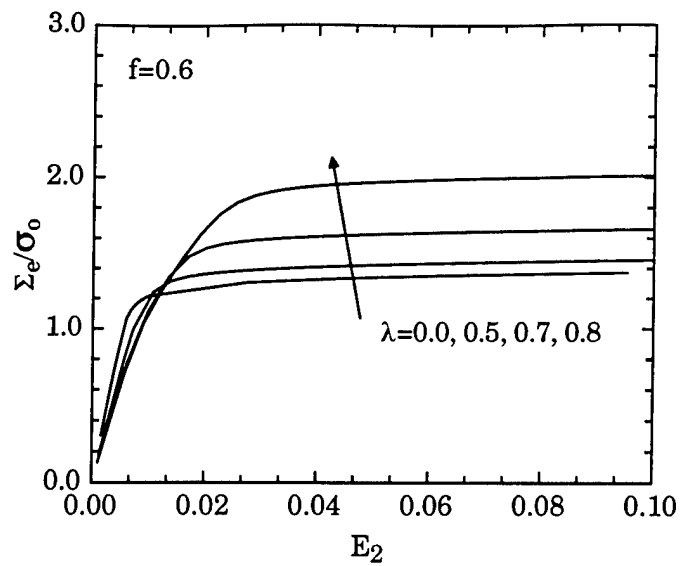


Figure 8(c). Stress strain curves for various ratios of biaxial loading,  $f = 0.6$ .

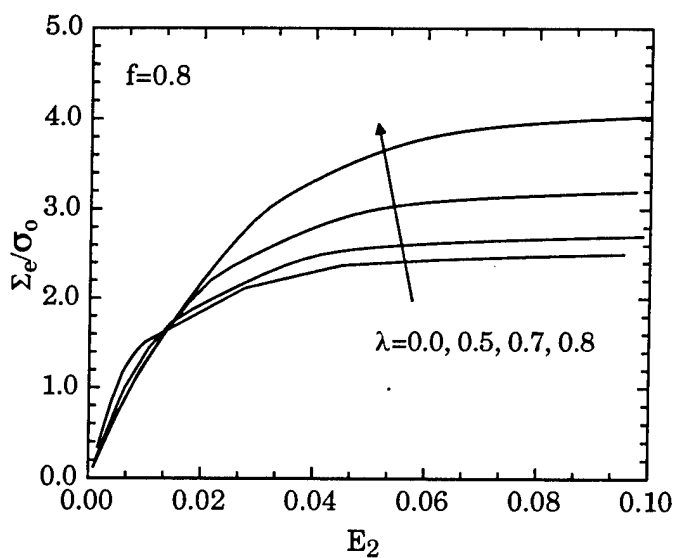
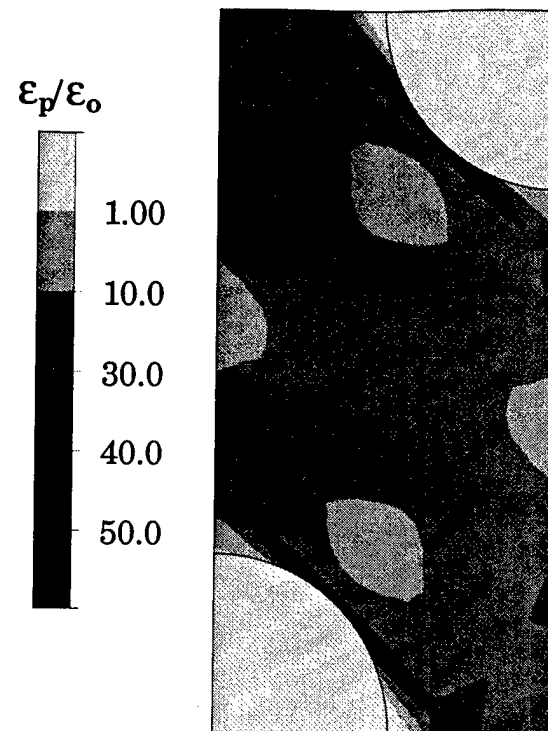
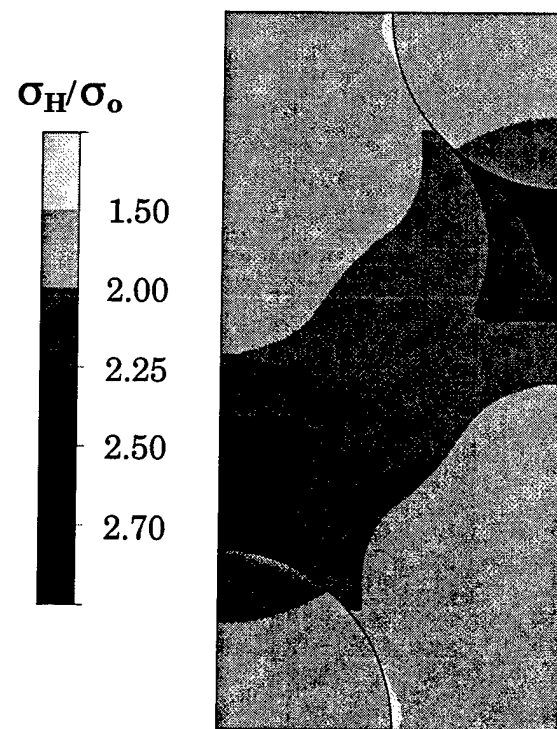


Figure 8(d). Stress strain curves for various ratios of biaxial loading,  $f = 0.8$ .



9(a). Contour plot of equivalent plastic strain under biaxial loading,  $f = 0.2$  and  $\lambda = 0.5$ .



9(b). Contour plot of hydrostatic stress  $\sigma_H$  under biaxial loading,  $f = 0.2$  and  $\lambda = 0.5$ .

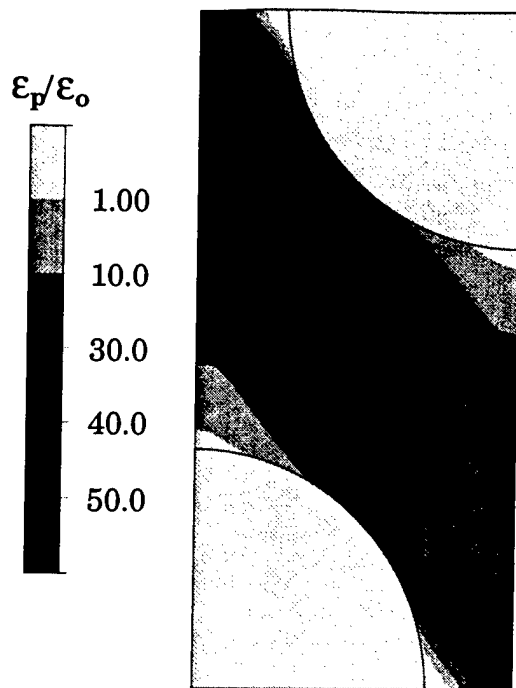


Figure 10(a). Contour plot of equivalent plastic strain under biaxial loading,  $f = 0.4$  and  $\lambda = 0.5$ .

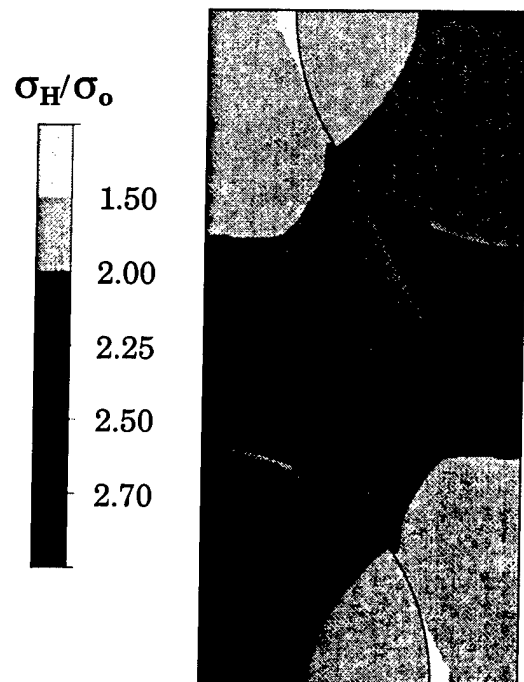


Figure 10(b). Contour plot of hydrostatic stress  $\sigma_H$  under biaxial loading,  $f = 0.4$  and  $\lambda = 0.5$ .

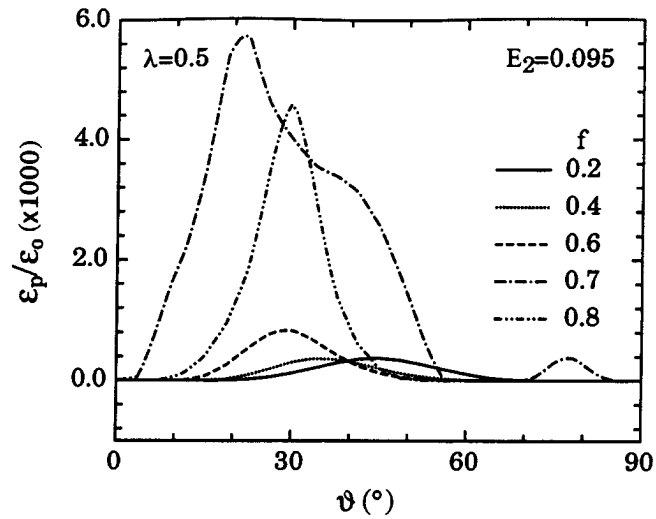


Figure 11(a). Distribution of equivalent plastic strain in Nb matrix at interface for various ratios of volume fraction under biaxial loading,  $\lambda = 0.5$ .

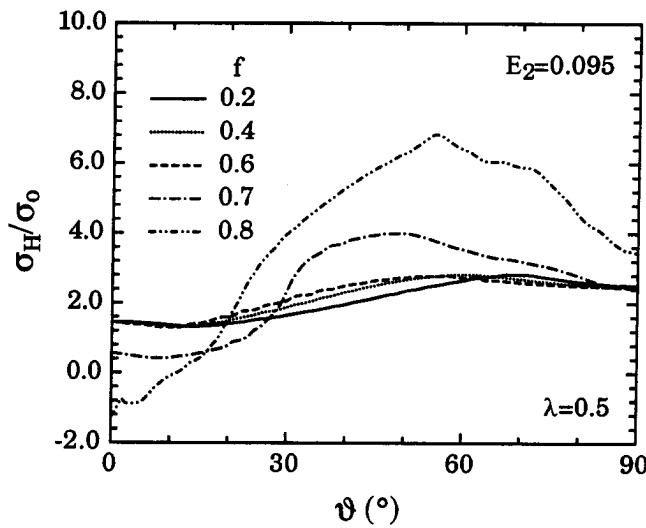


Figure 11(b). Distribution of hydrostatic stress in Nb matrix at interface for various ratios of volume fraction under biaxial loading,  $\lambda = 0.5$ .

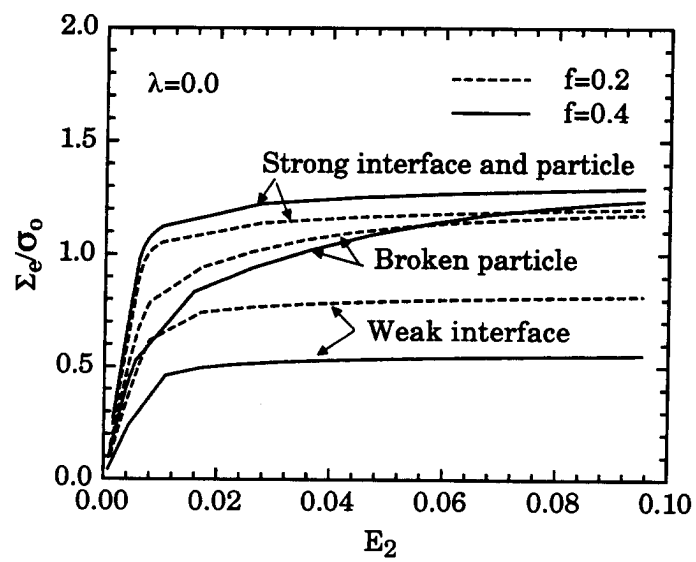


Figure 12. Comparison of stress strain curves for strong interface and particle, broken particle and weak interface under uniaxial loading.

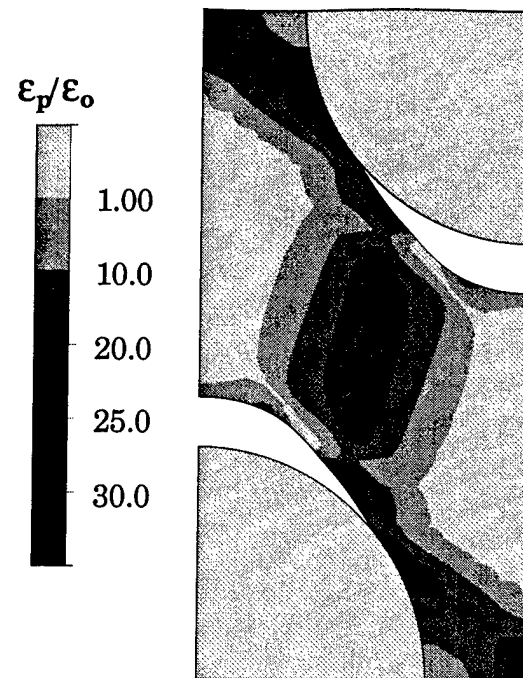


Figure 13(a). Contour plot of equivalent plastic strain for weak interfaces under uniaxial tension,  $f = 0.4$  and  $\lambda = 0.0$ .

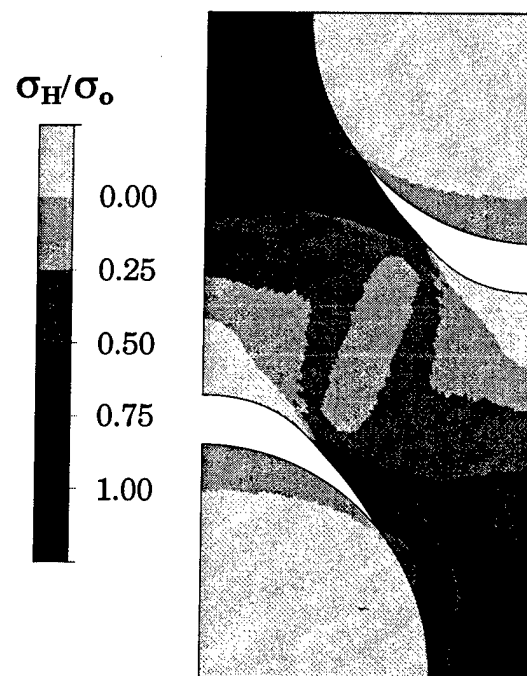


Figure 13(b). Contour plot of hydrostatic stress  $\sigma_H$  for weak interfaces under uniaxial tension,  $f = 0.4$  and  $\lambda = 0.0$ .

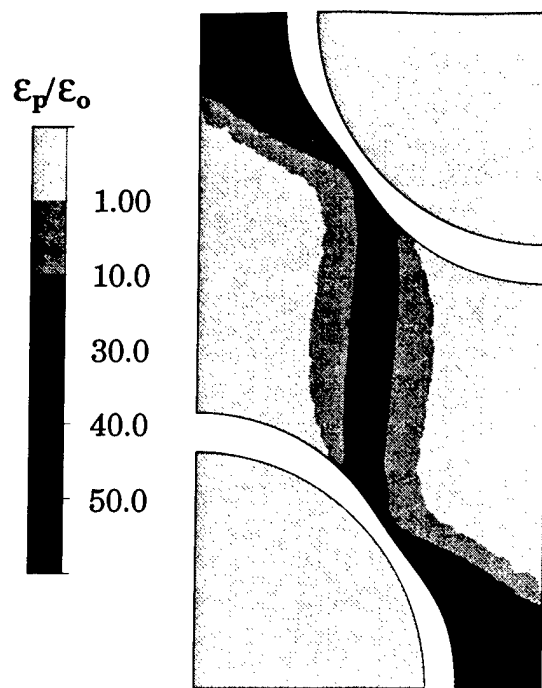


Figure 13(c). Contour plot of equivalent plastic strain for weak interfaces under biaxial loading,  $f = 0.4$  and  $\lambda = 0.5$ .

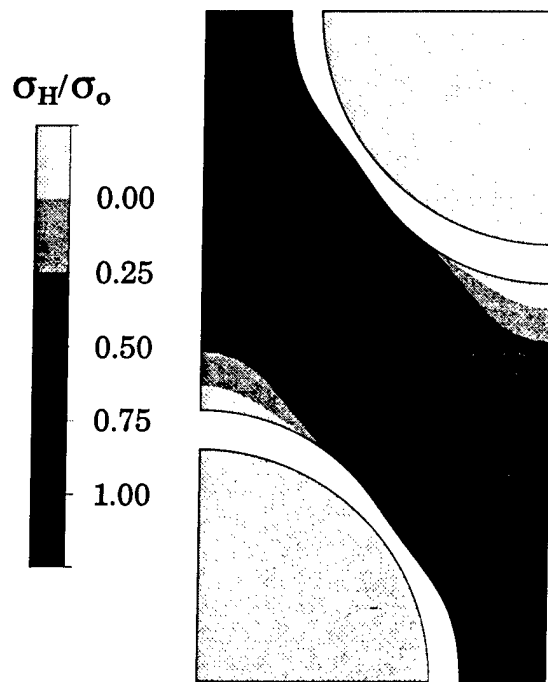


Figure 13(d). Contour plot of hydrostatic stress  $\sigma_H$  for weak interfaces under biaxial loading,  $f = 0.4$  and  $\lambda = 0.5$ .

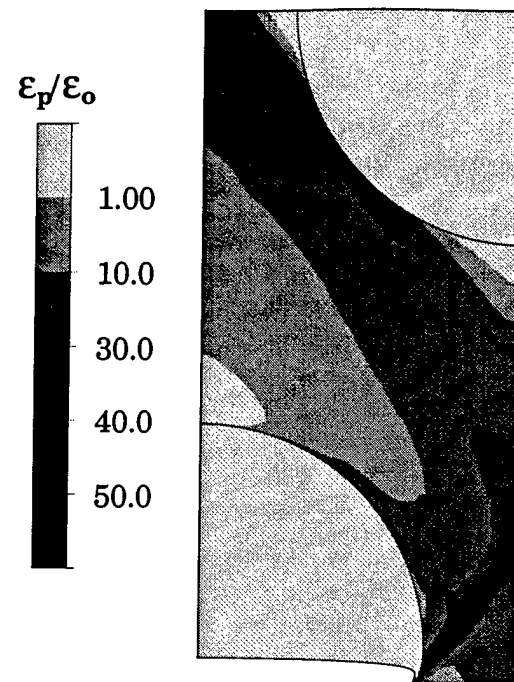


Figure 14(a). Contour plot of equivalent plastic strain for broken particle under uniaxial tension,  $f = 0.4$  and  $\lambda = 0.0$ .

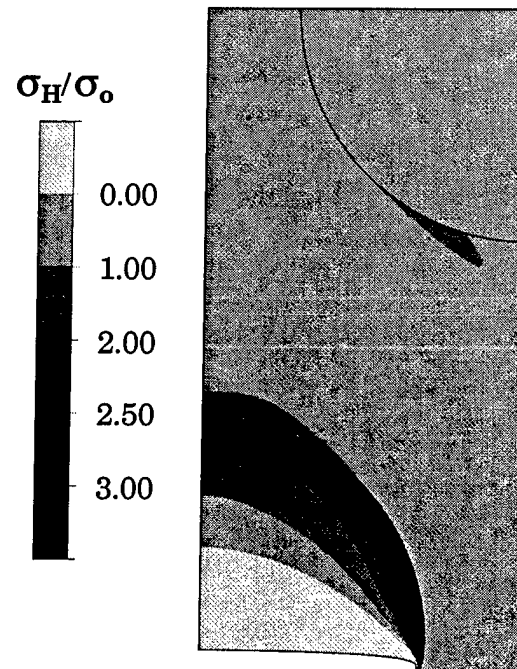


Figure 14(b). Contour plot of hydrostatic stress  $\sigma_H$  for broken particle under uniaxial tension,  $f = 0.4$  and  $\lambda = 0.0$ .

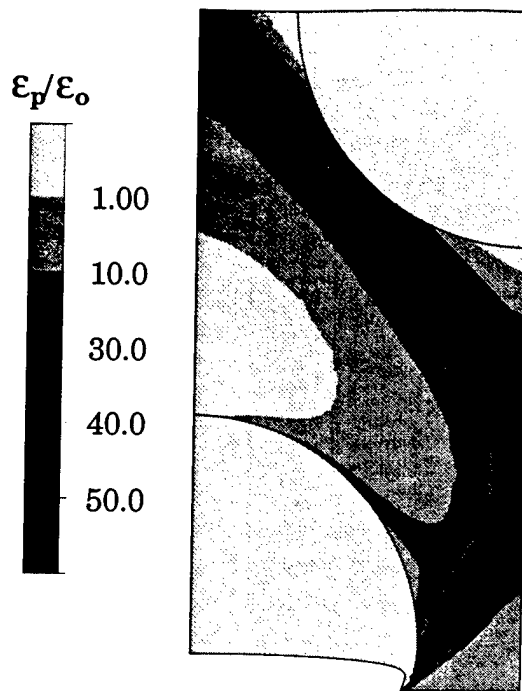


Figure 14(c). Contour plot of equivalent plastic strain for broken particle under biaxial loading,  $f = 0.4$  and  $\lambda = 0.5$ .

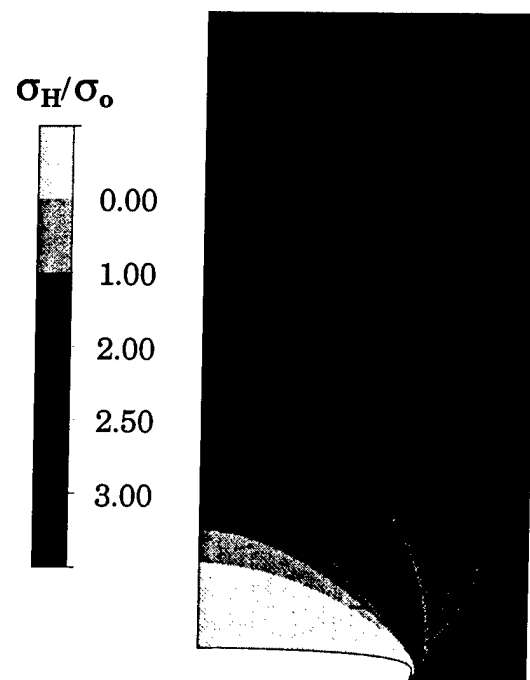


Figure 14(d). Contour plot of hydrostatic stress  $\sigma_H$  for broken particle under biaxial loading,  $f = 0.4$  and  $\lambda = 0.5$ .

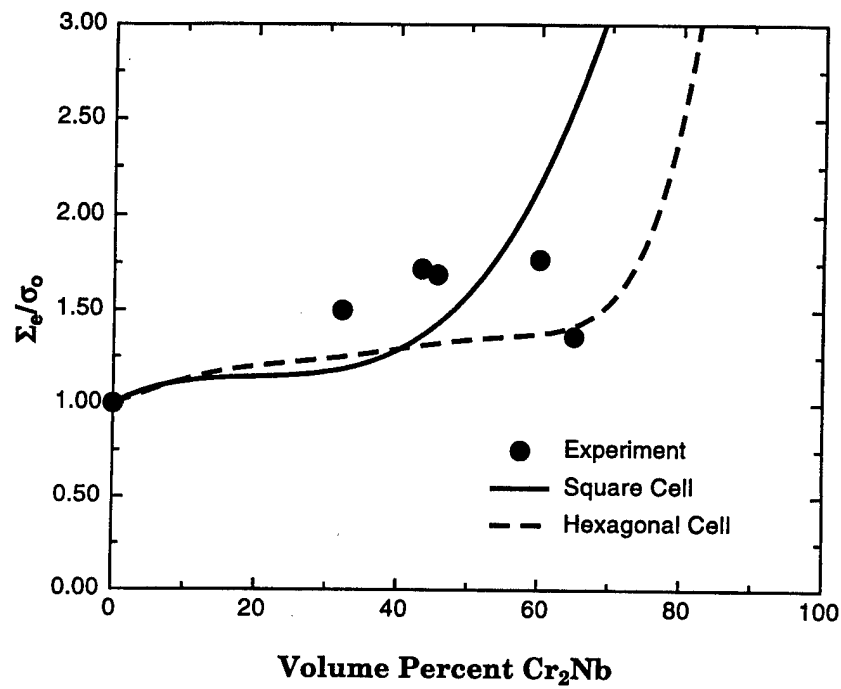


Figure 15. Comparison of calculated and observed values of the strengthening ratio,  $\Sigma_0/\sigma_0$ , as a function of volume fraction of  $\text{Cr}_2\text{Nb}$  particles for the  $\text{Nb}/\text{Cr}_2\text{Nb}$  *in-situ* composites.

**Evidence of Void Nucleation and Growth on Planar Slip  
Bands in a Nb-Cr-Ti Alloy**

**Kwai S. Chan and David L. Davidson**

**Metallurgical and Materials Transactions A**  
**(in press)**

EVIDENCE OF VOID NUCLEATION AND GROWTH ON PLANAR SLIP BANDS IN  
A Nb-Cr-Ti ALLOY

Kwai S. Chan and David L. Davidson  
Southwest Research Institute, San Antonio, TX 78238

ABSTRACT

Dimpled fracture via void nucleation, growth, and coalescence is common in alloys containing hard particles or inclusions, which act as void nucleation sites. Void-covered fracture surfaces have also been observed in planar slip materials. However, the process by which dimples form in the planar slip materials is not understood because these materials generally do not contain hard particles or inclusions. An intersecting slip process was recently proposed as a possible mechanism for the formation of dimpled fracture in the planar slip materials. In this paper, experimental evidence of void nucleation and growth on planar slip bands in a Nb-Cr-Ti solid solution alloy (Nb-13Cr-37Ti in atomic pct) is presented. The experimental observations are compared against the intersecting slip model and Peierls stress calculation to elucidate the mechanism of dimpled fracture in planar slip materials.

## INTRODUCTION

Void nucleation usually occurs at hard particles or inclusions in engineering alloys such as copper [1], steels [2] and Al-alloys [3]. The process commences with interface decohesion or fracture of the hard particles, depending on the strength of the interface relative to the particle. Subsequent growth of the voids around the nucleation site invariably leave the particle at the bottom of the voids. On the other hand, dimpled fracture also occurs in materials such as Ti [4] alloys that exhibit planar slip behavior but do not normally contain hard particles. Dimpled fracture has also been reported for Nb-Cr-Ti [5,6], Nb-Al-Ti [7,8], and Nb-Si [9] solid solution alloys. The Nb-Cr-Ti alloy was a b.c.c. Nb solid solution that contained 13 a/o% Cr and 37 a/o% Ti and exhibited a large grain size ( $\approx 1500 \mu\text{m}$ ). The slip character was planar [5] and the fracture toughness exceeded 100 MPa/m when measured on 5 mm thick compact-tension specimens [5,6]. The voids in this Nb-Cr-Ti solid solution alloy occurred on fracture surfaces that contained a combination of cleavage, slipband decohesion, grain boundary cracking, and dimpled fracture facets [5,6]. For this planar slip material, the void nucleation process responsible for the observed dimpled fracture remains elusive. The lack of understanding applies to other materials also. In Ti<sub>3</sub>Al-based [10] and FeAl-based [11] intermetallic alloys, the fracture surfaces are also characterized by cleavage facets but dimpled fracture faces containing void-like features have been observed. Like the planar slip metals, the origin of these void-like features in these intermetallics have not been identified.

The formation of a cleavage crack by slip on two intersecting planes was proposed by Cottrell [12]. Nucleation of a microcrack by decohesion on a slip plane containing a dislocation pileup was proposed and analyzed by Stroh [13]. Recently, Chan combined intersecting slip and slipband decohesion into one mechanism to explain the formation of dimples in planar slip materials [14]. Figure 1 shows a schematic illustration of the proposed dimpled fracture mechanism. The process commences with planar slip on a set of planes impinging on another set of slip or cleavage planes, Figure 1(a). The void nucleation process commences when impinging slip leads to microcrack formation at either the intersecting slipband or cleavage plane, Figure 1(b). Upon further deformation, the microcracks grow into voids as the result of continual slip on the slip planes, Figure 1(c), and coalescence by linkage with voids on upper and lower planes that shear the common intersecting slip planes, Figure 1(d). The proposed model has been used to explain the fractographic observations of parallelepiped, cuboidal, and spheroidal voids in Nb-Cr-Ti alloys [14]. Direct experimental observation of the dimpled fracture process in Nb-Cr-Ti alloys, if possible, is therefore of utmost interest for testing the validity of the intersecting slip model.

The objective of this paper is to present the results of an investigation whose goal was to study the mechanism of dimpled fracture in planar slip Nb-Cr-Ti alloy. Fracture toughness tests were performed on compact-tension specimens in a scanning electron microscope (SEM) equipped with a loading stage. The near-tip void nucleation process was identified by in-situ observations and post-mortem fractographic analysis. The experimental observations were compared against the intersecting slip model and Peierls stress calculation to develop a better understanding of the dimpled fracture process in planar slip materials.

## EXPERIMENTAL PROCEDURES

The material studied was a Nb-Cr-Ti solution alloy with the composition of Nb-13Cr-37Ti (in a/o%). The interstitial contents were 0.04 wt.% oxygen, 0.012 wt.% N, and 0.02 wt.% C. The alloy was processed at United Technology Research Center (East Hartford, CT) by vacuum arc melting of elemental materials into rectangular buttons [6]. Each button was remelted repeatedly for eight times in order to improve the chemical homogeneity. The cast ingot buttons were then heat-treated in a vacuum at 1500°C for 8 hours, then for 48 hours at 1200°C followed by furnace cool. The heat-treatment procedure was selected to be identical to that used in a previous study for *in-situ* composites [5,6]. The microstructure was a single b.c.c phase with a grain size of approximately 1500  $\mu$ m. Compact-tension specimens were prepared by electro-discharge machining to the size of 19.9 mm in width, 19.1 mm in height, and 4.8 mm in thickness. A notch was introduced to the specimen by cutting with a diamond wheel. Subsequently, the surfaces of the specimens were mechanically polished, followed by fatigue precracking, and then further polished by an ion etching technique. Fatigue precracking was conducted at a stress intensity range of 8 MPa $\sqrt{m}$  and a stress ratio, R, of 0.1. Tapered tensile specimens 42 mm in length, 3.8 mm in width, and 2.5 mm in thickness were also fabricated.

Fracture toughness testing was performed at ambient temperature in an SEM via a loading stage [15]. The near-tip region was photographed as a function of the stress intensity, K, levels in increments of 2-3 MPa $\sqrt{m}$ , starting at 15 MPa $\sqrt{m}$  and continued until the specimen failed. The photographs were used to determine the amount of crack extension and to identify the near-tip deformation and fracture processes. The fracture surfaces of the specimens were examined using SEM. A tensile test was performed at ambient temperature in the SEM under a slow loading rate, but the loading rate was not measured. The specimen was deformed to a strain of 6.5% and then terminated.

## RESULTS

Figure 2 shows the microstructure of the Nb-Cr-Ti solid solution alloy. This alloy exhibited very planar slip, as shown in Figure 3. These planar slip lines from intersecting slip systems were observed in the tensile specimen after a strain of 6.5%. The fracture resistance of the Nb-Cr-Ti alloy is extremely high, as evidenced by the K-resistance curve shown in Figure 4. The near-tip deformation and fracture processes are complicated and include crack-tip slip emission, grain boundary cracking, cleavage, and dimpled fracture in the non-tip region. Experimental evidence of crack tip slip, grain boundary cracking, and cleavage are presented elsewhere [14]. Only the K levels at which these processes occurred are summarized in Figure 4. The high fracture toughness was the result of slip emission from the crack tip; this process occurred at K levels between 50 and 80 MPa $\sqrt{m}$ . Slip emission from the crack tip facilitates extensive crack tip blunting and suppressed cleavage crack propagation from the crack tip, which is the subject of another publication [16]. Crack extension occurred at K = 98 MPa $\sqrt{m}$  by decohesion of a grain boundary located ahead of the crack tip. This resulted in the formation of an intact ligament between the grain boundary microcrack and the main crack tip. Further increase in the K level led to plastic fracture of the ligament and extensive blunting of the grain boundary crack due to crack-tip slip.

The formation of any type of voids near the crack-tip was first detected in the near-tip region at  $K = 98 \text{ MPa}\sqrt{\text{m}}$ . Figure 5(a) shows the voids in the near-tip region at  $K = 102 \text{ MPa}\sqrt{\text{m}}$ . Plastic void growth occurred and additional voids were nucleated when  $K$  was increased to  $106 \text{ MPa}\sqrt{\text{m}}$ , Figure 5(b), until the specimen fractured. A close-up view of the voids at  $K = 106 \text{ MPa}\sqrt{\text{m}}$  is shown in Figure 6, which shows coalesced voids along a slip plane that is indicated as Slip 2 in the figure. SEM microscopy revealed the voids formed at the intersections of slip traces on the surface, resulting in their irregular shapes. The intersecting slip plane, Slip 1, is also indicated. The latter is not as evident and more difficult to see because of the severely deformed surface and the angle of view. Post-mortem examination of the failed specimen by SEM revealed the presence of two sets of aligned intersecting microcracks, Figure 7. Some of the apparent microcracks were actually slip lines, which are indicated by arrows in Figure 7. The microcracks exhibited crack openings while the slip lines did not. This observation suggested that the microcracks formed by decohesion along intersecting slipbands. Close examination indicated the presence of voids inside many of the microcracks. Despite residing within the microcracks, these voids manifested the various stages of growth reminiscent of, but different from, the void sheet mechanism [17]. Figure 8(a) shows three isolated voids inside a microcrack. Voids that are partially coalesced are shown in Figure 8(b), while a microcrack formed with completely coalesced voids showing dimpled fracture are illustrated in Figure 8(c). Dimpled fracture surfaces, Figure 9, were observed at the region where the void growth process was observed on the side. Thus, the fractographic surfaces were consistent with the features observed on the specimen surfaces. However, other types of fractographic features were also observed on other portions of the fracture surfaces. Figure 10 presents a fracture surface that exhibits traces of two set of intersecting slip planes, one of which manifested substantial decohesion and the presence of microcracks. Figure 10 is reminiscent to the microcracks shown in Figure 7 and the microcrack nucleation process depicted in Figures 1(b) and (c).

## DISCUSSION

The result of the present investigation confirms the previous observation [5] that Nb-Cr-Ti solid solution alloy fails by a combination of fracture processes, including slip band decohesion, cleavage, grain boundary decohesion, and dimpled fracture. The sequence of the fracture events is slipband decohesion, grain boundary cracking, cleavage, and dimpled fracture. In addition, the result shows that dimpled fracture occurs by a void nucleation, growth, and coalescence process within planar slip bands at relatively high  $K$  levels. The voids are nucleated by decohesion of small segments of the slipbands, Figure 6. Void nucleation at slipband commences at  $K$  levels above  $92 \text{ MPa}\sqrt{\text{m}}$ , while grain boundary decohesion takes places at  $K = 98 \text{ MPa}\sqrt{\text{m}}$ . The dimples observed in this investigation are generally rounded when compared to the parallelepiped and cuboidal voids observed previously [14]. The void shape appears to be dictated by the slip line spacing, the number of intersecting slip planes, and the waviness of slip. Rounded dimples are more prevalent when the intersecting slip lines are closely spaced and involve two or more slip planes.

The voids in the Nb-Cr-Ti alloys differ from the traditional voids observed in copper, steels, and aluminum alloys in two main areas: (1) absence of particles or inclusions at the bottom of voids in the Nb-Cr-Ti alloys since voids in this material initiate by slipband decohesion, and (2) voids in the Nb-Cr-Ti alloys are generally more shallow and less rounded when compared to the traditional voids, which are deeper and rounded in copper, steels, and aluminum alloys. These differences in the void characteristics in Nb-Cr-Ti alloys and the traditional voids are illustrated schematically in Figure 11.

The formation of slipband microcracks by intersecting slip depicted in Figure 1 is clearly supported by the experimental evidence shown in Figures 7 and 10. Microcrack formation by this process differs from the Cottrell mechanism [12] since the intersecting slip does not lead to crack formation on a cleavage plane. Instead, the intersection slip leads to decohesion of the slip planes themselves. In this sense, the crack formation process resembles the slip plane decohesion process postulated by Stroh [13], but one that operates on two intersecting planes.

The proposed model does not rely on a particular dislocation reaction for the fracture process to proceed. Instead, it requires dislocation pileups on the intersecting planes as in Stroh's mechanism [13]. A recent analysis [18] has shown that the dislocation pileups on the intersecting planes exert large normal stresses mutually, which reach a maximum when the angle between the intersection planes is 70.5°. It is presumed that these large normal stresses cause separation of the slip planes. The formation of aligned slipband microcracks has been reported for a lamellar TiAl alloy [18]. In this case, the microcracks formed on intersecting (111) slip planes that were oriented at the 70.5° angle.

The set of intersecting slip planes where microcracks were observed in the Nb-Cr-Ti alloy tested in this study could not be identified because the crystallographic orientation of the particular grain had not been determined prior to fracture testing. Planar (112) slip on intersecting planes, however, have been identified in other grains in the same specimen. Slipband fracture on the (112) plane has also been observed [14]. In addition, (110) slip in this alloy tends to be wavy [14]. Thus, it is probable that the microcracks formed on intersecting (112) planes. The (112) planes can be oriented at either 33.6° or 48.2° apart. Thus, the normal stress and the propensity for slipband decohesion would be different among the (112) planes. The planes separated by an angle of 48.2° would experience a higher normal stress than those for the 33.6° angle.

Slipband decohesion was observed on some planes and not on others. This observation can be rationalized on the basis of two factors: (1) the orientation of the intersecting slip planes, as discussed earlier, and (2) the planarity of slip, which is required for the formation of dislocation pileups. The latter can be understood on the basis of recent Peierls stress calculations performed on the Nb-Cr-Ti alloys for slip on the (110) and (112) planes by edge and screw dislocations. The procedures by Wang [19] and Foreman [20] were used. The results of this calculation, which is presented in Figure 12 and described in detail elsewhere [16], shows that the Peierls stress value depends on Ti addition. At 37 a/o% Ti addition, Ti addition reduces the Peierls stress for both edge and screw dislocations on the (110) plane, but has little effect on the (112) screw dislocations. The decrease in the P-N stress for the (110) screw dislocation is

expected to promote cross slip and reduce the planarity of slip on the (110) plane. On the other hand, the high P-N stress of the (112) screw dislocation is expected to lead to planar slip on the (112) plane. Planar slip can result in dislocation pileups which, in turn, can cause normal stress concentration on and decohesion of the slip planes [5].

Wavy slip on the (110) was indeed observed near the crack tip [14], and planar slip and decohesion on (112) plane were also observed [5]. The result suggests that the (112) planes are prone to decohesion because of a high Peierls stress for screw dislocations and difficulty in activating cross slip. To describe the observations shown in Figure 8, the proposed intersecting slip mechanism must operate at a microscopic scale and nucleate microcracks of a submicron ( $< 1 \mu\text{m}$ ) size. Once nucleated, the microcracks may grow into voids via the intersecting process as suggested in Figure 1. This is supported by the evidence shown in Figure 6, which shows the formation of voids on two intersecting slip lines as postulated in the model. More direct evidence of the void formation process is not available and is difficult to obtain because the void initiation process occurs at a size level that is at or beyond the resolution of SEM. It is also quite difficult to catch the void formation process in progress at the right time and the search area in the crack tip region is large when a submicron sized void is to be located.

## CONCLUSIONS

The results of this work led to the conclusions as follows:

1. Dimpled fracture in Nb-Cr-Ti alloys occurs by void nucleation, growth, and coalescence within planar slip bands. These voids are more shallow and less rounded when compared to traditional voids in copper, steels, and aluminum alloys. In addition, voids in the Nb-Cr-Ti alloys do not have particles at the bottom of the cup.
2. Slipband decohesion, grain boundary decohesion, and cleavage proceeded dimpled fracture by void nucleation, growth, and coalescence in Nb-Cr-Ti alloys.
3. Decohesion of slipbands and possibly void nucleation in Nb-Cr-Ti alloys occurs by an intersecting slip process. The decohered slipbands appear to serve as the void nuclei for further growth and coalescence, eventually leading to dimpled fracture.

## ACKNOWLEDGEMENTS

This work was supported by the Air Force Office of Scientific Research through Contract No. F49620-95-0043, Dr. Spencer Wu, Program Manager. The technical assistance by B. Chapa and the clerical assistance by Ms. L. Salas, both of SwRI, are appreciated.

## REFERENCES

1. K. D. Puttick: *Phil. Mag.*, Vol. 4, 1959, pp. 964-969.
2. T. J. Baker and J. A. Charles: *J. Iron Steel Inst.*, Vol. 210, 1972, pp. 702-706.
3. G. T. Hahn and A. R. Rosenfield: *Met. Trans.*, Vol. 6A, 1975, pp. 653-670.

4. J. C. Chesnutt, C. G. Rhodes, and J. C. Williams: Fractography – Microscopic Cracking Processes, ASTM STP 600, C. D. Beachem and W. R. Warke, eds., American Society for Testing and Materials, Philadelphia, PA, 1976, pp. 99-138.
5. Kwai S. Chan: *Met. Trans. A.*, Vol. 27A, 1996, pp. 2518-2531.
6. D. L. Davidson, K. S. Chan, and D. L. Anton: *Met. Trans. A*, Vol. 27A, pp. 3007-3018.
7. J. Dipasquale, D. Gahutu, D. Konitzer, and W. Soboyejo: *Materials Research Society Proceedings*. Materials Research Society, Pittsburgh, PA, Vol. 364, 1995, pp. 1347-52.
8. V. K. Sikka and E. A. Loria: *Mat. Sci. Eng*, Vol. 239-40, 1997, pp. 745-751.
9. M. G. Medira, R. Goetz, D. M. Dimiduk, and J. J. Lewandowski: *Metall. Trans. A.*, Vol. 26A, 1995, pp. 1767-1776.
10. K. S. Chan: *Met. Trans. A.*, Vol. 23A, 1992, pp. 183-199.
11. H. Chiu and X. Mao: *Met. Mat. Trans. A.*, Vol. 27A, 1996, pp. 3817-3825.
12. A. H. Cottrell: *Trans. AIME*, Vol. 212, 1958, pp. 192-203.
13. A. N. Stroh: *Proc. Roy. Soc. A.*, Vol. 223, 1954, pp. 597-606.
14. Kwai S. Chan: In Recent Advances in Fracture, R. K. Mahidhara, A. B. Geltmacher, P. Matic and K. Sadananda, eds., TMS, Warrendale, PA, 1997, pp. 137-157.
15. A. Nagy, J. B. Campbell, and D. L. Davidson: *Rev. Sci. Instrum.*, Vol. 55, 1984, pp. 778-82.
16. K. S. Chan and D. L. Davidson: *Met. Trans. A*, Submitted (1998).
17. H. C. Rogers: *Transaction of TMS-AIME*, Vol. 218, 1960, pp. 498-506.
18. K. S. Chan: Micromechanics of Advanced Materials, S. N. G. Chu, P. K. Liaw, K. S. Chan, R. J. Arsenault, K. Sadananda, W. W. Gerberich, C. C. Chau, and T. M. Chung, eds., TMS, Warrendale, PA, 1995. pp. 113-120.
19. J. N. Wang: *Acta Metall.*, Vol. 44, 1996, pp. 1541-1546.
20. A. J. E. Foreman: *Acta Metall.*, 1955, Vol. 3, pp. 322-330.

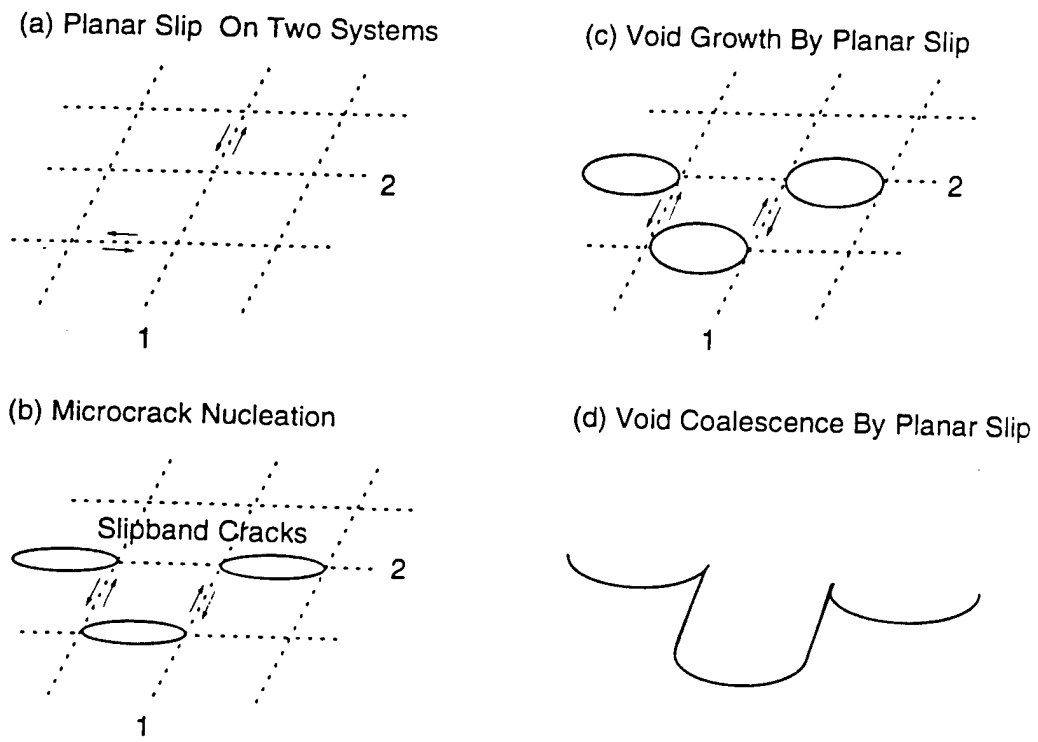


Figure 1. Proposed void nucleation, growth, and coalescence by intersecting slip for planar slip materials [14]: (a) planar slip on two intersecting slip systems, (b) microcrack nucleation by decohesion on planar slipbands on a set of slip planes, (c) opening up of slipband microcracks into voids by slip on the intersecting slip planes, and (d) dimpled fracture surfaces formed after void coalescence by planar slip.

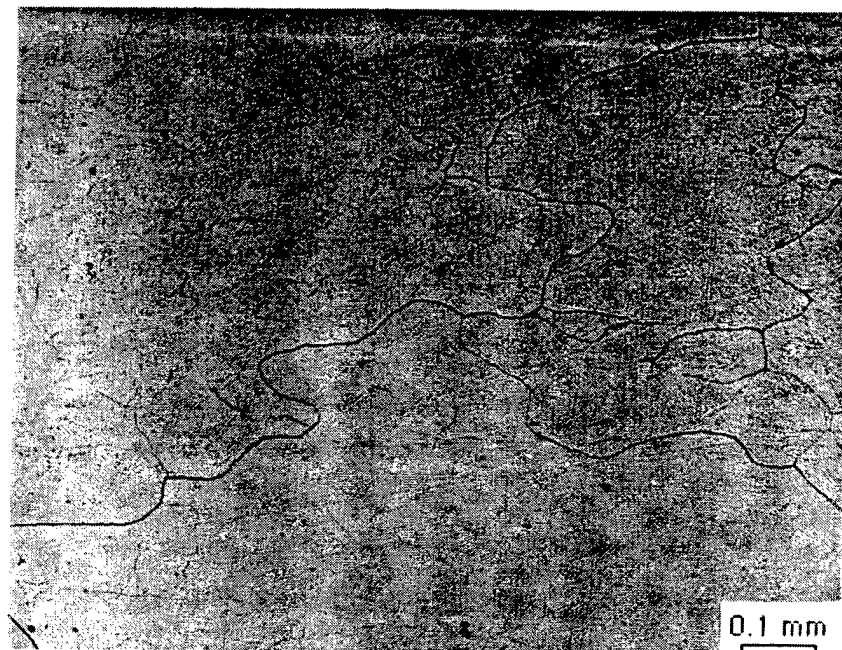


Figure 2. Optical micrograph of Nb-13Cr-37Ti solid solution alloy shows a single-phase, large-grained microstructure with a 1500  $\mu\text{m}$  average grain size.

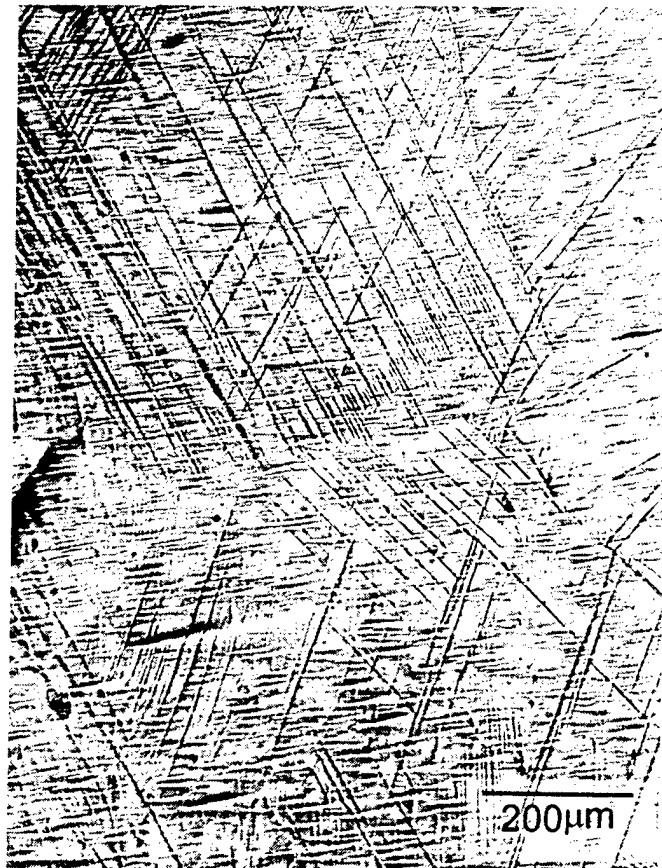


Figure 3. Planar slip on intersecting slip systems in Nb-13Cr-37Ti at ambient temperature.

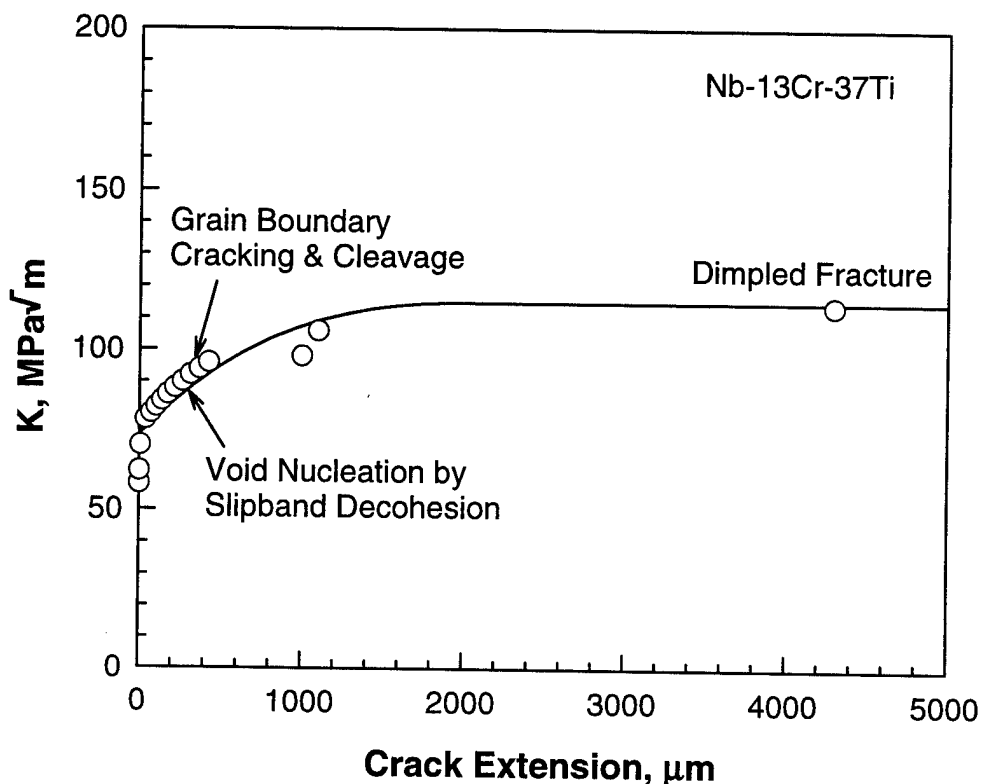
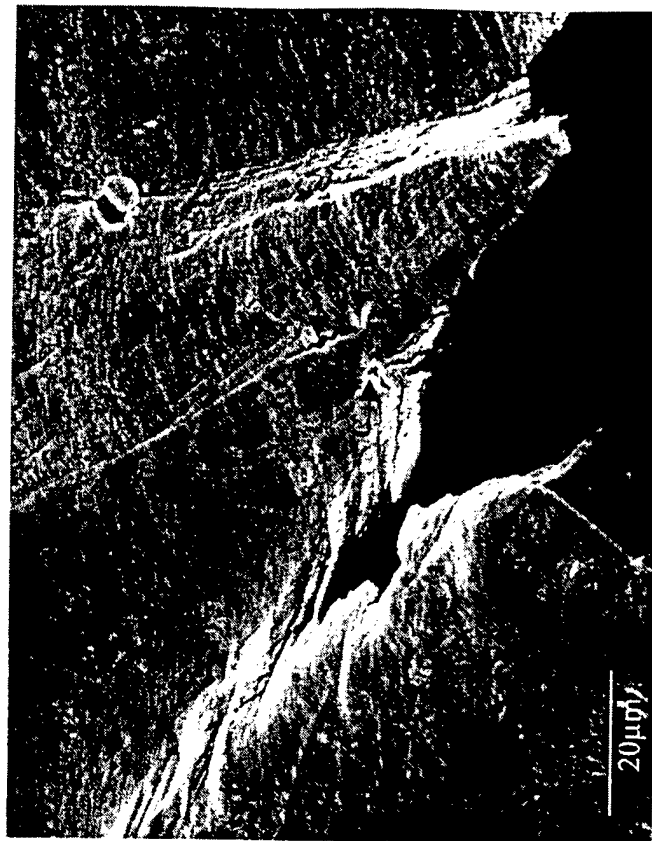


Figure 4. K-resistance curve for the tough Nb-Cr-Ti alloy (Nb-40Ti-13Cr) showing the K levels for the onset of void nucleation by slipband decohesion, grain boundary cracking and cleavage, and dimpled fracture.



(a)

(b)

Figure 5. Void nucleation by decohesion of small segments of planar slipbands in the crack-tip plastic zone: (a)  $K = 98 \text{ MPa}\sqrt{\text{m}}$ , and (b)  $K = 106 \text{ MPa}\sqrt{\text{m}}$ .

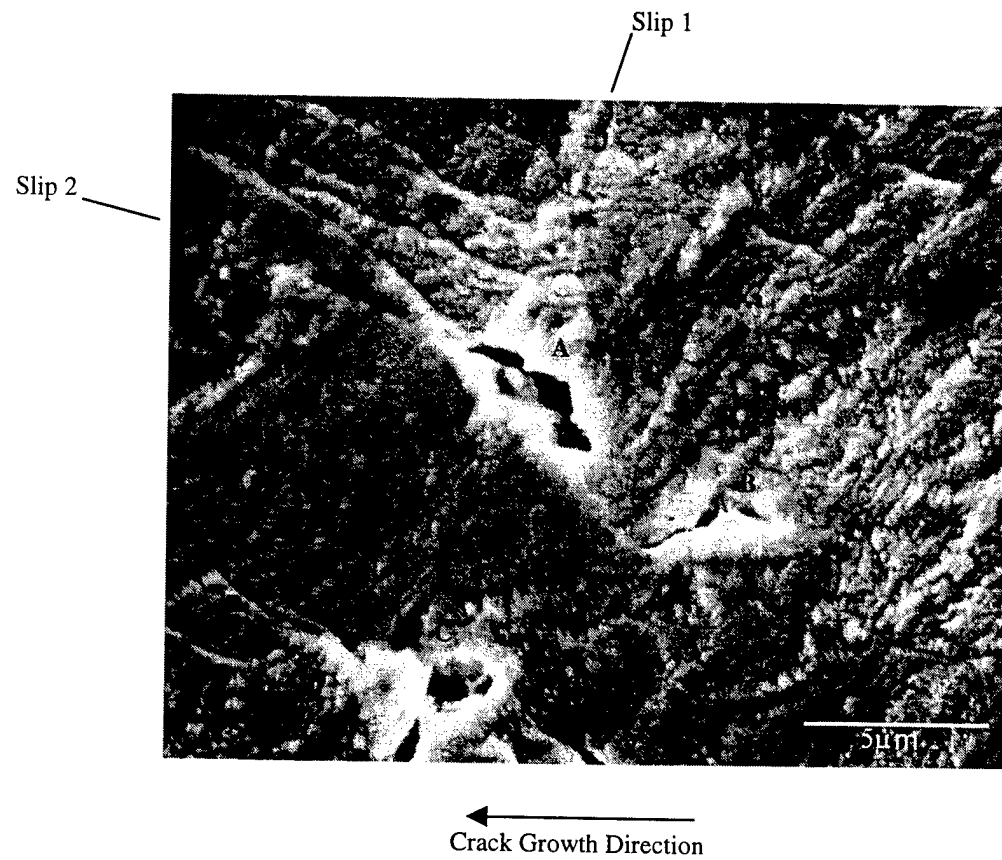


Figure 6. A close-up view of the coalesced voids along a planar slipband at  $K = 106 \text{ MPa}\sqrt{\text{m}}$ .

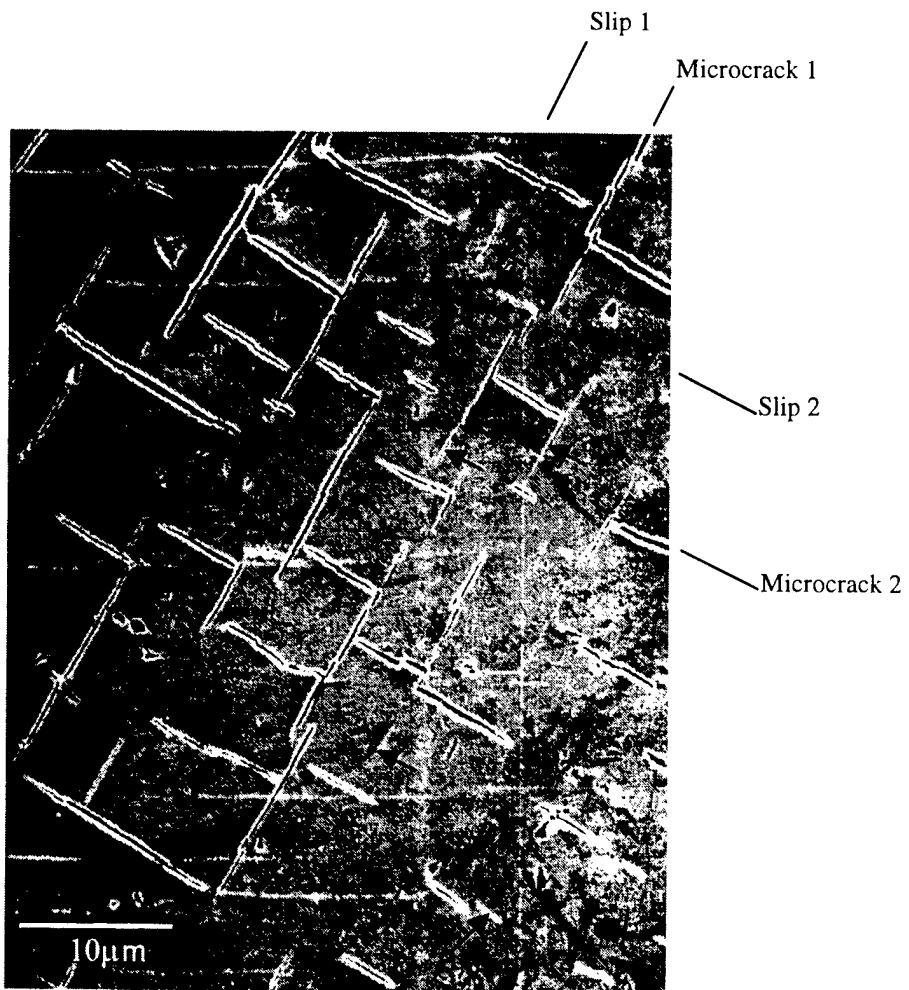
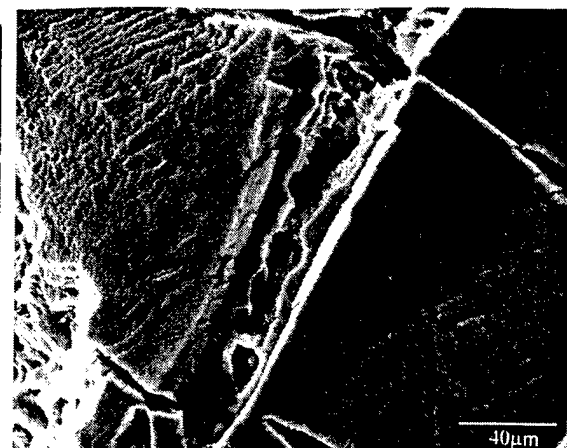


Figure 7. Two sets of aligned microcracks formed in the Nb-13Cr-37Ti alloy at  $K = 112 \text{ MPa}\sqrt{\text{m}}$ . Arrows indicate slip lines. The microcracks appeared to form by decohesion on two intersecting planar slipbands.



(a)



(b)



(c)

Figure 8. Evidence of void nucleation, growth, and coalescence within planar slipbands: (a) void formation, (b) void growth and coalescence, and (c) dimpled fracture within a slipband. Observations made in a specimen that fractured at 112 MPa/m.

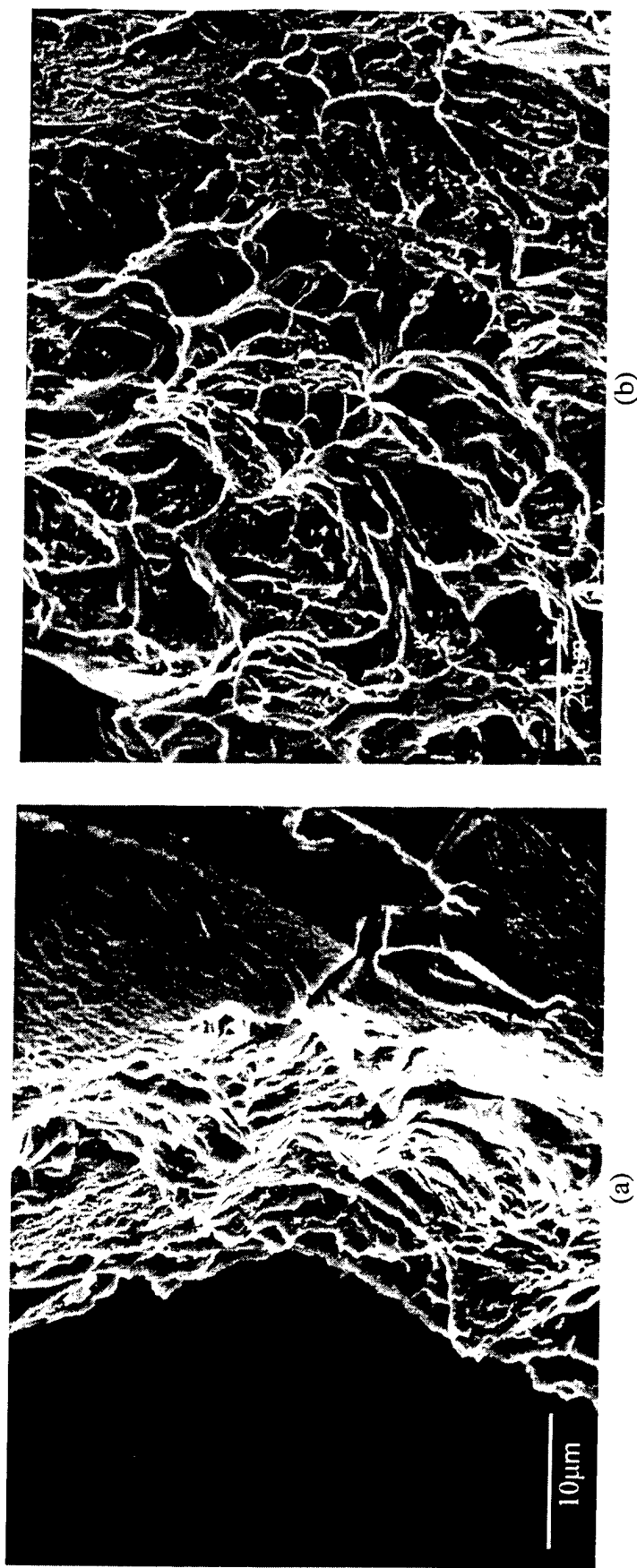


Figure 9. Dimpled fracture in Nb-Cr-Ti alloy: (a) fracture surface in relation to slipband cracks, and (b) dimples formed by void nucleation, growth, and coalescence on planar slipbands. Specimen fracture at  $K = 112 \text{ MPa}\sqrt{\text{m}}$ .

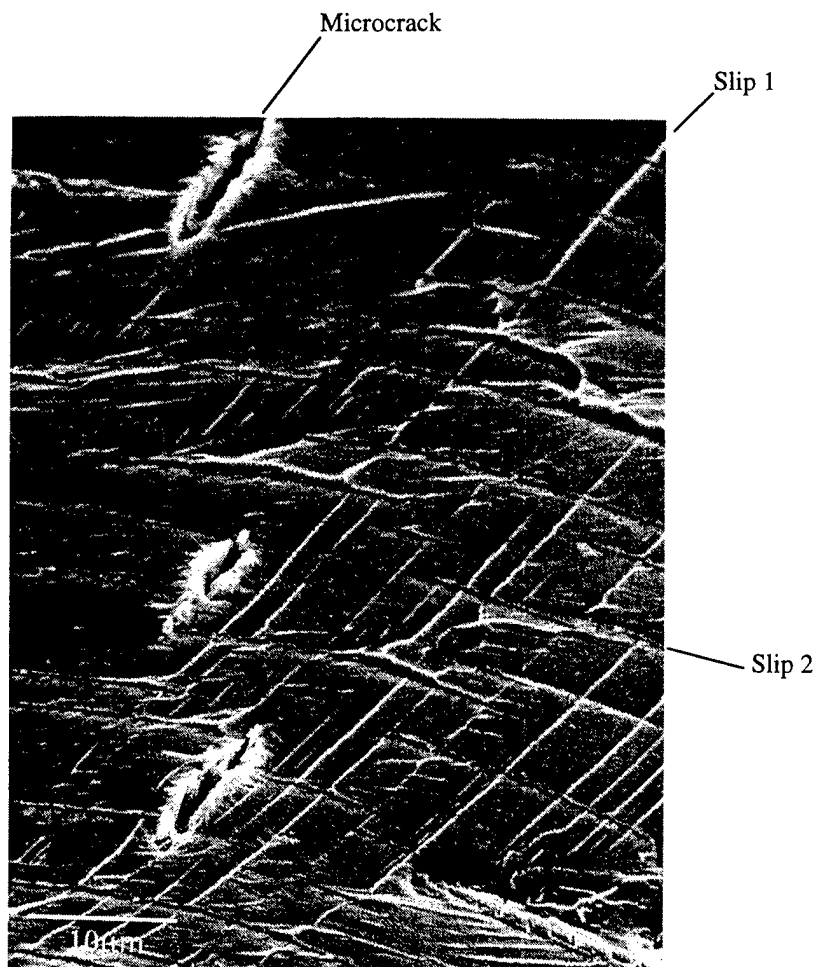


Figure 10. Fracture surfaces showing decohered microcracks on intersecting slip planes in the interior of the fractured specimen. Specimen fractured at  $K = 112 \text{ MPa}\sqrt{\text{m}}$ .

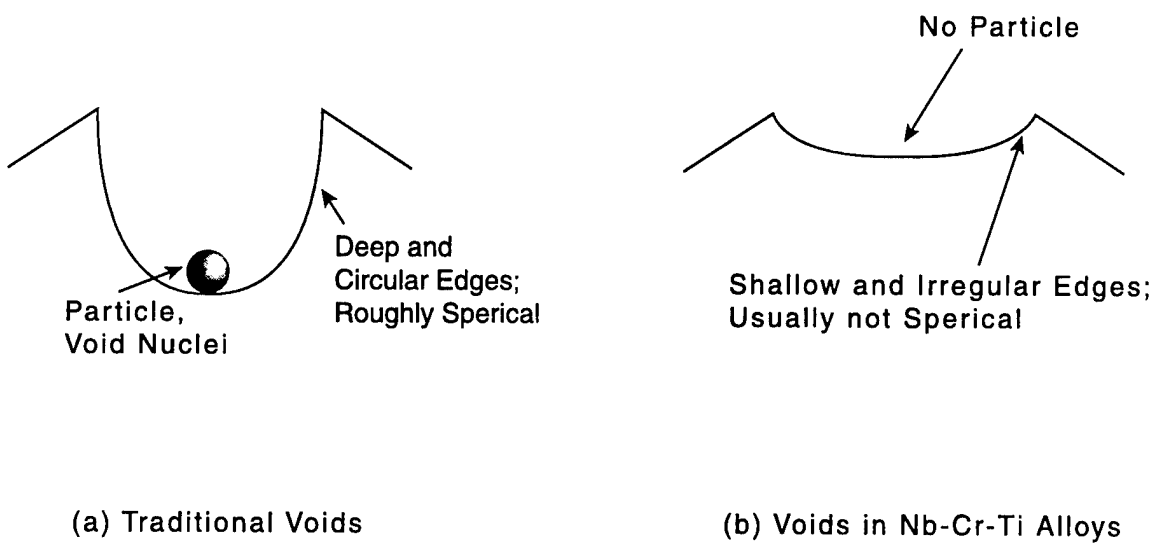


Figure 11. A comparison of the characteristic microvoids in Nb-Cr-Ti alloys against the traditional microvoids in materials such as copper, steel, and aluminum alloys.

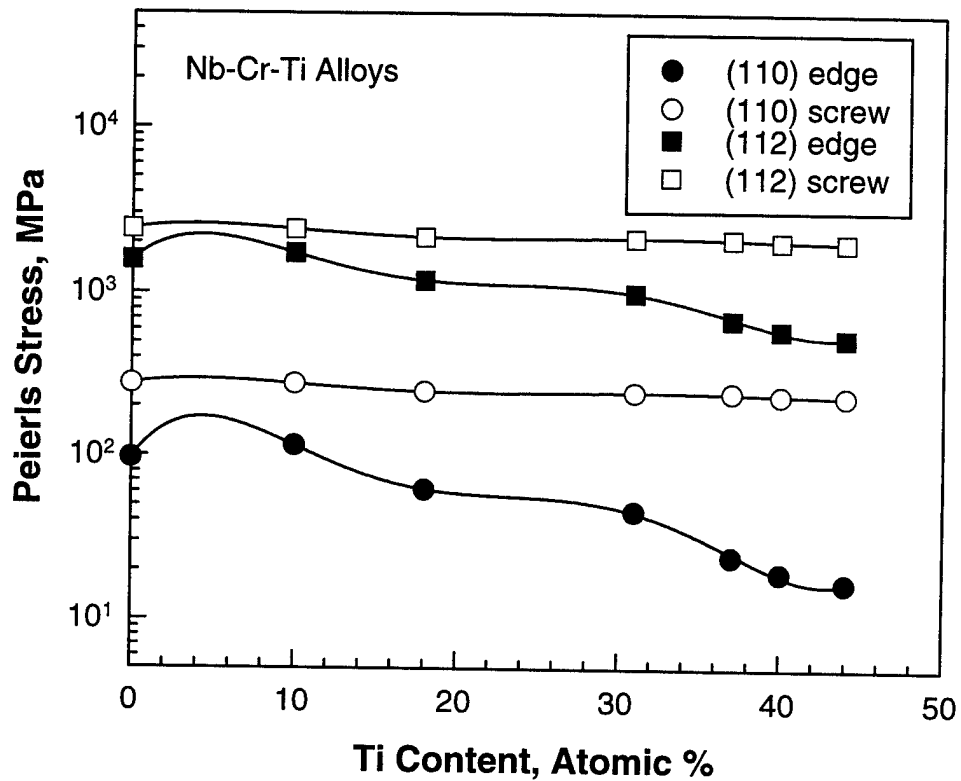


Figure 12. Values of Peierls stress calculated for  $\langle 1\ 1\rangle$  edge and screw dislocations on the (110) and (112) planes as a function of Ti content. The higher Peierls stress for (112) screw compared to the (112) edge is thought to be responsible for planar slip and decohesion on the (112) plane observed in the Nb-Cr-Ti alloys.

## List of Figure Captions

Figure 1. Proposed void nucleation, growth, and coalescence by intersecting slip for planar slip materials [14]: (a) Planar slip on two intersecting slip systems, (b) microcrack nucleation by decohesion on planar slipbands on a set of slip planes, (c) opening up of slipband microcracks into voids by slip on the intersecting slip planes, and (d) dimpled fracture surfaces formed after void coalescence by planar slip.

Figure 2. Optical micrograph of Nb-13Cr-37Ti solid solution alloy shows a single-phase, large-grained microstructure with a 1500  $\mu\text{m}$  average grain size.

Figure 3. Planar slip on intersecting slip systems in Nb-13Cr-37Ti at ambient temperature.

Figure 4. K-resistance curve for the tough Nb-Cr-Ti alloy (Nb-40Ti-13Cr) showing the K levels for the onset of void nucleation by slipband decohesion, grain boundary cracking and cleavage, and dimpled fracture.

Figure 5. Void nucleation by decohesion of small segments of planar slipbands in the crack-tip plastic zone: (a)  $K = 98 \text{ MPa}\sqrt{\text{m}}$ , and (b)  $K = 106 \text{ MPa}\sqrt{\text{m}}$ .

Figure 6. A close-up view of the coalesced voids along a planar slipband at  $K = 106 \text{ MPa}\sqrt{\text{m}}$ .

Figure 7. Two sets of aligned microcracks formed in the Nb-13Cr-37Ti alloy at  $K = 112 \text{ MPa}\sqrt{\text{m}}$ . Arrows indicate slip lines. The microcracks appeared to form by decohesion on two intersecting planar slipbands.

Figure 8. Evidence of void nucleation, growth, and coalescence within planar slipbands: (a) voids formation, (b) void growth and coalescence, and (c) dimpled fracture within a slipband. Observations made in a specimen that fractured at 112  $\text{MPa}\sqrt{\text{m}}$ .

Figure 9. Dimpled fracture in Nb-Cr-Ti alloy: (a) fracture surface in relation to slipband cracks, and (b) dimples formed by void nucleation, growth, and coalescence on planar slipbands. Specimen fracture at  $K = 112 \text{ MPa}\sqrt{\text{m}}$ .

Figure 10. Fracture surfaces showing decohered microcracks on intersecting slip planes in the interior of the fractured specimen. Specimen fractured at  $K = 112 \text{ MPa}\sqrt{\text{m}}$ .

Figure 11. A comparison of the characteristic microvoids in Nb-Cr-Ti alloys against the traditional microvoids in materials such as copper, steel, and aluminum alloys.

Figure 12. Values of Peierls stress calculated for  $<1\ 1>$  edge and screw dislocations on the (110) and (112) planes as a function of Ti content. The higher Peierls stress for (112) screw compared to the (112) edge is thought to be responsible for planar slip and decohesion on the (112) plane observed in the Nb-Cr-Ti alloys.

## SUMMARY AND CONCLUSIONS

1. The high fracture toughness of 50Nb-13Cr-37Ti, as made by casting technology, was thoroughly investigated to find the reason for its greatly enhanced fracture toughness ( $K_c = 60\text{-}100 \text{ MPa}\sqrt{\text{m}}$ ). The reasons for increased toughness were found to be the increased mobility of dislocations emitted at the crack tip. Alloying of Nb-Cr with Ti caused a reduction in the Peierls-Nabarro stress required to move dislocations, particularly edge dislocations. The ease of edge dislocation motion was confirmed by transmission electron microscopy. The reduction in P-N stress is a direct result of decreasing through alloying the valence electrons that bond the material.
2. Two phase materials (*in situ* composites) lying along the tie line on the phase diagram between the high fracture toughness matrix 50Nb-13Cr-37Ti alloy and  $\text{Cr}_2\text{Nb}$  were made by casting. Materials with 22 and 38 v/o  $\text{Cr}_2\text{Nb}$  were investigated and found to have greatly reduced values of fracture toughness ( $K_c = 16$  and  $18.5 \text{ MPa}\sqrt{\text{m}}$ ) The dispersion and size of the  $\text{Cr}_2\text{Nb}$  were found to be important variables that control fracture toughness.
3. Reasons for the poor fracture behavior of the composites fabricated by conventional casting were identified: (1) the approximately  $15 \mu\text{m}$  particles of  $\text{Cr}_2\text{Nb}$  ( $K_c \approx 1.3 \text{ MPa}\sqrt{\text{m}}$ ) were found to break at antishielding locations relative to the crack tip, and (2) particles were found to constrain deformation in the matrix, to reduce the strain at the crack tip, and the size of the plastic zone. Fractography indicated that microvoid formation and coalescence was not the dominant mode of fracture; fracture was by cleavage.
4. The experimental results suggested that  $K_c$  could be increased by reducing the size of the  $\text{Cr}_2\text{Nb}$  particles, which would prevent their fracture. But a reduction in particle size was also expected to increase constraint in the crack tip process zone, elevating the stress, which would induce cleavage fracture.
5. Rapid solidification casting of the same compositions used in (2) was used to produce materials with smaller  $\text{Cr}_2\text{Nb}$  dimensions, but a poor dispersion of particles with high contiguity was the resulting microstructure. These materials demonstrated low fracture toughness ( $K_c = 7.5$  to  $10 \text{ MPa}\sqrt{\text{m}}$ ).

6. Composites with the same compositions were next fabricated by mechanical alloying (MA), which should allow a mixing of elements without the formation of the intermetallic. Subsequent heat treatment then allowed the intermetallic to be precipitated under controlled conditions. The Defence Research Agency of England made the materials using a facility that was especially built to avoid interstitial contamination of reactive metals.

7. The maximum fracture toughness measured for the MA materials was  $\approx 12$  MPa $\sqrt{m}$  for a composite with  $\approx 25$  v/o Cr<sub>2</sub>Nb. In this material, the intermetallic was reasonably well dispersed and quite small (0.1 to 1  $\mu$ m). The crack path was not preferential to the Cr<sub>2</sub>Nb particles or the matrix, although interfacial fracture sometimes occurred. Fracture toughness was limited because the small size of the particles at this volume fraction resulted in a high plastic constraint in the matrix, which resulted in low crack tip fracture strains at the onset of fast fracture.

8. The effects of plastic constraint on matrix fracture were included in a material model in which the variables were particle size and volume fraction. The conclusion drawn from this work was that fracture toughness cannot be expected to exceed  $\approx 25$  MPa $\sqrt{m}$  for a 40 v/o composite containing spherical Cr<sub>2</sub>Nb particles, even when the microstructure has been optimized. Fracture toughness is prevented from rising to higher levels by the limited deformation of the matrix within the process zone of the crack tip that results from the constraint of particles.

9. To achieve a higher fracture toughness with Cr<sub>2</sub>Nb particles at the 40 v/o reinforcement level will require that a way be found to produce Cr<sub>2</sub>Nb that deforms before fracture; i.e., has a higher fracture toughness.

10. If a Cr<sub>2</sub>Nb-based composite cannot be formulated in which the particles deform before fracture, then it will be necessary to find another intermetallic on which to base the composite to achieve higher fracture toughness values.

11. Fracture experiments performed on Nb-10Si, containing crystalline Nb<sub>5</sub>Si<sub>3</sub> that was formed in situ, indicated that plasticity in the intermetallic was possible at ambient temperature near the tip of a crack. Fracture toughness experiments performed elsewhere as a function of volume fraction of Nb<sub>5</sub>Si<sub>3</sub> resulted in values close to rule-of-mixture levels.

12. Fracture studies of two solid solution Nb-Ti alloys, containing both Al and Cr, indicated that fracture toughness was reduced when these two elements were present together. One alloy was made by Los Alamos National Laboratory, and the other by Reference Metals, Inc. The reason for low fracture toughness was found to be that cracks propagated by cleavage fracture at low levels of strain. This result suggests that alloying increased unstable stacking energy, making the nucleation of dislocations from the crack tip difficult, which promotes cleavage crack formation. A TEM investigation of Ti-V-Cr-Al alloys just published indicates that 4 at.% Al causes alloys to become ordered, thereby reducing their deformability.

13. Work on similar alloys by Jackson and Jones at GER&D found that ductility was reduced when the alloy contained both Al and Cr, in contrast to materials where only Cr or Al was present.

14. Fatigue crack growth rates are similar for all the materials examined at  $10^{-9}$  m/cycle and below. Values of  $\Delta K_{th} \approx 6 \pm 1$  MPa $\sqrt{m}$  for all the materials. Alloys containing Al tended to have lower values of  $\Delta K_{th}$ , while materials containing Cr<sub>2</sub>Nb had higher values. The slope of the da/dN- $\Delta K$  curve is high (40-70) in the near-threshold region.

15. The slope of the fatigue crack growth rate curve at rates greater than  $10^{-9}$  m/cycle depends on the magnitude of fracture toughness: the higher the toughness, the lower the slope of the da/dN- $\Delta K$  curve.

## PUBLICATIONS FROM THIS PROGRAM

1. "Microcrack Nucleation By Slipband Decohesion," by K. S. Chan, **Proceedings of the James LI Symposium on Micromechanics of Advanced Materials**, edited by S. N. G. Chu, P. K. Liaw, R. J. Arsenault, K. Sadananda, K. S. Chan, W. W. Gerberich, C. C. Chau, and T. M. Kung, TMS, Warrendale, PA, 1995, pp. 113-120.
2. "The Fracture Toughness of Niobium-Based, *In-Situ* Composites," by K. S. Chan, Metallurgical and Materials Transactions A, Vol. 27A, 1996, pp. 2518-2531.
3. "The Fracture Resistance and Crack-Tip Micromechanics of *In-Situ* Intermetallic Composites," by K. S. Chan and D. L. Davidson, JOM, Vol. 48, No. 9, September 1996, pp. 62-68.
4. "The Effects on Fracture Toughness of Ductile Phase Composition and Morphology in Nb-Cr-Ti and Nb-Si *In-Situ* Composites," by D. L. Davidson, K. S. Chan, and D. L. Anton, Metallurgical and Materials Transactions, Vol.27A, 1996, pp. 3007-3018.
5. "The Effect of Microstructure on the Fracture Resistance of Nb-Cr-Ti *In-Situ* Composites," D. L. Davidson and K. S. Chan, Scripta Materialia, Vol. 38, No. 7, 1997, pp. 1155-1161.
6. "Near-tip Fracture Processes in Ductile Materials," by K. S. Chan, **Recent Advances in Fracture**, edited by R. K. Mahidhara, A. B. Geltmacher, P. Matic, and K. Sadananda, TMS, Warrendale, PA, 1997, pp. 137-157.
7. "Shear-Induced Cleavage Fracture," by K. S. Chan, **Proceedings of George R. Irwin Symposium on Cleavage Fracture**, edited by K. S. Chan, TMS, Warrendale, PA, 1997, pp. 207-220.
8. "Constraint Effects on Fracture Toughness of Intermetallic Alloys and *In-Situ* Composites," by K. S. Chan, **Proceedings of International Symposium on Structural Intermetallics - II**, edited by M. V. Nathal, R. Darolia, C. T. Liu, P. L. Martin, D. B. Miracle, R. Wagner, and M. Yamaguchi, TMS, Warrendale, PA, 1997, pp. 11-20.

9. "Fracture Toughness and Fatigue Crack Growth in Rapidly Quenched Nb-Cr-Ti *In-Situ* Composites," by K. S. Chan, D. L. Davidson, and D. L. Anton, Metallurgical and Materials Transactions, Vol. 28A, 1997, pp. 1797-1808.
10. "Fatigue Crack Growth through Alloyed Niobium, Nb-Cr<sub>2</sub>Nb, and Nb-Nb<sub>5</sub>Si<sub>3</sub> *In-Situ* Composites," by D. L. Davidson, Metallurgical and Materials Transactions A, Vol. 28A, 1997, pp. 1297-1314.
11. "Effects of Ti Addition on Cleavage Fracture in Nb-Cr-Ti Solid Solution Alloys," by K. S. Chan and K. L. Davidson, Metallurgical and Materials Transactions A, 1998 (in press).
12. "Evidence of Void Nucleation and Growth on Planar Slip Bands," by K. S. Chan and D. L. Davidson, Metallurgical and Materials Transactions A, 1998 (in review).
13. "Transition metal alloys: elastic properties and Peierls-Nabarro stresses and barrier energies" by D.L. Davidson, Materials Science and Engineering, 1998 (in review).
14. "Cluster model for calculation of unstable stacking energy to assist in alloying of transition metals " by D.L. Davidson and R.E. Beissner (in preparation).
15. "The fatigue Resistance of TiAl-based Alloys," by K.S. Chan, JOM, v. 49, 1997, pp 53-58.
16. "The Fracture Resistance of a Binary TiAl Alloy" by K.S. Chan, J. Onstott, and K.S. Kumar, Metallurgical and Materials Transactions A, 1998 (in review).
17. "FEM Simulation of Effects of Microstructure, Stress State, and Interface Strength on Flow Localization and Constraint Development in Nb/Cr<sub>2</sub>Nb *In-Situ* Composites" by K.S. Chan and G. Lin, Metallurgical and Materials Transactions A, 1998 (in review).
18. "Fatigue Life Analysis of Unexpected Failure in a Lamellar TiAl Alloy" by K.S. Chan, in Fatigue Behavior of Titanium Alloys, edited by R.R. Boyer and D. Eylon, TMS, Warrendale, PA, 1998 (in review).

19. "The Fatigue and Fracture Resistance of a Nb-Cr-Ti-Al Alloy" by D.L. Davidson and K.S. Chan, Metallurgical and Materials Transactions A, 1998 (in review).
20. "Statistical Simulation of Small Crack Fatigue Crack Nucleation and Coalescence in a Lamellar TiAl Alloy" by K.S. Chan, B. Wittowsky, and M. Pfuff, Metallurgical and Materials Transactions A, 1998 (in review).